Master's thesis

NTNU
Norwegian University of Science and Technology
Faculty of Engineering
Department of Marine Technology

Emilie M. Hyrum Dahl
Andreas Øyhus-Revling Stien

Identification of Marine Plastics using Hyperspectral Imaging and Raman Spectroscopy

Master's thesis in Engineering and ICT
Supervisor: Asgeir J. Sørensen
June 2019

NTNU
Kunnskap for en bedre verden

Emilie M. Hyrum Dahl
Andreas Øyhus-Revling Stien

Identification of Marine Plastics using Hyperspectral Imaging and Raman Spectroscopy

Master's thesis in Engineering and ICT
Supervisor: Asgeir J. Sørensen
June 2019

Norwegian University of Science and Technology
Faculty of Engineering
Department of Marine Technology

NTNU
Norwegian University of
Science and Technology

NTNU Trondheim
Norwegian University of Science and Technology
Department of Marine Technology

MASTER THESIS IN MARINE CYBERNETICS

SPRING 2019

FOR

STUD. TECHN. EMILIE M. HYRUM DAHL
& STUD. TECHN. ANDREAS ØYHUS-REVLING STIEN

Identification of Marine Plastics using Hyperspectral Imaging and Raman Spectroscopy

Work description (short description)
The master thesis aims to contribute in the development of an in situ detection of marine microplastic on a sensor-carrying platform. This will involve trying to detect and characterize plastic particles and compare to other organic material. Furthermore, imaging methods regarding underwater hyperspectral imaging and Raman spectroscopy will be studied and compared. Then, different methods for detection and classification using statistical, and possibly big data, methods will be used to analyze the data. Lastly the sensors will be tested on a sensor-carrying platform.

Scope of work

1. Describe the problem of microplastics in the oceans and the current situation and work done on the topic of underwater hyperspectral imaging
2. Carry out a pilot study that demonstrates the application of underwater hyperspectral imaging camera for detection and classification of microplastic in the infrared light spectrum
3. Carry out a pilot study that demonstrates the application of Raman spectroscopy for detection and classification of microplastic in the infrared light spectrum
4. Analyse and write a report demonstrating the findings and evaluate further work based on these

The report shall be written in English and edited as a research report including literature survey, description of mathematical models, description of control algorithms, simulation results, model test results, discussion and a conclusion including a proposal for further work. Source code should be provided. It is supposed that Department of Marine Technology, NTNU, can use the results freely in its research work, unless otherwise agreed upon, by referring to the student's work.

The thesis should be submitted within 11. June.

Advisors: Lise Lyngsnes Randeberg, Geir Johnsen and Emlyn John Davies

Professor Asgeir J. Sørensen
Supervisor

Emilie M. Hyrum Dahl
Student

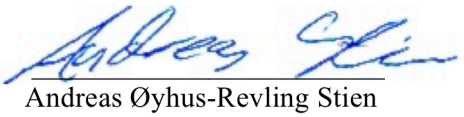

Andreas Øyhus-Revling Stien
Student

Preface

When choosing a theme for the master thesis, the selection of the topic was passion driven. Within the last years, we have participated in case competitions and campaigns concerning this immense challenge. The main topic of this thesis, plastic and its expansive consequences, is close to our hearts and is genuinely engaging us. Hopefully, and very likely, our commitment will remain - also after this thesis.

This thesis is submitted in partial fulfillment of the requirements for the degree of Master of Science (M.Sc.) at the Norwegian University of Science and Technology (NTNU). The main work is completed at the Department of Marine Technology, NTNU, while part of the work has been conducted at the Department of Electronic Systems, NTNU, the Department of Biology, NTNU, the Department of Materials Science and Engineering, NTNU, SINTEF Ocean and from a boat, MS Hasse, in Lofoten.

In December 2018, a project thesis was delivered as a pre-project to the master thesis. The research and results from the project thesis have, partly, created the grounds for the work done in the master thesis. The master thesis can, therefore, be viewed as a continuation of the project thesis, Stien and Dahl (2018).

The work supporting this thesis is three-folded. In order to achieve consistent and precise knowledge, a study of relevant literature was done. This study includes research on both specific methods and techniques used, as well as initiatives and solutions to solving the problem in general. The research regarding these topics was done mainly by studying a set of scientific papers.

However, even with the most recent publications, there is still research done - not yet published. The second part of this thesis was, therefore, to travel around Trondheim meeting with the experts, acquiring new knowledge. After which, the problem description finally took form.

We realized that we wanted to arrange and manage the entire research process, from start to finish. We did everything from mapping the field, to collecting and processing the material, to creating the laboratory set-up and building the database, and finally analyzing the data. This execution and completion of the research represent the third and last part of the three-folded process.

Last semester, we attended two, particularly relevant, module courses, *TTK19 Structures and Contexts in Complex Systems* - a course on how to handle Quantitative Big Data, and *TTK20 Hyperspectral remote sensing* - providing in-depth knowledge on relevant hyperspectral imaging techniques. This insight helped the understanding of the task at hand, giving valuable knowledge, much reflected in this thesis.

Trondheim, June, 2019

Emilie M. H. Dahl

Andreas Ø.R Stien

Acknowledgments

This work has been carried out at the Centre for Autonomous Marine Operations and Systems (AMOS). The authors of this thesis would particularly like to thank our supervisor Professor Asgeir J. Sørensen, at IMT NTNU, who have given us guidance and support throughout the whole year - he is simply priceless. Similarly, a enormous gratitude is directed to Professor Lise Lyngsnes Randeberg, Department of Electronic Systems NTNU, functioning as a second supervisor. She has given us guidance, equipment and eagerly shared of her vast expertise within the field of hyperspectral imaging.

We would also like to give our appreciation the research team at SINTEF Ocean, with Senior Research Scientist Emlyn John Davies in front, for bringing broad support concerning both scientific advice and arranging the field trip to Lofoten.

Furthermore, Ph.D. candidate Asgeir Bjørgan has provided accurate and comprehensive insight on methods for unsupervised learning, which we are profoundly grateful.

Moreover, great gratitude should also be directed towards Professor Geir Johnsen at the Department of Biology NTNU, who - from Hawaii - provided insight and expertise that greatly assisted the research. Ph.D. candidate Aksel Alstad Mogstad, at the Department of Biology NTNU, is also acknowledged for bringing personal ideas to the table and giving support when needed.

Throughout this study, a large number of scientists and friends have helped us out. We will not name them all, but give a special recognition to a few; Staff engineer Grethe Stavik Eggen and Head Engineer Trude Johansen, both at Department of Biology NTNU, Ph.D. candidate Fredrik Samdal Solberg, TrollLabs NTNU, Postdoctoral Fellow Bartlomiej Gawel, Department of Materials Science and Engineering NTNU, Professor Frank Ove Westad, Department of Engineering Cybernetics NTNU, Staff Engineer Sebastian Bete, NV Faculty Administration NTNU and Research Scientist Julia Farkas, SINTEF Ocean.

Abstract

The ocean plays a great part in life on earth, not only as a source of oxygen and food for living beings but also as a vital influence on the climate and weather. The ocean, with all that comes with it, is simply a necessity for life on earth. Nevertheless, that same ocean is not taken care of. Plastic and subsequently microplastic contamination is currently present at the highest and lowest points on the planet, permeating almost every aspect of modern day life with its wide applicability.

The road towards a clean sea contains several legs and does at the very least require a mapping of the ocean columns, determining critical areas. Proper methods and technology for mapping and monitoring need to be addressed. This promptly calls for the development of in-situ detection methods. Hyperspectral Imaging and Raman spectroscopy may be such technologies, in principle able to extract the chemical structure of the object to be viewed by collecting spectral signatures at the areas of illumination. This study will cover *whether it is possible to classify specific types of microplastics underwater by identifying their spectral signatures.* The research includes the investigation of plastic identification using NIR Hyperspectral imaging, Hyspex SWIR 320-e, Norsk Elektro Optikk AS, Skedsmokorset, Norway (2019), in the interval of 960-2400 nm and Raman Spectroscopy, Witec UHTS 300 SMFC VIS Raman Spectroscope, WITec GmbH (2019), at 532 nm.

Moving across the two techniques, the general lines of the experiments are more or less identical. The studied material consists of plastic samples ordered from CARAT GmbH. These samples are of different type, color and condition (varying from pristine samples to sorted, recycled plastic, to post-consumer particles). In addition, the samples were milled to add a category - size, creating a total of 25 categorized samples. These samples are meant to build a supervised model, predicting unknown plastics. The unknown particles were collected from the sea outside Svolvær, Lofoten - 17 particles in total. In order to retrieve data, sample measurements were performed in three ways, using bare plastic, plastic in water and the untreated, unclassified, sea-influenced samples.

Within the two methods, the data was unequally processed and analyses. The Raman data was filtered using a Savitzky–Golay filter, before building a partial least squares discriminant analysis (PLS-DA) model, analyzed in Unscrambler X, CAMOAnalytics (2019). The infrared hyperspectral data, on the other hand, was analyzed using K-means clustering and Spectral Angle Mapper (SAM) algorithms for classification purposes.

The conclusions suggested by the results are that the predictions, and hence the models, seem to classify plastics independent on size, color and environment. This reasoning also applies to plastics under a film of water, as well as sea-influenced plastic particles. However, variations in condition appear to influence the spectral signature of the associated plastic type, altering the general signature of the specific type. This leaves the mapping and classification method more suitable for plastics that recently entered the ocean.

Sammendrag

Dagens Næringsliv (DN) hadde følgende overskrift 28. Mai i år (forfatter: Jørn Aass); "Alarmerende forskning: Plast i havet påvirker oksygenet vi puster inn". Plastforsøpling påvirker havet, som igjen er en sentral del av livet på jorden – både i vann og på land. Likevel, blir ikke havet tatt vare på. I dag, er plastforurensning et faktum, både på de høyeste fjelltoppene og i de laveste havgropene. Med sin brede anvendelighet gjennomsyrer forurensningen nesten alle aspekter av det moderne liv.

Veien mot et rent hav inneholder flere etapper og krever, på det minste, en kartlegging av havrommet for å bestemme kritiske områder. Dette krever en omgående utvikling av in situ-deteksjonsmetoder. Hyperspektral avbildning og Raman spektroskopi kan være slike teknologier. I prinsippet skal de begge kunne trekke ut den kjemiske strukturen til det observerte objektet ved å samle spektrale signaturer fra områdene belyst. Denne rapporten vil dermed forsøke å avdekke om det er mulig å klassifisere mikroplast under vann, ved å identifisere deres respektive spektrale signaturer. Studiet som støtter avhandlingen, omfatter undersøkelser av plastidentifikasjon ved hjelp av nær infrarød hyperspektral avbildning (Hyspex SWIR 320-e, Norsk Elektro Optikk AS, Skedsmokorset, Norway (2019), i intervallet 960-2400 nm) og Raman spektroskopi (Witec UHTS 300 SMFC VIS Raman Spectroscope, WITec GmbH (2019), ved 532 nm).

Ved anvendelsen av de to teknikkene, er de generelle linjene i forsøkene stort sett identiske. Det studerte materialet er det samme, bestående av plastprøver fra CARAT GmbH. Disse prøvene er av forskjellig type, farge og tilstand. Tilstanden varierer fra uberørte, til sortert, resirkulert plast, til plast kastet fra seg av forbrukere. I tillegg ble prøvene malt med formål om å legge til "størrelse" som enda en kategori. Totalt ble dette 25 kategoriserte prøver. Formålet med disse kjente prøvene er å bygge en supervised maskinlæringsmodell, som skal kunne predikere plasttypen på ukjent plast. Testsettet med ukjente plastprøver, er basert på prøver samlet fra havet utenfor Svolvær, Lofoten. Disse ukjente partiklene, utgjør 17 av totalt 42 prøver. For å hente ut representativ data, ble prøvemålingene gjennomført på tre måter. Først, ved måling av ren, kjent plast, dernest målinger av samme plast i vann, før, tilslutt, målinger av de ukjente plastpartiklene fra Lofoten.

Innenfor de to metodene ble dataene ulikt behandlet og analysert. Raman-dataene ble filtrert ved hjelp av et Savitzky-Golay-filter, før det ble konstruert en partial least squares discriminant analysis (PLS-DA)-modell, analysert i Unscrambler X, CAMOAnalytics (2019). De hyperspektrale dataene ble derimot analysert ved hjelp av algoritmer som K-means clustering og Spectral Angle Mapper (SAM). Dette for klassifikasjonsformål.

Foreslått konklusjonen er at prediksjonen av plast synes å klassifisere plast uavhengig av størrelse, farge og tilstand. Dette gjelder også plast under et tynt lag med vann, og sjøpåvirket plast. De spesifikke spektrene kan imidlertid ikke variere for mye når det gjelder industri- og miljøendringer. Dermed kan det se ut som klassifiseringsmetodene kun er egnet for plast nylig entret havet.

Contents

List of Figures

Chapter 1

Introduction

The tremendous amount of plastic entering the ocean is affecting the marine environment to a large degree. The first step towards a plastic-free ocean is discovering ways to detect microplastic. This chapter will address the "big picture", motivating the work supporting this thesis, before highlighting the main findings obtained in this area.

1.1 Motivation

Today, the applications of plastics are many, making the material popular worldwide. 381 million metric tons of plastic is produced yearly, and the production is projected to nearly double within the next 10-15 years, Geyer et al. (2017). As pieces of plastic degrade over time, the resulting tiny pieces, defined as microplastic, float around as deadly toxins. In 2014, 15 to 51 trillion particles of microplastic were estimated to hover the seas, van Sebille et al. (2015). A vast number of sea animals are known to confuse microplastics with food, often carrying fatal consequences for sea life, again harming human health.

No doubt the motivation towards solving one of this worlds most significant challenges is vast. However, the essential sources to plastics in the seas come from humans dumping garbage in oceans and rivers. 80% of microplastics found in the ocean, originates from human-made, land-based sources, such as bags and bottles, Jambeck et al. (2015). If all dumping ended today, the plastic would still remain in the ocean, causing damage over and over again. In order to reduce the impact, one must first identify the particles.

A good way to work with materials, identify them or learn about their properties, is to study how light interacts with them, one of these studies being spectroscopy. By definition, spectroscopy examines how light behaves in the target and may recognize materials based on their different spectral signatures. An object's respective fingerprint is described through a spectrum. This spectrum is the resulting representation of the amount of light in different wavelengths, showing how much light is reflected, emitted and transmitted from the target. The analysis of the spectrum can reveal unique molecular properties of an object, contributing to an identification of the object.

Spectral signatures can, thus, be thought of as fingerprints. While fingerprints are often used

to identify a person, spectral signatures can be used to identify materials. The objective of this study is, hence, to identify different types of plastic using their spectral signatures. Within spectroscopy, the authors are curious about using two techniques for this purpose, namely hyperspectral imaging and Raman spectroscopy, Pettersen et al. (2013).

The research question driving this project is therefore centered around whether microplastics and their related spectral signatures, in fact, can be separated. Going even further, the question should also involve water, formulating the following research question.

1.2 Research Question

Is it possible to identify plastics in various sizes and in various conditions, underwater, using a hyperspectral imager in infrared light or the Raman spectroscopy? The conclusion of this report will, accordingly, also include a recommendation on whether there is any point in going further with the research - towards an in situ investigation.

1.3 Main Contributions

The main scientific contribution is that the results, from the study completed in this thesis, suggests that both the hyperspectral imager and the Raman spectroscopy methods succeed in identifying, and classifying, microplastics underwater. However, restrictions on both methods are a fact. Whenever organic marine matter block the field of view, e.g. growth, the method fails to identify the microplastics beneath. Also, the specific spectra will vary in terms of industrial or environmental changes, leaving the mapping and classification method suitable for plastics that recently entered the ocean.

1.4 Thesis Outline

This section describes the outline of the thesis. Figure 1.4.1 is a visual description trying to catch the relationships within and between the chapters presented below.

CHAPTER 1

Chapter 1 is an introduction containing the motivation behind the research question, and a short answer to this question, highlighting the main contributions of the work.

CHAPTER 2

Chapter 2 gives a background view on the topic. What has been done so far? What type of sensors and methods has been proven sufficient? And what are the key takeaways relevant when embarking this study?

CHAPTER 3

Chapter 3 takes care of the fundamentals of light, describing, in detail, the properties of light and its areas of usage. In addition, spectral signatures are introduced.

CHAPTER 4

Chapter 4 introduces the optics of spectrometry. The information in this chapter explains the blocks building the basis of the hyperspectral technology.

CHAPTER 5

Chapter 5 elaborates on imaging, the imaging process and different aspects of it. This chapter reveals how hyperspectral imaging and Raman spectroscopy utilize light to extract information from an object - this, based on the details of Chapter 4.

CHAPTER 6

Chapter 6 describes how the data retrieved from the plastic measurements can be computed and analyzed. In this thesis, several methods for classification have been used, all elaborated here.

CHAPTER 7

Chapter 7 describes the structure of the process for the entire study, both scientifically relevant and for pure knowledge-gaining discussion sessions.

CHAPTER 8

Chapter 8 presents Paper I, *Identification of Marine Plastics using Hyperspectral Imaging in Infrared Light*. This chapter also contains extended material and discussion, beyond what is included in the articles, yet complementing scientific paper I.

CHAPTER 9

Chapter 9 presents Paper II, *Identification of Marine Plastics using Raman Spectroscopy*. This chapter also contains extended material and discussion, beyond what is included in the articles, yet complementing scientific paper II.

CHAPTER 10

Chapter 10 compare and discusses the two papers. This chapter is not only an extended discussion of the results, but a comparison of the two approaches used in each article.

CHAPTER 11

Chapter 11 gives a short conclusion, pulling strings from the results and discussions. In addition, ideas on further work are presented.

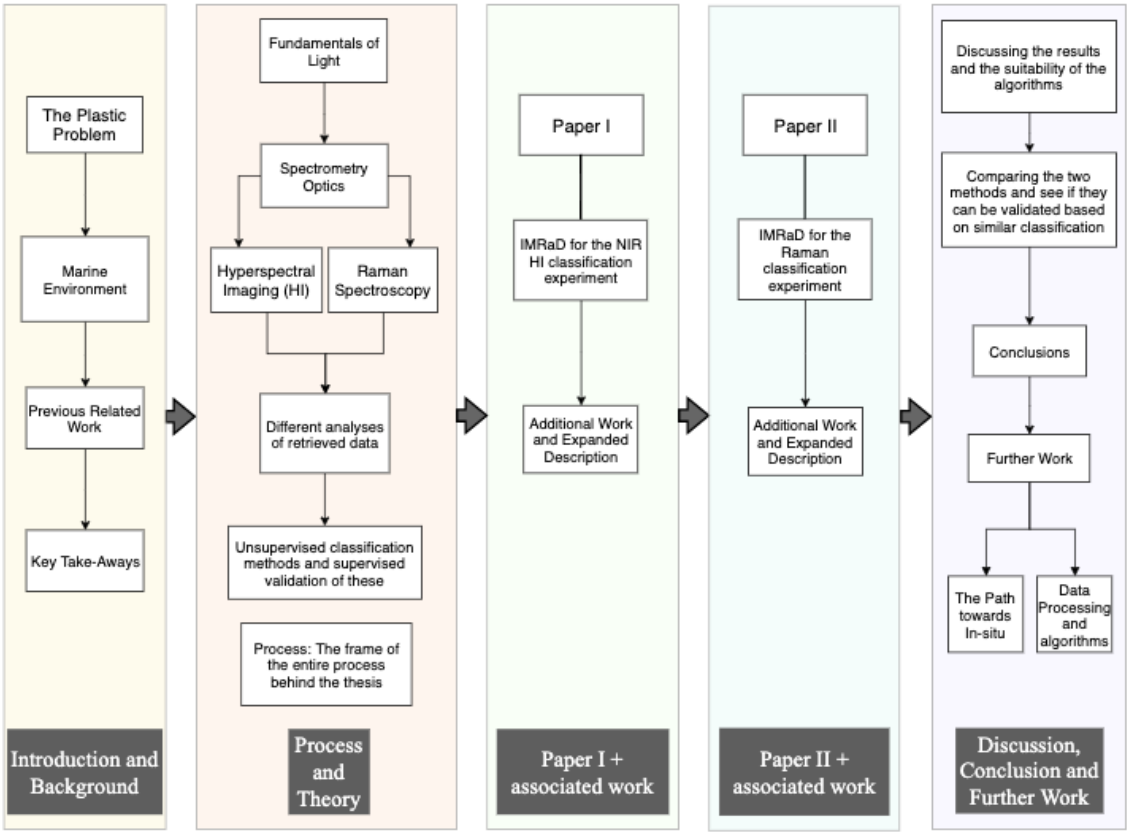

Figure 1.4.1: Thesis outline, roughly sketched

Chapter 2

Background

2.1 Plastic

The following paragraphs are largely inspired by Callister and Rethwisch (2018).

Plastic is a term used in a wide range of fields to describe properties and behavior of materials, in addition to the common type of materials. This report will use the term plastic solely to describe the type of material.

2.1.1 Chemistry

Polymers are large macromolecules, consisting of several repeated units. The molecules have a broad range of properties, resulting in polymers playing an essential part in society. Wool, cotton, DNA, wood and leather are all naturally occurring polymers, utilized for centuries. In recent times, it became possible to synthesize polymers and manufacture a sub-group of polymers called, plastics.

The majority of polymers are hydrocarbons, meaning they mostly consist of hydrogen and carbon bonded to each other in addition to miscellaneous other elements. The molecules consist of extremely long backbones of carbon, with side bonds to other elements or new branched chains. The backbone is the combination of thousands of basic hydrocarbons. The term polymer refers to many repeated, *poly-*, units, *mer*. Basic hydrocarbon units are combined, either naturally or synthetically in the case of plastics, to form the large molecules. It could either be one or multiple kinds of base units. Depending on the base units, the polymer will have different properties.

A crucial aspect determining the properties of a polymer is the structure of the chains. Different polymers will form different chains, either linear, branched or crosslinked. The chain type will determine how the molecules will pack and form intermolecular bonds. The chain types are largely determined by the base units. Modern techniques allows control over the polymer structure during the synthesizing.

Due to the simple nature of the molecule, linear chains will pack tightly. Subsequently, the molecules will form extensive "van der Waals" and hydrogen bonds. The resulting polymers are

therefore strong. Branched chains are linear molecules with branched side-chains. The increased complexity of the molecule makes it more difficult to pack and, consequently, reduces the density. The intermolecular bonds are, as a result, generally weaker and the polymer is less strong. Finally, the crosslinked polymers are parallel linear chains that are joined together by covalent bonds, rather than intermolecular bonds. The result is a strong, but flexible, polymer.

The molecular structure and base units of the polymer, affect the properties. The elements of the base units, apart from the hydrogen and carbons, will determine properties due to the chemical properties of the side groups. Also, the molecular weight of the polymer plays a significant role in the strength of the polymer. A higher molecular weight will result in a stronger polymer. In addition, the molecular structure is the basis for the packing of the molecule. The tighter packing will result in a more dense polymer, with less surface area and, subsequently, a generally lower level of degradation. The packing will also determine the level of crystallinity, which again results in stronger intermolecular bonds.

2.1.2 Common Plastics and Applications

All of these properties are essential as they are the cause of the unique position that plastics hold in society. The materials typically have low densities, with mechanical properties different from metallic and ceramic materials. Plastics are usually less stiff, and weaker than metals and ceramics. However, on account of the strength and stiffness per mass, the plastics are comparable. The combination of strength, weight and elasticity has made the material extremely popular, with it being used in everything from food wrapping to prostheses. The properties of plastic highly vary depending on the type and the side chains of the basic polymer structure, as well as the additives blended into most plastics. The latter could potentially be highly toxic and a source of the toxicity of plastic. Another key property making plastic popular is its chemical and biological inertness, generally making it non-biodegradable. In short, plastics are inexpensive, lightweight, strong, durable, corrosion-resistant materials, with high thermal and electrical insulation properties. The result is the annual production in 2015, as previously mentioned, exceeding 380 million tonnes and plastic penetrating all aspects of life Geyer et al. (2017).

Plastics are classified in different groups according to their chemical structure. Besides containing Carbon-Hydrogen bonds, these are all structurally different and they are classified accordingly. The result of the varying structure is varying properties. Different groups of plastic, therefore, have different typical use. Polyethylene (PE), polypropylene (PP), polyethylene terephthalate (PET), polyvinyl chloride (PVC) and polystyrene (PS), are the five most common types of plastic, in large part covering the global plastic production, Johnson (2017).

Polyethylene

The monomers in polyethylene (PE) has the chemical formula C_2H_4. Polyethylene is the most common type of plastic. The reason is the broad application of it in consumer products. Plastic bags, bottles and food wrapping are examples of polyethylene. However, these three products seem to have significantly different material. For instance, plastic bags are rarely as rigid and durable as bottles. This variation in polyethylene creates two sub-types defined by the degree of density – HDPE and LDPE, high-density polyethylene and low-density polyethylene, respectively.

The LPDE-monomers are more branched, meaning that a chain is replacing an atom - for instance a hydrogen atom. As a result, the monomers are less tightly packed, leading to a lower density. As LDPE is more branched than HDPE, its intermolecular forces are weaker.

Polypropylene

Polypropylene (PP) is the second most common plastic consistent of propylene with the chemical formula C_3H_6. PP has properties similar to polyethylene, but it is slightly harder and more resistant to fatigue. The plastic type is found in a variety of products like food packaging, labeling, and clothing.

Polyvinyl Chloride

Polyvinyl chloride (PVC) with a number of vinyl chloride monomers formulated by C_2H_3Cl, is in third, as the third most produced types of plastic. PVC can be both rigid and flexible. The rigid form is used in constructional applications in piping and electrical wire insulation, while the softer and more flexible form is used in many applications replacing rubber.

Polyethylene Terephthalate

Polyethylene terephthalate (PET) consists of repeated ethylene terephthalate monomers, with the chemical formula $C_{10}H_8O_4$. Typically PET is used in plastic bottles and fibers for clothing. For the latter use, the type is commonly known as polyester. Depending on the specific particle size and crystal structure, the semi-crystalline material, PET, might appear transparent.

Polystyrene

Polystyrene (PS) is an inexpensive plastic type commonly used for packaging purposes, with the chemical formula being $(C_8H_8)_n$. PS increasingly exists in the outdoor environment, particularly along shores. The plastic is naturally clear, hard and brittle. The latter fact is perhaps the main reason to why larger pieces of PS easily turn into microplastic.

2.1.3 Microplastics

There is no agreed upon definition of microplastic. However, the most common definition is based on the size. The term *micro* stems from microscopic, which refers to particles smaller than 1 millimeter. However, the first international research workshop on the occurrence, effects and fate of microplastic marine debris, in 2008 and hosted by NOAA Arthur et al. (2009), suggested an upper size limit of 5 millimeters. GESAMP (Group of Experts on the Scientific Aspects of Marine Environmental Protection), an independent group of experts on the marine environment, advising the UN and other major international organizations, chose to define microplastics in the range of 1 nanometer to 5 millimeters, GESAMP (2015). This thesis will adopt the same definition.

The following paragraphs are inspired by GESAMP (2015), Browne et al. (2007) and Booth et al. (2018)

Microplastics are small particles of plastic in the size range of 1 nanometer to 5 millimeters, larger particles are called mesoplastic, while the smaller particles are called nano plastic. The microplastic either enters the environment as microplastic or larger pieces of plastic deteriorate and fragment into microplastic. The origins of microplastics are classified as primary or secondary. Particles that entered the environment as microplastic are called primary. If it deteriorated and disintegrating as a consequence of interacting with the environment and other external forces, it is classified as secondary. The distinction helps distinguish sources of particles, as there will be different channels for the plastic entering the environment. Primary microplastic mainly consists of scrubbers used to clean surfaces. The cleaning materials contain microbeads of plastic in order to scrape off an outer layer. This could either be in the cosmetic industry, industrial or home cleaning products. Secondary microplastics are microplastics originating from larger pieces of plastic fragmenting into smaller particles, or particles fragmenting of the larger pieces.

The most significant source of microplastic is secondary. Plastic debris fragment in the environment as a result of photolytic, chemical, mechanical and/or biological degradation. Sunlight and oxygen will cause the plastic to oxidize, deteriorating the chemical structure by bond cleavage which reduces the molecular mass of the polymer. The result is a more brittle plastic, which fragments more easily. The plastics experience different levels of oxidization due to additives, causing differences in how easily it will result in microplastic. In a marine environment, there will also be a higher level of environmental stress on the plastic due to waves and abrasion from sediment particles. Weathering would occur rapidly on beaches, but at low rates in floating debris. In general, floating debris will have a slow rate of degradation due to the aphotic and low-oxygen environment.

The density of the microplastic will influence the fate of the plastic. The particles will either sink or float with a varying rate depending on their buoyancy. However, due to the marine environment, the buoyancy will change. Marine snow and growth on the particles will result in the plastic sinking at slow rates, and the majority of microplastics ending up at the sea bottom. However, the sinking rate is very low, and it takes a long time for the particles to reach the bottom. The particles could subsequently be carried large distances by underwater currents on the way down. Resulting in consequences of the microplastic could, therefore, occur far from its origin.

2.1.4 Impact

The impact of microplastics on marine biota is vast. Ingestion of plastic particles has been detected in all oceanic regions and numerous species Oluniyi Solomon and Palanisami (2016). However, research is lacking as the field is relatively new.

The main impacts of microplastics on marine biota are measured to be through ingestion and general exposure, with ingestion being of the greatest concern. The general exposure is mainly a concern due to gills, as the size and shape of microplastic makes entanglement highly unlikely. The smallest of the microplastics, in the range of 8 to 10 micrometers, were discovered to enter and be retained in shore crabs through their gills Watts et al. (2014). The study shows the impact of microplastics, apart from ingestion, which is by far the most significant impact.

The relative size of the microplastic will cause the particles to accumulate in smaller organisms similar to what has been seen in larger organisms Browne et al. (2007). The effect of an accumulation of plastic relative to an animals size has been thoroughly documented in larger species such as whales and birds, and is, without doubt, a negative impact. The effect on smaller organisms is similar and comparable to larger organisms.

Furthermore, once ingested, the plastic particles may leach chemicals into different systems of the organisms. Additives in the original plastic are known to be toxic. The additives are meant to improve certain properties of the plastic, but when exposed to wildlife, it is discovered to be toxic. It can leach, either during and after the accumulation in the digestive system, or the plastic could transition into the body tissue Hussain et al. (2001) and leach directly into other parts of the organism Gallo et al. (2018). The result is organisms being exposed to chemicals from the plastic as a result of its presence.

Further, adsorption to the particle surface will cause an introduction of toxins in the organism. Hydrophobic organic chemicals (HOC) may latch onto the microplastic. It has been shown that toxic chemicals are attracted to the polymers due to their common hydrophobic properties Hartmann et al. (2017). Research has shown some types of plastic having $10^5 - 10^6$ times higher concentration of the toxins PCB and DDE than the surrounding seawater Mato et al. (2001). Subsequently, when the microplastic is ingested, the organism will be exposed to the chemicals Ziccardi et al. (2016). In all situations where microplastic result in an exposure to toxins due to ingestion, th eplastic particle will act as a vector. Due to the introduction of toxins into the foodweb, the microplastic is, as mentioned, regarded as a vector for the chemicals. Either as a result of the chemicals accumulating on the particle or due to the preexisting chemicals in the particle.

2.1.5 Issue with Microplastics

The biggest issue with microplastic is, as mentioned, due to ingestion by marine biota. It has been shown that a large variety of marine life across trophic levels, indeed, ingest microplastics. The issue, therefore, penetrates the whole food chain and will affect human life as well. A recent study, not yet published and awaiting peer-review, has even shown presence of microplastics in humans from several different places in the world Parker (2018). Ingestion of microplastics poses several issues. The plastic could accumulate, transition into tissue, leach chemicals, or introduce toxins through adhesion, as discussed in the previous section.

It is important to keep in mind that the effect of microplastic is much larger indirectly than the direct effect on the organisms. The largest concern is bioaccumulation. When the microplastic acts as a vector for toxins, it does so on species at the very bottom of the food chain. Even though it might not be fatal for the organisms directly affected by the plastic, species higher up in the food chain are severely affected. As a consequence of 10% of energy being transferred between trophic levels, higher level species will indirectly ingest large amounts of the organisms, directly affected by the microplastics and its role as a vector for toxins. The result is bioaccumulation. Small amounts of toxins accumulate through the food chain, causing severe problems in higher level species. The chemicals are stored in tissue and fat of the organisms, and when the higher level organisms indirectly ingest the originally affected organisms, in a matter 10 to the power of

the trophic level, the exposure to the toxins are also tenfold. The consequences could be severe. A famous example of the effect of bioaccumulation is the polar bear. The animal, located at the top of its food chain, rarely directly exposed to mercury. However, due to bioaccumulation, the bear exhibit high levels of the toxic element St. Louis et al. (2011). Microplastic pose the same problem. It introduces toxins at a base level of the food chain, causing severe ripples throughout.

Due to the nature of the food chain, the direct effects of microplastics could, potentially, be disastrous. If species on the bottom of the food chain are severely affected by the effects of microplastic, they could affect higher level species. Smaller species make up the foundation for other species in the form of being the main source of feed. If the foundation falls due to the toxins or effects of the microplastics, there could be severe effects on the species based on the original species. The result could be a domino effect, causing widespread ripples.

In summation, the size of the microplastics results in it negatively affecting the very base of the food chain. Also, the properties of the material itself, result in it attracting toxins. The combination of the two makes microplastic a vector of dangerous, and often unnatural, substances in the marine environment. The vector hits the very core of many marine ecosystems and pose a danger to a number of organisms, either directly or indirectly.

2.1.6 Sample Collection & Analysis

As of today, the collection of microplastics is tedious work, regardless of environment. Marine microplastics are collected similar to marine plankton: by towing a manta sampler at slow speeds behind a vessel. The trawl-like tool filters the water and collects the filtered samples in a container at the cod end. The collected filtered water is, subsequently, filtered again using a fine filter and a pump.

Finally, the filters are prepared in the lab using chemicals to remove the organic matter from the particles. Towards the end, the particles are individually analyzed in order to identify microplastics. Based on the measured volume of trawled water, one may calculate the concentration of microplastics.

The work is time-consuming, expensive and impractical. It illustrates the need for a change and technological innovation. As part of the thesis research, the authors collected microplastics via the traditional process described above. The process took two full days at sea.

Partly the reason why it is such a time-consuming process to identify plastics, is the wide range of varieties. As previously mentioned, plastics are used in almost all aspects of life and industry, resulting in the need for a high range of different properties. In order to achieve this quality, a range of additives added to the material, makes the sub materials differ from each other. Even though the additives only make up for a marginal part of the materials, it makes them possible to distinguish them from each other.

Plastics are carbon-based polymers - nothing unique, merely naturally occurring polymers based on carbon, but without the backbone of carbon, formed based on oil. In order to identify plastic from naturally occurring polymers or other particles in general, one uses the traits due to the

unique properties of the material or its chemical composition.

Many of these traits are similar across materials. However, based on a given set of characteristics, one may identify plastic particles. The issue arise when having to recognize and combine a wide number of properties, as it requires several dimensions of information about the particle. In order to achieve this, one may sort to a combination of sensors and sensor merging. Each sensor identifies certain properties, and based on these, one may easier boil it down to either plastic in general or a specific plastic type.

2.2 Marine Environment

The following section will introduce the marine environment and its effect on plastics. The ocean is a complex and intricate environment, affecting everything related to it. Therefore, this section will include a brief introduction to interactions between oceans and plastics, with its biological, chemical and physical effect. The section largely based on a report by Booth et al. (2018), delivered to the Norwegian environmental agency, and lecture *Ocean systems for marine biomass production*, held by Nicole Aberle-Malzahn in the course TMR 4137: *Sustainable use of Marine Resources*.

2.2.1 Marine Ecosystem

Covering over 70% of the planet and 99% of habitable space on the planet, the ocean is the biggest ecosystem on the planet. Food production in the sea is critical to the planet, and arguably all species depend upon the ocean - directly or indirectly. With 25 % of all species in the ocean being smaller than 1 millimeter, and 99% smaller than 10 centimeter, Bar-On et al. (2018), it is hard to argue against the importance of plastic introduced to the ecosystem of these species. Photosynthesis and phytoplankton, creates the basis of all biomass production in the sea is the photosynthesis and phytoplankton. These are eaten by the zooplankton, subsequently eaten by a larger organism, moving up the food chain, and resulting in it being a crucial resource for life. Given the large number of species within the size range of microplastic, the effects could be catastrophic.

When organisms in the marine ecosystem die and deteriorate, marine snow is formed. The particles have a large sinking rate and are an essential aspect of transporting energy down the water column. The marine snow plays a crucial role in the marine ecosystem Lampitt (2001). The microplastic will mix with the marine snow. The result is a reduced buoyancy for the plastic and an inaccessible surface. The conclusion is plastic possibly entering the food web as a hitchhiker, but also a reduced deterioration, apart from the biodegradation, due to the inaccessible surface.

As a result of microbial colonization, growth will be caused by bacteria and other organisms in the ocean. The growth will form a biofilm around the plastic, and similar to the marine snow, reduce the photolytic degradation. The biofilm will also contribute to increased biodegradation and lowered density. It is also shown to increase the trophic transfer, due to the increased nutritional value, as a result of the biofilm Rummel et al. (2017). Therefore, the interaction between particles and the marine ecosystem, goes beyond the ingestion and exposure. The microplastic will also cause problems to due exposure to other aspects of the ecosystem as well.

2.2.2 Chemical Reactiveness

The reactions happening in the marine environment are affected by a great number of parameters. Each of, which plays an individual role, as well as in combination with other parameters. These decide the rate of reaction happening in the ocean, either chemical or biological, regardless of the plastic. The main parameters handled in this report are temperature, amount of sunlight, oxygen and the water itself. These greatly affect many processes concerning the ocean.

Temperature is crucial in any chemical reaction, and plays a role in the reaction rate. The higher the temperature, generally, the higher the reaction rate. The rate doubles with every 10 °C temperature increase. In a marine environment, the temperature will depend on the geographical position and the depth at which one measures. Therefore, warmer and shallower climates will be more reactive. This affects the plastic as the degradation will occur faster closer to the equator, due to both the higher temperature and the higher amounts of sunlight.

Sunlight is one of the main reasons for plastic degradation. The same mechanisms that enable photosynthesis and provides the basis for marine biomass production, also degrade plastic. Temperature and sunlight have a clear correlation, with an increasing amount of sunlight closer to the equator. Therefore, photolytic degradation will occur more rapidly closer to the equator. Also, due to water diminishing the light, depth will also play a part, resulting in the same dependence as with temperature.

Oxygen is a key component in photolytic degradation. The oxygen will oxidize the plastic and therefore help degrade it. The result is oxygen levels being important to the level of plastic degradation, but also for biodegradation and microbial community. With high levels of oxygen, there is more marine life. The biota will interact with the plastic and take part in breaking it down through biodegradation. The degree of response to biodegradation varies across plastic types, based on their structure. The biofilm will, however, be susceptible to photodegradation due to the fact that the surface is covered to a larger degree.

Finally, the water itself plays an important role. It contains other substances which will affect the chemical reactions in the sea. For example, the level of suspended material will affect the penetration of sunlight. The presence of algae or sediments will filter the sunlight. Thus, more unclear the waters, will result in less sunlight being present. Also, hydrolysis plays a part, as the water molecules will react with substances. The reactions will be catalyzed by the presence of acid, base or enzymes. With regards to plastic, a more hydrophobic plastic will be less receptive to hydrolysis. However, hydrophobic materials have a tendency to attach to each other, which is one of the reasons for toxic chemicals attaching to the plastic.

2.2.3 Oceanic Forces

Several forces act within the ocean, creating a complex environment. Currents and waves affect all matters of the ocean. Due to the forces, water is transported and often mechanically degraded. The forces, in combination with land, also promote mechanical degradation, such as seen at beaches or in shallow waters.

Currents transport large amounts of water around the world. These go in distinct paths. When the water travels great distances, so does the materials suspended or floating on top of that water. The result is material in the sea possible moving great distances. The effects of the pollution is possibly no longer occurring at the pollution site. The currents also move different temperatured water, making areas of the globe inhabitable, acting as an essential parts of the world climate.

Waves are mostly caused by the wind. The wind blows consistently over large bodies of water, causing waves with possibly large forces involved. Combined with the plastic mechanical degradation occurs, the waves will fragment the plastic, causing it to break down faster. In shallow waters, where the waves will cause increased movement, microplastic will occur more rapidly. The effect of the grinding caused by wave and shore, results in a higher rate of degradation.

2.3 Sensor-carrying Platforms

In order to perform underwater detection and mapping, for continuous autonomous monitoring of the oceanic microplastics concentration, a suitable sensor carrying platform is needed.

As mentioned earlier, plastics are circling the entire ocean, including the ocean surface, water columns, and seabed. Platforms like Unmanned Aerial Vehicle (UAV), often used as a sensor carrier in on-land missions, can, therefore, be out-ruled. When further deciding on a suitable platform to carry the sensors, Unmanned Underwater Vehicles (UUV), are typically relevant, including platforms such as Autonomous Underwater Vehicle (AUV), Remotely Operated Vehicle (ROV) and Gliders, Stein M. Nornes (2017).

ROVs are robots that are remotely maneuvered from a control room, often from a ship or a platform. These provide detailed mapping and sampling in the target area, with high-resolution data on the target. The umbilical attached to the ROV at one end, and the ship at the other end, gives unlimited electrical power and high bandwidth communication. However, the need of this umbilical limits the spatial coverage (usually lower than 1000 m^2, Nilssen et al. (2015), Stein M. Nornes (2017).

An AUV however, is independent of an umbilical and can operate without ships or associated platforms present. Similar to the ROV, the AUV has a high spatial resolution data, providing detailed seafloor and water column mapping. In addition, the covered area per time is more than ten times the range of an ROV. Furthermore, comparing the AUV and the Glider, in the literature of Nilssen et al. (2015), an even larger spatial range can be observed for the Glider. Nevertheless, the wide payload capacity of the AUV and the high spatial resolution data, makes the AUV a more suitable choice for the desired purpose described above.

2.4 Previous Related Work

As the problem is becoming more visible and threatening, a manifold of initiatives and technologies, with the purpose of solving the problem, have been developed within the past years. REV Ocean is an initiative by Kjell Inge Røkke, who, together with Nina Jensen, have established REV

Ocean to *contribute to saving the world's oceans*. The idea is research-ships acquiring knowledge, creating awareness and collecting plastic waste, REV Ocean (2018). The Ocean Cleanup is another initiative, solely determined to collect plastics from the five largest garbage patches in the world, using currents to catch and concentrate the plastic, The Ocean Cleanup (2018). Tomra is a company exploiting the characteristics of spectroscopy, identifying specific chemical and molecular properties of the objects to be viewed, TOMRA (2018).

In this thesis, however, the plastic identification will concern other, existing, technologies. Existing technologies are often used in new ways, generating innovation. In further reading, utilization and exploitation of hyperspectral imaging and Raman spectroscopy, within different fields, will be presented.

The use of Raman spectroscopy and hyperspectral imaging is not particularly new and is already widely used in several fields, such as geology. In previous studies, it has been used in a wide range of experiments and testing. However, not all of these apply to the focus established within this thesis. This is mainly because many of the previous applications focus on, and utilize, different aspects of the data. The following section will thus focus on the use of Raman spectroscopy and hyperspectral imaging for classification purposes, and mainly in relation to the ocean or under water.

2.4.1 Underwater Hyperspectral Imaging with Remote Operated Vehicles

The use of hyperspectral imaging (HI) has been exploited in several fields for a long time. However, the use of HI under water, is relatively new. In combination with Remote Operated Vehicles (ROVs) or Autonomous Underwater Vehicles (AUVs), it opens the possibility for autonomous underwater imaging.

Johnsen et al. (2016a) gives an overview of the use of underwater hyperspectral imaging (UHI) deployed on an ROV. The paper identifies the benefits of using UHI as increased number of resolutions (e.g., spatial resolution, spectral resolution, radiometric resolution and temporal resolution). It delivers a photomosaic of the are of interest, which lets the end user detect and classify Objects Of Interest (OOI), and of course the possibility of increased autonomy and the benefits that comes with it - such as reaching more inaccessible areas etc.

2.4.2 Monitoring, Identification & Taxonomy

The use of hyperspectral imaging, in relation to water, often revolves around the identification of pigmented marine biota, mainly plankton and algae. This is either done for monitoring purposes or taxonomy. Concerning Raman spectroscopy, this relation rather involves identification if chemical composition.

Mehrubeoglu et al. (2013) investigated the hyperspectral image response in pure and mixed algal cultures in a lab environment. The paper aimes to identify the algal composition using constrained linear spectral unmixing and the system's performance. The laboratory set up consisted of a halo-

gen lamp, spectrometer, lens, camera and sample. Measuring transmittance, the light source was placed beneath the sample instead of above. It achieved a high prediction rate. The paper goes in great detail on noise elimination. The focus gives an insight into the error prediction and noise on spectral signatures, even though these are not much different than noise in general.

Pettersen et al. (2014) elucidate reflection signatures of marine organisms and the corresponding species-specific absorption and discuss the use of optical fingerprint from UHI for automated identification of organisms through the use of a UHI mounted on an ROV. Identification was made based on an existing library of signatures acquired in a laboratory setting. The study seeks to accomplish the same recognition with respect to organisms, as this project is seeking with respect to plastic. Thus, some elements are relevant for the classification of plastic using the UHI.

Dumke et al. (2018) used underwater hyperspectral imaging to identify marine megafauna. To identify the benthic megafauna, the paper established a set of reference spectra from already identified organisms and performed semi-autonomous supervised classification. The paper uses a UHI mounted on an ROV. There is relevancy concerning the classification of objects based on a preexisting set of signatures in an inaccessible environment with low to no natural light.

Volent (2011) seeks to detect and monitor the phytoplankton bloom, spatially and temporally, through the use of water sample, bio-optical data from satellites and a Ferrybox in combination. The paper presents an improved monitoring scheme. The report does not go in particular detail on the actual use of hyperspectral imaging, but rather on the water sampling and processing. However, the Ferrybox is relevant for an alternative microplastic monitoring system apart from an AUV. In that case, the sensor cabinet of a ship would contain a hyperspectral imaging unit to detect the plastic. The system would not be too different from the preexisting fluorescence sensor. It is important to keep in mind that such a system is beyond the scope of the current project.

Karlsson et al. (2016) consists of the most similar research, to the authors' knowledge. The paper aims to identify microplastics from filtrates, based on hyperspectral imaging, to gain information on the spatial location of the plastic. The samples used in testing were obtained from filtrates of surface water collected using a trawl. Further, the collected microplastic was tested in a laboratory setting and compared to spectra of household plastics. The reference spectra were obtained by scanning the household plastic on a white reflective Teflon background. The results were most prominent in the wavelength range from 1000 nm to 2500 nm, yielding a 100% recognition. This shows the possibility of identifying plastics in the infrared spectrum. The paper has several key aspects relevant for the project and was a source of references and execution concerning the project.

C. Epstein et al. (2019) claims to have used Raman spectroscopy to monitor the speedy characterization of carrier proteins, explaining the grounds of the chain sequestration mechanism. The rapid motions of carrier proteins pose a challenge when it comes to locating and capturing the proteins. Conventional spectroscopic methods are inadequate. Due to the fundamental part, the carrier proteins play in the biosynthesis, this detection is, however, a necessity. This way of using Raman Spectroscopy can undoubtedly compare to the method used in this thesis, as it concentrates on chemical texture and molecular recognition.

Gulick et al. (2019) have been diving into the relationship between a change in type I Colla-

gen and aging, examining a rat tail. When a person ages, or is exposed to a disease, the type I collagen protein experiences structural and biochemical changes, possibly impacting the organs. Using Raman spectroscopy, the researchers observed an increase in Raman bands as the collagen went from adult to old, indicating higher straightness of type I collagen fibers. Using Polarized Raman mapping to confirm, the conclusion was indeed higher straightness of collagen tissues with aging. This is, again, an example of how Raman spectroscopy is used to study molecular characteristics, with resemblances to the research done in this document. However, the organic material of a rats tail appears different than the pieces of plastics.

To give a broader spectrum of dimensions of data, the Raman method has also been researched used in combination with other methods. Xiong et al. (2019) poses to combine Raman spectroscopy with the common fluorescence detection, recovering a more significant number of functionalities and grounds for analyses. As the fluorescence detection allows exquisite sensitivity on a molecule level but lacks adequate chemical information, while the Raman technique, in fact, assures the lacked information within the molecular structure, the combination ensures a highly detailed sensor. The idea is to develop hybrid spectroscopy by implementing vibrational Raman characteristics into the fluorescence spectrum. Looking into different methods as this thesis does, the success of this merge appears inspiring.

2.4.3 Identification of Man-made Objects

Underwater archaeology and the identification of plastic isn't the most obvious overlapping fields. However, the identification of man-made objects with large variations has several similar aspects. Man-made objects often depict certain properties not found in nature. Successfully identifying objects or materials, are often critically dependent on having a library of signatures to compare with - in this regard, the two largely overlap. The following paragraphs summarize relevant articles concerning the identification of man-made objects or materials using either hyperspectral imaging or Raman spectroscopy.

Similarly, man-made objects and synthetic materials exhibit, are normally not found in nature, neither on a physical, nor on a chemical level. In this sense, the classification of objects based on exclusion depending on characteristic properties, is shared with a wide range of fields. In this regard, Raman spectroscopy has previously been used to identify man-made objects based on chemical composition.

Ødegård et al. investigated the use of ROV-based UHI in marine archaeology. The paper chose to not use end-member recognition to classify the objects in 48 optical classes, but rather used Spectral Angle Mapper based on a library of end-members. It also identified the possible use of underwater robotics in combination with UHI, and future possibilities of robotics in the field of archaeology. The results showed few, if any, instances of false positives and a potential for UHI used in detection and identification.

Ødegård et al. (2018) is an extension of the previous paper. It depicts the use of UHI in marine archaeology. From the laboratory testing to the in situ testing and the data analysis and classification method used. Similarly to the previous paper, this one also uses SAM in order to classify the data into different classes. Nevertheless, the number of classes is greatly reduced, and

the final total is six classes based on the different materials, expected to be found in archaeological detection. Furthermore, the report also presents the raw data conversion and the principal component analysis of the data. The results are somewhat mixed. However, the conclusion is that it successfully classified objects and that it shows a promising new method. The level of misclassification varied between materials. The paper is highly useful concerning the classification of plastic as it depicts all the steps from testing to data analysis, which is all relevant for this project.

Zada et al. (2018) describes the use of Scattered Raman Spectroscopy for quick identification of microplastics by having measurements at fewer wavelengths. It is aimed at being a proof of concept, and thus limits the testing on live samples. The paper uses the most common plastics, based on volume, and seeks to find a limited number of wavelengths from their respective full-Raman spectra. After extracting said wavelengths, the classification was tested on filtered microplastics originating from the Rhine and filtered glitter nail polish. The five most discriminant wavenumbers in the range 1250 cm^{-1} to 1800 cm^{-1} were chosen based on Partial Least-Square Discriminant Analysis. The method favored points with a large overlap between the spectra, rather than clean peaks. The paper managed to reduce the time needed to identify the particles successfully. The collection and processing of the spectra before choosing the wavenumbers are highly relevant for this thesis. Also, the general aim to identify plastics largely overlap. However, there are some differences in the approaches chosen.

Allen et al. (1999) aims to compare Raman spectroscopy to NIR spectroscopy in the use of identifying common household plastics for recycling purposes. The paper uses K nearest neighbor and Cyclic subspace regression to identify the plastic types. These methods are closely related to K-means clustering and PCA. The plastic samples were collected from a common household, and the full spectra were collected. These were subsequently preprocessed using second-derivative Savitsky-Golay. The full spectra were used in the identification as opposed to peak information. The paper managed to correctly identify all types of plastic included. Even though the paper is 20 years old, it aims to investigate large parts of the same as the author, minus the water. It is highly relevant in the sense of data processing and subsequent logic. Also, considering the similar approaches between the two, the approach shows its relevance.

Lenz et al. (2015) is an assessment of the possibility of using Raman micro-spectroscopy for classification. The study compared visual microscopy and Raman micro-spectroscopy. It also aims to analyze plastic particles collected from the North-Atlantic. The paper successfully identified the degraded particles. The study used qualitative analysis of each spectrum to identify the plastic. It concluded on Raman being more effective than regular microscopy and having the potential for both bench-top analysis and *in situ*-testing.

2.4.4 Key Take-Aways

There are several similarities between previous work and the project. Despite the fact that, there is only one other article directly the same issue of identifying plastics through hyperspectral imaging, there are still several aspects of the research that are relevant. There are also several papers aiming to identify materials using Raman Spectroscopy. Mainly the data processing, classification and gathering are relevant across the papers. This is due to the material being identified being secondary to the way it is identified.

Among the main takeaways, are the use of PCA, PLS-DA, SAM and other algorithms, as well as the preprocessing of the data. The methods utilized to recognize objects of interest and prepare the data, are, in essence, the same as the objective of the thesis. There are somewhat different detection criteria due to the nature of the OOI. However, the mentined detection methods are highly relevant techniques. The papers also provide relevant references on the emerging field of Underwater Hyperspectral Imaging and research conducted in the field of Raman Spectroscopy.

Furthermore, the takeaways from Karlsson et al. (2016) and Zada et al. (2018) are more obvious. The papers aim to identify the same particles, however, it does so of filtrates. The use of the infrared spectrum is also highly relevant. The PCA performed on the data will have a lot of the same aspects. It is also interesting to see the focus of the papers and what aspect of plastic they aim to identify. In addition, the laboratory testing in order to obtain the reference spectra, is highly relevant for the project. Finally, Lenz et al. (2015) is relevant and highly accurate, offering a number of decidedly useful points. When conducting the research for this thesis, these articles proved essential guidance and learning.

Chapter 3

Fundamentals of Light

In order to understand how an image is retrieved at the end of a spectrometer, knowledge regarding properties of light, is important. This chapter, therefore, describes the fundamentals of light, its behavior and how it can be utilized. Light has different properties in different environments, determining the degree of utilization. The lecture notes from TTK20: Hyperspectral Remote Sensing, Signernes (2018), have been used in large part throughout this chapter, and have also provided all illustrations - if not stated otherwise.

3.1 Light

Light is electromagnetic radiation. The human eye can detect electromagnetic radiation within wavelengths of 400 and 750 nm, approximately. This electromagnetic spectrum is called visible light. Radiation with a shorter wavelength than 400 nm is called ultraviolet, whereas infrared radiation has a longer wavelengths than visible light.

3.1.1 Infrared and Near-Infrared

The following paragraphs are largely based on Peatross (2015).

Infrared and Near-Infrared light is identical to visible light apart from its wavelength. Both are electromagnetic radiation, but with different wavelengths. The infrared spectrum spans from 780 nanometers in the Near-Infrared region, to 50.000 nanometers in the Far-Infrared region. The radiation is also commonly known as heat radiation, even though all electromagnetic radiation will heat any surface that absorbs them. However, most objects in room temperature will emit infrared radiation as thermal radiation.

All objects with a temperature different from absolute-zero will emit thermal radiation. This is a result of the change in the dipole moment of molecules and atoms when they interact. The interaction will cause the electrons of the atoms or molecules to shift, causing a change in the poles. This change results in electromagnetic radiation. The emitted radiation is determined by Planck's law. It so happens that at room temperature, most objects radiate in the infrared spectrum.

The distribution and available electrons depend on the molecular bonds. The bonds between the atoms will put restraints on the types and possible vibrations of the materials. Hence, the vibrations causing the radiation will be dependent on the chemical composition. Similarly, the absorption of radiation of an object depends on the chemical composition. As a result, one may gain great insight into the chemical composition of the material, depending on the emitted or absorbed energy. At room temperature, this radiation will be in the infrared spectrum, opening possibilities for identifying materials based on infrared radiation.

3.1.2 Fundamental Behaviour of Light

When light from a light source hits an object surface, the light is reflected before eventually reaching the eye. In this task, the endpoint will not only be the human eye, but other viewpoints, for instance, a camera lens. The observation of the reflected colors in the viewpoint is affected by properties of the object surfaces, the light intensity of the light source and the traveling distance of the light, Yamashita et al. (2007).

Light can be defined as tiny packets of energy called photons. These have wave-like properties. Because of this, a wave of light can be represented as a sine function. The two-dimensional wave amplitude can be expressed as follows

$$E(x,t) = E_0 \sin(kx \pm \omega t) \tag{3.1}$$

E_0 represents the maximum amplitude of the wave. The wave repeats itself periodically with the period T. k is the wave number defined by $k = \frac{2\pi}{\lambda}$, λ is the wavelength, while ω is the angular velocity expressed as $\omega = \frac{2\pi}{T}$.

The wave can also be expressed as the real part of a complex number, $z = E_0(\cos(\phi) + i\sin(\phi))$, where ϕ is the phase shift represented by $\phi = kx + \omega t$. Using Euler's formula: $e^{i\phi} = \cos(\phi) + i\sin(\phi)$, a three-dimensional wave can be expressed by

$$\mathbf{E}(\mathbf{r},t) = \mathbf{E}_0 e^{i\phi}, \tag{3.2}$$

where $\mathbf{r} \in \mathbf{R}^3$ is the position of the phase now defined as

$$\phi = \mathbf{k}\cdot\mathbf{r} - \omega t + \xi, \tag{3.3}$$

where $\mathbf{k} \in \mathbf{R}^3$ is the three-dimensional wavenumber and ξ is the initial phase of the wave.

3.2 Interference

Interference considers the case when two or more waves act together. At a given point where the waves interact, the result will be the sum of the waves. Depending on the phase difference, the

interference is either constructive or destructive. Constructive interference will result in an amplified wave, while destructive will result in the opposite.

Starting with two solitary waves, respectively S_1 and S_2, interacting with each other at P, as illustrated in Figure 3.2.1. From (3.2), the S_1 and S_2 are represented by

$$\begin{aligned} \mathbf{E}_1 &= \mathbf{E}_{01} e^{i\phi_1} \\ \mathbf{E}_2 &= \mathbf{E}_{02} e^{i\phi_2} \end{aligned} \tag{3.4}$$

with their associated phase shift expressed as illustrated in (3.3)

$$\begin{aligned} \phi_1 &= \mathbf{k}_1 \cdot \mathbf{r}_1 - \omega t + \xi_1 \\ \phi_2 &= \mathbf{k}_2 \cdot \mathbf{r}_2 - \omega t + \xi_2 \end{aligned} \tag{3.5}$$

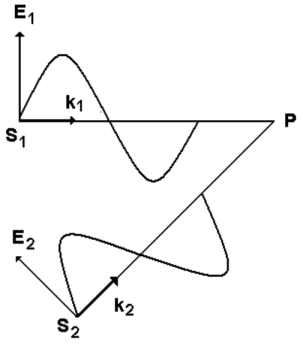

Figure 3.2.1: Two waves, S_1 and S_2, interfering

At a given point, the two waves will act together. One can conclude that the resulting wave, $\mathbf{E}$, must be the sum of the two vectors interacting, $\mathbf{E} = \mathbf{E}_1 + \mathbf{E}_2$. This applies to the resulting phase difference too, which thereby can be retrieved from (3.5): $\sigma = \mathbf{k}_1 \cdot \mathbf{r}_1 - \mathbf{k}_2 \cdot \mathbf{r}_2 + (\xi_1 - \xi_2)$. Now, the intensity of the final wave can be found by multiplying this resulting wave-vector, $\mathbf{E}$, with its conjugate, $\mathbf{E}^*$

$$\begin{aligned} \mathbf{I} \approx \mathbf{E} \cdot \mathbf{E}^* &= (\mathbf{E_{01}} e^{i\phi_1} + \mathbf{E_{02}} e^{i\phi_2}) \cdot (\mathbf{E_{01}} e^{-i\phi_1} + \mathbf{E_{02}} e^{-i\phi_2}) \\ &= \mathbf{E_{01}}^2 + \mathbf{E_{02}}^2 + \mathbf{E_{01}} \cdot \mathbf{E_{02}} (e^{i(\phi_1 - \phi_2} + e^{-i(\phi_1 - \phi_2)}) \\ &= \mathbf{E_{01}}^2 + \mathbf{E_{02}}^2 + 2\mathbf{E_{01}} \cdot \mathbf{E_{02}} \cos(\phi_1 - \phi_2) \\ &= \mathbf{E_{01}}^2 + \mathbf{E_{02}}^2 + 2\mathbf{E_{01}} \cdot \mathbf{E_{02}} \cos\sigma \end{aligned} \tag{3.6}$$

The intensity in the equation above, (3.6), represents constructive interference at its maximum, whenever $cos(\sigma)$ is equal to 1, and expresses destructive interference at its minimum, when $cos(\sigma)$ equals -1. Constructive interference is hence present when the phase shift, σ is expressed as:

$$\sigma = 2n\pi, \tag{3.7}$$

where n is the spectral order, a positive or negative integer.

The equation may be extended to include N number of waves with a constant phase difference between the waves and the same wave number and amplitudes for all waves considered, illustrated in Figure 3.2.2.

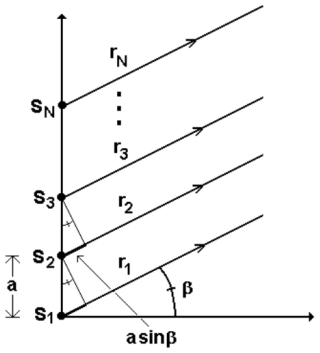

Figure 3.2.2: N number waves propagating with a constant distance a

The N waves are emitted by S_N coherent and monochromatic sources separated by a constant distance, a, at an angle β. As the waves are coherent, the phase difference between the waves are constant. This means that the second term in (3.5) can be ignored because $\xi_1 = \xi_2 = ... = \xi_N$. The phase difference is thus a result of the path difference between the waves, $\sigma = \mathbf{k} \cdot \mathbf{r}$. From Figure 3.2.2 $\mathbf{r}$ can be retrieved as $asin(\beta)$, while $k = \frac{2\pi}{\lambda}$. Combining this with (3.7), *the grating equation* is found

$$n\lambda = asin(\beta) \tag{3.8}$$

Through rotating vector sums, the equation for the total amount of waves may be obtained.

$$E = E_{01}\frac{\sin(\frac{1}{2}N\sigma)}{\sin(\frac{1}{2}\sigma)} \tag{3.9}$$

The intensity is proportional to E^2, and if plotted as a function of the wavelength λ and angle β the maxima occur when constructive interference occurs, which illustrates 3.8, the grating equation. The resulting intensity plot is depicted in Figure 3.3.1b. The plot shows the intensity for various wavelengths in different spectral orders at different diffracted angles.

$$I = I_0\left(\frac{\sin(\frac{1}{2}N\sigma)}{\sin(\frac{1}{2}\sigma)}\right)^2 = I_0\left[\frac{\sin(N\pi a\sin(\beta)/\lambda)}{\sin(\pi a\sin(\beta)/\lambda)}\right]^2 \tag{3.10}$$

3.3 Diffraction

While interference is a result of individual sources interacting with each other, diffraction is present when a wave is distorted by an external object, with a comparable dimension to the wavelength of the wave. Figure 3.3.1a exemplifies diffraction with a slit as the external object.

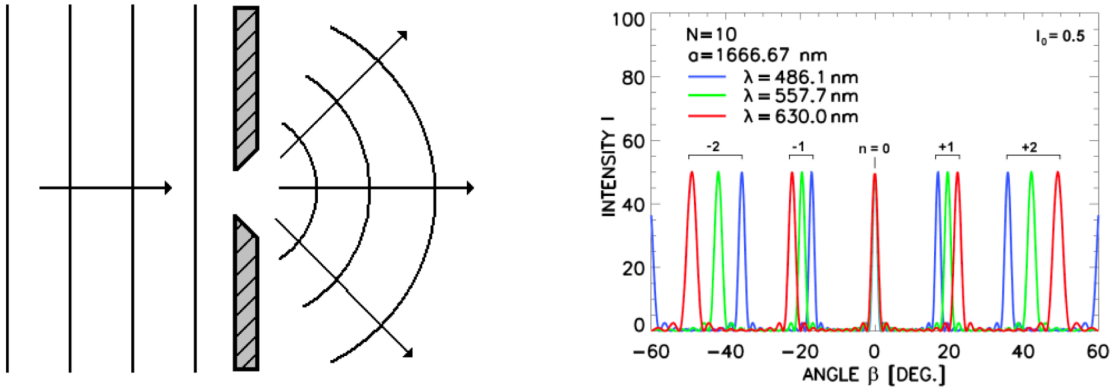

(a) Diffraction at a slit

(b) Intensity as a function of wavelength and spectral order

Figure 3.3.1: Single slit diffraction with the corresponding intensity plot

Huygens-Fresnel principle treats every point of a wavefront as a source of secondary wavelets. These sources form new wavefronts defined as the diffracted waves with amplitudes of dE_{01}. Combined, these form a new united wavefront. The resulting amplitude and intensity is derived in the same fashion as with interference from multiple sources. The result is

$$E = E_0 \left[\frac{\sin(\pi b \sin(\beta)/\lambda)}{\pi b \sin(\beta)/\lambda} \right] \tag{3.11}$$

$$I = I_0 \left[\frac{\sin(\pi b \sin(\beta)/\lambda)}{\pi b \sin(\beta)/\lambda} \right]^2 \tag{3.12}$$

In order to obtain the desired diffraction one uses multiple slits, which results in a grating, shown in figure 3.3.2. The grating will result in a number of new waves equal to the number of slits in the grating.

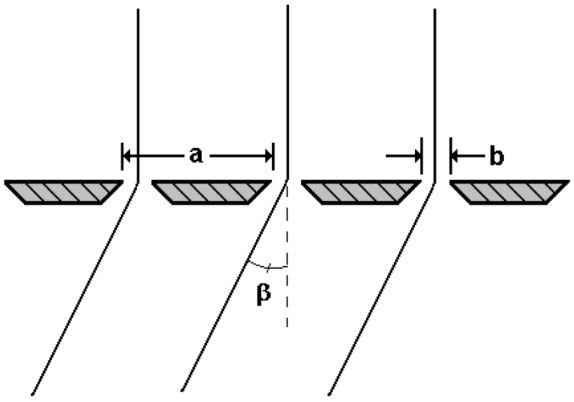

Figure 3.3.2: Grating of multiple slits

The resulting intensity is, therefore, the interference caused by the number of slits, N, modulated by the diffraction from one slit. As previously seen, the combined intensity is due to the interference of waves from multiple sources is multiplied by the intensity due to interference per source. The

resulting intensity plot is shown in figure 3.3.3. The plot is similar to the 3.3.1b concerning the intensity, spectral orders and diffracted angle. However, the effect of the two components modulated results in the depicted graph and the "double" graph as a result of the modulation.

$$I = I_0 \left[\frac{\sin(N\pi a \sin(\beta)/\lambda)}{\sin(\pi a \sin(\beta)/\lambda)} \right]^2 \times \left[\frac{\sin(\pi b \sin(\beta)/\lambda)}{\pi b \sin(\beta)/\lambda} \right]^2 \tag{3.13}$$

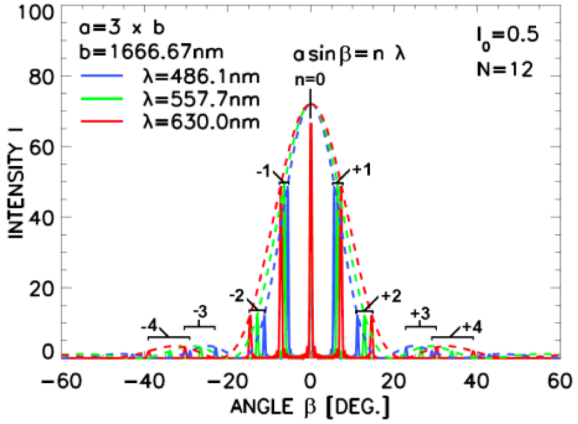

Figure 3.3.3: Intensity of diffracted light by a grating as a function wave length and spectral order

3.4 Geometric Properties of Photons

All electromagnetic radiation, including light, consists of photons. Just as all objects that have mass are built up of atoms, light rays are the result of many energy-consistent photons. To determine the amount of light (number of photons) passing through a spectrometer, etendue and throughput must be defined, Linder and Hansen (2019).

3.4.1 Etendue

The amount of light detected by the instrument is described by the acceptance area, or the field of view, photons can travel into. Etendue is the maximum geometric extent allowing traveling photons and thereby characterizing an optical system's ability to accept light. Figure 3.4.1 is an illustration showing how to review etendue.

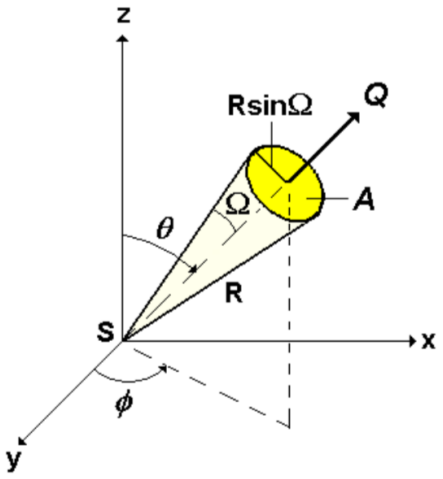

Figure 3.4.1: Set-up explaining Etendue

S describes the emitting source of light, while Q is the solid angle of which the light propagates into (or out of). By definition, etendue, G is found by $G := \int\int dSdQ$. For a simple spectrometer like the one viewed in this assignment, $G = S \cdot Q = \pi S sin^2(\Omega)$.

An instrument is defined to be optimally constructed when it can ensure an absence of light loss. This requires constant etendue throughout the instrument without any reduction from geometrical blocking. The latter implies the similarity $G_2 = G_3$, or $\pi S_2 sin^2(\Omega_2) = \pi S_3 sin^2(\Omega_3)$. The relations between the latter properties will be easier to understand after looking at the figure describing a spectrometer, Figure 4.3.1 in Section 4.3.

The optimal exit slit width can be calculated from constant etendue through the elements involved - starting at the entrance slit, eventually reaching the exit slit. From the entrance slit, the etendue can be expressed by

$$G_2 = \frac{G_A cos(\alpha)}{f_2^2} \cdot w \cdot h \tag{3.14}$$

Similarly can the etendue from the exit slit be described as follows

$$G_3 = \frac{G_A cos(\beta)}{f_3^2} \cdot w' \cdot h' \tag{3.15}$$

w and h, is the entrance width and height, while w' and h', explain similar properties at the exit slit. $G_A cos(\alpha)$ and $G_A cos(\beta)$ defines the illuminated area of the grating as seen from the entrance and exit slit, respectively. Using similarity of form, $h \cdot f_2 = h' \cdot f_3$. Using all of the above, the resulting optimal exit slit width can be found by the following similarity

$$w' = \frac{cos(\alpha)}{cos(\beta)} \cdot \frac{f_3}{f_2} \cdot w \tag{3.16}$$

Expressing the exit slit as a function of the entrance slit, reveals useful information on the spectral bandpass and resolution discussed in Section 4.3.1.

3.4.2 Flux

Flux is defined as the number of photons traveling into a solid angle Q, when emitted from a source, S, per unit time [sec]. By this definition, flux Φ can be expressed as

$$\Phi = \frac{photons}{s} \tag{3.17}$$

Flux can describe both the light intensity and the radiance. The intensity, I, can be found by computing the flux, Φ per unit solid angle [sr]

$$I = \frac{\Phi}{Q} = \frac{photons}{sr \cdot s} \tag{3.18}$$

The radiance, B, is the intensity through a unit surface area, A [cm], where A is the yellow area in Figure 3.4.1. Given (3.17), B can also be described as the flux of photons per unit area and solid angle.

$$B = \frac{I}{A} = \frac{photons}{cm^2 \cdot sr \cdot s} \tag{3.19}$$

Applying the terms above to the definition of etendue, the photon flux through the geometric extent being the etendue, can be described as a function of etendue and radiance.

$$\Phi := B \cdot G \tag{3.20}$$

As will be shown in Section 3.4.3, (3.20) is useful when evaluating the fluxes of photons entering and leaving a spectrometer.

3.4.3 Throughput

Throughput defines the amount of flux hitting the detector, charge-coupled device (CCD), at the end of the spectrometer. Simply put, throughput is the usable flux. From (3.14) and (3.15), the following similarities can be stated. Assuming that B_2 is the total radiance of the light source, (3.21) describes the flux entering the entrance slit, while (3.22) describes the flux exiting the spectrometer system.

$$\Phi_2 = B_2 \cdot G_2 = B_2 \cdot \frac{G_A cos(\alpha)}{f_2^2} \cdot w \cdot h \tag{3.21}$$

$$\Phi_\lambda = B_r \cdot G_3 = B_\lambda \cdot E_\lambda^n \cdot T_\lambda \cdot \frac{G_A cos(\beta)}{f_3^2} \cdot w' \cdot h' \tag{3.22}$$

In (3.22), B_r, describes the remaining radiance at the end of the spectrometer, and includes the spectral radiance, B_λ, multiplied with reducing factors due to loss. E_λ^n describes the efficiency of the used grating at spectral order n. T_λ is a factor describing losses due to the geometry of the components in the spectrometer. For an optimal spectrometer with an unrealistically efficient gradient, both E_λ^n and T_λ are equal to 1.

3.5 Light in Fluid

The light in any fluid diminishes due to two factors: absorption and scattering. The absorption will cause the light to diminish altogether, as the fluid molecules absorb the radiant energy and convert it into kinetic, chemical energy or both. The scattering causes the light to change direction, without changing the wavelength. The photons are dispersed as they penetrate the fluid. This will increase the chance of absorption due to the direction change extends the travelled distance. The total attenuation is a result of the complex and nonlinear interaction between the two. The complexity has lead to the radiative transport equations having no exact solution. Apart from the inherent properties of the medium, the particles suspended in the fluid column will also play a part in diminishing the light. These two main effects are illustrated in figure 3.5.4 by the end of the section.

The previous and following sections are largely inspired by Yamashita et al. (2007) and Smith and Baker (1981) as well as lectures from TMR4240:*Marine Control Systems 1*, which also provided illustrations.

3.5.1 Inherent Optical Properties (IOP)

The optical properties of a fluid may be divided into inherent and apparent optical properties. The inherent optical properties (IOP) are those that have operational values invariant of changes in the radiance distribution at a given point in the medium. On other words, the properties are constant with respect to light distribution. The properties directly describe the true characteristics of the medium with respect to scattering and absorption. IOP are dependent on the electromagnetic properties of the medium and any dissolved and suspended material. The inherent optical properties are particularly important in high-resolution imaging.

The inherent optical properties describe the scattering and absorption of the light in the fluid, and are crucial with respect to the radiative transfer in water. The flux of the light passing through a fluid is reduced compared with the entering light. The change per length z is described by

$$\frac{d\Phi}{dz}(z) = -\mu(z)\Phi(z) \tag{3.23}$$

Where $\frac{d\Phi}{dz}$ is the flux change per length, Φ the original flux and μ is the attenuation coefficient describing the combined effect of scattering and absorption on the photons.

Apparent Optical Properties

The apparent optical properties (AOP) on the other hand, have operational values that depend on the radiance distribution at a given point in the medium. Similar to the inherent optical properties, AOP is also dependent on the dissolved and suspended material in the medium. However, the properties also depend on the geometry of the light distribution. AOP are important when investigating the penetration of radiant energy to depth in the ocean water.

3.5.2 Light Attenuation

The attenuation in water is describe by the attenuation coefficient. A nonlinear coefficient depending on the wavelength, it is derived for pure, clear water. It is the sum of the absorption and scattering coefficients. In reality, the effect of salinity and other material dissolved and suspended in the medium will also affect the penetration depth of the light. The total coefficient is a sum of the different effects resulting from the properties of water, all having a nonlinear relationship with the wavelength.

The effect of light attenuation on intensity rather than flux is described by the equation below. It is derived by integrating the equation above 3.23 with respect to intensity, instead of flux. $I_\lambda(z)$ is the light intensity of the wavelength, λ is the wavelength of the light, z is the distance between the light source and the viewpoint, $I_{0,\lambda}$ is the light intensity of the wavelength at the light source and c_λ is the attenuation coefficient of wavelength λ.

$$I_\lambda(z) = I_{0,\lambda} exp(-c_\lambda \cdot z) \tag{3.24}$$

Do keep in mind that the light attenuation coefficient is empirical and, therefore, cover a large range of complex interactions.

Absorption

Atoms, and thereby molecules, contain electrons. Given the specific atom, these electrons hold a specific natural frequency. When light hits a molecule and the photon matches the gap between the energy levels in the targeted atom, the electrons will be given a vibrating motion. Then the frequency of the light is equal to the electrons natural frequency. The vibration is a result of energy absorption – energy taken from the light. This way, the electrons absorb the energy of the light by turning it into vibrational energy, which cannot, directly, be converted back to light.

The light absorption coefficient of water varies depending on the wavelength of the light. Figure 3.5.1 depicts the increase in absorption with increased wavelength. The increase describes why underwater photography is blue tinted. Longer wavelengths are not able to penetrate the depths, due to the lower energy in the radiation, and thus red colors diminish. Wavelengths of even greater magnitude, such as near-infrared and infrared, are absorbed at an even higher rate. Subsequently, measurements of infrared radiation underwater are more difficult.

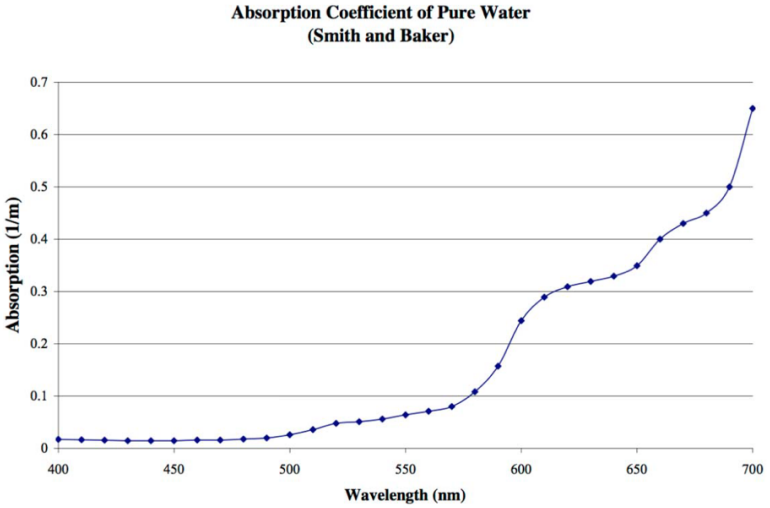

Figure 3.5.1: The absorption coefficient as a function of the wavelength, Smith and Baker (1981)

.

Water absorbs wavelengths covering a wide range of electromagnetic radiation. For light with wavelengths larger than 200 nm, this absorption is due to rotational transitions and intermolecular vibrations. As the H2O-molecule has a particularly small moment of inertia on rotation, a rich vibrational-rotational spectrum appears, sometimes containing millions of absorption lines.

The water absorption spectrum is, therefore, very complex. The water molecule may vibrate in several ways, at several states affected by the environment. For the specific case of H2O, the absorption spectrum is displayed in Figure 3.5.2. The spectrum may vary based on the condition of the water and placement of measurement - for instance, whether one looks at the open sea or the coastal areas. However, the trends, represented in the figure, should more or less remain. The spectrum clearly shows how the water absorption is at its lowest in visible light, making this range of wavelengths more optimal when detecting objects underwater, Chaplin (2018). Moving beyond infrared light, the radiation is, at a larger degree, absorbed. Nevertheless, an intensive NIR-source can leave sufficient light if the distance between the light source, object and imager is small enough. However, as the source close up on the target, the spatial coverage, commonly exploited using a hyperspectral imager, goes away.

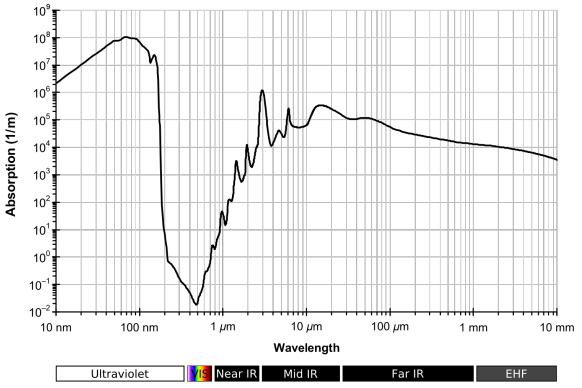

Figure 3.5.2: Absorption spectrum of liquid water, Kebes (2016)

Scattering

During the photon-fluid interaction, the photon might either change its direction, its energy, or both. Either of these processes is called scattering. More precisely, scattering can be described as the change in the direction of light flux produced by individual parcels of particulate matter called 'scatterers'. This means that light, or other moving particles, are forced to deviate from the straight trajectory they were on to begin with, due to the collision between the light wave and the fluid.

As mentioned, inherent optical properties are dependent on several properties. Similar to water, materials absorb and scatter light as a function of wavelength. If comparing particles of the same volume, they will scatter light differently based on shape. Also, particles with the exact same shape will scatter light differently based on volume. A change in the material, size or shape (or the composition) will alter the optical properties, Williams (1973).

In the ocean, the physical characteristics of the fluid are highly affected by the surroundings, as previously mentioned with the AOP. As an example, a change in the concentration of plankton or being in coastal waters instead of the open ocean, will contribute to a significant change in both the resulting absorption and scattering.

The vast majority of the light is scattered elastically at the same wavelength and frequency, and thus energy, as the incoming light. However, a tiny portion of the light is scattered inelastically at a different wavelength and frequency. This is due to the fact that the electrons excited by the incident light either absorbs some of the energy or adds to it. Due to the law of conservation of energy, the change in energy in the light is inversely matched in the material. Usually in the form of vibrational energy, which in turn is largely based on the molecular bonds in the material. The result is a small fraction of the scattered light being emitted at a different energy level based on the composition of the material. The phenomenon is called Raman scattering and is the basis of Raman spectroscopy, more thoroughly described later in this chapter.

3.5.3 Transmittance

The remaining light after the effect of light attenuation is the transmitted light. It will have been affected by the medium it has crossed and subsequently will have changed. The result is a possible signature of the suspended particles in the fluid. As previously mentioned, the properties of fluids change depending on the matter suspended. Hence, it is possible to account for the inherent effect of the fluid and then attain the effect other particles will have had on the light.

3.5.4 The Behavior of Light in Air

Light in air behaves differently than in water. In the air, the light will next to no attenuation, which means that the reflection can be expressed by the light intensity, I_λ, describing the colors observed on the object.

$$I_\lambda(L, z) = \frac{S_0 \cdot \kappa_\lambda \cdot cos^3(\alpha)}{z^2} \tag{3.25}$$

In (3.25), I_λ represents the reflected light intensity at a given wavelength, lambda, while S_0 is the light source. L is the distance between the object and the viewpoint, while z describes the distance from the object to the light source. Furthermore, κ_λ describes the reflectance ratio of the object's surface at a given wavelength, λ. α is the angle between the ray vector from the light source and the normal vector of the object surface. Figure 3.5.3 illustrate this with a simple set-up.

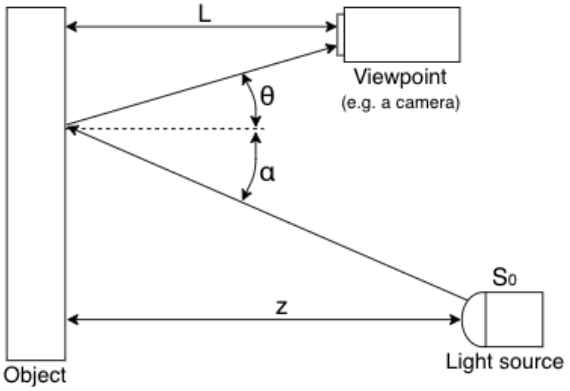

Figure 3.5.3: Light reflection in liquid

However, these properties cannot be directly drawn when doing the same underwater. In water, light attenuation will be present and affect how the light is reflected. In addition, light is possibly scattered at stages resulting in a change in the direction. In the figure, these stages are leaving the light source and after hitting the object, Sørensen (2018). This will be elaborated in the following sections.

3.5.5 Artificial Lighting

Natural light is only available in the top 50 meters of the ocean, due to the absorption of light in water. Even in shallower waters, a light source is essential in order to achieve satisfactory results. In photography, the light has to travel twice the distance from the source to the object, given the viewpoint and the light source are at the same point, as it has to reflect off the object and return. Figure 3.5.4 illustrates the effect the marine environment will have on artificial light.

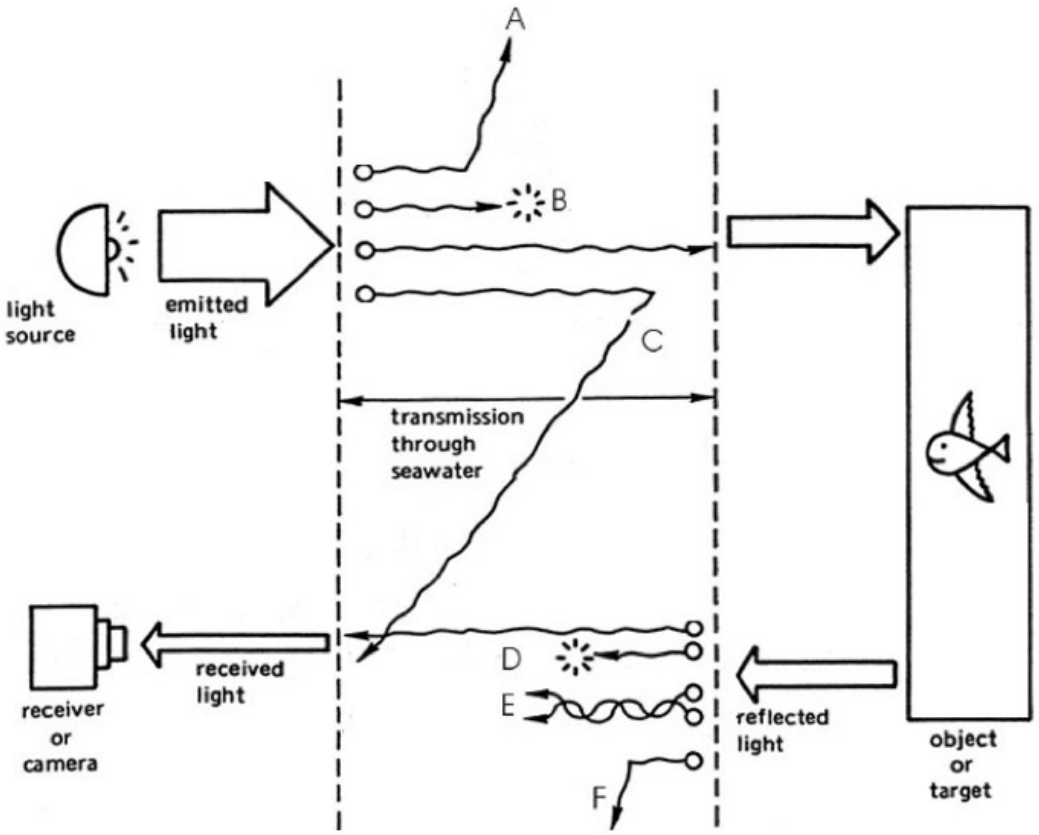

Figure 3.5.4: Artificial light positioned relative to the object and camera. The illustration also depicts inherent optical properties of the water. **A**: Outward scattering of emitted light **B**: Attenuation of emitted light **C**: Back-scattering of emitted light **D**: Attenuation of reflected light **E**: Scattering of reflected light **F**: Outward scattering of reflected light, Sørensen (2018)

The effect of light attenuation of a light source is previously described by the equation 3.24. $I_\lambda(z)$ is the light intensity of the wavelength, i is the wavelength of the light, z is the distance between the light source and the viewpoint, $I_{0,\lambda}$ is the light intensity of the wavelength at the light source and c_λ is the attenuation coefficient of wavelength i.

$$I_\lambda(z) = I_{0,\lambda} exp(-c_\lambda \cdot z) \tag{3.26}$$

When a camera and an artificial light source is used under water, there is the effect of light attenuation, but also the effect of reflection of light. Both will have an impact on the intensity of a given wave length at the viewpoint. By combining the equation of reflection of light in air and the attenuation equation above, the result is the equation for diffuse reflection of light in liquid. It describes the light intensity of a given wavelength depending on the distance from the object to the light source and the distance from the viewpoint to the object.

$$I_\lambda(l, z) = \frac{I_{0,\lambda} \kappa_\lambda \cos^3 \alpha}{z^2} exp\big(- c_\lambda \big(\frac{z}{\cos \alpha} + \frac{l}{\cos \theta} \big) \big) \tag{3.27}$$

Where α is the angle the light hits the object relative to the normal of the object, θ is the angle of the reflected light from the object relative to the same normal, κ_λ is the reflectance ratio of the reflective surface, l is the distance from the object to the viewpoint, z the distance from the light source to the object surface, $I_{0,\lambda}$ is the light intensity of the wavelength at the light source and c_λ is the attenuation coefficient, the wavelength is specified by λ.

Calculating the intensity is still not as straight forward as the equation suggests. The light intensity at the light source $I_{0,\lambda}$ and the reflectance ratio of objects, κ_λ, is often hard to obtain. These may be estimated by color registration of acquired images. Furthermore, the light source in underwater photography are often close to overlapping, making the $z \approx l$ and thus α and θ close to 0, subsequently $\cos\alpha, \cos\theta \approx 1$. The resulting equation is

$$I_i(z) = \frac{I_{0,\lambda}\kappa_\lambda}{z^2} exp\big(-c_\lambda \cdot 2z\big) \tag{3.28}$$

3.6 Spectral Signatures

The aforementioned effects on light differ based on materials. Light will be absorbed or reflected differently depending on the surface it has interacted with. The light returning from any given object, will have been affected differently at different wavelengths. The result is that it is possible to identify the materials which have affected the light based on the difference in the incident and transmitted light. The materials will reflect and absorb based on their chemical composition, and with the right instruments, this effect will be possible to record. The effect may be far from visible to the human eye, either due to the limited number of wavelengths we are able to see, or because of slight differences too small to notice.

However, by dispersing the light, one may detect the intensity of different wavelengths. If there is a sufficient amount of recorded wavelengths, the attained signature will be unique. The intensity will vary based on the interactions the light has had. By comparing the relative change, one can identify the interaction. This final measure is called a spectral signature and can be obtained through spectroscopy. The different intensities make up a continuous line, unique to different materials and possible to recognize.

Chapter 4

Optics of Spectrometry

This chapter addresses building blocks essential to understand the field and utilization of spectroscopy. The chapter also acts as a foundation sustaining the scope of imaging, presented in the next chapter, Chapter 5, Imaging. Chapter 5 takes spectroscopy levels further, by presenting its real exploitation value. Similar to Chapter 3, the following sections are largely inspired by the lecture notes from TTK20: Hyperspectral Remote Sensing, Signernes (2018). The source has also provided illustrations, if not stated otherwise.

4.1 Fundamentals

4.1.1 Spectral Reflectance

Reflection occurs when the wavelength of the light do not match the natural frequencies of the object it reflects off. Whenever the waves strike the object, the electrons in the atoms will vibrate. However, this is not the same type of vibration as the one discussed above (Section 3.5.2). Now, the electrons vibrate in small amplitudes for no more than brief periods of time. This causes the energy to re-emit as a wave of light, rather than turn into vibrational energy and be absorbed at resonance vibration.

The spectral reflectance, also called the optical fingerprint, can be described as the percentage of the light amount reflected off an object at each wavelength. As mentioned, different objects absorb and reflect different wavelengths. In plants, red and blue wavelengths are highly absorbed, leaving the reflected color to be more or less green. Mathematically speaking, the spectral reflectance, $R(\lambda)$ is upwelling irradiance coming off the object, $Lu(\lambda)$, divided by the spectral downwelling irradiance towards the object, $Ed(\lambda)$, Johnsen et al. (2013).

$$R(\lambda) = \frac{Lu(\lambda)}{Ed(\lambda)} \tag{4.1}$$

Where $Lu(\lambda)$ denotes the raw data of the object, including signature from light source, while $Ed(\lambda)$ is the spectral radiance from measurements of spectrally neutral reflectance standard, Johnsen et al. (2016b).

Note: For (4.1) to hold true, all surfaces are assumed to behave like Lambertian reflectors, Johnsen et al. (2016b), meaning that the reference surface has a perfectly diffuse/matte property. This ensures that the radiant intensity, regardless of the reflected direction, is proportional to the cosine of the angle of the surface's normal. This is known as Lamberts Cosine law, Signernes (2018).

In order to build a tool able to detect this spectral reflectance, and return the optical fingerprint, properties of spectroscopy are essential to explain. The remaining part of this chapter are components of such a tool.

4.1.2 Reflective Gratings

The grating equation, (3.8), assumes a grating transmitting light. The reflective grating, however, reflects the light. This grating consists of a polished surface with parallel grooves - as shown in Figure 4.1.1. Between the grooves, parallel mirrors constitute the grating, each mirror acting as a source of interference.

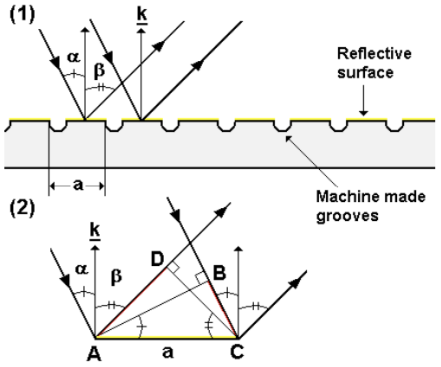

Figure 4.1.1: (1) Reflective grating. (2) Resulting rays, where the red lines describe the associated phase difference

As explained in Section 3.1, the phase difference of waves propagating from coherent sources is $\sigma = \frac{2\pi}{\lambda} \cdot \mathbf{r}$. Of the figure above, Figure 4.1.1, $\mathbf{r}$ can be calculated as $(BC - (-AD))$. Hence, the phase difference as a function of reflective grating can be presented as

$$\begin{aligned} \sigma &= \frac{2\pi}{\lambda}(BC + AD) \\ &= \frac{2\pi}{\lambda}(a\sin(\alpha) + a\sin(\beta)) \end{aligned} \tag{4.2}$$

At maximum intensity, $\sigma = 2/pin$, the reflecting grating equation is found

$$n\lambda = a(\sin(\beta) + \cos(\alpha)) \tag{4.3}$$

Once again, n is the spectral order. α is the incident angle, and β represents the diffracted angle of the grating.

If there is a blazed grating, i.e., each reflective surface between the grooves are tilted relative to the grating, the equation is modified in order to account for the blaze angle, ω_b.

$$\lambda_b = \frac{2a}{n} \sin(\omega_b) \cos(\alpha - \omega_b) \tag{4.4}$$

4.1.3 Angular Dispersion

Angular dispersion is a measure of how the diffracting waves are spread, per unit wavelength. The angular dispersion of a grating is defined as $d\beta/d\lambda$. This can be derived by differentiating the grating equation, (4.3).

$$\frac{d\beta}{d\lambda} = \frac{n}{acos(\beta)} \tag{4.5}$$

4.2 The GRISM

A GRISM is a combination of a grating and a prism - hence the name. The GRISM is a prism stacked in series with a transmission grating, as can be observed in Figure 4.2.1.

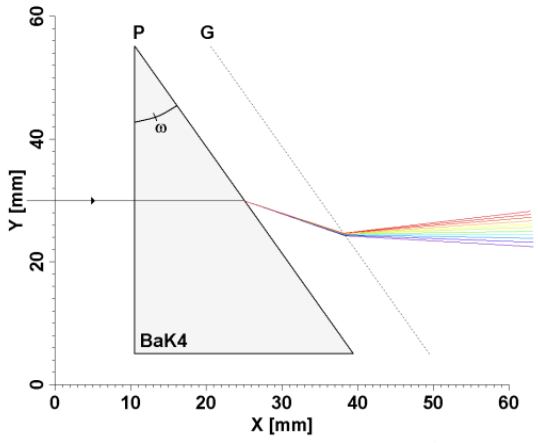

Figure 4.2.1: GRISM: Light passing through a prism, P, dispersing blue light more than red, and a grating, G, diffracting red light more than blue

For a grating, the intensity maximum for each spectral order n, increases with increasing wavelength. A prism, however, has no spectral orders and refracts blue light more than red. The net effect is a compact spectrum able to obtain a straight through center wavelength, parallel to the optical axis of the system. This on-axis effect makes it easy to stack additional optics in both ends of the GRISM. Due to the absence of off-axis effects, image quality is preserved.

When calculating the angular dispersion of a GRISM, the result is equal to the angular dispersion of a grating (4.5), except for one additional term. This turns out to be a non-negative term, implying that the GRISM has an increased angular dispersion compared to a grating alone.

4.3 System Optics

Rays travelling through a spectrometer can be described by an optical diagram like the one presented below in Figure 4.3.1.

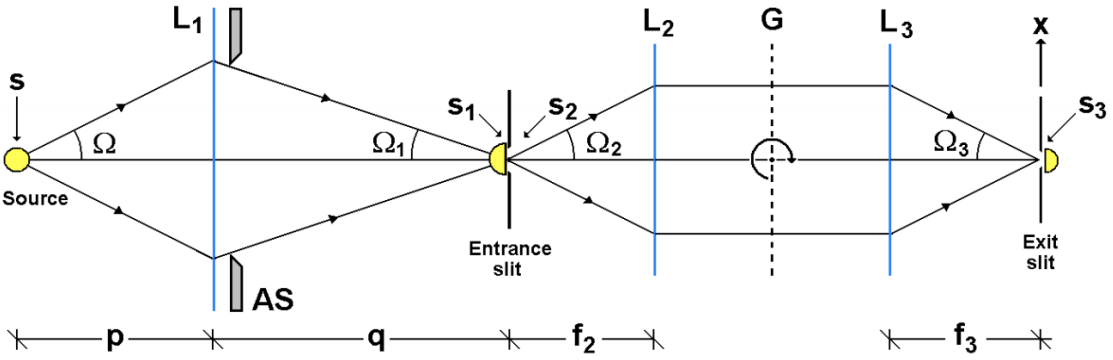

Figure 4.3.1: Optical diagram of a Spectrometer

S represents the source of light. S illuminates the front lens, L_1, with the incident angle Ω. Furthermore the front lens focuses the light onto the entrance slit, resulting in the imaged area, S_1. G is the grating, either transmitting or reflecting, in which L_2 collimates with light passing through the entrance slit area, S_2, at an angle Ω_2. The diffracted beam of light from the grating is then focused onto the exit slit by L_3, as a function of wavelength. This makes S_3 the area of the diffracted entrance slit image.

f_2 and f_3 are the corresponding focal lengths of L_2 and L_3. Note that as long as L_1, L_2 and L_3 are able to focus or collimate the beam of light, they can be mirrors instead of lenses.

4.3.1 The Spectral Bandpass and Resolution

Spectral bandpass and resolution both characterize the instrument's ability to separate adjacent spectral lines. The bandpass specifically defines the spectral interval to be isolated. This is assuming the light source is a continuum. As will be shown below, the bandpass is mainly dependent on the width of the grating, entrance and exit slit widths and the spatial resolution of the CCD.

The isolated spectral interval (bandpass) can be found from the recorded Full Width at Half Maximum (FWHM) of a monochromatic spectral line. In reality, there is no perfect spectrometer. This is why the bandpass is approximated to FWHM. Figure 4.3.2 shows the effect of the spectral resolution of a monochromatic line. As displayed, the bandpass at wavelength λ_0 can be found at half intensity, B.

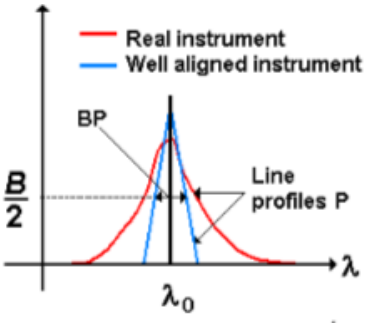

Figure 4.3.2: Spectral resolution of monochromatic line

Note that the assumption of a monochromatic spectral line does not restrict to only one line. Any spectral structure can be considered as the sum of infinite single monochromatic lines at different wavelengths.

The spectral bandpass can then be calculated as the wavelength distribution along the x-axis multiplied by the exit slit width. This wavelength distribution is called *the linear dispersion*, and is defined as $d\lambda/dx$. Using the angular dispersion from (4.5) and the similarity $dx = f_3 d\beta$, the spectral bandpass can be calculated. As known from (3.16) in Section3.4.1, the exit slit width, w' is dependent on the entrance slit width, w through $w' = \frac{cos(\alpha)}{cos(\beta)} \cdot \frac{f_3}{f_2} \cdot w$.

$$FWHM = \frac{d\lambda}{dx} \cdot w' \quad = \frac{d\lambda}{d\beta}\frac{d\beta}{dx} \cdot w' \quad = \frac{acos(\beta)}{n}\frac{1}{f_3} \cdot w' \quad = \frac{acos(\alpha)}{n \cdot f_2} \cdot w \tag{4.6}$$

In (4.6), α is the incident angle and β is the diffracted angle. f_2 and f_3 are, as mentioned, the focal lengths associated with the lenses L_2 and L_3 respectively.

4.3.2 The GRISM Spectrograph

In section 4.2, the GRISM, and how it could obtain a straight through center wavelength parallel to the optical axis, was elaborated. Therefore, using a GRISM as the dispersive element is popular when designing a spectrometer. Figure 4.3.3 shows a typical 3D configuration of a GRISM spectrograph in hyperspectral image mode, illustrating the basic elements of hyperspectral imaging. Of the illustration, one can observe how the elements are stacked at the right next to each other (on axis), supporting the previously stated properties of the GRISM. This on-axis design reduces geometrical aberrations and thereby improves the resolution.

Similar to the spectrometer already discussed above (section 4.3), the front lens focuses light onto the entrance slit S_1, while L_2 collimates the GRISM. The diffracted light is then focused onto the image detector (CCD), by L_3.

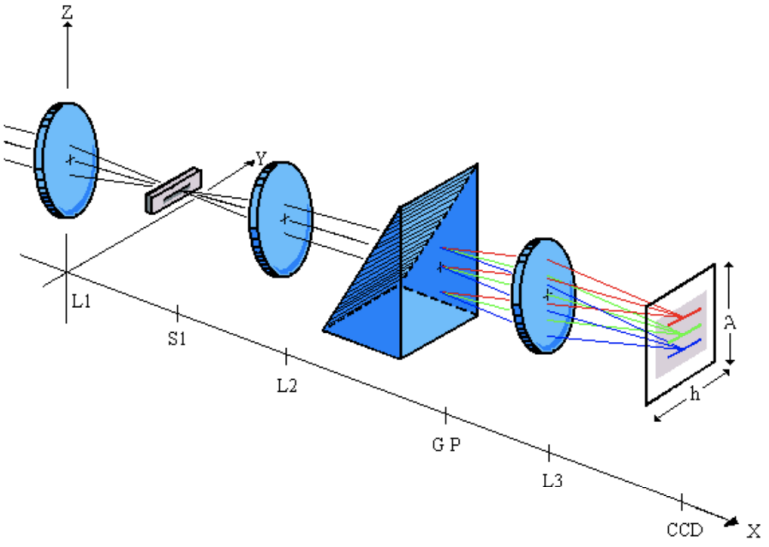

Figure 4.3.3: The GRISM spectrograph

Chapter 5

Imaging

This chapter illuminates the imaging process - from the commonly known digital image to the hyperspectral image, containing an additional dimension of information improving the resolution of the image.

5.1 The Digital Image

From the mid-20th century, images have been stored in a digital format, Geladi et al. (2007). A digital image is an array of rows i, and columns j, consistent of i x j gray-values. A gray-value, better known as an intensity or a pixel, is simply one of many small squares in an image. If the image is to consist of colors, however, a third dimension is needed. This dimension is characterized as the depth, and can be found as the height in Figure 5.1.1b). The depth is three layers deep, consisting of red, green and blue. What was previously a gray pixel is now a voxel illustrated in 5.1.1b), with the triplet of red, green and blue - each of which contains different information. Note that the height of the voxel is almost undetectable, as the voxel only consists of the tiniest distinguishable element (with three wavelengths) of a 3D object, Geladi et al. (2007).

However, if the interval separating the layers is chosen to be a shorter wavelength, the number of layers will increase. The resulting image is then called a multivariate image, illustrated in Figure 5.1.1c). If k denote the depth dimension and thus determine the number of wavelengths which in turn will constitute the number of layers, the resulting array will be of the size i x j x k.

For the human eye to be able to perceive a color image, only three wavelengths/layers are needed, namely red, green and blue. It, therefore, rarely makes sense to create multiple layers unless the goal is to capture information the eye cannot see. This is where hyperspectral imaging enters, by definition it has more than 100 layers and can express each pixel as a spectrum.

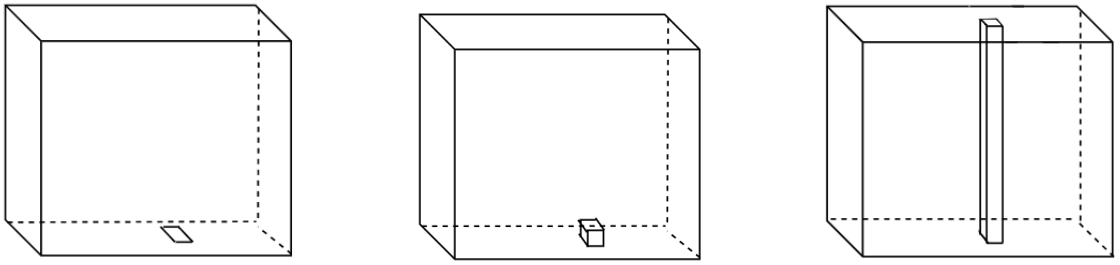

(a) Pixel (b) Voxel (c) Multivariate Image

Figure 5.1.1: a) Pixel, b) Voxel and c) Multivariate image

5.2 Hyperspectral Imaging

In order to study the reflecting light from the target, or the transmitting light through the target, a spectrometer is needed. A spectrometer, presented in Chapter 4, is an instrument that splits the incoming light into a spectrum. Measuring these spectra is the most common way to use hyperspectral imaging.

Hyperspectral imaging uses a hyperspectral camera (imaging spectrometer) to collect spectral information. As mentioned, the difference between a hyperspectral image and a regular photo is that the hyperspectral camera measures hundreds of thousands of spectra instead of a single spectrum, creating not only a multispectral image, but a hyperspectral image. In contrast to multispectral imagers, sensitive in only a few wavebands, the hyperspectral imagers measure the spectral reflectance per image pixel of the particular OOI, leaving a complete reflectance spectrum for each pixel in the image, Pettersen et al. (2013).

In detail, a spectrograph, illustrated in Figure 4.3.3, generates images from the entrance slit, as a function of wavelength. The amount of images detected by the CCD at the exit slit is dependent on the entrance slit width and the element's ability to diffract colors. The width of the exit slit, being dependent on the width of the entrance slit, was derived in (3.16) in Section 3.4.1, describing optimal etendue. A large number of detected images at the exit slit will directly improve the spectral resolution of the instrument. The resulted image recorded by the CCD is called a spectrogram (an illustration of a spectrogram can be found as the last element in Figure 4.3.3). The spectrogram contains both spectral and spatial information and can be described by the intensity distribution and position along the slit.

However, the information retrieved is information about the covered area of the target object, which is nothing but a film covering only a small part of the object. In order to obtain the object's full spatial extent, the entire object surface needs to be sampled.

In order to do so, the recording instrument must be moved relative to the target. The velocity, ν of the instrument is crucial, and must be coupled with the sampling frequency. The instrument will undersample (miss samples of the target area) if the distance moved during readout time, τ, exceeds the length of the measured area, dx (displayed in Figure 5.2.1). This requirement is shown

in (5.1).

$$\nu \cdot \tau \leq dx \tag{5.1}$$

This way, the image at the entrance plane moves across the slit so that the CCD can record spectrograms for each track of the object. This is called the push broom technique, which will be illustrated in Section 5.2.2. When summarizing all samples, information on the continuous image can be retrieved.

The required movement is based on the instrument and target moving relative to each other. Hence the movement can be created in two ways. Either the instrument can move, or the viewed target can be moved while keeping the imager still. If the target is located at a conveyor belt, it might be suitable to keep the instrument still. However, as mentioned, the magnitude of the relative movement is important. This means that if the conveyor belt is moving too fast, the instrument needs to move as well, in order to reduce the relative movement.

Figure 5.2.1 describes the situation where a hyperspectral imager is attached to an airplane moving at a velocity, ν. In the illustration, S is the slit, while w is the associated width. z describes the altitude above ground level. The front lens is denoted L_1, and has a focal length of f_1.

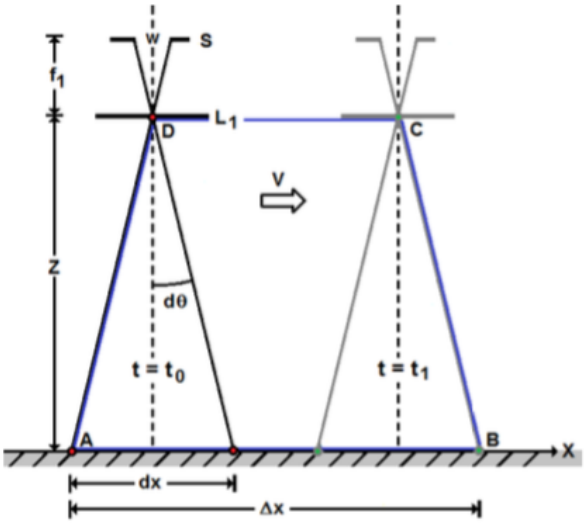

Figure 5.2.1: Spatial resolution - field of view from a moving airplane, Signernes (2018)

It is common to believe that the spatial resolution is dependent on the number of pixels present along the wavelength axis of the detector. However, the amount of information is described by the number of spectral layers the hyperspectral imager can produce (illustrated as the height of the column in Figure 5.1.1c)). The spectral layers define a dimension independent of the pixel-plane, only dependent on the bandpass (see section on bandpass) and the spectral range of the instrument. Using the similarity of form, dx can be calculated from the lengths of the figure.

$$dx = \frac{z \cdot w}{f_1} \tag{5.2}$$

During the exposure, the airplane has moved from the first state to the second. This distance can be calculated from the time spent at the constant velocity held: $distance = \nu \cdot (t_1 - t_0) = \nu \cdot \Delta t$.

The spatial resolution becomes equal to the distance from A to B. Of the figure, this distance is observed as

$$\Delta x = dx + \nu \cdot \Delta t \tag{5.3}$$

(5.2) shows how dx, an thereby also the spatial resolution, is connected to the spectral bandpass through the slit width, w, as described in Section 4.3.1.

Concerning plastic, this translates to receiving both spatial and spectral information on the plastic material composition. The hyperspectral imager can be used as a taxonomical identification tool to make optical fingerprints of marine organisms. This is only if the pigment composition and corresponding absorption signature of the organism are known and can be used to verify the reflectance signature, Pettersen et al. (2013).

When the hyperspectral camera is taken underwater, the lighting is limited. The UHI is, therefore, using its own light sources, in contrast to passive techniques using ambient light, Johnsen et al. (2016b).

For the purpose of this project, there are two methods for camera configurations relevant, point-scanning image and line-scanning image.

5.2.1 Point-Scanning Image

Point-scanning image can be used to measure a complete spectrum in one pixel. In every spot, all layers are measured vertically from this spot. To make the whole picture, the camera must scan across the entire surface, spot by spot, Geladi et al. (2007).

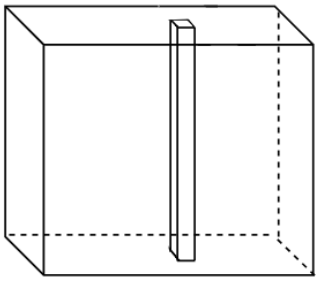

Figure 5.2.2: Point-scanning

5.2.2 Line-Scanning Image

The line-scanning image technique uses a two-dimensional detector, perpendicular to the surface of the measured target. This detector collects the spectrum of a whole line in the image, in one single scan. By moving the scan line with a push broom technique, one can map the entire image by combining all sets of spectra, Geladi et al. (2007).

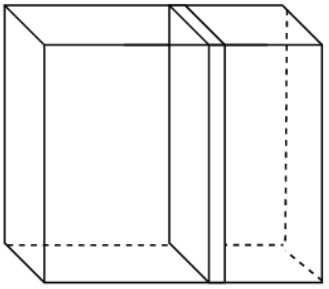

Figure 5.2.3: Line-scanning

5.3 Raman Spectroscopy

As mentioned, spectroscopy can be utilized in several ways. The optical signature can be retrieved using a hyperspectral imager, viewing reflected (or transmitted) light, or extracted from the light scattered from the OOI. The Raman method is based on the latter property, scattered light (Section 3.5.2) - more specifically, Raman scattering. By diffracting the Raman scattering, one may measure its intensity at the different wavelengths. The intensities are then compared to the incident light and the difference is identified. Based on the change, due to specifics in the material scattering the light, one can retrieve a spectrum unique to the material, the Raman spectrum.

5.3.1 Fundamental Theory

Whenever a sample is exposed to light, the light will either be transmitted through the sample or scattered. Nevertheless, a small part of the light is always scattered by the sample at different wavelengths. To characterize the scattering light beam, the properties of emitting photons are compared to incident photons. Let us name the frequency of the incident light beam f_i, while f_s is the frequency of the scattered beams.

Inside the molecules of the sample, electrons have different vibrational levels based on energy differences. Whenever a photon interacts with an electron in the sample, the electron absorbs energy from the incident photon. This energy, transferred from the incident photon to the electron, can be expressed by Planck's constant times the frequency of the incident light, $E = h \cdot f_i$. The result is the electron being excited to a higher vibrational level. The electron will, in turn, fall back in position as it release the energy. If the energy is equal to the energy of the incident photon, the electron will settle at its initial level, and emerge another photon - with the same frequency as the incident photon: $E_i = E_s \rightarrow f_i = f_s$. This is called Rayleigh scattering and is the most common type of scattering, Band and Avishai (2013).

However, when losing energy from the virtual energy state, the electrons can sometimes respond differently. It might emit photons with a different frequency than that of the incident photon, $f_s \neq f_i$. This scattering is approximately $10^{-5}\%$ of the total scattered light and is called the Raman scattering, Inagaki and Kang (2016).

When an excited electron releases energy, defined within the Raman scattering, it can either return

to a higher energy state or a lower energy state than the initial state. The nature of these states can be observed in the Raman spectrum. When electrons absorb energy, f_s is less than f_i, and Stokes lines appear in the spectrum. Similar when $f_s > f_i$, the electron emits energy, and anti-stokes lines can be observed.

The emitted light, at different wavelengths, is diffracted with a regular spectroscope, resulting in a spectrum of Stokes lines. This way, by studying the resulting spectral peaks, one can identify molecules within the sample. The intensity of the spectral lines determines the concentration of a molecule in a sample.

Due to the fact that only 1 in 10 million photons are affected by Raman scattering, it is essential that the incident light is highly concentrated. Also, in order for it to be easier to compare, one strives to use a monochromatic light source due to the predictable signature. As a result, lasers are used in Raman spectroscopy as it delivers high-intensity uniform light.

In summation, Raman spectroscopy is the spectroscopy of the Raman scattering and identifying the change in intensity per measured wavelength. It is essential to recognize that the fundamentals of Raman spectroscopy are identical to the theory laying the grounds for the hyperspectral techniques, namely Chapter 3 and Chapter 4. Raman spectroscopy is similar to any other spectroscopy in that light is dispersed and the intensity is measured at a number of wavelengths. The spectroscopy is performed in a similar fashion, carrying the same possibilities. The main difference, however, separating the Raman method from the hyperspectral technique, is the type of diffracted light - producing the final spectrum. As mentioned, the Raman spectrometer separates the limited portion of Raman scattering, holding a change in energy, while the hyperspectral spectrometer includes all light emitted and transmitted. Due to the clear stokes lines, the resulting Raman spectrum has more distinct peaks associated with specific frequencies.

When performing measurements using the Raman scattering technique, it is essential to recognize that the Raman spectrum contains information from no more than a thin layer of the object surface. The measured surface thickness, with the WITec instrument used in this thesis, is approximately 30–60 nm. Therefore, to ensure the correct signature of the object, homogeneity throughout the sample is important, WITec GmbH (2019).

5.3.2 Spectral Characteristics

As previously mentioned, there are clear peaks in Raman spectra, which corresponds to distinct covalent bonds. The following paragraphs aim to cover the interpretation of such peaks, and are mostly based on Socrates (2002).

Peaks in Raman spectra are not described based on the specific properties of the corresponding bonds. On the other hand, the peaks are acquired through systematic empirical measuring and mapping.

The functional groups of materials may be identified based on their respective peaks. Based on known peaks, it is possible to identify a given substance based on the presence or absence of characteristic peaks from aggregates. However, it is important to note that there are variations in the

peaks due to differences in bonds. The bonds may either be of different geometric shapes or vibrate in a certain way. The mode of vibration is dependent on both the spatial geometry and the electronegativity of neighbouring atoms or functional groups. In other words, the bonds may twist and bend such that the peaks change. Also, there might be noise or other contaminants affecting the spectra. The result is the occurrence of peaks in certain intervals, rather than at exact wavelengths.

The position of bands is in part a result of the amount of energy absorbed by the bonds. The bonds will have different levels of strength and different possible modes of vibration. All of which will have different stiffness. The stiffer the bonds, the more energy is required to create vibrations. The same goes for the vibrational modes of the bonds. Certain types of motion require more energy. Subsequently, when larger amounts of energy are absorbed, it is reflected in bands at higher frequencies. Do note that considering individual vibrations in groups or atoms of molecules, is a simplification. Molecules do generally vibrate as a whole.

Furthermore, functional groups may not have one peak, but several. This is a consequence of their complexity. There are often multiple bonds acting together, forming the group and resulting in multiple peaks. Also, some might not be present at all. Due to inactivity caused by geometric properties or the measured wavelength interval.

In addition, the spectra reflect the composition of skeletal groups, i.e., the backbone of the molecule. This is highly important in the identification of polymers. The bonds forming the base of the molecule will naturally appear in the spectra. These will often have high intensities due to their sheer quantity - at least concerning polymers.

The intensities of the peaks varies. Mainly due to the number of a given functional group in the substance molecule. A high amount of a functional group will result in a higher number of given bonds, and thus higher intensities. Hence, the relative intensities of the peaks may indicate the relative presence of groups.

In summation, the presence of one particular peak should not be used individually to prove the presence of a group or the identity of a material. There are variations one must be aware of, which could make the peaks ambiguous. The observation of peaks based on expectation, due to a priori knowledge, should not be regarded as conclusive evidence of the presence of a particular group. In order to qualitatively confirm the presence of a substance, one should rather use correlation charts that depict the presence of correlated bands. One should also keep in mind that the absence of peaks is equally an indication as the presence.

Due to the highly sensitive nature of Raman Spectroscopy, one might encounter spurious bands. These are bands that do not belong to the sample. Mostly, they are due to poor sampling technique, general sample handling, instrumental effect, or others. The presence of contaminants is the most common reason for these, and one must be careful to handle them and be aware of their possible presence.

Below are some of the most common peaks in organic chemistry, the table is collected from Adar (2016).

Functional Group	Position (cm^{-1})	Remarks
>S-S<	500–550	
C-C	~1060 and 1127	Polyethylene
C-C	700–1260	Highly mixed in complex molecule
Aromatic ring	~1000	Monosubstituted
Aromatic ring	~1000	1,3 disubstituted
Aromatic ring	~1000	1,3,5 trisubstituted
Aromatic ring	~860	1,4 disubstituted
CH_3 umbrella mode	~1375	
CH_3 and CH_2 deformations	1410–1460	
>C=C<	~1650	
>C=C<	~1623	Ethylene
>C=0 mixed with NH deformation	1620–1690	Amide I
>C=O	1710–1745	Changes for ketone, aldehyde, and ester
C≡C	2100–2300	
SH	2540–2600	
$>CH_2$	2896 and 2954	Ethane
$>CH_2$	2845 and 2880	Polyethylene
CH_3	2870 and 2905	Polypropylene
$R_1R_2R_3CH$	2880–2890	Methine CH
CH	~2900	Cellulose
CH	~3015	Olefinic CH
CH	~3065	Aromatic CH
CH	3280–3340	Acetylenic CH
NH	3150–3340	Broadened and shifted by H-bonding
OH	3000–3600	Broadened and shifted by H-bonding

Figure 5.3.1: Table of Raman frequencies of common functional groups

Chapter 6

Data Analysis

This chapter is intended to leave the reader with the insight required to analyze data acquired using spectroscopy. It covers methods of signature recognition, in addition to general classification techniques. The latter are techniques applied in a wide range of fields, but also commonly used with spectral data. Finally, basic methods of signal processing are presented.

6.1 Signature Recognition

The following paragraphs are largely based on the theory presented in Keshava and Mustard (2002) and Graña and Veganzones (2012).

6.1.1 Endmember Signatures

A large number of spectral signature recognition methods are based on endmemberso. The use of endmembers is common practice in geology, a field with a tradition of using spectral recognition. These represent the extremes with respect to purity. The same rationale is used in signature recognition. There are signatures from completely pure samples, which represent the *correct* signature of the material. The endmember signatures are the signatures that are chosen to represent the pure surface of the material.

An aspect of the laboratory testing is to investigate whether it is possible to find such endmember signatures for plastic, and if so, record them. This would be beneficial, not only in recognition of plastic, but also for future work where the identification of each type of plastic is desired.

6.1.2 Spectral Angle Mapper

Spectral Angle Mapper (SAM) maps the difference in angle between unidentified spectra and reference spectra. The spectra are treated as vectors in an n-dimensional space, where n is the number of bands, i.e. wavelengths. The spectra will be represented in the space based on the intensities per band, which have a respective axis. A small angle between the two spectra will

indicate a high similarity, while a large angle will indicate a low similarity. The angle is calculated by

$$\alpha = \cos^{-1}\left(\frac{\sum_{i=1}^{n} t_i r_i}{\sqrt{\sum_{i=1}^{n} t_i^2} \cdot \sqrt{\sum_{i=1}^{n} r_i^2}}\right) \tag{6.1}$$

where α is the angle, t is the target pixel, r is the reference pixel, n the number of bands and i the given band. Do keep in mind that bands and wavelengths are used interchangeably, however, these are correlated such that $\lambda_i = X/n \cdot i$. λ, the wavelength of a band is equal to the band number, i, multiplied by the measured interval, X, divided by the total number of bands, n.

The classification based on the angle is typically based on a given limit value. If the angle does not fall below the value for any spectrum, it is unclassified.

6.1.3 K-means Clustering

The following paragraphs are largely based on James (2013a).

K-means clustering is a common unsupervised classification method. This means it will classify samples with similar values without any indication of what is being classified. The algorithm seeks to structure the data based on the data set itself. K-means clustering will in this sense classify samples by creating a specified number of subgroups, or clusters, with similar properties.

More specifically, the algorithm will create sets satisfying two properties:

1. $C_1 \cup C_2 \cup \cdots \cup C_K = 1, \ldots, n$. All observations of the data set must belong to at least one of the K clusters.
2. $C_k \cap C_{k'} = \emptyset$. The clusters do not overlap. Hence, observations will only belong to one cluster.

However, these properties do not determine what observation belongs to what cluster. As previously mentioned, one seeks to cluster similar observations. This will result in a minimized variation within each cluster. Or, one may relate observations to each cluster by minimizing the variation in the cluster, which will result in the desired outcome. In other words,

$$\min_{C_1,\ldots,C_K} \left\{ \sum_{n=1}^{K} W(C_n) \right\} \tag{6.2}$$

where $W(C_n)$ is the measure of the variation in cluster C_n, which is a measure of how much the observations differ from each other in the given cluster.

The most common way to solve this problem is to use the Squared Euclidean Distance. Also known as the length of a straight line in any dimensional room, and the basis for the Pythagorean

theorem. The distance is defined as

$$W(C_n) = \frac{1}{C_n} \sum_{i,i' \in C_n} \sum_{j=1}^{p} (x_{ij} - x_{i'j})^2 \tag{6.3}$$

where C_n is the number of observations in cluster k. The variation is, in other words, defined as the sum of all the pairwise squared Euclidean distances between the observations of the cluster, divided by the number of observations in the given cluster. The result is the following equation, which states the optimization problem defining K-means clustering,

$$\min_{C_1,\ldots,C_K} \left\{ \sum_{n=1}^{K} \frac{1}{C_n} \sum_{i,i' \in C_n} \sum_{j=1}^{p} (x_{ij} - x_{i'j})^2 \right\} \tag{6.4}$$

However, the problem that arises is the large number of ways to partition all observations, and it being next to impossible to find the optimal solution. As a result, one aims to find a satisfactory solution as a local optimum rather than the optimal. This is achieved by initially assigning the K clusters randomly. Then calculate the cluster centroid, which is the vector of the p feature means of the observations in the given cluster. Finally, each observation is assigned to the cluster with the closest centroid, with respect to the Euclidean distance. These steps are repeated until an improved solution is no longer found and a local optimum is achieved.

6.2 Principal Component Analysis

Principal Component Analysis (PCA) proposes a method to simplify complex high-dimensional data. The method will simplify while simultaneously retain the trends and patterns, making it ideal in analyzing data. It summarizes features, transforming the data into fewer dimensions. The lower dimensional, simplified, data has a lower computational cost and a decreased error rate due to less test correction as a result of fewer features associated with outcomes. PCA may be compared to clustering, and is an unsupervised learning method. It will recognize patterns regardless of the source of the data.

The following theory is based on lecture notes given in the course TTK20: *Introduction to Big Data Cybernetics*, which also provided the illustration, combined with The Unscrambler User Manual (1996), Shlens (2005) and Lever et al. (2017).

6.2.1 Principal Components

The lower dimensional data are called principal components (PCs). The inputs are projected on to the principal components with the goal of finding the most ideal summary of the data, using a limited number of PCs. The components are chosen based on the variance. The first component is chosen with minimum distance between the data and their projection onto the components. Minimizing the distance that coincides with maximizing the variance. Therefore, PC1 is chosen as the line holding the highest variance along the line. In order to create a new space, the components need to be uncorrelated. Linear algebra dictates that the PCs thus must be orthogonal. Therefore,

the following components are based on the previous criterion in addition to orthogonality. The result is the maximum possible number of PCs being either the number of samples or features, whichever is smaller. A higher number of PCs will result in a combination of either features or samples causing correlation and thus violating the orthogonality. The PCs are evaluated based on the percentage captured by each component. The sum of all components used in the analysis will be the total percentage captured. The projection of the original measurements to a two-dimensional plane may be seen in Figure 6.2.1. The figure also depicts the principal components being chosen. The projection is equivalent to a larger number of dimensions, but is impossible to illustrate due to the requirements of more than three dimensions.

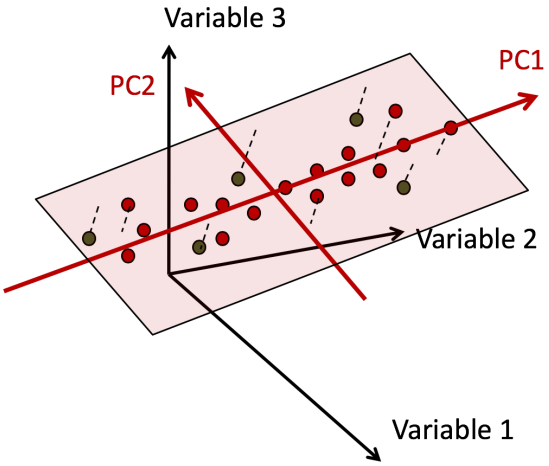

Figure 6.2.1: Fundamentals of Principal Component Analysis (PCA)

6.2.2 Fundamental Mathematics

The data set is assumed to be represented by a $m \times n$ matrix $\mathbf{X}$. The n columns are the samples/observations, while the m rows are the variables. The matrix is to be linearly transformed into the matrix $\mathbf{Y}$ of the same dimensions, which requires an $m \times m$ matrix $\mathbf{P}$.

$$\mathbf{Y} = \mathbf{PX} \tag{6.5}$$

The equation represents a change of basis, and $\mathbf{P}$ is a transformation matrix. The resulting equation is seen below. Here $\mathbf{p_i}$ are the rows of $\mathbf{P}$, $\mathbf{x_i}$ are the columns of $\mathbf{X}$, and $\mathbf{y_i}$ are the columns of $\mathbf{Y}$.

$$\mathbf{PX} = \begin{bmatrix} \mathbf{p_1} \\ \mathbf{p_2} \\ \vdots \\ \mathbf{p_m} \end{bmatrix} \begin{bmatrix} \mathbf{x_1} & \mathbf{x_2} & \dots & \mathbf{x_n} \end{bmatrix} \tag{6.6}$$

$$\mathbf{Y} = \begin{bmatrix} \mathbf{p_1} \cdot \mathbf{x_1} & \dots & \mathbf{p_1} \cdot \mathbf{x_n} \\ \vdots & \ddots & \vdots \\ \mathbf{p_m} \cdot \mathbf{x_1} & \dots & \mathbf{p_m} \cdot \mathbf{x_n} \end{bmatrix}$$

The standard Euclidean inner product tells ut that the original data, $\mathbf{X}$, is being projected on to the columns of $\mathbf{P}$. The rows of $\mathbf{P}$, therefore, form the new set of basis vectors for representing the columns of $\mathbf{X}$. The rows of $\mathbf{P}$ will represent the principal component direction, and thus the principal components. Hence, it is essential to choose the appropriate change of basis in order to have the most accurate or best re-expression of $\mathbf{X}$.

As previously mentioned, the principal component analysis is based on the variance of the data in the original basis in order to define independence. The original data is intended to be de-correlated through finding what directions the data has the largest variance, which subsequently define the new basis. The variance of a random variable, Z, with mean μ is defined as

$$\sigma_Z^2 = E[(Z - \mu)^2] \tag{6.7}$$

By extending the definition to include vectors, the result is

$$\sigma_{\mathbf{r}}^2 = \frac{1}{n}\mathbf{r}\mathbf{r}^T \tag{6.8}$$

Where $\mathbf{r}$ is a translated set of n measurements, where each discrete measurement in the vector $\tilde{\mathbf{r}} = (\tilde{r}_1, \tilde{r}_2, \ldots, \tilde{r}_n)$ has had the mean μ_r subtracted.

The definition can be further extended to include other measurements. Given a second vector of the same number of measurements, n, and zero mean, $\mathbf{s} = (s_1, s_2, \ldots, s_n)$, the covariance of the two, $\mathbf{r}$ and $\mathbf{s}$, measurements can be obtained. The above-mentioned variance is in fact a special case of the covariance where the two variables are identical. To account for the variables not being identical, n in the division is exchanged with n-1.

$$\sigma_{\mathbf{rs}}^2 = \frac{1}{n-1}\mathbf{r}\mathbf{s}^T \tag{6.9}$$

The definition can be generalized to include a data matrix $\mathbf{X}$, with m columns representing the number of variables and n rows representing the number of samples. The matrix therefore consists of m row vectors, each of length n. These represent all the samples per variable.

$$\mathbf{X} = \begin{bmatrix} x_{11} & x_{12} & \ldots & x_{1n} \\ x_{21} & x_{22} & \ldots & x_{2n} \\ \vdots & \vdots & \ddots & \vdots \\ x_{m1} & x_{m2} & \ldots & x_{mn} \end{bmatrix} = \begin{bmatrix} \mathbf{x_1} \\ \mathbf{x_2} \\ \vdots \\ \mathbf{x_m} \end{bmatrix} \tag{6.10}$$

Therefore, the equation for the matrix of covariances will follow the same pattern as for the two sample covariance. The matrix will contain the covariances everywhere apart from the diagonal axis, which will contain the variances.

$$\mathbf{C_X} = \frac{1}{n-1}\mathbf{X}\mathbf{X}^\mathbf{T} = \begin{bmatrix} \mathbf{x_1}\mathbf{x_1}^T & \mathbf{x_1}\mathbf{x_2}^T & \ldots & \mathbf{x_1}\mathbf{x_m}^T \\ \mathbf{x_2}\mathbf{x_1}^T & \mathbf{x_2}\mathbf{x_2}^T & \ldots & \mathbf{x_2}\mathbf{x_m}^T \\ \vdots & \vdots & \ddots & \vdots \\ \mathbf{x_m}\mathbf{x_1}^T & \mathbf{x_m}\mathbf{x_2}^T & \ldots & \mathbf{x_m}\mathbf{x_m}^T \end{bmatrix} \tag{6.11}$$

Principal Component Analysis builds on linearly transforming the original data into $\mathbf{Y}$, and a fundamental assumption is that the variables of $\mathbf{Y}$ are orthogonal or as close as possible. From

linear algebra it follows that variables being orthogonal corresponds to them being independent or uncorrelated. Therefore, the covariance matrix of $\mathbf{Y}$, $\mathbf{C_Y}$, should maximize the diagonal entries and minimize the off-diagonal entries. The minimum possible covariance is zero, and thus $\mathbf{C_Y}$ should be a diagonal matrix in order to achieve an optimal Principal Component Analysis.

The vectors of the new basis, $\mathbf{p_1}, \mathbf{p_2}, \ldots, \mathbf{p_m}$ are assumed to be orthogonal, which results in the possibility of proceeding with the use of linear algebra.

$$\begin{aligned}
\mathbf{C_Y} &= \frac{1}{n-1}\mathbf{Y}\mathbf{Y^T} \\
&= \frac{1}{n-1}(\mathbf{PX})(\mathbf{PX^T}) \\
&= \frac{1}{n-1}(\mathbf{PX})(\mathbf{X^T}\mathbf{P^T}) \\
&= \frac{1}{n-1}\mathbf{P}(\mathbf{XX^T})\mathbf{P^T} \\
\mathbf{S} &= \mathbf{XX^T} \Rightarrow \\
\mathbf{C_Y} &= \frac{1}{n-1}\mathbf{PSP^T}
\end{aligned} \tag{6.12}$$

Where $\mathbf{S}$ is an $m \times m$ symmetric matrix, since $(\mathbf{XX^T})^\mathbf{T} = \mathbf{XX^T}$. Every square matrix is orthogonally diagonalisable, such that $\mathbf{S} = \mathbf{EDE^T}$. $\mathbf{D}$ is the diagonal matrix, containing the eigenvalues of $\mathbf{S}$ as its diagonal entries and $\mathbf{E}$ are the ortonormal eigenvectors of $\mathbf{S}$. It is at this point the design of $\mathbf{P}$ becomes essential. If the transfomation matrix is chosen to have its rows equal to the eigenvectors of $\mathbf{S}$, $\mathbf{P} = \mathbf{E^T}$. Combined with the fact that $\mathbf{E^T}\mathbf{E} = \mathbf{I}$, then

$$\begin{aligned}
\mathbf{C_Y} &= \frac{1}{n-1}\mathbf{PSP^T} \\
&= \frac{1}{n-1}\mathbf{E^T}(\mathbf{EDE^T})\mathbf{E} \\
&= \frac{1}{n-1}\mathbf{D}
\end{aligned} \tag{6.13}$$

As previously mentioned, the size of the variances relate to their importance. Since the variances are equivalent to the diagonal entries of the matrix $\mathbf{D}$, the size of the diagonal entries tells what variables are most essential in the analysis.

6.2.3 Score Plot

The results of the PCA are summarized in score plots and loading plots. These are interpreted based on patterns. Due to the orthonormality of the PC matrix, any trends apparent in the original data will be kept intact. The score plot is the transformed data represented in a scatter plot, where the principal components make up the axes. Therefore, patterns in the score plot will represent patterns in the original data. Specifically, three main patterns are interesting in the scatter plots: clustering, outliers and time-based patterns. Clustering will show what data cause similar effects, and will possibly have similar properties. Clusters may be used to classify new data obtained after the first analysis. Simply because similar data would depict similar trends and thus lie in the same clusters. Outliers will portray properties dissimilar to the other. This may be caused by errors in the data or from large deviations. The latter will be of interest. A result of the large deviation is

also a higher contribution to the PCs, giving it higher leverage. To interpret the contributions of each factor, one often also create bar plots in order to assess what has the most significance on the results. Finally, any sequence of data will possibly portray trends which will be apparent in the PCA results. Figure 6.2.2 illustrates the scores of a scatter plot. The axis consists of the principal components.

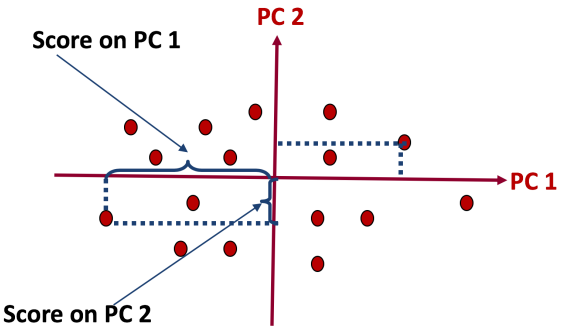

Figure 6.2.2: Example of a score plot

6.2.4 Loading Plot

Loading plots are plots depicting the influence each feature has on the principal components. The plots will thus show what feature has the most significance. As a result, variables with little contribution will have close to zero loading, variables with strong positive correlation will have similar weights and variables with strong negative correlation will be positioned diagonally opposite each other with similar loading (except for the sign). The loading plot will also make it possible to further simplify the data as insignificant features, variables with low loading may be eliminated. One can also see redundancy in the variables. Variables causing the same score plot positioning will overlap in the loading plot. Figure 6.2.3 depicts the loading plot for PC2 and PC1 combined. The vertical axis defines the effect on the second principal component and the horizontal axis illustrates the effect on the first principal component. Each point is a variable with the corresponding variable name labeled above. The ellipse on the plot depicts the Hotelling's T^2 plot, which is described below.

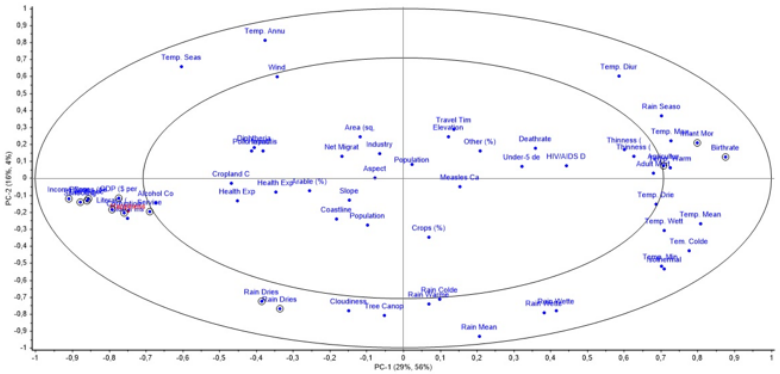

Figure 6.2.3: Example of a loading plot with an hotelling's T^2 ellipse

6.2.5 Residuals

Furthermore, the PCA provides a model and thus predicted values, in the new space. These will differ from the data resulting in errors, also called residuals. The measured data will, therefore, equal the sum of the PCA model and the model error or residuals. A plot of the residuals will thus reveal coherency with the model. Large deviations could reveal an inconsistency with the model, which could reflect a problem with the process at the time of capturing the data in question. In order to break down what variables causing the deviation, one would, normally, generate a contribution plot showing the residuals for each PC - as opposed to the squared prediction error utilized in the residual plot. The derivation of the residuals are described below, where **E** is the matrix of residuals, **X** the data and **TP'** the model, where **P'** marks the transposed of **P**

$$\mathbf{E} = \mathbf{X} - \hat{\mathbf{X}} = \mathbf{X} - \mathbf{TP}' \tag{6.14}$$

To interpret the residuals, one equates the Square Prediction Error, which is simply the absolute value of the residuals. The value is then plotted to see what observations have the highest residuals. The plot will include a line depicting a given percentage, such that all residuals above the line will be of the percentage, e.g., top 5% deviation. The equation below describes the calculation, and the figure 6.2.4 depicts the plot. The vertical axis describes the residual value. The horizontal red line describes the 95% percent, i.e., 95% of samples are located below the line.

$$SPE = \sqrt{\mathbf{e}'_{\mathbf{i},\mathbf{A}}\mathbf{e}_{\mathbf{i},\mathbf{A}}} \tag{6.15}$$

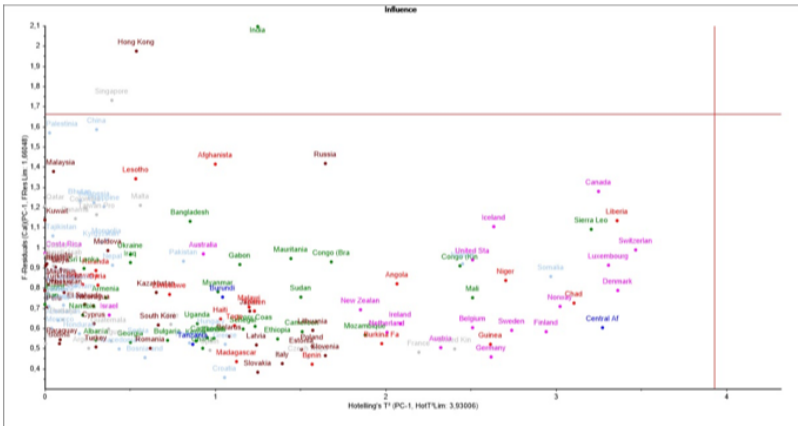

Figure 6.2.4: Plot of residuals and hotellings T^2

6.2.6 Hotelling's T^2

Finally, there is the Hotelling's T^2 value. The value help screen the components of the PCA, summarizing all the score-values. Considering a model of 2 components, the value is highly useful. Depending on a percentage limit, the equation will form an ellipse. The points inside the ellipse will be within the respective percentage limit. It is expected that the percentage of the confidence limit lies within the ellipse. The confidence limit is equivalent to the confidence limit one would

expect for a normal distribution. The ellipse will help identify outliers, but only as a guide. Figure 6.2.5 illustrates the ellipses of Hotelling's applied to the previously depicted Loading plot. The outer ellipse represents 99%, while the inner represents 95%.

Combined with the residuals, it allows for the identification of poorly modeled measurements and measurements with high leverage. Figure 6.2.4 depicts the residuals and the Hotelling's value. The Hotelling's will depict the leverage and the residual the model fit. A high Hotelling's T^2, but a low residual would be concerning as it might indicate a model that is designed to describe the high leverage measurement.

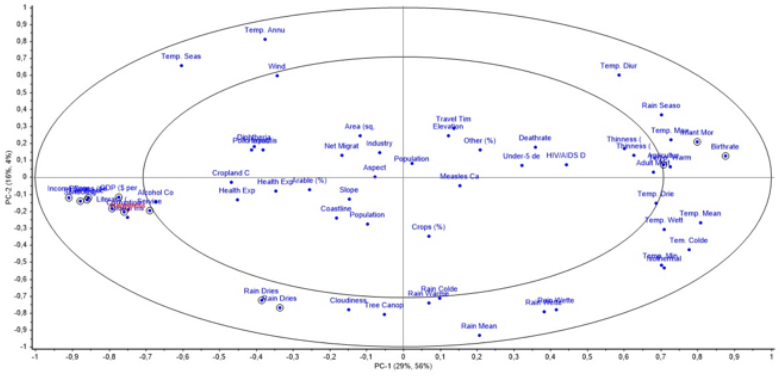

Figure 6.2.5: Example of a Hotelling's T^2 plot

6.3 Partial Least Square Discriminant Analysis

Partial Least Square Discriminant Analysis is a method of processing large amounts of data and utilize it in order to make predictions. The following paragraphs will describe the basic principles of the method.

6.3.1 Partial Least Square - Regression

Partial Least Square - Regression(PLS-R) is a technique that combines features from PCA and regression. PLS-R differs from PCA in that instead of finding the maximum variance of the samples by projecting onto a hyperplane, it rather finds the linear regression by projecting both predicted and observable variables to a new space.

The basic notions of a PLS analysis are to locate the latent variables which best explain $\mathbf{X}_i$, $\mathbf{Y}_i$ and the relationship between the two. The method hence seeks to describe the $\mathbf{X}$-space, the $\mathbf{Y}$-space and the relationship between the two spaces.

More precisely, the method extracts two sets of scores. $\mathbf{t}_i = \mathbf{X}_i\mathbf{w}_i$ for the $\mathbf{X}$-space and $\mathbf{u}_i = \mathbf{Y}_i\mathbf{c}_i$ for the $\mathbf{Y}$ space.

The final objective of building the PLS model is to find the scores that result in the maximum covariance. That is, $Cov(\mathbf{t}_i, \mathbf{u}_i) = \varepsilon\{(\mathbf{t}_i - \bar{\mathbf{t}_i})(\mathbf{u}_i - \bar{\mathbf{u}_i})\}$. When the scores are found and the model

built, one simply needs to input new X-variables for a response, based on the aforementioned correlation, between the **X** and **Y** space.

The actual calculation of the scores is usually performed using iterative methods, such as NIPALS. These methods will not be presented in this thesis, as they are deemed unnecessary and irrelevant when understanding the final results.

To perform the intended regression, one can use the found latent variables of the **X**-space, followed by the correlation between the **X** and **Y** space to find the resulting y-variables.

Due to the similar nature of PLS and PCA, the interpretation of the results are highly similar. PLS will have loading and score plots interpreted in the same fashion as with PCA, only that there will also be plots for the **Y** space. Another difference, is that there will be a prediction of how well the model fits, if one includes a test set. The test set will reveal the quality of the model by assessing how well the model predicts y-values compared to the actual value.

6.3.2 Linear Discriminant Analysis

Discriminant analysis seeks to classify samples into two or more categories based on linear combinations of features. The method is closely related to PCA in that it seeks linear combinations of variables to describe the data. The following is largely based on James (2013b).

Based on a set of observations, **X**, and known categories, **Z**, the method tries to find a combination of the observation variables which predicts the respective category.

Discrimination is achieved by setting the variable weights to maximize the ratio of the variance between the classes and the variance in the class itself. The combination is achieved through a discriminant function. The function linearly combines variables, and their respective weights, of an observation and yields a score per predetermined class.

$$Z_{ik} = b_{0i} + b_{1i}X_{1k} + \cdots + b_{Ji}X_{Jk} \tag{6.16}$$

where Z_{ik} is the discriminant score of the discriminant function i of observation k, with $i = 1, \ldots, G-1$. The number of discriminant functions must be smaller than the number of classes G. X_{jk} is the variable j of observation k, with $j = 1, \ldots, J$, where J is the number of variables per observation. b_{ji} is the discriminant weight of variable j and function i.

$$max = \frac{\sum_{g=1}^{Q} I_G(\bar{Z}_g - \bar{Z})^2}{\sum_{g=1}^{Q}\sum_{i=1}^{I_g}(\bar{Z_{gi}} - \bar{Z}_g)^2} = \frac{SS_b}{SS_W} \tag{6.17}$$

where is the dicriminant criteria, I_g the size of class g, $\bar{Z}_g$ the mean of group g, Z_{gi} the ith discriminant value of class g, SS_b the sum of squared deviations between classes and SS_b the sum of squared deviations within classes.

Following the calculation of each discriminant function, these are simply to be used to find the resulting discriminant scores and subsequent discriminations.

6.3.3 PLS-DA

By performing a discriminant analysis based on a PLS model, one gets the PLS-DA method. The PLS model is built on the training data, which also includes category or class variables for the discriminant analysis. The resulting model will be able to predict the class of the sample data according to the previously built model.

6.4 Picture Processing

The following section describes basic methods to process hyperspectral images and their respective spectra.

6.4.1 Standard Normal Variate Transform

The standard normal variate transform makes it possible to compare similar spectra, but of different intensity. The transform alters the data by centering it and making it relative to its own standard deviation. Thus, making peaks comparable as they are no longer absolute, but rather relative.

6.4.2 Savitsky-Golay

The Savitsky-Golay filtering technique is a form of polynomial smoothing. The filter aims to increase the precision of the data, without distorting the signal tendencies. In order to smooth the signal, the method uses Linear Least Square to perform linear regression on a subset of adjacent points. This regression is performed for every point of the graph, with the subset centered at the given point, Savitzky and Golay (1964).

After a polynomial has been fitted to the subset, it is evaluated at the given point, e.g., by derivation.

Uniquely for the Savitsky-Golay method is that the points are equally spaced, making it possible to predict the coefficients of the polynomial of finite order related to the regression. The samples, which may be regarded as discrete, are subsequently combined with the predetermined coefficients through convolution. In turn, the signal will be smoother, but still retaining key features with respect to spectral analysis.

Maximum Noise Fraction (MNF)

Based on a principal component analysis. However, instead of ordering the components based on variance, the components are ordered increasingly, with respect to signal-to-noise ratio(SNR), (S/N). Thus, one can heavily filter the components as it will reduce noise, while minimum signal degradation, Green et al. (1988).

Depending on the SNR of a component, one may either completely remove it or smooth it. Complete removal is only a viable option if the component has a high amount of noise. Even if the

lower order components do contain more noise, they still have a significant effect on the total signal. Therefore, these require smoothing. Because the lower components contain a larger noise fraction, one may assume a smaller information loss due to smoothing, than with higher level components. The smoothing is based on the between-band correlation.

Chapter 7

Research Process

Given the exploratory character of the project, the work process was far from linear. The research largely included meetings, literature searches and experiments. The result was an iterative work process which gradually revealed the necessary steps required to move forward. The nature of the progress made it difficult to fit the process in the standardized IMRaD methodology, as decisions were continuously made based on results from either meetings or experiments. The following chapter is intended to give the reader insight and understanding of the underlying research process. This includes introducing leads we did not follow - after all. Compared to the rest of this report, the format is atypical, communicating in a tone that combines the language of preface and method. Note that a more detailed description of the scientific portion of the process will follow in the next chapters, Chapter 8 and Chapter 9.

The process tree below, Figure 7.0.1, illustrates the framework and structure of the process, while Figure 7.0.2 displays a table that complements the tree with details.

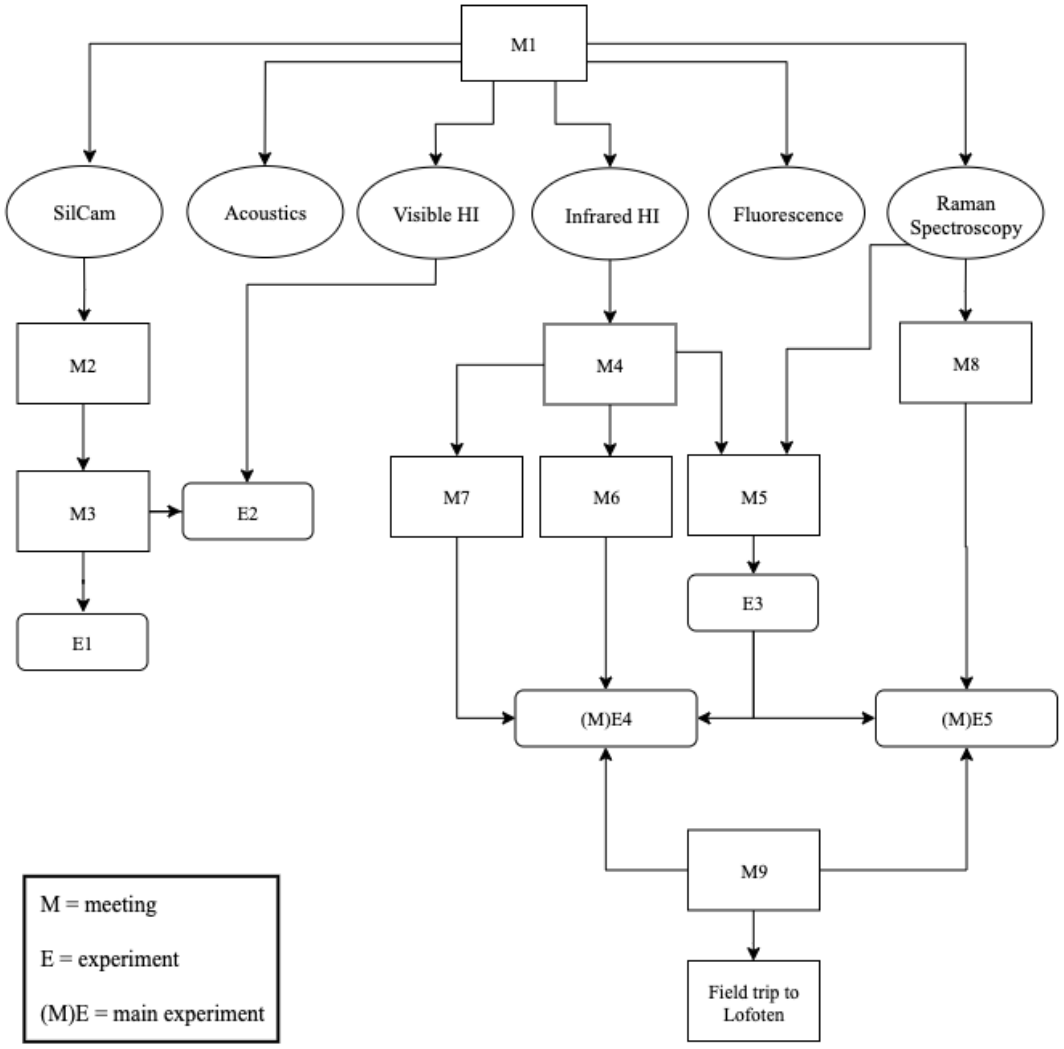

Figure 7.0.1: The process tree, consisting of meetings and experiments

Progress	**Participants** (excluding the authors)	**Description**
M1	Ståle Johnsen (SINTEF), Emlyn Davies (SINTEF), Martin Ludvigsen (NTNU), Asgeir J. Sørensen (AMOS)	Brainstorming and planning session. Discussing the assignment and its relation to the SOMM-cooperation. The outcome involved the six detection methods presented in the tree.
M2	Emlyn Davies, Aksel Alstad Mogstad (NTNU), Andy Booth (SINTEF)	Planning session for the first experiment.
M3	Torfinn Sparstad (NTNU), Grethe Stavik Eggen (NTNU)	Torfinn showed us how to drain liquid nitrogen, while Grethe introduced us to her lab and helped us with suitable equipment when grinding the plastic.
M4	Lise Lyngsnes Randeberg (NTNU)	This row includes several meetings in a short time period, discussing and planning the use of hyperspectral imaging in infrared light
M5	Martin Wagner (NTNU)	Discussing how to use the Cryomill and applications of a plastic detecting method in general.
M6	Fredrik Samdal Solberg (NTNU)	Planning the construction of the first laboratory set-up, showing him our design.
M7	Sebastian Bete (NTNU), Astrid Salvesen (NTNU)	Planning the welding process of the ordered fused silica discs – welding them into petri dishes.
M8	Bartlomiej Gawel (NTNU)	Discussing if Raman spectroscopy could be a possible method of plastic detection. Bartlomiej also showed us the laboratory and necessary functions.
M9	Emlyn Davies, Julia Farkas (SINTEF)	Planning the field trip to Lofoten. We walked around SINTEF and assemble all material necessary in order to collect and filter sea-mass.
E1	Emlyn Davies, Aksel Alstad Mogstad	Location: SINTEF Ocean. Testing the SilCam (transmission), for the combined sensor (SilCam and a Spectrometer)
E2	Aksel Alstad Mogstad	Location: Trondheim Biological Station. Measuring plastic particles placed in cuvettes – using transmission of visible light. See Chapter 8, Method for extended description.
E3	Trude Johansen (NTNU)	Location: Department of Biology. Trude helped us initiating the milling process (continuous follow-ups), pulverizing all plastic particles.
(M) E4	Lise Lyngsnes Randeberg	Location: Department of Electric Systems. See Paper I for extended description.
(M) E5	Bartlomiej Gawel	Location: Department of Materials Science and Engineering. See Paper II for extended description.
Repeated meetings	Asgeir J. Sørensen, Lise Lyngsnes Randeberg, Emlyn Davies	Throughout the semester we have had a number of additional meetings and follow-ups, not mentioned here, as no new topics were added in these sessions.

Figure 7.0.2: The process tree table, complimenting the process tree

At the starting line (M1), several methods for mapping and classification of plastics were discussed. Among the most prominent, SilCam and hyperspectral imaging stuck out as the winning two, resulting in the focus of the thesis. The idea was to combine the shape and size information from the SilCam, with the object color information from the Hyperspectral imager in visible light, Stien and Dahl (2018). By using the same light source for both technologies combined, a beam splitter could collimate the light into the spectrometer and the SilCam at the same time, using transmittance (M2). Due to a large number of properties recognized, this combined sensor would possibly be able to identify the object. (However, as it turned out, this was not going to be the focus of our thesis.)

We decided to move forward with the plan and measure the plastic particles in transmittance. In order to do so, significantly smaller particle sizes were needed. Therefore, we bought a coffee

grinder at Clas Ohlson and went down to the Department of Biology to freeze and grind the plastic particles (M3). Since we had realized we needed to ensure brittleness also when grinding the particles, the liquid nitrogen freezing of the samples, was essential. Then we returned to SINTEF Ocean to complete the experiment (E1). As it turned out, the pieces were still too large, floating on top of the water tank. We realized we could place the plastic particles in a cuvette, and shake the cuvette to suspend the particles just long enough to retrieve in-water measurements (E2).

Furthermore, inspired by the discussions in M1 and supplementary literature, we were optimistic and eager to embark the hyperspectral imaging using infrared light. We reached out to Silja, who three years ago, wrote her master thesis on a related subject. She gave us the name of her brilliant supervisor. This is how we came in contact with Lise Lyngsnes Randeberg (M4). Over the next few days, we had several meetings with Lise. We later changed the focus of the thesis — infrared hyperspectral imaging was the new main theme. Lise made us aware of a few challenges when embarking on the laboratory experiment. First, the plastic particles needed to be pulverized down to 200 microns. Our "coffee ground" particles were no longer sufficient. Second, the laboratory set-up for transmitting infrared light needed to be designed and formed.

First things first, we contacted Martin Wagner from the department of biology (M5), by recommendation from Torfinn. Martin had recently bought a brand new tissuelyser (cryomill) for the exact purpose of pulverizing materials — such as plastic. The process was long lasting and thorough. After two weeks of milling with assistance from Trude and Grethe (E3), the plastic samples were fully pulverized.

Figure 7.0.3 shows the intended laboratory set-up. This was built with help from a friend at TrollLabs, Fredrik (M6). The result was laser cut petri dish holders in wood, pictured in Figure 7.0.4. In addition, as the infrared radiation is absorbed by glass, the petri dishes had to be custom made to our experiment. After doing some research, we found the least infrared-absorbing material to be fused silica. This material was ordered as optically purposed discs, before being weld into petri dishes by Sebastian Bete (M7) from the glassblower-workshop at NTNU.

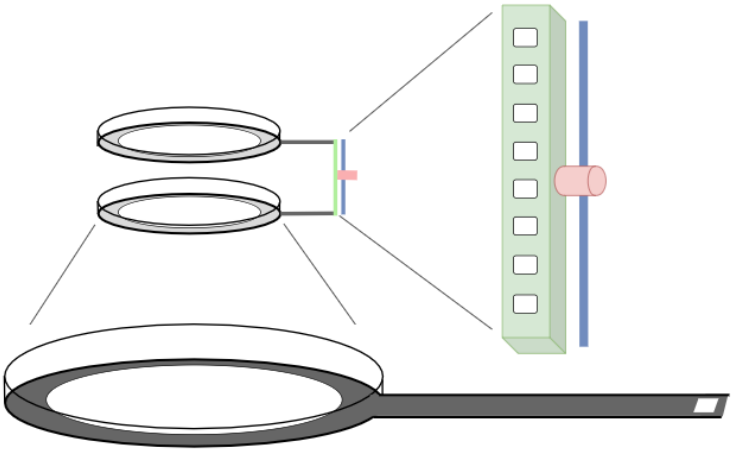

Figure 7.0.3: Designed sample holder

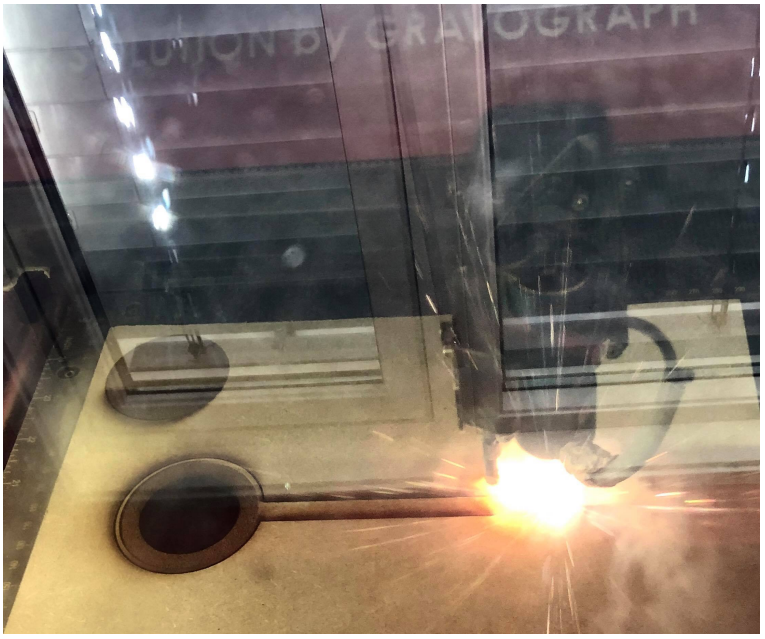

Figure 7.0.4: Laser cutting the dish-holder

Now, the plastic was pulverized and the laboratory set-up completed - (M)E4 was in order. A thorough description of the experiment can be found in the method section in Paper I, *Identification of Marine Plastics using Hyperspectral Imaging in Infrared Light*, Chapter 8.

Later, we received an email from Emlyn about venturing the field of Raman spectroscopy. In our previous meeting with Emlyn, we had expressed our interest in the field, and he responded accordingly by introducing us to Bartlomiej Gawel and Andreas Erbe. We met with Bartlomiej the next day (M8). This meeting was mainly driven by curiosity and was never entirely meant to result in another experiment — yet, it did. (M)E5 was then commenced. A thorough description of the experiment can be found in the method section in Paper II, *Identification of Marine Plastics using Raman Spectroscopy*, Chapter 9.

Furthermore, a trip to Lofoten was arranged. Emlyn, Frode and Bjarne from SINTEF, was attending a field trip to Lofoten in early April, and Emlyn had organized for us to join them. We exploited the trip by bringing a manta sampler, a net trawled by the side of the boat to collect mass from the sea — hopefully containing microplastic. Figure 7.0.5 shows two photos from the collection process in Svolvær, Lofoten.


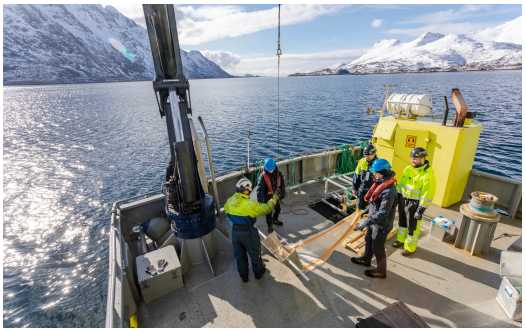

Figure 7.0.5: Photos from collecting plastic samples outside Lofoten, Norway. Photos courtesy of Emlyn John Davies.

Returning home, (M)E4 and (M)E5 were repeated using collected Lofoten particles as samples. Lastly, the data retrieved from the lab measurements were analyzed. The resulting product of this entire process, constituting our master thesis, is two papers, one abstract, one poster and, last but not least, this report.

Chapter 8

Paper I: Identification of Marine Plastics using Hyperspectral Imaging in Infrared Light

The following chapter contains the first paper which constitutes a significant part of the work. The paper describes the method, acquired results, and the analysis of said results, using hyperspectral imaging in infrared light to identify plastic. The paper contains all relevant methods and work performed to achieve the results. In this regard, both papers combined replaces the standardized *Methods* and *Results* usually found. It is also an independent deliverable, to be submitted to a relevant scientific journal. Furthermore, the format of a scientific paper puts restraints on the amount of included results and method. This chapter also contains additional results and work relevant for the thesis. These are meant to leave the reader with a more in-depth understanding of the process than from the paper alone. The latter describes work excluded due to it not yielding promising results, but nonetheless being a prominent method.

8.1 *Identification of Marine Plastics using Hyperspectral Imaging in Infrared Light*

Identification of Marine Plastics using Hyperspectral Imaging in Infrared Light

Andreas Ø. R. Stien (NTNU), Emilie M. H. Dahl (NTNU), Lise Lyngsnes Randeberg (NTNU),
Asgeir J. Sørensen (NTNU) and Emlyn John Davies (SINTEF)
Centre for Autonomous Marine Operations and Systems (AMOS), Department of Marine Technology,
Norwegian University of Science and Technology (NTNU) , NO-7491, Trondheim, Norway

Abstract—Plastic and subsequently microplastic pollution is currently present at the highest and lowest points on the planet. Proper methods and technology for mapping and monitoring need to be addressed. This promptly calls for an in-situ detection method to be developed. The research supporting this paper includes the investigation of underwater plastic identification using Near-Infrared Hyperspectral imaging in the interval of 960-2400 nm. The studied samples vary from pristine samples to sorted recycled plastic, to marine plastic particles collected from the sea in Northern Norway, outside Svolvær, Lofoten. The measurements are performed using bare plastic, plastic in water and the untreated in situ samples. K-means clustering, and Spectral Angle Mapping (SAM) algorithms are utilized for classification purposes. The results indicate the possibility of distinguishing plastic from biological matters. The research, however, failed to correctly identify the type of plastic, due to contaminants on the particle surface. Still, the use of hyperspectral imaging for underwater particle classification appears promising.

1 Introduction

TODAY the applications of plastics are many, making the material popular worldwide. More than 380 million metric tons of plastic are produced yearly, and the production is projected to nearly double within the next 10-15 years [1]. In the oceans, the critical outcomes of plastic pollution have been eye-opening [2]. Today, a manifold of initiatives and research within the field is introduced. As plastic is non-degradable, and the debris currently polluting the oceans need to be removed. This requires methods for in-situ plastic mapping and monitoring for efficiently targeting areas of interest.

Concerning plastic detection, several recent studies have been carried out. These mainly concern sorting land-based garbage and plastics. H. Kawazumi, A. Tsuchida, T. Yoshida, and Y. Tsuchida [3], have successfully used Raman spectroscopy to sort polystyrene, polypropylene and acrylonitrile-butadiene-styrene copolymer from shredded post-consumer plastics. Y. Zheng, J. Bai, J. Xu, X. Li, and Y. Zhan [4], claim to have identified a test-set of unknown plastic waste with an identification accuracy of 100%. The latter study was performed using a near-infrared(NIR) (1000–2500nm) hyperspectral imager, combining two-dimensional object imaging with spectroscopy.

Furthermore, microplastics contamination from seawater filtrates have been proven recognizable [5]. The mentioned discovery is at the forefront of this area of research, taking a step towards classifying sea influenced plastic. T. M. Karlsson, H. Grahn, B. van Bavel, and P. Gelad [5], have tested the hyperspectral method within three different wavelength intervals, concluding with 1000-2500 nm as the most applicable wavelength range for this purpose.

Most of the research completed within the field of plastic identification is land-based, and likewise concerning the use of a hyperspectral camera. It is not until recently that the hyperspectral technology has been tested underwater. This was done by the NTNU spin-off company Ecotone, which is the first industrial mover in underwater-application, separating living tissue in underwater seaweed [6].

In 2018, Ø. Ødegård, A. A. Mogstad, G. Johnsen, A. J. Sørensen [7], studied and applied the underwater hyperspectral imager (UHI) on the seabed at 61m. They managed to retrieve spectral signatures from archaeological artifacts and classify the material. Yet, hyperspectral underwater plastic detection seems to remain uncovered.

The literature presented above provides valuable knowledge, allowing this research to take an additional step. This paper aims to combine the hyperspectral identification of plastics with underwater testing. In order to classify plastic, the experiments should be performed within the frequency range proven fit (approximately 1000-2500 nm). However, longer optical wavelengths are highly sensitive for under water applications and are rapidly attenuated by seawater. Hence, the procedure is challenging when performed in-situ in the oceans [8].

The study's laboratory setup and methodical approach are as follows. As transmittance is measured, the set-up includes two Hyspex halogen light sources within the near-infrared range below the measured sample. The hyperspectral camera is of type Hyspex SWIR 320-e [9]. The measurements are performed with known plastic samples in various sizes and various conditions - with and without water in between the sample and the imager. Using k-means and spectral angle mapper as classification methods, the known plastic samples function as the ground-thruthed dataset, and is correspondingly used to build the model. A portion of the dataset contains measurements with water. This subset constitutes the first test set. The second test set applied includes unknown plastic contamination collected

from seawater.

This paper is organized as follows. In Section 2, the spectroscopy is presented. Section 3 explains the hyperspectral imaging and its likely underwater challenges. Materials and methods are elaborated in Section 4, while the results are displayed in Section 5. Section 6 discusses the results presented in the previous section along with possible sources of error, before the conclusions in Section 7.

2 Spectroscopy

A way to work with materials, identify them or learn about their properties, is to study how light interacts with them, one of these studies being spectroscopy. Light absorption, reflection and transmittance from an object can be measured over several wavelengths.. This leaves a spectrum describing the receiving light, which again gives rise to the spectral signature of the object measured. Spectral signatures can be thought of as fingerprints. While fingerprints are often used to identify people, spectral signatures can be used to identify materials.

If the frequency (wavelength) of the incoming radiation is resonant to the frequency of the molecule vibration level, the molecules in the illuminated target will vibrate. In this case, measurements of the resulting spectrum, provided by the spectrometer, may reveal relevant molecular properties.

All types of plastics consist of organic bonds. The vibrational frequencies of organic bonds correspond to infrared wavelengths. Hence, infrared radiation may be a necessity when identifying the characteristics of plastic on a molecular level. Whenever a plastic molecule is exposed to infrared radiation, the organic bonds will absorb the radiation energy. This will, again, excite the molecules to a higher vibrational energy state. The wavelength of the absorbed radiation is thus directly associated with the difference in energy between the present and the previous vibrational energy state [10].

3 Imaging

For the human eye to be able to perceive a color image, only three wavelengths are needed, namely red, green and blue (RGB). It therefore rarely makes sense to create multiple layers unless the goal is to capture information the eye cannot see. This is where hyperspectral imaging enters the playing field, which by definition has more than 100 layers and can express each pixel as a spectrum. The following section describes the imager, highly inspired by [9]'s website.

3.1 Hyperspectral Imaging

The most common way of using imaging spectroscopy (hyperspectral imaging), is to measure the resulting spectra from the spectrometer [11]. Hyperspectral imaging combines digital imaging and spectroscopy, measuring hundreds of continuous spectral bands for each pixel in a digital image, allowing access to a spatial dimension. This allows the hyperspectral imager to classify objects in the scene based on their spectral properties. When an object is exposed to infrared light, molecules may, as previously explained, vibrate due to the absorption of the infrared radiation. A hyperspectral imager will be able to register this vibrational transition, making it possible for the detector to recognize the specific substances of the material. Concerning plastic, this translates into receiving information on plastic material composition, based on the chemical bonds the plastic type consists of.

3.2 Operating Principle

Moving across the scene of the image, the hyperspectral imager is line-scanning the scene. The technique uses a two-dimensional detector, perpendicular to the surface of the measured target. This detector collects the spectrum of a whole line in the image, in one single scan. By moving the scan line with a push broom technique, one can map the entire image by combining all sets of spectra, [12].

More detailed, as the camera moves across the image scene, the light from the specific line passes through the entrance and onto the focusing mirror, further focusing the light towards the next mirror, as shown in Fig. 1. After collimation, the different wavelengths are separated by a transmission grating. From here, the light goes through a lens, focusing it onto the detector array at the end of the system. For every pixel interval along the line, a corresponding spectrum is projected in the detector array. In this way, the data retrieved from this array will, piece-wise, contain two-dimensional hyperspectral images. Putting these thin slit images together, a data cube is created, adding a third dimension to the image. The final product is then a three-dimensional hyperspectral image with one spectral dimension and two spatial dimensions [12].

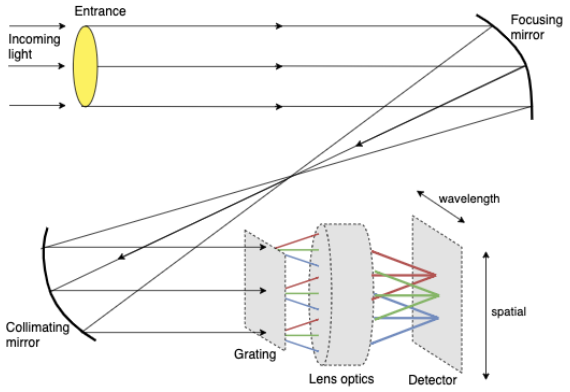

Fig. 1: Optics of a Hyperspectral Imager, inspired by [9]

3.3 Underwater Challenges

Light behaves differently in water than in air. The main difference is that, in contrast to in the air, light in water is attenuation to a much greater degree, [8]. Water absorbs wavelengths covering a wide range of electromagnetic radiation. As the H2O-molecule has a particularly small moment of inertia on rotation, a rich vibrational-rotational spectrum appears, sometimes containing millions of

absorption lines. The water absorption spectrum is therefore very complex. The water molecule may vibrate in several ways, at several stages affected by the environment. For the specific case of H2O, the absorption is at its lowest when the light frequency spans the visual interval. Moving beyond infrared light, the radiation is, at a larger degree, absorbed. Nevertheless, an intensive NIR-source can leave sufficient light if the distance between the light source, object and imager is small enough. However, as the source moves closer to the target, the spatial coverage, commonly exploited using a hyperspectral imager, goes away.

Infrared light is more sensitive than visible light, leaving the signal vulnerable to small variations, causing the intensity to rapidly decrease. To mention a few; the scattering of light can be dominant, leaving useful rays at wastage. Shadow patterns underwater can also be an issue, as it contributes to variations in the lighting, making the extracted image less representative when describing the surroundings, [6]. Another important concern is the condition of the water. The signal intensity can, for instance, be dependent on temperature and salinity [13].

3.4 Data Analysis

3.4.1 K-means

The theory behind the k-means clustering is based on assigning each data point to a cluster. The number of clusters is pre-specified and determines the number of randomly placed centroids in the space. For each iteration the algorithm runs, two operations are performed. First, all data points are assigned to the closest centroid, grouping the associated points into one class per centroid. Next, an average of all samples per class provides a new position for the center of the centroid. Once again, all points are assigned to the closest centroid, and so on. Eventually, the result of a new iteration involves an identical mapping as for the previous run, and every sample is assigned the most correspondingly accurate class [14].

3.4.2 Spectral Angle Mapper

Spectral Angle Mapper (SAM) maps the difference in angle between an image spectra and a reference spectra. The spectra are treated as vectors a n-dimensional space, where n is the number of bands used each time. A small angle between the two spectra will indicate a high similarity and a large angle will indicate a low similarity. The angle is calculated based on the inverse cosine of the sum of the target pixel multiplied by the reference pixel over all bands divided by the length of the target pixel and reference pixel multiplied with each other [15],

$$\alpha = \cos^{-1}\left(\frac{\sum_{i=1}^{n} t_i r_i}{\sqrt{\sum_{i=1}^{n} t_i^2} \cdot \sqrt{\sum_{i=1}^{n} r_i^2}}\right) \tag{3.1}$$

where α is the angle, t is the target pixel, r is the reference pixel, n the number of bands and i the given band. The classification based on the angle is typically based on a given limit value. If the angle does not fall below the value for any spectrum, it is unclassified.

4 Materials and Methods

For the research behind this paper, five types of plastic have been studied. These are the most common types of plastic, in large part covering the global plastic production [16], namely Polyethylene (PE), polypropylene (PP), polyethylene terephthalate (PET), polyvinyl chloride (PVC) and polystyrene (PS). Within these five types, samples with varying conditions have been used, as presented in Table 1. These samples are ordered from CARAT AS in Germany [17], while the remaining samples are collected from the sea outside Svolvær, Lofoten.

Condition	Type
Post-Industrial Recyclate Pellets	PE: LDPE/LLDPE
Post-Consumer Recyclate Regrind	PE-HD
Environmental Pellets	PE: LDPE/HDPE
Environmental Fragments (Regrind)	PE-HD
Pristine Pellets	PP-Homopolymer
Post Consumer Recyclate: Pellets	PP Mixture
Pristine Pellets	PS General purpose
Post Consumer Recyclate Regrind	PS Mixture
Pristine Pellets	PET Amorphous
Post Consumer Recyclate Regrind	PET Amorphous
Pellets	PVC Soft
Pellets	PVC Hard

TABLE 1: Table of tested plastic types, including condition and associated type

The ordered plastics are intended to serve as the foundation of the model classifying unknown microplastics collected from Lofoten.

4.1 Pulverizing Plastics

In order to pulverize the ordered plastic, the samples were milled into microplastic using a tissuelyser, Retsch - Mixer Mill MM 400. The apparatus consists of two steel containers and one steel bullet per container. To avoid samples adhering to the inside of the containers and the ball, they are clad in teflon. The equipment shakes the containers with a given sample, and their respective steel bullet, at a predetermined frequency for a predetermined amount of time. The result is that both bullet and sample are being shaken, causing the bullet to break up the sample in small particles of varying sizes.

The act of shaking the containers and the bullet, breaking the sample, induces heat in the chambers. Working with plastic, the heat will lead to the plastic softening or even partly melting, leaving the particles flattened or melted. At this stage, it is hard to crush the pieces, extracting the desired particle sizes. In order to ensure the brittleness of the plastic, liquid nitrogen was used. With a boiling point of -196 degrees, the samples were chilled sufficiently.

Once the containers and samples were sufficiently cooled, the samples were run in intervals ranging from 2 to 5 minutes before being re-chilled - see Table 2 for a detailed procedure for each plastic type. Re-chilling occurs at every dashed line in the table. Depending on the plasticity of

the samples, the plastic was chilled more rapidly and milled shorter in order to maintain the desired brittleness caused by the low temperature. The samples were milled and re-chilled until they visually appeared adequately fine. Between the different samples, the containers and bullet were thoroughly cleaned in order to minimize contamination.

Type of plastic	Frequency in Hz	Minutes milled
PP pristine	30	0,5-0,5-2-2-3-5-5
HDPE	30	5-5-10
LDPE	30	5-10
PS pristine	30	5-5
PP recycled	30	5-5-5-5-5-5-5
PET flakes	30	5-5-5-5
PET pristine	30	5-5
PVC modified	30	5
PVC soft	30	2-5

TABLE 2: The milling process, described by the amount of minutes the specific plastic type was milled, at what frequency

After being milled, the samples were sifted in order to control what particle sizes were available. The particles were run through two sieves, one with a grid of 630 microns and the second of 200 microns. The remaining particles at the bottom and at the second sieve were collected. The procedure assured the finest samples being smaller than 200 microns, while the middle stage was in the interval of 630 microns down to 200 microns. The samples were sifted for 30 minutes each, using a Retsh AS-200 basic - vibratory sieve shaker. The samples were collected in glass vials according to their size interval. The sieves were cleaned using pressurized air in between samples.

Even though most materials are brittle at low temperatures, the PE samples did not respond in a similar fashion. As a consequence, the samples did not pulverize when milled. Rather than fragment into fine particles, the plastic flattened or shredded. This occurred for all PE samples, regardless of density. In order to still acquire particles of PE, the samples were frozen and run through a coffee grinder.

The plastic was placed in a petri dish and liquid nitrogen was added. After the liquid nitrogen was next to fully evaporated, the mixture was poured into the coffee grinder. In an effort to maintain some of the cold temperatures, some of the residue liquid nitrogen was also poured into the grinder. To avoid having to thoroughly clean the collection tray, it was clad in aluminum foil. The foil is also less affected by static electricity. This makes it easier to retain more of the sample when transferring it to a different container. Between each different sample, the grinder was thoroughly cleaned using water and pressurized air.

Even though the samples were to be measured in the infrared and near-infrared spectrum, they were separated by color, to test if the colorant has an effect, also outside the visible spectrum.

4.2 Collecting Plastic in Lofoten

When collecting plastic from the sea outside Svolvær, Lofoten, a "manta sampler" was used, as shown in Fig. 2. The manta ray consists of a head (3), a body (4) and a tail (5). The head is an aluminum mouth serving as a collection frame with an area of $60,6 \cdot 17,6$ cm, collecting water (1) from the sea surface. To create desired buoyancy, foils (2) are attached on each side of the head. The body, attached to the back of the head, is a net – narrowing down to a diameter of 5 cm towards the tail. The body can be seen as a trawl of masks with a mesh size of 300 microns. At the end of the trawl, the tail is attached. The tail is a bottle gathering the mass that enters the trawl, like a cod end. The bottle partly consists of a net with a similar mesh size as in the trawl. This way, the bottle is not completely sealed but will allow excess water to flow through without carrying the masses to be examined.

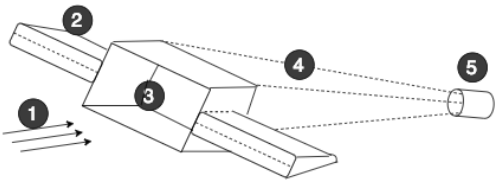

Fig. 2: Sketch of the Manta Sampler used to collect debris from the sea. 1 is the incoming water. 2 is foils keeping the sampler on the surface. 3 is the inlet at 17,6x60,6. 4 is the net with a mask size of 300 microns. 5 is the end bottle, collecting mass

The collection procedure was carried out as follows. The manta was attached to a large crane fixed to the boat, MS HASSE. The crane operator on board led the net down to the sea surface so that the manta was placed in a position leading the surface water through the net (1). Furthermore, the skipper was asked to keep a constant speed of 3 knots. The manta was kept in a stable position for a variety of time, see Table 3.

After the given amount of time, the manta was lifted back up, by the same crane, and led to the gunwale. Here, a regular water hose was used to clean the net, so that all mass attached to the side of the net, was flushed down into the tail along with the water from the water hose. Finally, the bottle (tail) was detached from the manta and carried to the next station, addressing further filtration of the collected mass.

The filtration process began with pouring the contents of the bottle into a funnel. The bottom of the funnel was a filter with a mesh size of 100 microns. In order to capture the excess water, a glass bottle was placed below the filter. To accelerate the filtration process, the funnel was attached to a pump, creating a vacuum below the filter. The filter and resulting unfiltered sea mass were placed in a glass tube and frozen down in a freezer.

Both the collection process and the filtering process were repeated for each sample. The location, length (in time), and sample number of the takes are listed in Table 3.

Location	Length (minutes)	Day	Sample no.
68 19.864N 14 43.890E	30	1	1
68 18.677N 14 43.760E	5	1	2
68 17.030N 14 42.424E	5	1	3
68 15.391N 14 41.655E	1	1	4
68 14.484N 14 41.523E	1	1	5
68 13.134N 14 37.766E	1	1	6
68 11.520N 14 35.648E	1	1	7
68 13.439N 14 33.660E	1	1	8
68 13.785N 14 34.126E	1	1	9
68 14.054N 14 34.494E	1	1	10
68 14.173N 14 34.551E	1	1	11
68 11.493N 14 35.642E	1	2	12
68 07.343N 14 29.641E	2	2	13
68 04.102N 14 18.301E	3	2	14
68 04.388N 14 02.358E	3	2	15

TABLE 3: Manta sampler process specifications, including the day of the trawling, the position of collection, the amount of minutes the manta net was trawled for at this location.

4.3 The Laboratory Experiment

The execution of all the following experiments was carried out in laboratory A073-326 at NTNU. A hyperspectral camera was used to image the samples in transmission in infrared light. The imager used was a SWIR-320m-e imaging spectrometer from Norsk Elektro Optikk AS (Norway) [9], operating in the spectral range from 960-2400 nm. In order to adjust the camera to wanted working distance, a close-up lens was inserted in the entrance aperture. The software used was Hyspex version 3.5, a program designed to operate and assist the imager.

Fig. 3 presents an illustration of the laboratory set-up. First, the samples were placed in a fused silica petri dish (2), custom made for this purpose – ordered from UQG optics and modified at NTNU Glassblåserverksted. When measuring in infrared, fused silica (quartz) is among the few materials suitable. This is because quartz does not absorb the wavelengths within the infrared range, such as for instance glass would. Since the measurements are based on transmittance, the light needs to penetrate the sample. Using a petri dish of quarts will thereby leave the rays from the light source undisturbed when penetrating the dish. Furthermore, the petri dishes were placed in a spoon-like holder (3), made of wood and custom made for the dimensions of the petri dishes. The spoon is cut from a wooden plate, using a laser cutter, Laser Solution by Gravograph, at TrollLabs at NTNU. The light sources (4) used are Hyspex halogen lamps, placed at each side of the samples. The light sources were placed below the sample, pointing upwards. The petri dishes were placed in the spoons, which again were attached to an arm (5). The arm was adjustable and rigidly attached to the operation table using a powerful magnet. This way, the position of the samples was fixed.

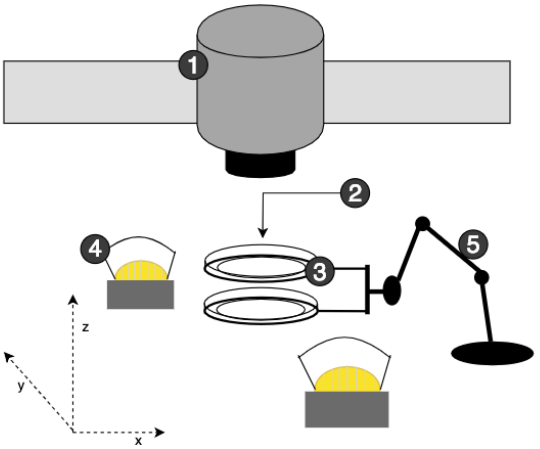

Fig. 3: Laboratory set-up. 1 is the Norsk Elektro Optikk (NEO) SWIR-320m-e imaging spectrometer. 2 is the sample (or the water) placed in the petri dish. 3 is the petri dish of fused silica. 4 is the hyspex infrared halogen light source. 5 is the arm holding the petri dishes with samples and water

When the lab was set, the imaging process could begin. First, a test scan was done, in order to make sure the samples were in focus. The imager, using the push broom technique, Section *3.2, Operating Principle*, starting from one side of the petri dish to the other, created an image of the microplastic samples. The test scan outputted a preview of the image, revealing any saturation due to reflection (as the red spots in Fig. 4). In these cases, the integration time was reduced step-wise until the test-scan no longer showed areas of contained saturated pixels. The frame period of the imager was adjusted according to the integration time. When necessary adjustments were completed, the software was set to record the image, storing the data in a folder on the computer. The data stored was three files per taking, one .hdr-file containing the associated settings, one .bmp-file displaying quality control graphs, and one .hyspex-file containing data for every pixel of the image.

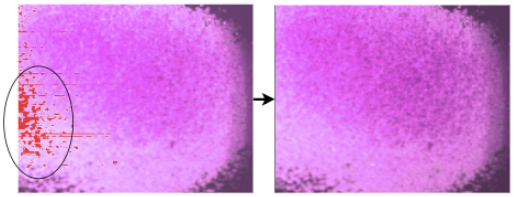

Fig. 4: PS pristine, with (left) and without (right) saturation

For every sample, an additional recording was done including water. $78,5cm^3$ of Sterilized water was placed in a petri dish inside the upper spoon, while the petri dish containing the samples, remained in the lower spoon, both illustrated in Fig. 3. This way the image was taken through water, simulating an underwater scenario. This procedure was repeated for every new plastic type measured.

4.3.1 Data Analysis

The data was analyzed using K-means clustering and Spectral Angle Mapping (SAM) algorithms. These were mainly

based on pre-existing software in the Sci-Kit learn and spectral package, which is a machine learning package [18], and a spectral processing package for Python. The algorithms were run separately in order to achieve independent predictions but also combined. Independently, SAM was run using both plastic, and plastic and water for endmember signatures, and K-means clustering with means based on several types of plastic. The K-means clustering was run with eight clusters and ten iterations. The relative tolerance to declare convergence was $1e^{-4}$. By combining the two algorithms one could utilize strengths from both methods. SAM was used to identify the means of a K-mean analysis, and subsequently classifying the clustered data. The result was turning the unsupervised method of K-means clustering into a supervised method. The signatures were extracted by taking the average of all signatures in a 20X20 pixel frame centered on the hyperspectral image.

5 Results

This section consists of both qualitative and quantitative analyses. The qualitative analysis includes a representative selection of spectral signatures from the microplastics measured. The plots displaying the signatures has intensity along y-axis and wavenumber along the x-axis. The quantitative analysis covers a selection of images from the supervised and unsupervised method, displaying type-predictions. These have pixel number along both axes.

5.1 Signatures & Qualitative Analysis

The following section depicts the notable spectral signatures captured from the plastic particles. The following signatures illustrate signatures of different sizes, colors and conditions. Also illustrated are the effect of water on the signatures and the signatures from the marine plastic particles. The signatures have been used in qualitative analysis and as endmember signatures in SAM.

The following plots in Fig. 5 show the signatures of same-sized HDPE particles, but with different color. The particles are in the size range 200 to 630 micron. The signatures show some minor differences. The apparent differences are similar to those seen in other samples different-sized, with more prominent features.

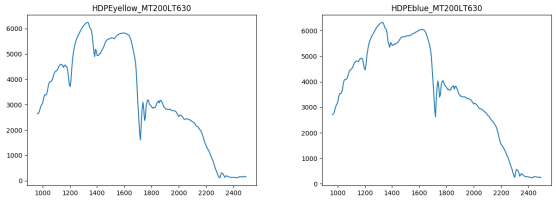

(a) Sample of yellow HDPE. (b) Sample of blue HDPE.

Fig. 5: Signatures of same-size HDPE with different color.

The signatures below are of blue HDPE particles in water and coarser, larger than 630 micron, particles than in Fig. 5. One may observe that the coarser sample of *blue* HDPE has a next to identical signature to that of fine *yellow* HDPE in Fig. 5a. The signature with water depicts the expected characteristics which correspond to the absorption spectra of water.

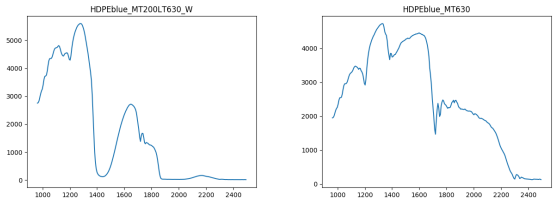

(a) Sample of HDPE in water. (b) Sample of coarse HDPE.

Fig. 6: Signatures of HDPE with and without water.

Fig. 7 show the signature of different-sized PP pristine. The fine particles are smaller than 200 microns, while the more coarse samples are in the interval 200 to 630 micron. One may see a rather significant difference between the two samples. The exact reason is unknown but will be discussed in the subsequent section.

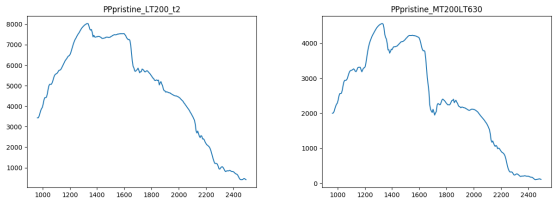

(a) Sample of fine PP pristine. (b) Sample of coarse PP pristine.

Fig. 7: Signatures of different-size PP pristine, depicting differences in spectra due to size.

The signatures of PET pristine and PET flakes, presented in Fig. 8, show next to identical signatures. This is regardless of the previous use of the PET flakes sample. The flakes are post-consumer, and most likely used in bottles. This differs from other samples, which depicted large differences between plastic types with different additives than the pristine.

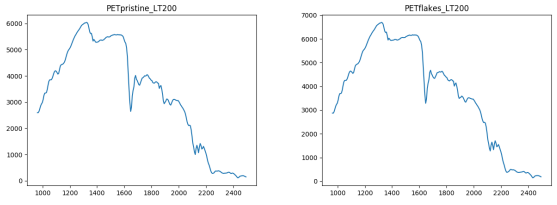

(a) Sample of fine PET pristine. (b) Sample of PET flakes.

Fig. 8: Signatures of plastic in different conditions.

The signatures below are of the particles collected in Lofoten, Norway. These depict an effect from the water present, this can be seen in the significant dip at 1450 nm. The signatures are still significantly different from that of organic matter.

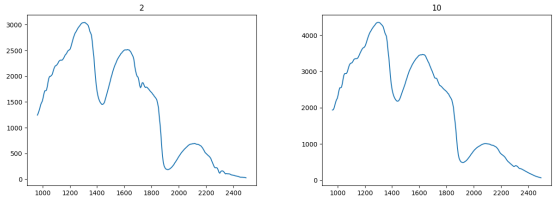

(a) Particle 2. (b) Particle 10.

Fig. 9: Signatures of particles from Lofoten.

5.2 Spectral Angle Mapper (SAM)

The following section presents the result from the classification of dry samples using Spectral Angle Mapper (SAM). The endmember signatures for the model are of dry plastic.

The illustrations show the resulting classification from the SAM algorithm. It is apparent that the algorithm largely classifies the plastic types correctly. This illustrates the possible effectiveness of the algorithm. The tested samples are PVC soft of size 200 to 630 microns and PET flakes smaller than 200 microns. The latter depicts the aforementioned similarity in signatures, as the particles are classified as PET pristine.

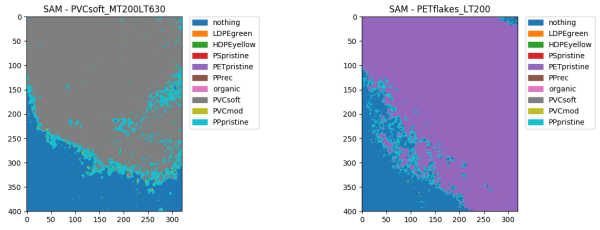

(a) Sample of PVC soft. (b) Sample of PET flakes.

Fig. 10: Results of SAM analysis with dry plastic for the endmember signatures.

5.3 SAM with Water

Here, the results from samples in water with a SAM algorithm based endmember signatures from plastic in water. Running a regular SAM algorithm did not manage to classify anything due to the large influence of the water.

Fig. 11 shows tests using the same plastic types as dry SAM. The difference is the presence of water and the particle size of the PVC soft, which is less than 200 micron. One may observe that the algorithm is unsuccessful in classifying the plastic. There is no clear edge on the identified plastics and it appears to be dependent on the thickness of the plastic or water layer.

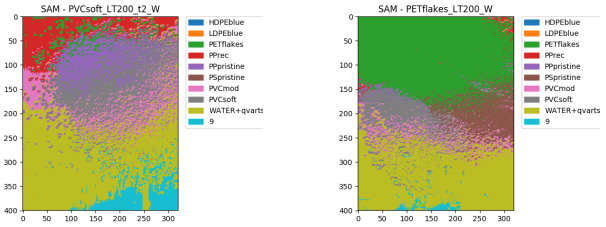

(a) Sample of PVC soft in water. (b) Sample of PET flakes in water.

Fig. 11: Results of SAM analysis with plastic in water for the endmember signatures.

5.4 K-means Clustering

The following results are from the use of K-means clustering. The models are either trained and run by themselves or a similar type and subsequently run. The algorithm classifies based on similarity, without an initial definition. Thus, none of the colors are classified. The corresponding classes are merged, resulting in a more intuitive illustration.

The presented results are of a model trained on a PET pristine sample with particles smaller than 200 microns. Fig. 12b shows the results of the model run by itself and thus illustrating the training of the model. Fig. 12a show the model, but with PET flakes particles smaller than 200 microns in water. The results appears promising with respect to classifying the plastic.

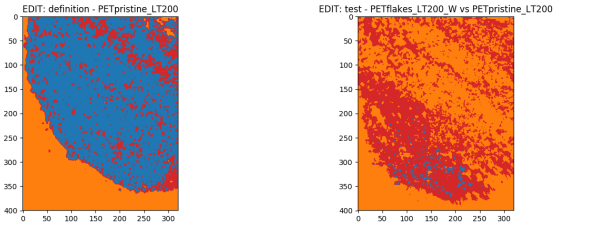

(a) Model based on PET Pristine sample. (b) PET flakes in water vs. PET pristine model.

Fig. 12: Results of K-means clustering with a model based on a PET Pristine sample, and the prediction for PET flakes in water based on said model.

5.5 K-means - Concatenated Photos

As previously mentioned, K-means clustering does not classify the samples involved. Thus, including a known truth in the sample will yield a form of classification. The following result has trained and run K-means clustering on a concatenated image of two PP types of size 200 to 630 micron and an unknown sample from Lofoten.

Additional results from K-means clustering on concatenated photos were left out to reduce space. However, the results from the tenth sample showed a clear indication of LDPE or HDPE.

Fig. 13 shows the principle of ground-truthing and

possible classification of one of the Lofoten samples. The similar clusters are merged in order to picture the reality of the clusters. One can observe the same clusters of the known plastic and the unknown sample from Lofoten. The result leaves an indication of the identity of the unknown sample.

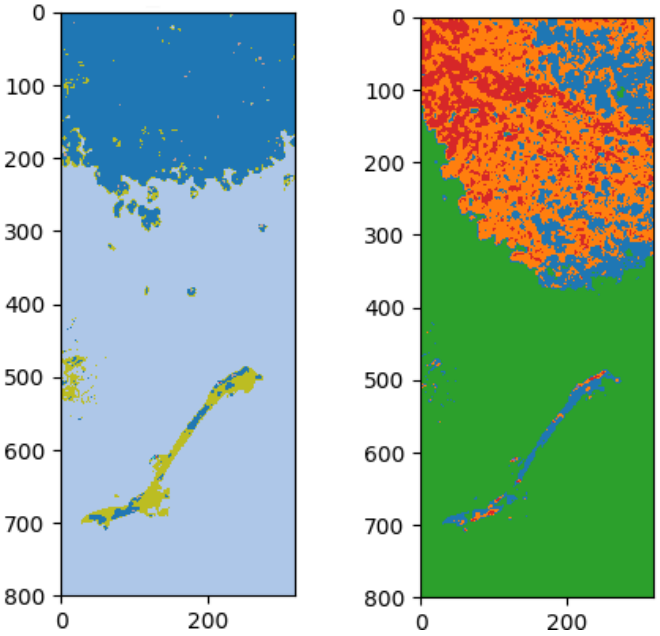

(a) PP pristine (b) PP recycled

Fig. 13: Concatenated photo of second sample from Lofoten and PP and K-means clustering.

5.6 SAM Combined with K-means

In order to identify the clusters formed, SAM was applied to the means of each cluster. Each cluster was subsequently changed to the respective classified type, eliminating the need to merge clusters. The result is an algorithm that classifies the plastic based on clusters. The following algorithm had endmember signatures based on solely plastic samples.

The depicted result is of PVC soft between 200 and 630 microns. The result shows high accuracy, which is to be expected based on the previous results.

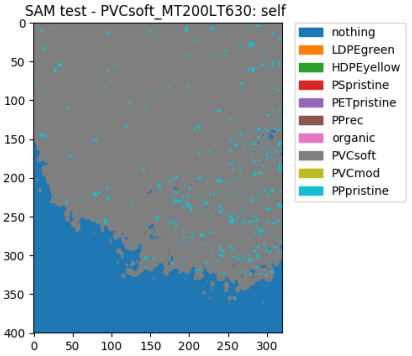

Fig. 14: K-means clustering of PVC soft, where the means of the clusters are classified using SAM based on dry end-member signatures

5.7 SAM with Water Combined with K-means

The previous method was combined with endmember signatures based on samples influenced by water based on previously improved results. The following results depict the highly improved result of the change.

The depicted result is of PVC soft smaller than 200 microns classified using SAM based on samples with water and K-means clustering. The results were more successful, with a higher degree of correct identification.

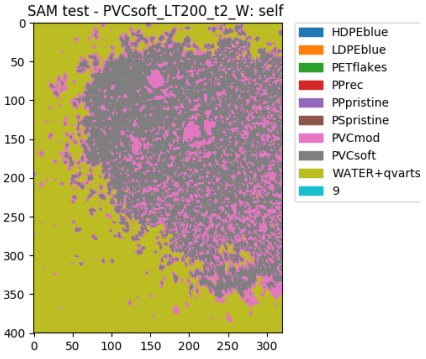

Fig. 15: K-means clustering of PVC soft, where the means of the clusters are classified using SAM based on endmember signatures in water

5.8 Identifying Samples from Lofoten

The following results illustrate the efforts made to identify the samples collected in Lofoten. The algorithm only yielded noteworthy results for the depicted samples, due to size. The included results illustrates the indications attained to identify the samples.

Sample 2, see table 3, did not respond to the aforementioned techniques. As pictured in Fig. 16a, certain areas of the samples are clearly non-organic matter. The organic matter dominating in other methods, Fig. 16b, illustrates this point.

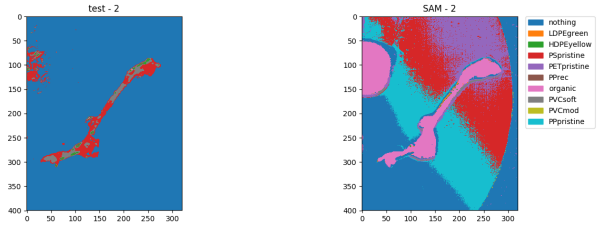

(a) Kmeans Clustering (b) SAM

Fig. 16: Results of classification of the second sample from Lofoten.

Sample 2, table 3, responded better. However, as is shown in Fig. 17a, the sample responded similarly to sample 10 with respect to being classified as organic matter. The combined algorithm of SAM and K-means yielded some indication of the identity of the sample, as may be seen in Fig. 17b. The result indicates LDPE as for both particles depicted in the image.

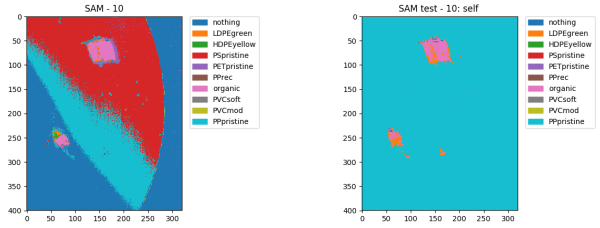

(a) SAM (b) SAM - K-means Clustering

Fig. 17: Results of classification of the tenth sample from Lofoten.

Furthermore, sample 11 and sample 14 were also believed to be PP by the use of ground-truthing and concatenated images. The total indicated plastic types are summarized in the table below.

Location	Assumed Plastic Type	Day	Sample no.
68 18.677N 14 43.760E	PP	1	2
68 14.054N 14 34.494E	PE	1	10
68 14.173N 14 34.551E	PP	1	11
68 04.102N 14 18.301E	PP	2	14

TABLE 4: Results from the identification of the samples collected in Lofoten.

6 Discussion

From the results, there are particularly a few attributes that need to be looked into. First, as plastic is known to come in a variety of sizes and colors, measurements of the specific types at different sizes and colors, are completed. Of these results, one can discuss whether these properties affect the resulting common signature for the associated type. Furthermore, the samples studied are of different conditions. The discussion should include whether a general type-signature can endure such environmental or industrial impact, altering the condition of the particle. Moreover, in-situ characteristics are applied at best efforts. As the samples are tested in and out of water, the contributing differences should be elaborated, as well as the comparison of sea-influenced plastic debris versus pure microplastics.

From the plots presented in the qualitative analysis, one can observe how significant peaks in the spectral signatures seem relatively independent of sample size. However, a common trend is that the characteristics appear more prominent in coarser samples. Peaks were sharper and the valleys deeper, as shown in Fig. 5b and Fig.6b. This is assumed to be an effect of the difference in light being let through. Coarser samples will have larger space between grains and larger surfaces. The assumption is that this results in higher reflectance internally among the particles and thereby more prominent characteristics in the resulting spectra - not to be mistaken with a higher transmittance, which the intensities illustrate.

Related differences can be found when comparing the two spectra of PP pristine samples of different sizes, i.e. Fig. 7. Considering that both samples are milled and hence have received much of the same stress, but with different duration, the reason behind the differences can be assumed equal to what is described above. However, due to different material properties of this specific type, the differences are more prominent than registered within the other samples.

Moving towards even smaller sample pieces, less than 200 microns, none of the algorithms managed to distinguish the plastic particles. The size of the pixels might be the reason why. A possible solution to this could be anomaly detection, identifying the outliers.

With respect to the question on whether sample color impacts the signature, the HDPE signature, representative for all samples with distinctive color measurements, show small differences between samples of different colors as can be seen in Fig. 5. The same trend was apparent in the LDPE samples. Even though the HDPE plots reveal some differences due to color, it does not persist in the different-sized samples, illustrated in Fig. 5a and Fig. 6b. The notion of there being minimal difference in the NIR spectra due to color and the subsequent additives is underlined by the SAM model recognizing the same different colored samples.

Concerning the impact of the condition of the plastic, the results were inconsistent. PET flakes and PET pristine classified as PET, while the remaining same-type samples did not classify according to their base type. Their signatures did not resemble each other, and the models classified the types individually based on condition. As a result, there is reason to expect the additives to alter the signatures. Furthermore, the change in the signature will require more advanced models to identify the individual types.

Looking at the results from samples containing water, these can be compared to the signature from identical

samples without water. Of the signature plots, Fig. 6, the distinction in the peaks comparing a) and b), are clear. However, the model manages to classify the water-included samples correctly. All samples containing water display the same properties. There is a prominent valley around 1400-1450 nm, and next to nothing after 1850-1900 nm. These features are coherent with the absorption spectrum of water and are not surprising. The same feature is displayed in the organic samples. These were frozen instantly after collection. Hence, large amounts of water were retained, which explains the similar characteristics.

The sea-influenced samples proved difficult to identify at this stage. In Fig. 13 and Fig. 16a the same areas are identified by the models. The result was consistent across models indicating an ability to classify the area as plastic despite what is seen in the SAM analysis. The same trend was apparent in particles no. 10. The area identified as LDPE in Fig. 17b was consistently identified as different from organic matter.

Based on the results of the testing it is hard to determine the exact type of plastic in sample 10. However, the results show a consistent separation between areas in the sample seen in Fig. 17b. Based on the consistent separation, results seen in the concatenated photo of sample 10 and LDPE/HDPE and the indication given in Fig. 17b, the particles in Fig. 17 are believed to be LDPE or HDPE.

The dark blue area is generally classified as different plastic types in Fig. 16. The consistent separation indicates the possibility of discriminating plastic from organic matter. Furthermore, the consistency in the concatenated photos in 13 indicates that the second sample from Lofoten may be PP.

Do note the size limitation. The lack of a quantitative measure of similarity in the clusters makes it difficult to assess the identity of the smaller particles. There might be variation that clusters the particles differently than the organic matter. However, this might also occur for other variations. Hence, it is difficult to assess the identification of smaller particles compared to natural variations as there is no consistent area of clustering. If one observes the signatures of the samples in figure7, one may observe a quite drastic difference from the plastic signatures presented in figure 9. These are still classified as plastic. Nonetheless, one could argue for the use of manual and qualitative identification each time this occurs. However, the scope of the project is to assess the possibility of an autonomous classification, which this is not. Also, it could be argued that the the smaller clustering on what was believed to be plastic particles was only investigated due to the a priori notion of it being plastic.

6.1 Sources of error

6.1.1 General

By pre-processing the data, one might expect there to be more clear results. The authors intended to keep the intensity of the samples and limit added noise by not pre-processing the data. The decision does result in noise not being excluded from the data. Also, the intensities are absolute, rather than relative to a standard.

Based on the aforementioned results and discussion, it might prove difficult to classify the exact type of plastic. However, using an approach based on K-means clustering and concatenated images, one could expect promising results. Also, it might have been wise to pre-process the images to have fewer clusters based on rather small differences, yet retain differences in intensities.

6.1.2 Spectral Angle Mapper

The SAM models, built with dry plastic, managed to correctly to identify the type of plastic regardless of color or size. However, the SAM algorithm does not have a Not Applicable (NA) class, which may result in overly optimistic results. Without an unclassified-class, every sample is forcefully classified. As a result, the samples are being classified to the class they are the closest to, regardless of them being far away from the specific class. This is a result of the untested robustness of the model.

Also, in situ measurements will involve an uncontrolled environment. One may therefore expect there to be unknown, or unmapped samples being measured. This may result in false positives if there are materials that are *the most* similar to plastic. Due to the controlled environment in which the tests were conducted, this was not of particular concern. It should, however, be taken into account before tesning in situ.

The endmember signatures in the SAM-water model were not collected with the mindset of them becoming endmembers. As a result, one would naturally expect a potential for improvement by collecting the signatures for this purpose. The measurements were made for the purpose of testing the original model. The need to build a SAM model based on samples with water occurred at a later stage. Hence, the model was built with the existing measurements as base. Clearer signatures and possibly different focus are, hence, believed to improve the results achieved in this paper.

6.1.3 K-means Clustering

The K-means models based on dry plastic managed to correctly identify the type of plastic regardless of color or size. Not surprisingly, combining it with SAM also yielded favorable results. It is important to notice that these results are based on dry plastic.

However, K-means models yield false positives when they are trained on one plastic type and applied to another. One may encounter false positives as the algorithm will classify samples according to their means. Naturally, the plastic will have more similar means than the empty petri dish. Resulting in overly positive results.

In order to prevent the false positives due to training on other models, the approach concatenating the images with a sufficiently high number of means is preferred. The approach will leave room for differences while containing a

ground truth. However, it requires more computing time as there will either have to be all plastic types in one photo or several photos with different plastic types.

K-means chooses its locations for the clusters randomly, with a minimum distance. The resulting clusters are hence non-consistent. The exact definition of the clusters is assumed to be somewhat the same, but not entirely identical. This reduces the robustness of the model.

The number of clusters was chosen based on visual improvement. This could have been done in a more scientific and accurate manner. An approach was tried with the use of SAM to classify the clusters. However, an improved and more accurate method is called for.

Also, the data was neither scaled nor centered. This resulted in clusters (meant to be one cluster), being separated due to differences in intensity, rather than features. By pre-processing the data, it might have been avoided. More relative data makes it easier to compare and hence cluster. Pre-processing would also have made the k-means method more effective, as it would have made the differences relative.

7 Conclusions

The hyperspectral imager method appeared to classify microplastics using infrared radiation. The work involved same-type plastic at various sizes or samples in different colors. Despite promising results for particles sized more than 200 microns, the method did not respond well to plastic particles in the range below 200 microns. Moreover, the model seemed to map correctly even when the infrared rays had to penetrate water. Variations in condition appeared to influence the spectral signature of the associated plastic type, altering the general type-signature. Concerning sea-plastics, the method appeared to function. However, the results cannot be validated as the nature of the samples are unknown. In order to verify the method as a working in-situ approach, additional research is needed. This reseach should covering experimental an set-up one step closer to the underwater scenery. Nevertheless, this investigation has furnished promising results. Consequently, the authors sincerely recommend an extensive commitment to further research within this field. The focus of the next steps should be experiments with larger amounts of water (preferably sea water) and a lower sample concentration - slowly moving towards in situ.

Acknowledgments

This work was supported by the Research Council of Norway through the Centres of Excellence funding scheme, Project number 223254 – AMOS. The authors of this paper wish to thank the supporting teams at AMOS and NTNU. Furthermore, Prof. Geir Johnsen providing useful information, much appreciated. The research team at SINTEF Ocean, should also receive a large portion of gratitude, concerning both scientific advice and arranging the field trip to Lofoten. The authors would especially like to acknowledge Julia Farkas (SINTEF) for loaning us her manta net. Lastly, Ph.D. candidate Asgeir Bjørgan has provided detailed insight on methods for unsupervised learning, which we are profoundly grateful for.

References

[1] R. Geyer, J. R. Jambeck, and K. L. Law, "Production, use, and fate of all plastics ever made," *Science Advances*, vol. 3, no. 7, 2017.
[2] F. Gallo, C. Fossi, R. Weber, D. Santillo, J. Sousa, I. Ingram, A. Nadal, and D. Romano, "Marine litter plastics and microplastics and their toxic chemicals components: the need for urgent preventive measures," *Environmental sciences Europe*, vol. 30, no. 1, p. 13, 2018.
[3] H. Kawazumi, A. Tsuchida, T. Yoshida, and Y. Tsuchida, *High-Performance Recycling System for Waste Plastics Using Raman Identification*, pp. 519–529. 09 2014.
[4] Y. Zheng, J. Bai, J. Xu, X. Li, and Y. Zhang, "A discrimination model in waste plastics sorting using nir hyperspectral imaging system," *Waste Management*, vol. 72, pp. 87 – 98, 2018.
[5] T. M. Karlsson, H. Grahn, B. van Bavel, and P. Geladi, "Hyperspectral imaging and data analysis for detecting and determining plastic contamination in seawater filtrates," *J. Near Infrared Spectrosc.*, vol. 24, pp. 141–149, Apr 2016.
[6] A. J. Sørensen, "Lecture notes, tmr4240: Control lecture navigation and payload sensors, NTNU, fall 2018," 2018. Accessed: 2018-11-03.
[7] Ø. Ødegård, A. A. Mogstad, G. Johnsen, A. J. Sørensen, and M. Ludvigsen, "Underwater hyperspectral imaging: a new tool for marine archaeology," *Appl. Opt.*, vol. 57, pp. 3214–3223, Apr 2018.
[8] A. Yamashita, A. Fujii, and T. Kaneko, "Three dimensional measurement of objects in liquid and estimation of refractive index of liquid by using images of water surface with a stereo vision system," pp. 974 – 979, Jun 2008.
[9] N. Skauli et al. Norsk Elektro Optikk AS, Skedsmokorset, "Hyperspectral imaging," 2019.
[10] M. Sakai, T. Ohmori, and M. Fujii, *Two-color picosecond time-resolved infrared super-resolution microscopy*, vol. 3 of *Handai Nanophotonics*, ch. 12, pp. 189 – 195. Elsevier, 2007.
[11] F. Signernes, "Lecture notes ttk20: Basic hyper spectral imaging, NTNU, fall 2018," 2018. Accessed: 2018-09-23.
[12] P. L. M. Geladi, H. F. Grahn, and J. E. Burger, *Multivariate Images, Hyperspectral Imaging: Background and Equipment*, ch. 1, pp. 1–15. John Wiley Sons, Ltd, 2007.
[13] W. S. Pegau, D. Gray, and J. R. V. Zaneveld, "Absorption and attenuation of visible and near-infrared light in water: dependence on temperature and salinity," *Applied Optics*, vol. 36, pp. 6035–6046, Aug 1997.
[14] S. P. Lloyd, "Least squares quantization in pcm," *IEEE Transactions on Information Theory*, vol. 28, pp. 129–137, 1982.
[15] F. Kruse, A. Lefkoff, J. Boardman, K. Heidebrecht, A. Shapiro, P. Barloon, and A. Goetz, "The spectral image processing system (sips)—interactive visualization and analysis of imaging spectrometer data," *Remote Sensing of Environment*, vol. 44, no. 2, pp. 145 – 163, 1993. Airbone Imaging Spectrometry.
[16] T. Johnson, "Most common plastics," Apr 2017.
[17] Carat GmbH, "CARAT Control and Research Analysis Thermoplastics," 2019.
[18] F. Pedregosa, G. Varoquaux, A. Gramfort, V. Michel, B. Thirion, O. Grisel, M. Blondel, P. Prettenhofer, R. Weiss, V. Dubourg, J. Vanderplas, A. Passos, D. Cournapeau, M. Brucher, M. Perrot, and E. Duchesnay, "Scikit-learn: Machine learning in Python," *Journal of Machine Learning Research*, vol. 12, pp. 2825–2830, 2011.

8.2 Complementary Results

In order to assess the identity of the samples from Lofoten, the results from testing the particles collected from the sea outside Lofoten, are presented.

8.2.1 Signatures

The following are the signatures captured from the samples in Lofoten. The signatures were retrieved by taking the average signature of areas of the particles believed to be plastic. The results show the effect the organic material has on the plastic. The center dip is likely due to the water on the sample. The samples were instantly put in the freezer after they were collected, and subsequently, when the particles were isolated, they were still covered in seawater or matter with high water content.

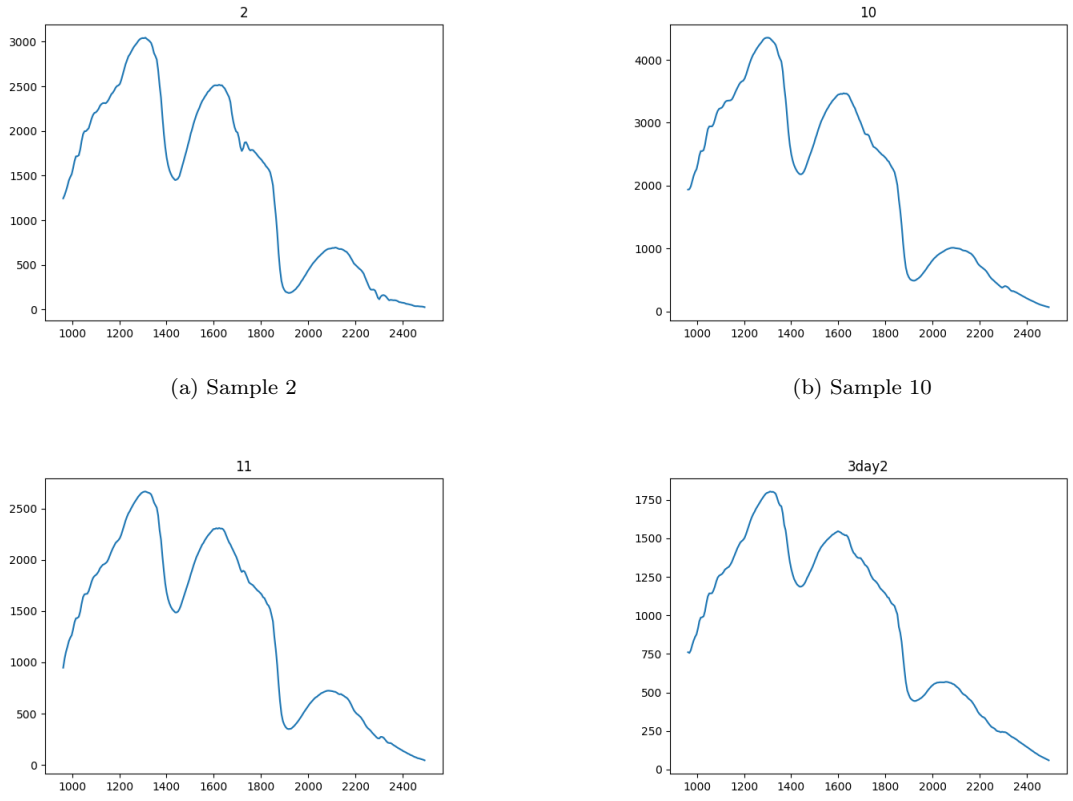

(a) Sample 2

(b) Sample 10

(c) Sample 11

(d) Sample 14

Figure 8.2.1: Signatures from Lofoten samples

8.2.2 Spectral Angle Mapper

The Spectral Angle Mapper (SAM) endmember signatures were based on dry plastic samples with the most consistent layer thickness. The signatures were acquired taking the average signature of all pixels at the center ten by ten pixels. The organic signature was attained using the image

containing the most organic matter and averaging this area, making sure there was no plastic contained in the matter. Figure 8.2.2 shows the results of running the algorithm on two of the collected samples. Based on the images, one may observe that the algorithm has troubles identifying the sea-influenced samples. This is likely due to the effect the water and organic matter has on the plastic.

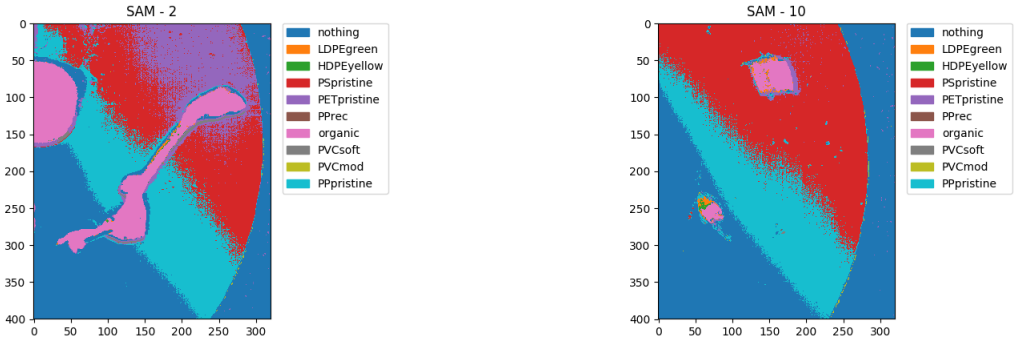

(a) Sample 2

(b) Sample 10

Figure 8.2.2: Results from the SAM Analysis

8.2.3 Spectral Angle Mapper - Endmember Signatures Including Water

The images below show the results from running an equivalent SAM analysis on two of the samples from Lofoten, only that the endmember signatures are based on samples including water. From the lack of improvement in results, by adding the water-based endmembers, SAM alone is assumed to be not particularly efficient. Note that the light blue 9 represents organic matter from Sample 9.

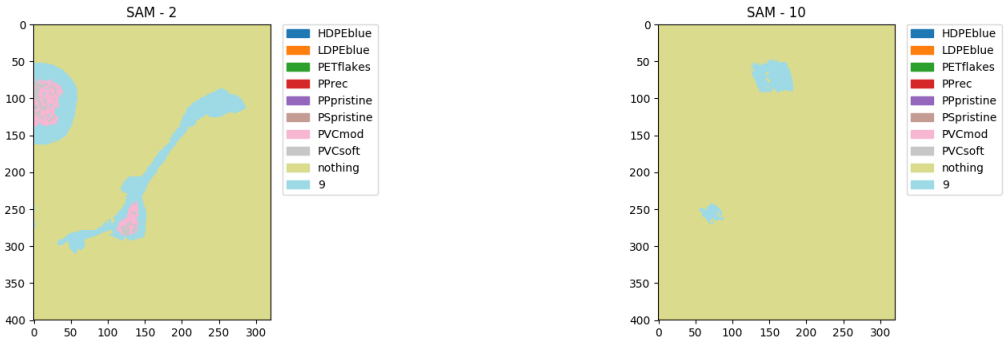

(a) Sample 2

(b) Sample 10

Figure 8.2.3: Results from the SAM analysis using samples with water for the endmember signatures

8.2.4 K-means

The following images portray the results from the K-means clustering algorithm on the samples from Lofoten believed to be identified. The results clearly display areas on the plastic that are locally different. Even though the cluster signatures were not combined at this point, the pattern persisted. Note that the colors of the clusters do not have meaning between the images, only locally.

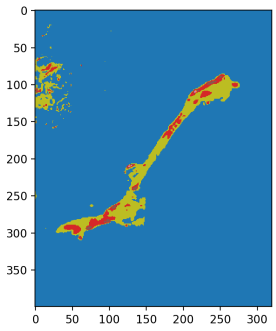

(a) Sample 2

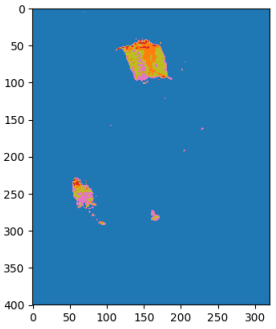

(b) Sample 10

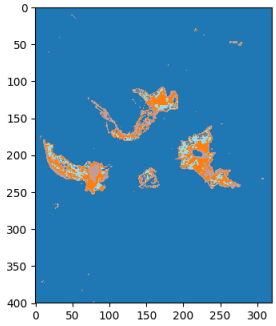

(c) Sample 11

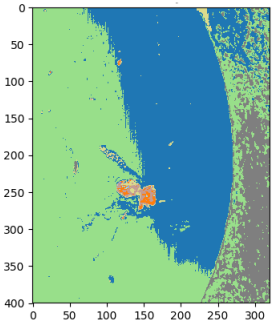

(d) Sample 14

Figure 8.2.4: Results from K-means clustering on the Lofoten samples

8.2.5 K-means Concatenated Images

Below are the results from concatenating the sample image with a number of plastic types, and subsequently running the K-means clustering algorithm. As variation in intensity results in individual clusters, the clusters containing similar spectral signatures have been merged. The featured images are those showing the most promising results. These were Sample 2 and PP pristine, Sample 10 and LDPE, Sample 11 and PP pristine, and Sample 14 and PP pristine. The fact that these were identified aligns with the fact that PP and PE are the most abundant particles in the sea, Lenz et al. (2015).

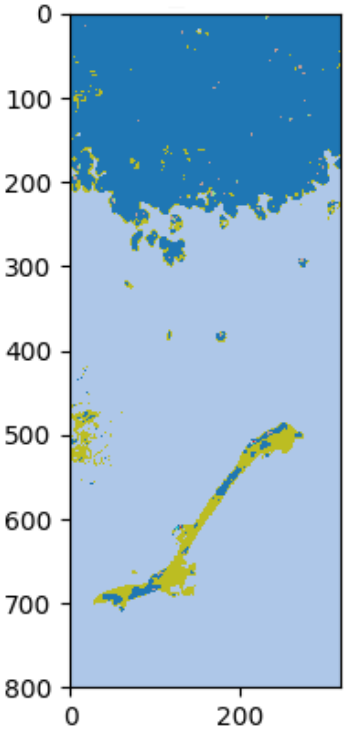

(a) Sample 2 concatenated with PP pristine

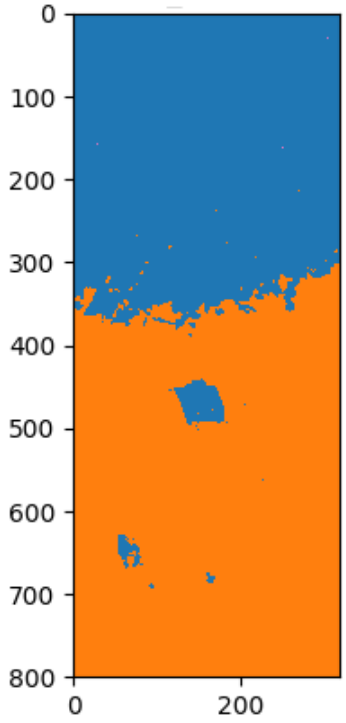

(b) Sample 10 concatenated with LDPE

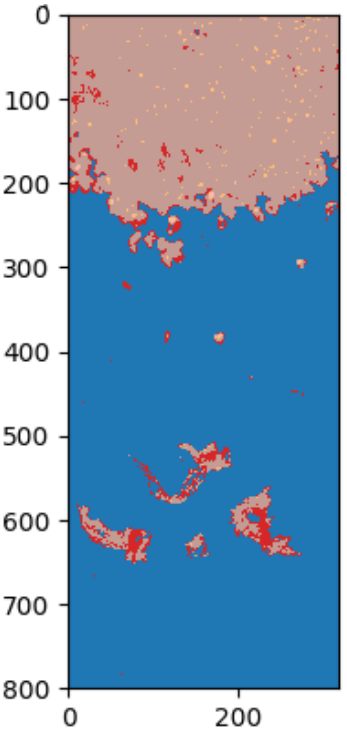

(c) Sample 11 concatenated with PP pristine

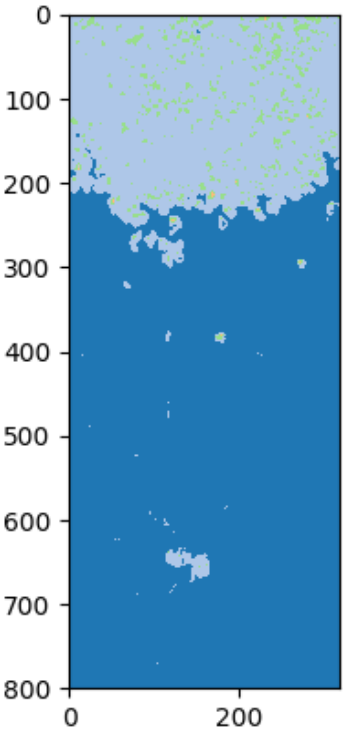

(d) Sample 14 concatenated with PP pristine

Figure 8.2.5: Results from the K-means clustering on the Lofoten samples concatenated with plastic types

The results from Paper 2 indicate sample 10 to be PP rather than LDPE. Following the contradicting results, both were revised. Below is the result of testing sample 10 against PP pristine and PP recycled. The results show the clear indication that the sample might be PP rather than PE as previously indicated.

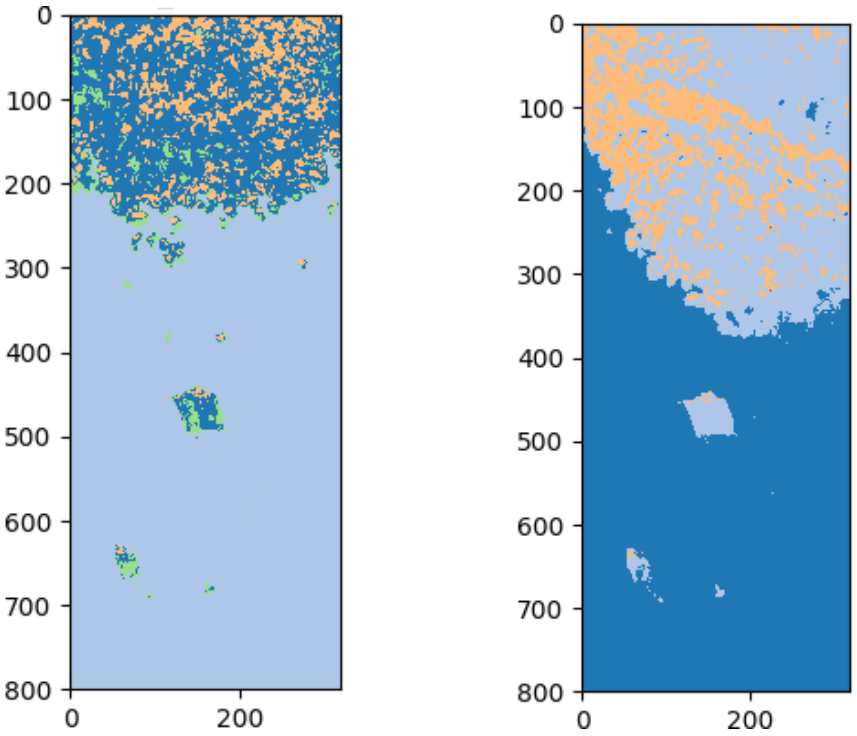

(a) Sample 10 concatenated with PP pristine

(b) Sample 10 concatenated with PP recycled

Figure 8.2.6: Revised results from the K-means clustering on the Lofoten samples concatenated with plastic types after reviewing the results from Raman spectroscopy

8.2.6 Combined SAM and K-means

Rather than manually combining clusters, they were also identified using SAM and then merged based on the classification. Below are the results of the stated method. Namely, Sample 2 and Sample 10 from Lofoten is presented. The exact reason why the background was identified as PP pristine is unknown.

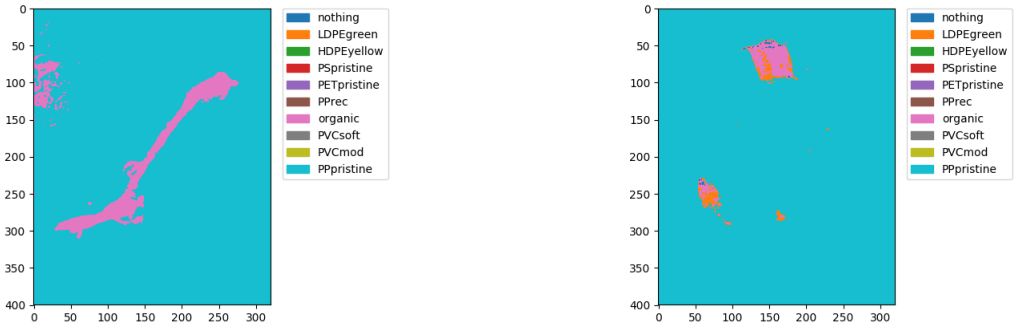

(a) Sample 2

(b) Sample 10

Figure 8.2.7: Results from the SAM combined with K-means clustering on the Lofoten samples

8.3 Additional Work and Expanding Description

Due to the format of scientific papers, certain parts of the work performed was not included. However, the scope and format of an article and a master's thesis, are different. Hence, description and work not included in Paper I is included below with more in-depth explanations.

8.3.1 PCA and PLS-DA

Additional work performed in processing and analyzing the data were PCA and PLS-DA. The data was processed using software designed for hyperspectral data, developed by Prediktera, called Evince. Unfortunately, the method did not yield favorable results and was consequently emitted from the article. The PLS-DA model failed to recognize the samples in water and any of the particles from Lofoten. However, to support the methods chosen in the paper, the technique used is included below.

8.3.2 Preprocessing

In order to make the spectra comparable, a baseline is needed. This is achieved by dividing all the signals on the reference. The reference was chosen to be a measurement of "nothing". All signals were divided on the reference ensuring the possibility of directly comparing spectra.

The ROI is of such a small magnitude that is assumed to be uniformly illuminated, hence it was not necessary with a correction of uneven light distribution.

Due to the fact that when multiple spectra interact, the result is a convolution of them, one had to remove the spectra of the water when working with samples containing water. The water will largely dominate the spectra, making it difficult to predict samples as the water spectrum will result in a prediction of water. Similarly, the organic matter had large portions of water, making the water spectrum dominate the prediction. Thus, the effect had to be removed. The closest thing

to removing the spectrum from the final spectra was to divide them by the water spectrum due to the nature of spectra interacting. Unfortunately, this also introduces additional noise to the data.

8.3.3 Building the PCA model

The samples chosen to form the model were identified as the hyperspectral images with the most consistent layers of plastic. This was to avoid background being identified as plastic samples, resulting in a faulty model. An even layer makes it easier to remove the background from the image.

The identified samples are then regarded as the "virgin" samples. These are merged into a single hyperspectral image along with two images of the references, with and without water. Also, a sample from Lofoten, containing large portions of the organic matter clearly distinguishable from plastic, was included. The latter was to have a class for the organic matter.

Once the merged file containing all the virgin files and the reference was imported into Evince, a PCA is formed, based on the aforementioned image. The resulting scatter diagram depicted a clear cluster representing the background which was marked and excluded from the model, and the PCA updated. Similarly, to limit the effects of irregular measurements on the model, far off measurements on the scatter diagram were also excluded. Illustrations depicting the process may be found in Appendix B.

After the most prominent background measurements were excluded, less prominent background measurements and weaker plastic measurements were also excluded. Due to the large amounts of data and the resulting redundancy, measurements close to the background were also excluded. This was to avoid background wrongly classified as plastic, affecting the predictive ability. Tn order to solely retain the organic matter as a virgin sample, the hyperspectral image containing the organic matter excluded all measurements from the edges. The plastic particles contained in the sample were known to be along the edges, and thus easily excluded.

Following the exclusion of the background, a Standard Normal Variation transform was run on the remaining data. The transform would leave clear clusters in the following scatter diagram. Each cluster was marked and classified with their respective type — the type of plastic or organic matter. However, due to overlap in the scatter diagram, plastic types were present in other clusters than their respective clusters. To avoid misclassification, samples present in other clusters were unmarked based on the contour diagram. The procedure was repeated until every plastic type was classified. To avoid misclassification, the plastic was classified based on the clusters instead of the contour diagram, taking advantage of the large amount of data and redundancy.

The classification based on the scatter diagram results in a relatively large amount of data being unclassified. Nevertheless, the misclassification is reduced because of it. With every plastic type and organic matter labeled, a PLS-DA was made based on the classification.

8.3.4 Testing and PLS-DA

Consequently, samples were classified using the PLS-DA model and qualitative analysis. Even though "another type" had the highest classification percentage, one could clearly see from the contour plot that a large amount of background and non-relevant areas were predicted to be another type, and largely mixed with other classified types. The correctly identified types were in large parts identified in the correct areas and were consistently predicted over the same area.

Tested samples were chosen based on samples not included in the creation of the model. Also, samples containing water were tested. Due to the presence of water, the samples were adjusted using a petri dish containing water as the reference, rather than the empty petri dish. Sadly, the model did not manage to classify the samples containing water and was severely affected by noise.

8.3.5 Conclusion

Due to the misclassification of water as organic matter and subsequently categorizing the pieces as solely organic matter, the PCA and PLS-DA was proved unsuccessful in identifying the samples from Lofoten .

Chapter 9

Paper II: Identification of Marine Plastics using Raman Spectroscopy

The following chapter contains the second paper which constitutes a significant part of the work. The paper describes the method, acquired results, and the analysis of said results, using Raman spectroscopy to identify plastic. The paper contains all relevant methods and work performed to achieve the results. In this regard, both papers combined replaces the standardized *Methods* and *Results* usually found. It is also an independent deliverable, submitted to Oceans 2019 in Seattle – Ocean Conference and Exposition. Furthermore, the format of a scientific paper puts restraints on the amount of included results and method. This chapter also contains additional results and work relevant for the thesis. These are meant to leave the reader with a more in-depth understanding of the process than from the paper alone.

9.1 *Identification of Marine Plastics using Raman Spectroscopy*

Identification of Marine Plastics using Raman Spectroscopy

Emilie M. H. Dahl (NTNU), Andreas Ø. R. Stien (NTNU), Asgeir J. Sørensen (NTNU) and Emlyn John Davies (SINTEF)
Centre for Autonomous Marine Operations and Systems (AMOS), Department of Marine Technology,
Norwegian University of Science and Technology (NTNU) , NO-7491, Trondheim, Norway

Abstract—Plastics have permeated almost every aspect of modern day life with its wide applicability. The tragic consequence is millions of pieces of plastic polluting and eradicating sea life every day. The road towards a clean sea contains several legs and does at the very least require a mapping of the ocean columns, determining critical areas. Determining technologies and methods for the detection of microplastics underwater are hence a necessity. Raman spectroscopy is such a technology, in principle able to extract the chemical structure of the object to be viewed by collecting spectral signatures at the point illuminated. This creates the foundation for the research done in this paper, covering whether it is possible to classify specific types of microplastics underwater by identifying their respective spectral signatures. Raman spectroscopy has been carried out on three different cases of samples. The first case involves known plastic, ordered from CARAT AS, meant to create the foundation of a partial least squares discriminant analysis (PLS-DA) model. The second case holds the same base but includes drops of water on top of the original sample. This case is meant to provide data testing the prediction of the PLS-DA model. The third case includes raw plastic pieces, collected from the sea outside Svolvær, Lofoten. The measurements of these samples create the grounds for the last test-set. The results suggest that the method indeed can classify microplastic correctly, both in water and sea-influenced pieces. However, the specific spectra cannot vary too much in terms of industrial and environmental changes, altering the condition and leaving the mapping and classification method only functional, and thereby suitable, for plastics that recently entered the ocean.

1 Introduction

TODAY the applications of plastics are many, making the material popular worldwide. 381 million metric tons of plastic are produced yearly, and the production is projected to nearly double within the next 10-15 years [1]. Over time, sun rays, wind and currents tear apart large pieces of floating plastic. The result is often tiny pieces at no more than a few millimeters a piece, defined as microplastic. In 2014, 15 to 51 trillion particles of microplastic were estimated to hover the sea [2].

If not for the toxic additives added to the plastics, the presence of these pieces would not be as damaging. However, additives are commonly added to plastics, designing the material for a specific application. As the plastic material is non-degradable, the result is a toxic-carrying vector, doing damage over and over [3]. Unfortunately, a vast number of sea animals are known to confuse microplastics with food [4]. As the additives accumulate up the food chain, the concentration of toxins increases - often carrying fatal consequences for sea life [5]. As plastic is non-degradable, the debris currently polluting the oceans need to be removed. This requires methods for in-situ plastic mapping and monitoring.

A way to work with materials, identify them, or learn about their properties, is to study how light interacts with them - spectroscopy. Light absorption, reflection, and transmittance can be measured, leaving the spectral signature of the object measured. Spectral signatures can be thought of as fingerprints. While fingerprints are often used to identify people, spectral signatures can be used to identify materials.

Besides containing Carbon-Hydrogen bindings, the different types of plastics are all structurally different [6]. Because of this, every type is classified according to its chemical structure, meaning that they all contain unique spectral fingerprints relative to each other. This creates the foundation for the research done in this paper, covering whether it is possible to classify specific types of microplastics underwater by identifying their associated spectral signatures. The research, therefore, requires an instrument able to isolate and withdraw this type of information. This is where the field of spectroscopy enters the court.

Raman spectroscopy is the method used in this paper. Similar to regular spectroscopy, Raman spectroscopy is based on different levels of intensity at different optical wavelengths. However, whereas regular spectroscopy is based on the intensity relative to a defined standard, Raman spectroscopy is based on the change in intensity from the incident light. The reason for this intensity change is a type of scattering, the Raman scattering, holding an abnormal frequency distinguishable to the detector in the spectrometer [7].

Previously, there have been studies to assess the possibility of using Raman spectroscopy to identify plastic and other polymers. Twenty years ago a study managed to identify post-consumer plastic using Raman spectroscopy and data processing closely related to those in this study [8]. Also, studies have concluded on the possible use in automatic plastic detection as opposed to manual detection using microscopy [9]. Similar, more recent, articles have come to the same conclusion [10].

The main scientific contribution of the research in this paper, answers the previously asked question as follows. It is indeed possible to classify specific types of microplastics

underwater by identifying their respective spectral signatures using Raman spectroscopy. However, the piece corresponding with the specific spectra, must not have undergone too much variation as a result of changes in condition, such as post-industrial, post-consumer or recycled.

The paper is organized as follows, the Raman scattering, properties and spectroscopy are presented more thoroughly in Section 2, communicating how spectral signatures were retrieved using a laser to initiate changes in the molecules, recognizable to the spectrometer. Furthermore, materials and methods describe the preparations and execution of the main experiment. This includes how the data was collected, both modification of known plastics from CARAT AS as well as the collection of raw plastics from the sea outside of Lofoten. The execution of the experiment is then presented in Section 3, explicating the set-up and procedure at the laboratory, measuring the plastics with and without water. Next, results are presented in Section 4, largely through plots. Finally, the results are discussed, compared and validated in Section 5.

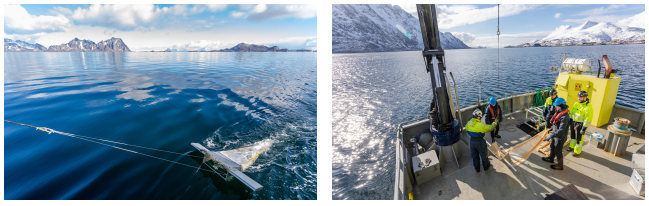

Fig. 1. Photos from collecting Plastic Samples outside Lofoten, Norway. Photos courtesy of Emlyn John Davies.

2 THEORY

This section will explain details of Raman spectroscopy, as well as properties of plastics relevant to the spectroscopy itself. Taking the whole sensor below the surface, can require addition consideration, also illuminated here.

2.1 Fundamentals of Raman Spectroscopy

Whenever a sample is exposed to monochromatic light in the visible region, photons are either scattered or absorbed by the sample. A small component of the scattered light, known as Raman scattering, involves an energy shift in the photos due to molecular vibrations instigated from the incident light, [7]. In order to characterize the scattering light beam, the properties of emitting photons are compared to incident photons. As illustrated in Fig. 2, the incident light beam has a frequency of f_i, while the scattering beams have a frequency, f_s.

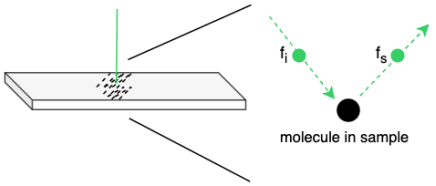

Fig. 2. Scattering with incident photon frequency, f_i and emitted photon frequency f_s. When $f_s \neq f_i$, the scattering is called Raman scattering [7]

Inside the molecules of the sample, electrons have different vibrational levels, based on energy differences. Whenever a photon from a monochromatic light interacts with an electron in the sample, the electron absorbs energy from the incident photon. This energy, transferred from the incident photon to the electron, can be expressed by Planck's constant, h times the frequency of the incident light, f_i, $E = h \cdot f_i$. The result in the electron being pushed to a higher vibrational level. The electron will, in turn, fall back in position as it loses the energy. If the energy lost is equal to the energy of the incident photon, the electron will settle at its initial level, and emerge another photon - with the same frequency as the incident photon: $E_i = E_s \rightarrow f_i = f_s$. This is called Rayleigh scattering and is the most common type of scattering [11]. However, when losing energy from the virtual energy state, the electrons can sometimes respond differently, emitting photons with a different frequency than the frequency of the incident photon, $f_s \neq f_i$. This scattering is approximately $10^{-5}\%$ of the total scattered light and is, as mentioned, called the Raman scattering [7]. When an electron looses energy, defined within the Raman scattering, it can either return to a higher energy state or a lower energy state than the initial state of the electron. The nature of these states can be observed in the Raman spectrum. When electrons absorb energy, f_s is less than f_i, and Stokes lines appear in the spectrum. Similar when $f_s > f_i$, the electron emits energy, and anti-stokes lines can be observed. The excited light is diffracted with a regular spectroscope, resulting in a spectrum of Stokes lines. This way, by studying the resulting spectral peaks, one can identify molecules within the sample. The intensity of the spectral lines determines the concentration of a molecule in a sample.

In order to detect the Raman shift, monochromatic light is common as it recognizes the Raman scattering as all scattering detected, apart from photons holding the incident frequency. This, combined with the fact that the Raman scattering occurs in such a low percentage of the total scattering, implies the need for strong incident light. The common result is the use of lasers.

2.2 Plastics

Polyethylene (PE), polypropylene (PP), polyethylene terephthalate (PET), polyvinyl chloride (PVC) and polystyrene (PS), are the five most common types of plastics, in large part covering the global plastic production, [6]. These types are categorized by their respective chemical composition, which gives rise to individual optical fingerprints. Some bonds creating specific molecules leave spectral lines at correlated wavelengths, provided in the same fashion as described above, Section 2.1. [8] holds a map of chemical bonds and corresponding peaks, frequently used when evaluating the resulting signatures in this paper.

2.3 Light (Laser) in Water

In order to use the sensor under water, the effects of water, inherent optical properties, need to be considered. In water, the light intensity decreases with the distance to the object.

This is due to light attenuation present in water, which again depends on the wavelength of the light. A. Yamashita, M. Fujii, and T. Kaneko [12], describes the variation of light intensity within the visible light spectrum, which includes the Raman laser, operating at a wavelength of 532 nm. A rough estimate of the remaining intensity of light at a 532 nm wavelength, shows that the intensity is more or less intact with approx. 90% intensity at a meters distance and attenuation length is 8.6 metres [13]. This is merely an estimate, as light attenuation varies with depth, temperature, and salinity. Nevertheless, the estimate implies that the light intensity of the laser is sufficient when viewing an object in the near distance. However, as the laser is focusing on a small area, the laser is highly sensitive to disturbances or uncertainties. The scattering of light can be dominant, leaving useful rays at wastage. Shadow patterns underwater can also be an issue, as it contributes to variations in the lighting, making the extracted image less representative when describing the surroundings, [14]. In addition, the restricted measurement interval of approximately one to two minutes can pose a challenge as the underwater scenery is seldom still.

3 Materials and Methods

Within this research, the five types of plastics presented in Section 2.2, have been tested. Individually, the types can vary depending on size, color, and condition. Ordered from CARAT AS in Germany, the resulting types include different conditions and colors; HDPE and LDPE (both in blue, gray, yellow, red), PET flakes (Post Consumer), PET pristine, PP pristine, PP recycled, PS pristine, PVC modified (hard) and PVC soft, [15]. Shredding these samples, leaves an additional categorization, categorization by size. In total, this results in a variety of different samples, all measured, compared, and analyzed. The remaining 17 samples are taken from the sea outside Svolvær, Lofoten. This way, the classified plastics from Germany are intended to serve as the foundation in the model classifying unknown microplastics collected in Lofoten.

3.1 Preparations

3.1.1 Pulverizing Plastics

In order to prepare the laboratory experiment, the ordered plastic was pulverized into microplastics at the laboratory in EU2-115, NTNU. The plastic pieces were milled using a tissuelyser, more specifically, Retsch - Mixer Mill MM 400. The tissuelyser consisted of a steel container and a steel bullet placed inside the container. Prior to the tissuelysing procedure, the container, bullet, and the plastics were cooled using liquid nitrogen. This was to ensure the brittleness of the plastic. After placing the plastics inside the container, the Mixer Mill shook the container so that the steel bullet was thrown back and forth with a frequency of 30 Hz, crushing the plastic pieces and eventually pulverizing them. As the milling process left the plastic heated, the cooling process was frequently executed, every fifth minute, maintaining clean breaks, cutting the bonds within the plastics instead of stretching them.

Even though most materials are brittle at low temperature, the brittleness of all the PE samples, regardless of density, were not sufficient. As a consequence, the samples did not respond well to the milling. Rather than fragment into fine particles, the plastic flattened or shredded. In order to still acquire particles of PE, the samples were frozen and run through a regular coffee grinder. The plastic was placed in a petri dish, and liquid nitrogen was added. When the liquid nitrogen had evaporated, the PE samples were poured into the coffee grinder and ground.

In order to control the available particle sizes, the samples were sifted using a Retsh AS-200 basic - vibratory sieve shaker. The particles were run through two sieves, one with a grid of 630 microns and the second of 200 microns, before the remaining particles in the bottom and at the second sieve were collected. The procedure assured the finest samples being smaller than 200 microns, while the middle stage was in the interval of 630 microns down to 200 microns.

3.1.2 Collecting Plastics

When collecting plastic at sea, a 300-micron mask sized mesh was attached to a large crane on board the MS HASSE. The crane led the net towards the surface, allowing surface water to flow through the net. At the end of the net, a bottle was attached, collecting material caught by the net. After a few minutes, the manta was lifted back up and led to the gunwale. Here, a water hose was used to clean the net, so that useful mass attached to the side of the net, was flushed down into the bottle. The bottle was then detached and examined. The content was poured into a funnel. The bottom of the funnel was a filter with a mesh size of 100 microns. Below the filter, a glass bottle was placed, meaning to capture the excess water. To accelerate the filtration process, the funnel was attached to a pump, creating a vacuum below the filter. The filter and resulting unfiltered sea mass were placed in a glass tube and frozen down in a fridge freezer. This procedure was repeated for each take.

3.2 The Laboratory Experiment

The laboratory experiment consisted of retrieving spectral signatures from the plastic samples using a laser and Raman spectroscopy. The laboratory set-up is illustrated in Fig. 3 and consisted of the following components, a Witec UHTS 300 SMFC VIS Raman Spectroscope [16], a Witec WMT 50 microscope, two lenses - Zeiss - 10x/0,25 (3) and Zeiss EC epiplan - 50x/0,75 (2) and a laser, Witec - wavelength: 532, <80 mW (1). The components were connected to the software used, Control FIVE.

Before retrieving valid data, parameter adjustments had to been done. As the laser was focusing a single point on the sample, the sample was moved relative to the laser and camera, scanning three times for every sample. This was done to avoid measurement errors by reducing the risk of scanning impure areas. Whenever these areas were discovered, as a clear deviation from the other signatures, the scan was removed, and the sample was

rescanned focusing on another area. The experiment was then conducted with the assumption that the probability of scanning the same kind of impurity was sufficiently low.

As each sample holds a difference in size, thickness, and individual properties, focusing the samples was done with different light intensity and different distance between the camera and the sample. However, due to the nature of the experiment, these parameters did not need to be identical. As the sought after properties were the signatures of the plastics, and because the peaks and outline of each signature are independent of the parameters mentioned above, it was deemed unwise to keep them constant. In addition, some particle surfaces help properties triggering saturation. Whenever this was the case, the laser intensity was reduced. The integration time was then increased compensating for the low laser intensity and reducing noise. After adjusting the parameters above, every scan could be taken from a clear and focused area of the sample.

First, the samples were scanned without water, Fig.3 (5a). Each plastic type was put on a 1 mm thick, 75 mm by 26 mm, microscope slide of glass (4). The microplastic was evenly spread throughout the slide. Furthermore, the sample was placed under the microscope, connected to the spectroscope (1). In order to do an initial search for single particles, the sample was viewed using the Zeiss - 10x/0,25 microscope (3). When a particle was located, the lens was switched to a finer one, the Zeiss EC epiplan - 50x/0,75 (2). This lens was used to give a clear focus on one particle. The operators were manually zooming and adjusting the brightness of the view, eventually settling when the preview frame on the software appeared sharp. Nevertheless, the focus aspect of the high precision tool picturing the particle was solely to find particles instead of the space between them. The laser would reflect on the particles regardless of the focus.

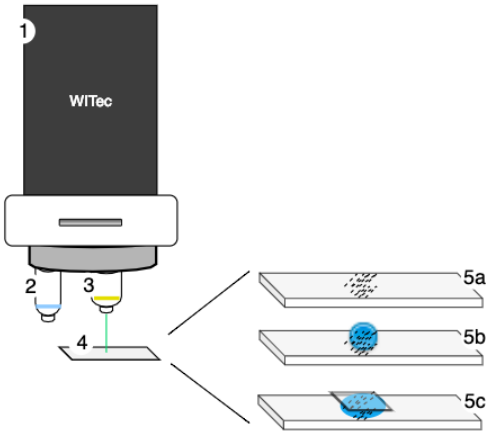

Fig. 3. Raman Spectroscopy, set-up. 1 is the WiTec Laser and Spectroscope, 2 is the ZeissEC epiplan 50x/0,75 microscope lens, 3 is the Zeiss 10x/0,25 microscope lens, 4 is the microscope slide carrying the sample, 5a,b,c is the three separate test cases.

In order to see if the resulting signatures were affected by particle size, the different sizes from the milling and sifting were scanned. However, as the PE samples acted abnormally relative to the other types and were ground, this type was not possible to pulverize into a size lower than 200 microns. As a result, the samples from the size category between 200 and 630 microns were tested first. The remaining size categories were then scanned and compared to the previous results.

Next, the same procedure was completed, but this time with water, Fig.3 (5b). Approximately 0.5 milliliters of distilled water was added to the sample. This was done using a pipette, placing the water as droplets on top of the sample before stirring the water and sample together. These samples were scanned as explained above.

However, because of the density and hydrophobic properties of the plastic, some particles tended to float. Since the experiments were conducted using reflection, the floating particles would not be measured as particles in water. In order to ensure water coverage, a 22x22mm top glass plate was added, bursting the water droplet and thereby forcing water in between plastic particles, Fig.3 (5c). These scans were also conducted the same way as previous scans.

In the latter case, it is essential to recognize that in order to reflect the plastic, the laser has to pass through the top glass twice. This makes conservation of purity critical concerning the top glass, as dirt or scratches could affect the transmittance of the laser. Therefore, the covering glass was thoroughly cleaned and repeatedly changed.

Finally, an empty sample containing the top glass and distilled water was scanned, both together and individually. These were retrieved so that they later could be extracted from the final signatures of the samples.

3.2.1 Data Analysis

Before conducting the analysis, dark noise was measured by having a sensor measure the signature without any light or laser. Subsequently, the acquired signature was extracted from each of the samples. Similarly, every signature being measured through water and a glass cover had the signature of the water and glass cover extracted from them. Due to the measurements being point-scans, variations in the measured signatures occurred. In order to make sure that the model was built on consistent signatures, these were chosen based on qualitative assessments by the authors. The dataset was then divided into one model-set, as the larger part of the initial dataset consisting chosen signatures, and two test-sets. The test-sets consisted of a set with data similar to the model-set, but randomly chosen samples, and one set with data from the measurements with water.

After cleaning the raw data, the analysis could begin. The software Unscrambler X, a commercial product designed for calibration of multivariate data, [17], was used to assist in interpreting the data. In order to recognize the plastic, each measured wavelength was assigned a variable. In order to be used in a partial least squares discriminant analysis (PLS-DA) model at a later stage, the samples were

subsequently classified based on their respective plastic type. The type would be the Y-variables with boolean values, while each measured wavelengths would be the X-variables with the measured intensity representing the values.

In order to dampen the noise of the measurements, while at the same time retaining characteristic peaks of the spectra, a Savitsky-Golay derivative transform was run on the dataset, [18]. The transform used the second derivative based on 13 data points. Thus, the first and last 13 measurements were lost. Losing 26 measurements per 1650 was deemed insignificant.

Following the transform, the PLS model was built based on the previously mentioned X- and Y-variables. The model was modified based on the residuals and influence of individual samples. Samples with high influence and residuals, i.e. influential and poorly described, were omitted. Due to the rather small sample size per plastic type, only samples with both high influence and residual were omitted.

Next, the dataset containing randomly chosen samples was transformed in the same manner and predicted based on the PLS model, leaving a PLS-DA. The factors chosen to predict the plastic types were chosen based on the loading of the factor. The loading line depicted the weight put on certain peaks and areas revealed which, compared to the absorption spectrum of water, made it possible to assess the possibility of utilizing the factor in situ. Even though the program itself recommended higher factors with lower deviation. The factors used to predict the plastic types were also based on the scatter plots depicting a high effect on a given plastic type. Subsequently, the factors with a high level of explaining would be emphasized in the process of predicting a given plastic type.

Also, given that the variables were either assigned 0 or 1, based on whether they belonged to a type or not, the cut-off rate would be 0,5. However, the model would still predict a correct plastic type with a clear margin, even when the sample would appear below the cut off rate. As all types had low levels of prediction, the lowered cut off rate was deemed justified.

4 Results

4.1 Qualitative Analysis (Signatures)

4.1.1 Varying Color

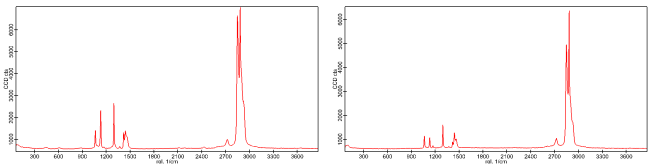

Fig. 4. HDPE gray (left), yellow (right), size between 200 and 630 micron

Fig. 4 presents two spectral signatures at different colors. However, the peaks appear to resemble each other at all associated wavelengths. Showing color-independent signatures.

4.1.2 Varying Size

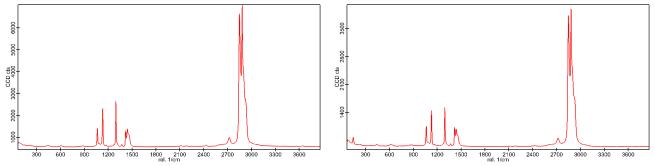

Fig. 5. HDPE size between 200 and 630 micron (left), HDPE size between more than 630 micron (right)

Fig. 5 presents two spectral signatures at different sizes. However, the peaks appears to be identical at all associated wavelengths.

4.1.3 Varying Condition

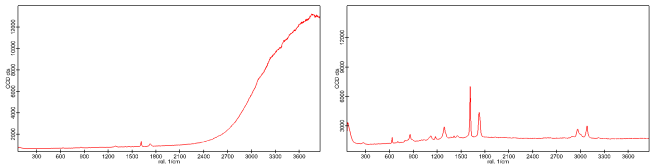

Fig. 6. PET flakes (left) vs PET pristine (right), size less than 200 micron

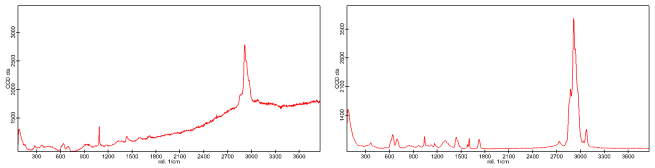

Fig. 7. PVC modified (left) vs PVC soft (right), size less than 200 micron

Fig. 6 reveals that PET at different conditions appears to have significant differences in their signatures. However, characteristic peaks are associated to similar wavelengths. Likewise for the PVC signatures in Fig. 7.

4.1.4 Water/No Water

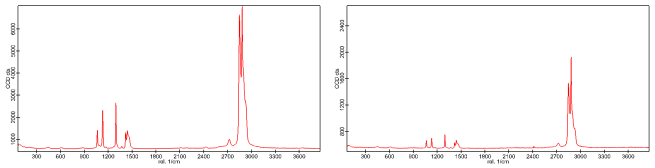

Fig. 8. HDPE without water (left), HDPE in water (right), size between 200 and 630 micron

Fig. 8 displays the signatures of HDPE in and out of water. The resemblance is strong. However, the intensity is, as expected, lower for HDPE in water.

4.1.5 *Varying Density*

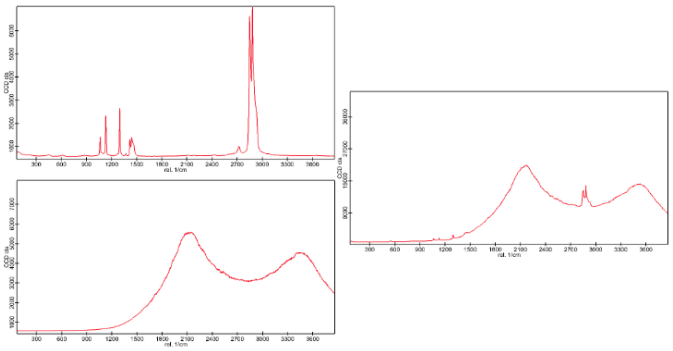

Fig. 9. HDPE (right and left top), LDPE (left bottom)

In Fig. 9, the HDPE on the right appears to resemble both HDPE and LDPE on the left.

4.1.6 *Plastic from Lofoten/Clean Dry Plastic*

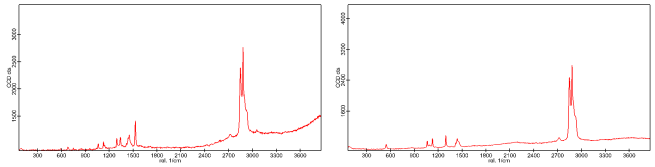

Fig. 10. A Lofoten collected plastic sample (left) that appears to resemble with the pure HDPE-samples

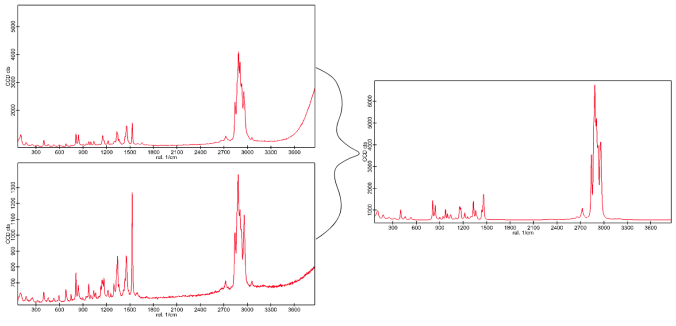

Fig. 11. Lofoten collected plastic samples (left top (10) and left bottom (5)) that appears to resemble with the pure PPpristine-samples (right)

Fig 10 presents the signature from a particle collected in Lofoten, which seems to resemble the pure signature for HDPE. Similar to the two plots on the left in Fig. 11 containing the spectral signatures from two particles collected at different places in Lofoten, resemble the pure signature for PP pristine.

4.2 Quantitative Analysis (PLS)

The model, based on known plastic, delivers loading plots represented by the plot presenting factor 1, displayed in Fig. 12, through the unscarmbler analysis. Comparing significant peaks in the plot with the optical signature of PET pristine - right plot in Fig. 6, the loading plot might indicate that facor 1 describes the specific plastic type of PET pristine. This procedure is completed for all factors (6 in total) and associated type of plastic.

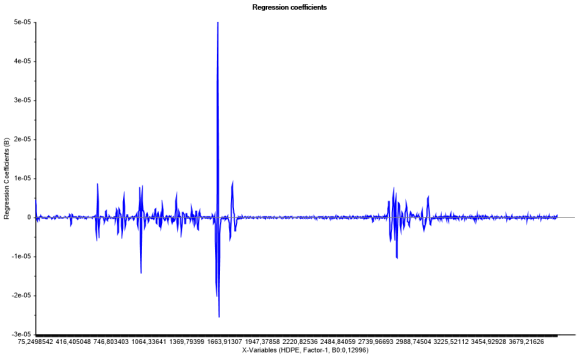

Fig. 12. Loading plot, factor-1

Moreover, the score-plots are viewed. From the score plot below, Fig. 13, the axis are chosen to be factor-1 and factor-2, respectively. It can be observed how the PET pristine (and PET-flakes with some deviation) type has a large variation in x, while PS pristine varies on the y-axis. PET pristine can thus be explained by factor-1 and so on - confirming the type description, based on factor, from the loading plots.

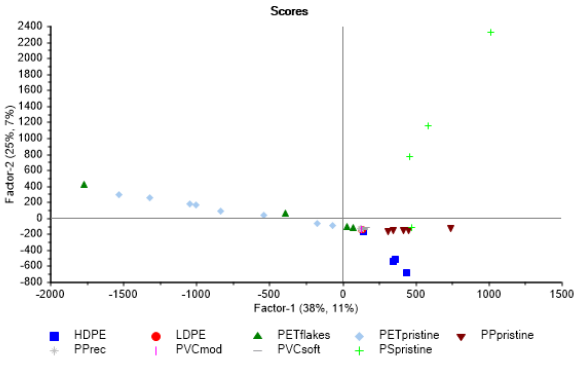

Fig. 13. Score plot, (factor-1,factor-2)

Three of the plastic types, PP rec, LDPE and PVC mod respectively, did not respond well to the modeling. These types did not give any variation within any of the factors. In the further prediction of new data, classifying these types is, hence, not realistic.

The first prediction is executed on a data set originating from the same samples used to create the model foundation. Viewing a representative prediction plot, Fig. 14, the same factors and associated plastic types, as learned from the scoring plot, were chosen (factor-2 with PS pristine).

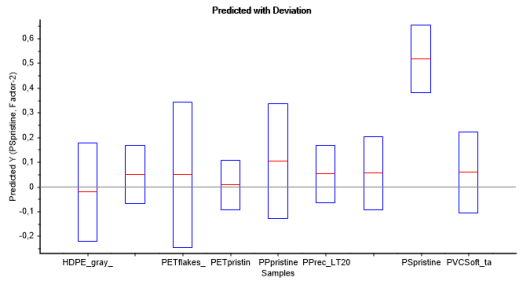

Fig. 14. Prediction plot, factor-2 with PS pristine

Fig. 14 shows a box plot prediction of PS pristine for samples representing all types of plastic included in the study. In the box plot, the sample acting as the most prominent, reflects the type predicted for. The height of the box, describes the variation. The result is a relatively superior prediction of the sample known to be PS pristine, as PS pristine. This with a factor prediction percentage of 0,5 and a relatively standard variation. This result represents the six remaining types.

Next, identical samples were tested, but this time in water. Fig. 15 is more or less representative for five of the previous six correctly classified types, them being PVC soft, PET pristine, PET flakes, HDPE and PS pristine.

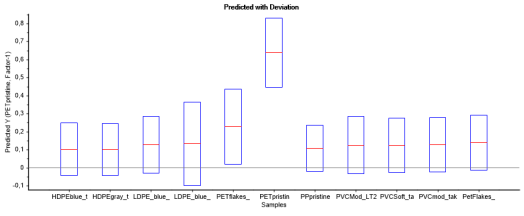

Fig. 15. Prediction plot, factor-1 with PET pristine in water

The plot above describes the prediction of PET pristine. All samples to be predicted are placed in water. In total, they represent all types of plastic included in the study. PET pristine in water-sample was successfully as PET pristine with a factor prediction percentage of 0,65.

Lastly, the plastic pieces from Lofoten were predicted, displayed in Fig. 16.

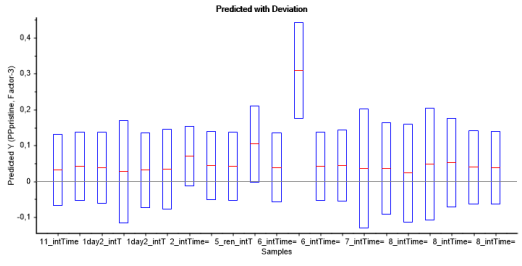

Fig. 16. Prediction plot, factor-3 with PP from the sea

Of the retrieved samples, Fig. 16 states that only one particle seems to consist of plastic, more specifically, PP pristine.

5 Discussion

From the results, there are especially a few attributes that need to be looked into. First, as plastic is known to come in a variety of sizes and colors, measurements of the different properties within the specific types, are completed. Regarding these results, one can discuss whether the properties affect the general optical signature for the given type. Furthermore, the samples studied are in different conditions. The section should include whether a general type-signature can endure such environmental impact. Moreover, in-situ resembling characteristics are applied. As the samples are tested in and out of water, the contributing differences should be elaborated, as well as the comparison of sea-influenced plastic debris versus pure plastics.

As for the mentioned properties, the size and color impact appears to be minimum. From the qualitative analysis, Fig. 4 reveals minor peak variation in wavelength positioning when comparing the signature from HDPE samples in gray and the corresponding signature for the yellow HDPE samples. Nevertheless, as same-type plastic at different sizes were equally classified, the analysis supports the assertion of color-independency. Similarly, the classification of same-type plastic at different sizes, showed an even lower variation in classifying the samples. This is also indicated in Fig. 5, revealing similar peaks at similar wavelengths. The signature from HDPE in water holds a lower intensity than the pure HDPE signature in air. This may be due to reduced intensity from attenuation by the water. For a quantitative verification from the model, Fig. 14, displaying the prediction of PS pristine, presents a representative result for six types, out of nine in total.

Looking at the results from plastics at various conditions, the trend is that most samples originating from the same type, yet holding distinct conditions, did not fully classify as the same type. An example can be found in the prediction plot in Fig. 15, predicting PET in water. The model manages to predict PET pristine with a factor prediction percentage of 0,65, while PET flakes only reached 0,25 in comparison. As the PET samples building the model is either PET pristine or PET flakes, one can argue that a data set including the variations of the two types, may succeed in classifying them as one, PET.

Looking at the spectral signatures in Fig. 6 and Fig. 7, displaying PET and PVC at different conditions, respectively, one can witness a resemblance. Comparing the associated signatures, significant peaks appear at the equivalent wavelength. This implies that the organic bonds within the plastic pieces are intact, again suggesting that the chemical structure of the piece might also be intact. Still, the shapes and intensities of the peaks are inconsistent, and the surrounding wavelengths carry a variety of signals detected by the CCD, leaving two different spectra.

This suggests that the industrial and environmental forces alter the chemical composition of the microplastic. The presumption can also be supported by the apparent change in signature based on density variations. Fig. 9

display the signatures of PE, the upper subplot show the signature of high-density PE, while the lower the signature of low-density PE. The middle plot, however, is also representing high-density PE, but seems to explain a hybrid of the two with important characteristics from them both. This is believed to be a result of the milling process of PE, carrying a risk of tearing and shredding the particles, rather than cleanly fragmenting them into fine particles. As a consequence of this, some high-density PE particles are assumed stretched, lowering the density of the particle and consequently adopting characteristics that indicate LDPE.

Earlier arguments supported the theory that the chemical composition of the microplastic did not change with color, size or condition. However, as this new observation shows that the peaks, associated with organic bonds, clearly differ with density, the earlier argument might no longer hold. One can hardly expect environmental forces to make clean milled-like breaks when tearing down the plastic pieces. If tear and wear from a coffee grinder can alter the chemical composition as much as the signature indicates, the strong forces of weather and oceans are believed to do the same. This may suggest that some environmentally affected microplastics may no longer be identifiable based on its spectral signature.

Studying the plots predicting samples with water, the prediction appears promising. Fig. 15 shows how the model predicts PET pristine in water as PET pristine, and thereby manages to classify the sample, despite possible disturbances from the water. As it turns out, this result is representative for five types out of the six types that were correctly classified for dry samples. Yet, additional test validation might be needed to verify the results from the samples containing water. This is due to the static properties of some types of plastic, making the plastic particles float on top of the water. If the laser focus was on these particles when measuring microplastics in water, the result may not represent microplastics in water. However, as several measurements were completed, at different sample areas for a variety of samples, the assumption of correct classification for plastic in water appears to hold.

Concerning the sea-influenced particles collected from Lofoten, the model appears to predict one of them as PP pristine, Fig. 16. Nonetheless, viewing the specific signatures, Fig. 11, a qualitative analysis may reveal that two particles, one collected at station 5 and one collected at station 10, resemble the spectral signature of PP pristine to a significant degree. Additionally, a particle retrieved from the station 6 collection, contains a signature matching the respective signature of HDPE as can be observed in Fig. 10. These results suggest plastic particles in 3 out of 17 collections in total. However, as the nature of the collected particles is unknown, the classification of the particles cannot be verified.

6 Conclusions

The results suggested that it is possible to recognize and classify some types of microplastics under water by identifying their spectral signatures, using Raman spectroscopy. Among the marine particles, three were identified as plastic. However, more research into how the effects of environmental changes affect the performance of the method is needed. Still leaving the mapping and classification method suitable for plastic that recently entered the ocean.

Acknowledgments

This work was supported by the Research Council of Norway through the Centres of Excellence funding scheme, Project number 223254 – AMOS. The authors wish to thank Prof. Geir Johnsen for providing useful information. A great appreciation is also directed towards the SINTEF team for assisting with great expertise - a special thanks to Julia Farkas for loaning us her manta net. Last, Postdoctoral Fellow, Bartlomiej Gawel, has providing necessary support at the laboratory. The authors are sincerely grateful.

References

[1] R. Geyer, J. R. Jambeck, and K. L. Law, "Production, use, and fate of all plastics ever made," *Science Advances*, vol. 3, no. 7, 2017.
[2] W. A. Protection, "How plastic pollution is affecting seals and other marine life," 2017.
[3] Y. Mato, T. Isobe, H. Takada, H. Kanehiro, C. Ohtake, and T. Kaminuma, "Plastic resin pellets as a transport medium for toxic chemicals in the marine environment," *Environmental Science & Technology*, vol. 35, no. 2, pp. 318–324, 2001.
[4] C. D. Rummel, A. Jahnke, E. Gorokhova, D. Kühnel, and M. Schmitt-Jansen, "Impacts of biofilm formation on the fate and potential effects of microplastic in the aquatic environment," *Environmental Science & Technology Letters*, vol. 4, no. 7, pp. 258–267, 2017.
[5] F. Gallo, C. Fossi, R. Weber, D. Santillo, J. Sousa, I. Ingram, A. Nadal, and D. Romano, "Marine litter plastics and microplastics and their toxic chemicals components: the need for urgent preventive measures," *Environmental sciences Europe*, vol. 30, no. 1, p. 13, 2018.
[6] W. D. Callister and D. G. Rethwisch, *Polymer Structures*, ch. 14, pp. 532 – 626. John Wiley & Sons, Inc, 10th ed., 2018.
[7] M. Inagaki and F. Kang, *Raman Spectroscopy*, ch. 7, pp. 125 – 152. Butterworth-Heinemann, 2016.
[8] V. Allen, J. H. Kalivas, and R. G. Rodriguez, "Post-consumer plastic identification using raman spectroscopy," *Appl. Spectrosc.*, vol. 53, pp. 672–681, Jun 1999.
[9] R. Lenz, K. Enders, C. A. Stedmon, D. M. Mackenzie, and T. G. Nielsen, "A critical assessment of visual identification of marine microplastic using Raman spectroscopy for analysis improvement," *Marine Pollution Bulletin*, vol. 100, pp. 82–91, nov 2015.
[10] C. F. Araujo, M. M. Nolasco, A. M. Ribeiro, and P. J. Ribeiro-Claro, "Identification of microplastics using raman spectroscopy: Latest developments and future prospects," *Water Research*, vol. 142, pp. 426 – 440, 2018.
[11] Y. B. Band and Y. Avishai, *Approximation Methods*, ch. 7, pp. 303 – 366. Academic Press, 2013.
[12] A. Yamashita, M. Fujii, and T. Kaneko, "Color registration of underwater images for underwater sensing with consideration of light attenuation," *Proceedings - IEEE International Conference on Robotics and Automation*, no. April, pp. 4570–4575, 2007.
[13] N. Jerlov, ed., *Chapter 3 Beam Attenuation*, vol. 14 of *Elsevier Oceanography Series*, ch. 3, pp. 47 – 66. Elsevier, 1976.
[14] A. J. Sørensen, "Lecture notes, tmr4240: Control lecture navigation and payload sensors, NTNU, fall 2018," 2018. Accessed: 2018-11-03.
[15] Carat GmbH, "CARAT Control and Research Analysis Thermoplastics," 2019.
[16] WITec GmbH, "Alpha00 R - Confocal Raman Imaging," 2019.
[17] CAMO Analytics, "Unscrambler x," 2019.
[18] A. Savitzky and M. J. E. Golay, "Smoothing and differentiation of data by simplified least squares procedures.," *Analytical Chemistry*, vol. 36, no. 8, pp. 1627–1639, 1964.

9.2 Additional Work and Expanding Description

Pre-processing of the data and manual control of the results was completed. Here complementing the paper, Paper II.

9.2.1 Extension of the Data Cleaning Process

In addition to locating outliers, and subsequently analyze and remove them accordingly, the Raman data were scaled. Viewing the intensities of the separate types, Figure 9.2.1, this seemed necessary, as large variation in intensity occurs across types. The top plot in Figure 9.2.2 also shows how the signatures of some samples could dominate. PET flakes is the type responsible for the intense spectrum. The signature has intensive peaks, reaching towards 60.000 - see Figure 9.2.9. This was characteristic for many PET flakes measurements. As can be viewed in all box-plots in Paper II, this sample, therefore, holds a notable variation. The challenge was then to lower the noise of the measurements, while at the same time retaining characteristic peaks of the spectra. After trying out a few scaling algorithms, the sense behind a derivative filter came to mind. Savitsky-Golay derivative transform filter with a second derivative was, consequently, applied. The resulting signatures can be viewed in the bottom plot in Figure 9.2.2

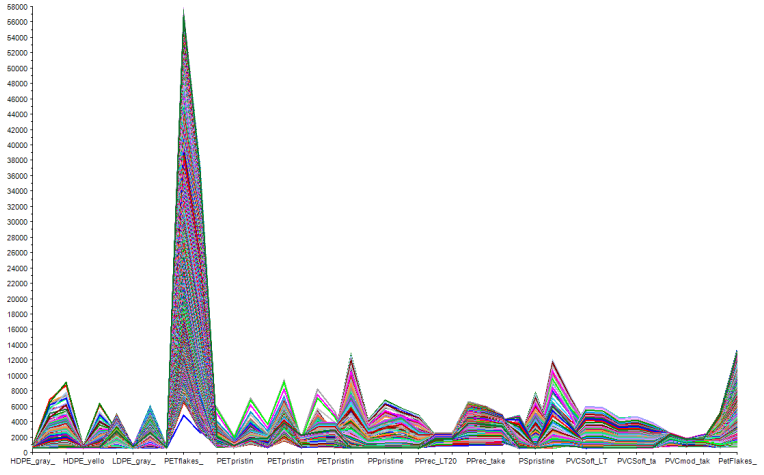

Figure 9.2.1: Intensities — Prior to Scaling

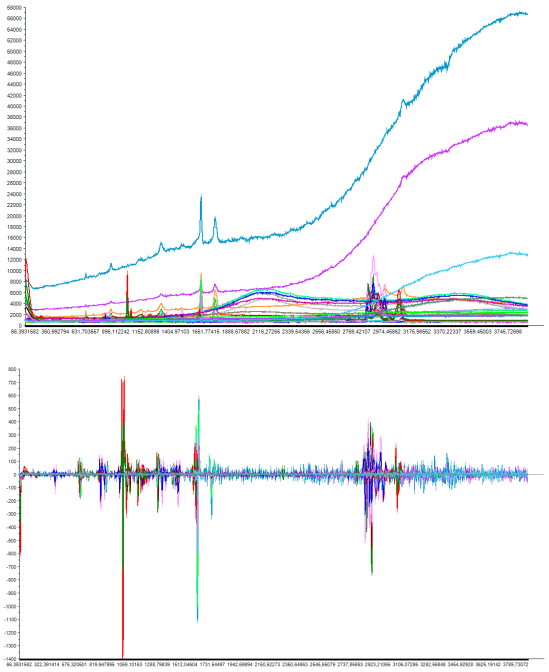

Figure 9.2.2: All signatures in the interval of up to 3800 [1/cm], unfiltered (top), filtered and scaled (bottom)

9.2.2 Choosing a Representative Frequency Interval

The results presented in the paper, suggest that the signature of plastics across conditions, even if originating from the same type, are too different to classify them as one. However, viewing and comparing the specific signatures, similarities can be found. The wavelengths corresponding to characteristic peaks, appear to lie in the intervals 800-1800 and 2700-3300 [1/cm] (these intervals are supported by Figure 5.3.1, defining peaks at specific wavelengths related to specific bonds in the molecules). A quick comparison of a smaller part of the resulting plots with literature plots illustrated in Figure 9.2.3, might expose a possible fingerprint within this range.

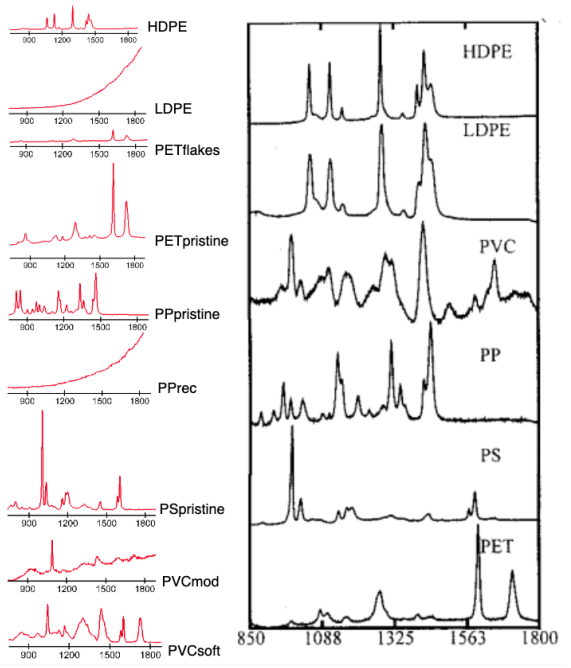

Figure 9.2.3: Comparing signatures with literature

However, the peaks in the latter interval tend to hold significantly higher intensities, possibly outweighing the lower interval. This means that if the lower interval consists of signatures able to distinguish the type of plastic, important information might be undermined and the spectral fingerprint not recognizable.

Based on this observation, another analysis was run. This analysis was completed with a reduced interval of wavelength, displayed in Figure 9.2.4. Apart from altering the dataset, using frequencies spanning only 800-1800 [1/cm], the procedure was the same as before. Regardless, the results of this analysis did not change the initial conclusion, rather reassured it.

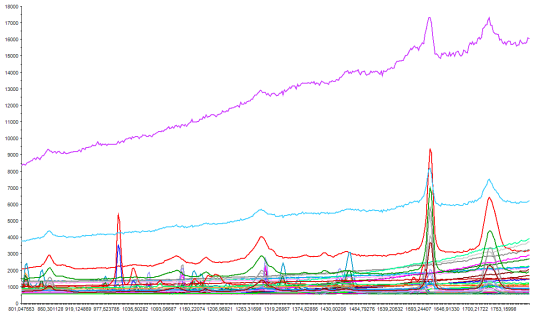

Figure 9.2.4: All signatures, 800-1800 [1/cm] interval

9.2.3 Manual Control of Signatures

The spectral signatures were controlled and verified in two ways. First, the signatures were compared to literature as presented above, Figure 9.2.3. All types seem to have a least one sub-type

(specific condition) with a signature close to the spectral signatures plotted to the right. However, a few types appears to deviate significantly. These are LDPE and PP recycled to a large degree, and PET flakes and PVC modified to a certain degree.

Moreover, the specific peaks within the signatures were compared to their related bonds 5.3.1. Section 2.1.2, describes the bonds of specific plastic types. PE, with double carbon bonds as well as carbon-hydrogen bonds, is expected to have peaks at 1060 and 1127 [1/cm], as well as at 2845 and 2880 [1/cm]. Looking at Figure 9.2.5, this seems accurate for the upper figure, HDPE. The signature representing LDPE however, hold peaks at more or less opposite positions.

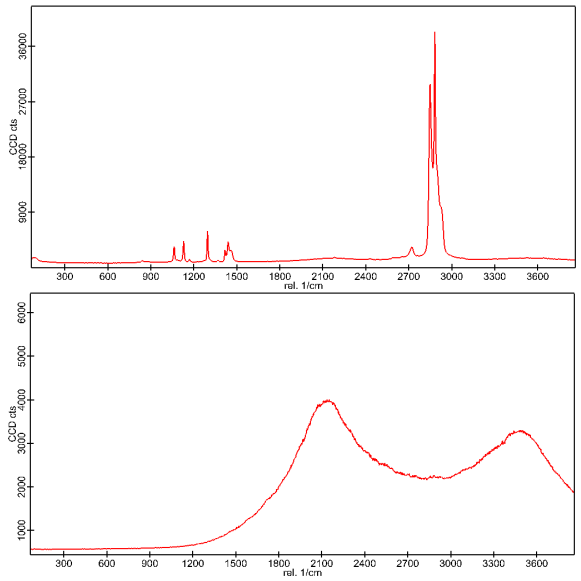

Figure 9.2.5: HDPE (top), LDPE (bottom)

Moreover, PP is exclusively consistent of CH_3 molecules, pointing towards significant peaks at 2870 and 2905 [1/cm]. Figure 9.2.6 displays the plotted signatures of PP pristine (left) and PP recycled (right). Unlike PE, the signature does not have carbon-carbon bonds, and the significant peak should be located in the specified area. Looking at PP recycled in the bottom plot, the trend appears similar to PE, with an unfamiliar, unexplainable signature.

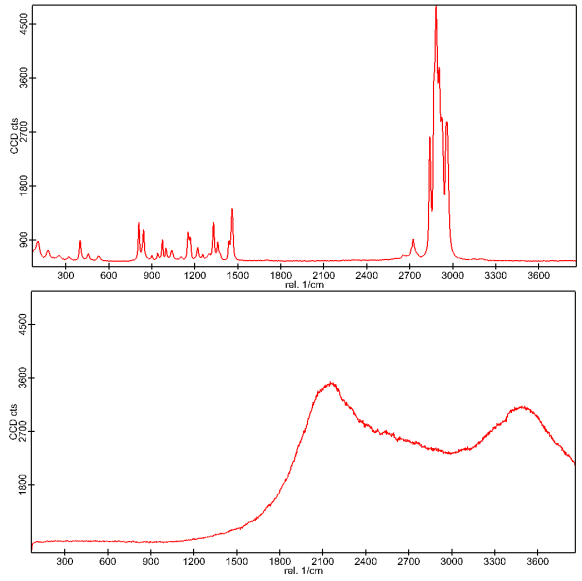

Figure 9.2.6: PP pristine (top), PP recycled (bottom)

PS holds a chemical composition consisting of the following molecules, C_8H_8. The focus should, hence, be at carbon-carbon bonds, as well as carbon-hydrogen bonds. Looking at the table in Figure 5.3.1, these bonds correspond to somewhere between 700 and 1260 [1/cm] (C-C), and at 2900, 3015, 3065 and 3280-3340 [1/cm]. Based on this, it appears likely that the signature in Figure 9.2.7, is the correct signature for PS.

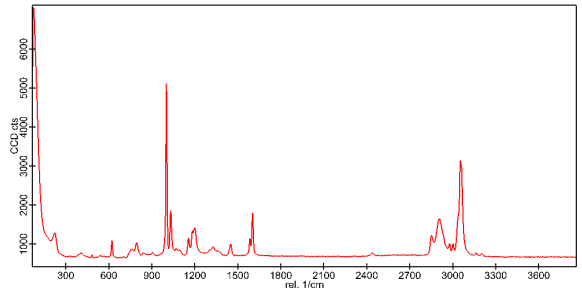

Figure 9.2.7: PS pristine

PVC consists of molecules subsequently consistent with carbon bonds, hydrogen bonds and chlorine atoms. It appears that chlorine atoms do not have a significant impact on the peaks within this range. The focus is hence on carbon-carbon bonds, as well as carbon-hydrogen bonds. Therefore, the relations found for PS apply to PVC as well. Looking at Figure 9.2.8, the peaks are positioned at almost identical wavelengths as for PS.

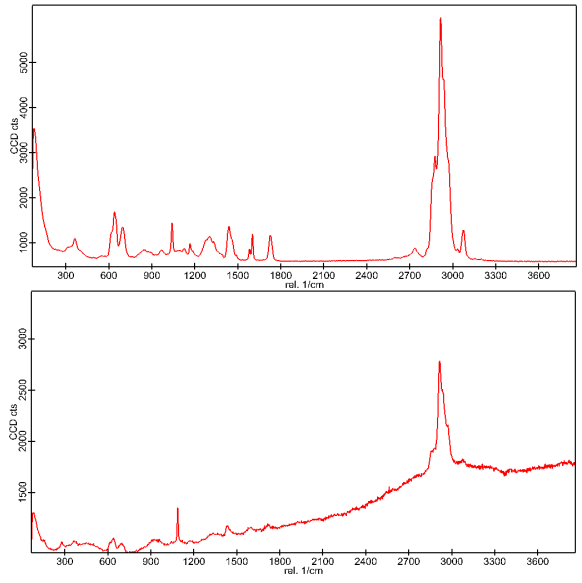

Figure 9.2.8: PVC soft (top), PVC modified (bottom)

PET, however, has a chemical composition represented by $(C_{10}H_8O_4)_n$. According to the table, carbon-oxygen bonds give rise to peaks at a different wavelength than the rest of the types. These peaks are found at 1620-1690 and 1710-1745 [1/cm] - quite accurate when looking at the representing signatures below, Figure 9.2.9.

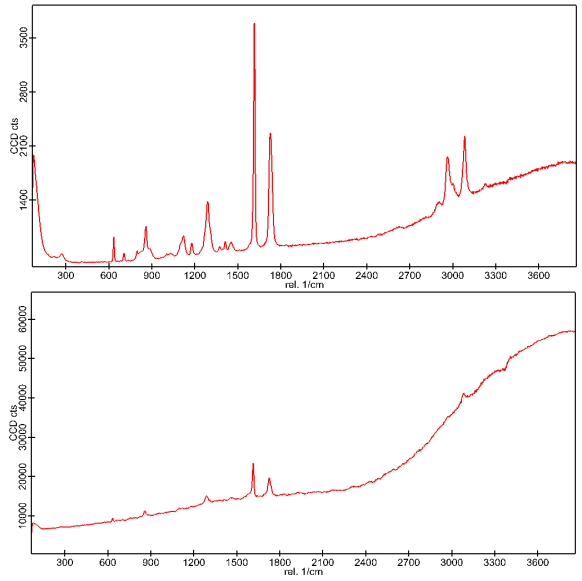

Figure 9.2.9: PET pristine (top), PET flakes (bottom)

In sum, HDPE, PET pristine, PP pristine, PS pristine and PVC soft seem to hold accurate signatures. PET flakes appear to resemble by trends. These short analyses correspond to the types that were classified by the model. Thus, some types or some measurements within LDPE, PP recycled and PVC modified, on the other hand, may be incorrect or holding such a considerable variation across the samples that the pattern is absent and, consequently, challenging to describe by the factors in PLS regression.

Chapter 10

Paper Comparison and Extended Discussion

The following chapter will summarize and compare the conclusions made by the scientific papers, which make up the backbone of this thesis. Also, extended results and methods will be included in the comparisons. The final goal is to assess whether the two are complementary and may be combined to achieve a general conclusion on the identity of the plastic collected in Lofoten.

10.1 Results & Discussion

The following paragraphs are the summarized results and discussion of their extended methods of the two papers.

10.1.1 I: Identification of Marine Plastics using Hyperspectral Imaging in Infrared Light

The results from the NIR hyperspectral imaging illustrates an indication for four of the collected plastic samples. These were respectively sample 2 as PP, sample 10 as PE, sample 11 as PP, and sample 14 as PP. In total, four samples have been identified as plastic with a relatively high margin of certainty. Other samples showed indications, but were emitted due to the lack of certainty. All samples were also classified based on the results of the individual imaging method.

The use of PCA and PLS-DA was proven unsuccessful when applied to the NIR hyperspectral images. Dry plastics were correctly classified. Nevertheless, none of the other samples were successfully classified. The reason might be the large difference between the samples due to thickness and focus, or the more drastic effect of water on the infrared spectra. The latter might cause larger trends of the spectra to be difficult to attain.

K-means based algorithms proved to be the most successful. However, the need for manual merging is problematic. In order to use the ground-truthed K-means algorithms, which solves the issue of

K-means being unsupervised, one will have to process the data manually. This is, in turn, not viable. The use of a supervised algorithm in combination could be a possible solution. Still, this must be a more refined classification than presented in the paper. The combined algorithm did not correctly classify particles, in contrast to the use of ground truthing.

10.1.2 II: Identification of Marine Plastics using Raman Spectroscopy

Through the use of Raman spectroscopy, three plastic samples were identified to be plastic and showed indications of their respective types. Of the three, one was classified using PLS-DA while the other two used qualitative classification. These three were respectively sample 5 as PP via PLS-DA, and sample 10 as PP and sample 6 as HDPE via qualitative classification. In total, three samples identified as plastic with a relatively high margin of certainty. Other samples, showed indications, but were emitted due to the lack of certainty.

Despite only classifying one sample from Lofoten, PLS-DA still proved successful. The method managed to classify the samples in water and consequently performed satisfactorily at this stage. The exact reasons for not identifying a larger number of samples are unknown. One explanation could be the change in the plastic due to the environmental impact from the sea. Also, given the nature of the collected data, PCA and PLS-DA was by far the superior choice.

10.2 Comparison

PLS-DA proved unsuccessful in NIR HI, despite being used with the data collected using Raman spectroscopy. This could be due to the nature of Raman signatures. It is less affected by glass and water and subsequently more consistent. Also, the essence of the data is different. The Raman signatures are collected individually, and thus being continuously double checked. The result was purer signatures and subsequently, less faulty data. The same followed from the single scans being individually chosen, and, therefore, not affected by falsely classified data. The latter was an issue with respect to HI. The large volume of background and varying focus could have affected the results. However, this measure will be made beforehand with respect to the building of the model. Subsequently, it is hard to rule out the use of PCA/PLS-DA as it could be argued that the fault lies in the model, and its data, rather than the method, and subsequent, the results.

Not much is preventing the implementation of the same methods used in Paper I, in the Raman spectroscopy experiment (Paper II). However, the scan size is increased if one is to do a full image using Raman. Transmittance was specifically chosen as it would circumvent the need to localize individual particles and reduce manual labor. However, the reasoning did not withhold in reality. Subsequently, one could fully combine the two using reflectance Raman spectroscopy and the algorithms from HI.

Due to the nature of the prediction algorithms used on the hyperspectral images, the level of certainty is not quantified in the HI classification. The lack of a clear measure makes it difficult to rule on contradicting predictions. One could argue that the size of clusters relative to the sample size in K-means, and angles in SAM, could be used. However, the algorithms utilized at this stage of the project did not include these. For further use and sensor merging, this would be an essential

feature.

The difference in results between the Raman spectroscopy and hyperspectral imaging, resulted in a re-evaluation of the results from sample 10. As may be seen in the extended results, in Figure 8.2.6, the revised results from hyperspectral imaging indicate that the sample might be PP. This corresponds well with the Raman results. However, the Raman results are unambiguous. The latter only indicates the sample being PP. Hence, there is a strong indication that the sample is indeed PP given the exclusion of PE from the Raman results. One could still argue that the SAM - K-means algorithm also had indications of PE. Nevertheless, SAM has previously proven to underperform, as may be seen in the results from sample 2 in figure 8.2.7a. Thus, sample 10 is believed to be PP rather than PE.

Both methods show size and color independent signatures, as expected. This proves the particles could be classified based on endmember signatures from consumer plastic. On the other hand, it is important to keep in mind that this project has tested a limited number of samples. One should acquire a more extensive endmember library using more likely plastics to be found in the ocean. This would also account for any other additives. This need is apparent when observing the different spectra of PP and PVC.

Given the limited results on samples collected in-situ, the superior algorithm is hard to determine. One could decide based on the results from the classification through water. Nevertheless, due to the different nature of the measurements, the results would not be directly comparable. Raman spectroscopy is less affected by the presence of water than the NIR-HI. Hence, it is hard to determine the most successful algorithm, which coincides with the varying preferences in the HI community.

Chapter 11

Conclusion and Further Work

11.1 Overall Conclusion

Now, at the end of this report, the research question asked at the beginning, *Is it possible to identify plastics in various sizes and in various conditions, underwater, using a hyperspectral imager in infrared light or the Raman spectroscopy?*, can be answered.

In conclusion, the plastic was classified independent of size, color and condition, by both imaging techniques. The two methods combined were able to detect 7 marine plastic particles. These were not only identified as plastic, but also as individual types. The exact choice of the preferred classification algorithm and imaging technique is undecided. With certain refinements, both methods are believed to have great potential for in situ use, individually and combined. Lastly, further work to improve the algorithms and methods of classification is recommended.

11.2 Further Work

The path to a functioning in-situ solution is comprehensive. This thesis is merely the beginning of a larger research process. This section, therefore, addresses the primary lines and key challenges along the way. It is intended to summarize the obstacles and necessary improvements, with respect to the two imaging techniques, identified throughout the work.

The road ahead can be divided into different areas of significance. A vast challenge when operating in-situ is the water mass, water quality and additional disturbances underwater, not accounted for. Moreover, optical restrictions may not cooperate with the underwater conditions, nor the available density of plastic particles. Finally, the plastic identification of the technologies and methods might deviate underwater.

11.2.1 Sampling

In this study, the water between the sample and lens is of millimeter size. In addition, the remaining surroundings have all consisted of air. A natural, and necessary next step would be to study a more considerable amount of water. For instance, a tank of water filled with plastic particles. Besides, rather than sterilized water, the tank could consist of sea water. This would account for the possible effects of salinity and other contaminants affecting the light, and subsequent image quality, as discussed in Chapter 2.

The research was done using portions of pulverized plastic particles. In situ, these particles are rarely clustered to the size of the experimental portion. The further process would, therefore, naturally include the use of a lower particle-amount, within the sample, when completing the measurements.

A set-up including a more humble particle-amount in a wider space of water is moving towards in situ resemblance. Using this approach, the experiment is forced to resemble reality. However, it is suggested to, simultaneously, work on getting the reality to resemble the experiment. This can be done by designing a sensor-carrying platform that can collect pulp from the water, filtering out the water, before performing measurements on the remaining mass. The mass thus contains, most likely, more plastic pieces than at the initial state.

Entering the topic of designing the sensor, optical challenges emerge. The hyperspectral imager utilizes a push broom technique. As explained in Section 5.2.2, this technique requires movement of the imager at an exact and kept velocity. Wind and underwater currents can, hence, have fatal consequences for this necessity. A thought for further research is thus to look at the possibility of designing a conduit that the water can flow through. This cable can have a turbine (or similar) at one end and thereby, positively or negatively, accelerate the water. This way the velocity can be adapted to the desired imager flow rate.

Point-scanning (Section 5.2.1), performed when completing the Raman measurements, is highly sensitive, as it requires the entire scenery to hold still throughout the entire processing time. Focusing on one specific particle over time can, therefore, seem unlikely. Further work should, therefore, include line-scanning of the Raman samples, possibly using a similar push broom technique as the hyperspectral imager.

Lastly, if the methods (Raman and NIR HI), single-handedly, do not hold up, an idea could be to combine them. When initiating this study, the plan was to combine the size and shape identification from the SilCam with man-made color-detection in the hyperspectral imager in visible light. As the infrared radiation made the plastic samples detectable to the hyperspectral imager, this became the focus. However, combining methods to retrieve more information appears even more productive and should be approached within the next steps - especially if using one of the strengthened methods from this study.

11.2.2 Data Processing

Concerning the classification algorithms, SAM and K-means, certain improvements are believed to be needed. These are specifically related to the introduction of a *Not-Applicable* class. Due to the nature of both classifications algorithms, all samples will be classified regardless of the distance to the given class as long as its the closest class. By introducing a maximum distance or angle, one could rely on the results having a base accuracy to them.

Furthermore, a quantitative measure of accuracy would make it easier to compare contradicting results. Given contradicting results, one has no way to compare the predictions directly. A measure would make the ruling easier as it would describe a level of certainty.

Given the previously explained nature of the work, the measurements were not made with the use of SAM in mind. Hence, one would expect there to be room for improvement with regards to the endmember signatures. Not only with respect to the specific measurements, but also to the signatures. The measured samples could be ensured to have more consistent layers and a higher degree of even focus. Also, the types of plastics creating the endmember signatures could include known post-consumer plastic, which could possibly cover the effects of contaminants and other effects not included in the clinically ordered post-consumer plastic.

On the last note, the primary focus in this thesis involves separating the plastic types from each other. However, in the long run, it is essential rather to be able to separate plastic from other organic material. This study has slightly entered the field, which, in further work, should be a more prominent focus - possibly the main focus. A recommendation for further action is hence to alter focus and look at plastic in its entirety, up against marine snow, algae, and other organic material.

Bibliography

F. Adar. Introduction to interpretation of raman spectra using database searching and functional group detection and identification. *Spectroscopy*, 31(7):16–23, 2016.

V. Allen, J. H. Kalivas, and R. G. Rodriguez. Post-consumer plastic identification using raman spectroscopy. *Appl. Spectrosc.*, 53(6):672–681, Jun 1999. URL `http://as.osa.org/abstract.cfm?URI=as-53-6-672`.

C. Arthur, J. E. Baker, and H. A. Bamford. Proceedings of the International Research Workshop on the Occurrence, Effects, and Fate of Microplastic Marine Debris. NOAA technical memorandum NOS-OR&R 30, 2009.

Y. B. Band and Y. Avishai. *Approximation Methods*, chapter 7, pages 303 – 366. Academic Press, 2013. ISBN 978-0-444-53786-7. doi: https://doi.org/10.1016/B978-0-444-53786-7.00007-1. URL `http://www.sciencedirect.com/science/article/pii/B9780444537867000071`.

Y. M. Bar-On, R. Phillips, and R. Milo. The biomass distribution on Earth. *Proceedings of the National Academy of Sciences of the United States of America*, 115(25):6506–6511, 6 2018. ISSN 1091-6490. doi: 10.1073/pnas.1711842115. URL `http://www.ncbi.nlm.nih.gov/pubmed/29784790http://www.pubmedcentral.nih.gov/articlerender.fcgi?artid=PMC6016768`.

A. M. Booth, S. Kubowicz, C. Beegle-Krause, J. Skancke, T. Nordam, E. Landsem, M. Throne-Holst, and S. Jahren. Microplastic in global and Norwegian marine environments: Distributions, degradation mechanisms and transport. *Miljødirektoratet.no*, M-918(April):1–147, 2018.

M. A. Browne, T. Galloway, and R. Thompson. Microplastic—an emerging contaminant of potential concern? *Integrated Environmental Assessment and Management*, 3(4):559–561, 2007. doi: 10.1002/ieam.5630030412. URL `https://setac.onlinelibrary.wiley.com/doi/abs/10.1002/ieam.5630030412`.

S. C. Epstein, A. R. Huff, E. S. Winesett, C. Londergan, and L. Charkoudian. Tracking carrier protein motions with raman spectroscopy. *Nature Communications*, 10, Dec 2019. doi: 10.1038/s41467-019-10184-2.

W. D. Callister and D. G. Rethwisch. *Polymer Structures*, chapter 14, pages 532 – 626. John Wiley & Sons, Inc, 10th edition, 2018.

CAMOAnalytics. Unscrambler x, 2019.

M. Chaplin. Water absorption spectrum. *London South Bank University*, 10(7):241–264, Oct 2018. doi: 10.9737/hist.2018.658. URL `http://www1.lsbu.ac.uk/water/water_vibrational_spectrum.html`.

I. Dumke, A. Purser, Y. Marcon, S. M. Nornes, G. Johnsen, M. Ludvigsen, and F. Søreide. Underwater hyperspectral imaging as an in situ taxonomic tool for deep-sea megafauna. *Scientific Reports*, 2018. ISSN 20452322. doi: 10.1038/s41598-018-31261-4.

F. Gallo, C. Fossi, R. Weber, D. Santillo, J. Sousa, I. Ingram, A. Nadal, and D. Romano. Marine litter plastics and microplastics and their toxic chemicals components: the need for urgent preventive measures. *Environmental sciences Europe*, 30(1):13, 2018. ISSN 2190-4707. doi: 10.1186/s12302-018-0139-z. URL https://www.ncbi.nlm.nih.gov/pubmed/29721401.

P. L. M. Geladi, H. F. Grahn, and J. E. Burger. *Multivariate Images, Hyperspectral Imaging: Background and Equipment*, chapter 1, pages 1–15. John Wiley Sons, Ltd, 2007. ISBN 9780470010884. doi: 10.1002/9780470010884.ch1. URL https://onlinelibrary.wiley.com/doi/abs/10.1002/9780470010884.ch1.

GESAMP. Sources, fate and effects of microplastics in the marine environment: a global assessment. (90):96, 2015. ISSN 1020–4873. URL www.imo.orghttp://ec.europa.eu/environment/marine/good-environmental-status/descriptor-10/pdf/GESAMP_microplasticsfullstudy.pdf.

R. Geyer, J. R. Jambeck, and K. L. Law. Production, use, and fate of all plastics ever made. *Science Advances*, 3(7), 2017. doi: 10.1126/sciadv.1700782. URL https://advances.sciencemag.org/content/3/7/e1700782.

M. Graña and M. A. Veganzones. An endmember-based distance for content based hyperspectral image retrieval. *Pattern Recognition*, 45(9):3472–3489, 2012. ISSN 00313203. doi: 10.1016/j.patcog.2012.03.015.

A. A. Green, M. Berman, P. Switzer, and M. D. Craig. A transformation for ordering multispectral data in terms of image quality with implications for noise removal. *IEEE Transactions on Geoscience and Remote Sensing*, 26(1):65–74, Jan, 1988. ISSN 0196-2892. doi: 10.1109/36.3001.

L. Gulick, C. Saby, H. Morjani, and A. Beljebbar. Age-related changes in molecular organization of type i collagen in tendon as probed by polarized shg and raman microspectroscopy. *Scientific Reports*, 9, May 2019. ISSN 2045-2322. doi: 10.1038/s41598-019-43636-2.

N. B. Hartmann, S. Rist, J. Bodin, L. H. S. Jensen, S. N. Schmidt, P. Mayer, A. Meibom, and A. Baun. Microplastics as vectors for environmental contaminants: Exploring sorption, desorption, and transfer to biota. *Integrated Environmental Assessment and Management*, 13(3):488–493, 2017. doi: 10.1002/ieam.1904. URL https://setac.onlinelibrary.wiley.com/doi/abs/10.1002/ieam.1904.

N. Hussain, V. Jaitley, and A. T. Florence. Recent advances in the understanding of uptake of microparticulates across the gastrointestinal lymphatics. *Advanced Drug Delivery Reviews*, 50 (1-2):107–142, 8 2001. ISSN 0169-409X. doi: 10.1016/S0169-409X(01)00152-1. URL https://www.sciencedirect.com/science/article/pii/S0169409X01001521?via/3Dihub.

M. Inagaki and F. Kang. *Raman Spectroscopy*, chapter 7, pages 125 – 152. Butterworth-Heinemann, 2016. ISBN 978-0-12-805256-3. doi: https://doi.org/10.1016/B978-0-12-805256-3.00007-6. URL http://www.sciencedirect.com/science/article/pii/B9780128052563000076.

J. R. Jambeck, R. Geyer, C. Wilcox, T. R. Siegler, M. Perryman, A. Andrady, R. Narayan, and K. L. Law. Plastic waste inputs from land into the ocean. *Science*, 347(6223):768–771, 2015. ISSN

0036-8075. doi: 10.1126/science.1260352. URL https://science.sciencemag.org/content/347/6223/768.

D. H. T. T. R. James, Garethand Witten. *Unsupervised Learning*, chapter 10, pages 373–418. Springer New York, New York, NY, 2013a. ISBN 978-1-4614-7138-7. doi: 10.1007/978-1-4614-7138-7_10. URL https://doi.org/10.1007/978-1-4614-7138-7_10.

D. H. T. T. R. James, Garethand Witten. *Classification*, chapter 4, pages 127–174. Springer New York, New York, NY, 2013b. ISBN 978-1-4614-7138-7. doi: 10.1007/978-1-4614-7138-7_10. URL https://doi.org/10.1007/978-1-4614-7138-7_10.

G. Johnsen, Z. Volent, H. Dierssen, R. Pettersen, M. Ardelan, F. Søreide, P. Fearns, M. Ludvigsen, and M. Moline. *Underwater hyperspectral imagery to create biogeochemical maps of seafloor properties*, chapter 20, pages 508 – 540e. Woodhead Publishing Series in Electronic and Optical Materials. Woodhead Publishing, 2013. ISBN 978-0-85709-341-7. doi: https://doi.org/10.1533/9780857093523.3.508. URL http://www.sciencedirect.com/science/article/pii/B9780857093417500200.

G. Johnsen, M. Ludvigsen, A. Sørensen, and L. M. Sandvik Aas. The use of underwater hyperspectral imaging deployed on remotely operated vehicles - methods and applications. *IFAC-PapersOnLine*, 2016a. ISSN 24058963. doi: 10.1016/j.ifacol.2016.10.451.

G. Johnsen, M. Ludvigsen, A. Sørensen, and L. M. S. Aas. The use of underwater hyperspectral imaging deployed on remotely operated vehicles - methods and applications. *IFAC-PapersOnLine*, 49(23):476 – 481, 2016b. ISSN 2405-8963. doi: https://doi.org/10.1016/j.ifacol.2016.10.451. URL http://www.sciencedirect.com/science/article/pii/S2405896316320390. 10th IFAC Conference on Control Applications in Marine SystemsCAMS 2016.

T. Johnson. Most common plastics. Apr 2017. URL https://www.thoughtco.com/most-common-plastics-820351.

T. M. Karlsson, H. Grahn, B. Van Bavel, and P. Geladi. Hyperspectral imaging and data analysis for detecting and determining plastic contamination in seawater filtrates. *Journal of Near Infrared Spectroscopy*, 24(2):141–149, 2016. ISSN 17516552. doi: 10.1255/jnirs.1212.

Kebes. Absorption spectrum of liquid water. *Wikimedia*, Jan 2016. URL https://commons.wikimedia.org/wiki/File:Absorption_spectrum_of_liquid_water.png.

N. Keshava and J. F. Mustard. Spectral unmixing. *IEEE Signal Processing Magazine*, 19(1):44–57, 2002. ISSN 1053-5888 VO - 19. doi: 10.1109/79.974727.

R. Lampitt. *Marine Snow*, pages 160 – 169. Academic Press, Oxford, 3 edition, 2001. ISBN 978-0-12-813082-7. doi: https://doi.org/10.1016/B978-0-12-813081-0.00218-4. URL http://www.sciencedirect.com/science/article/pii/B9780128130810002184.

R. Lenz, K. Enders, C. A. Stedmon, D. M. Mackenzie, and T. G. Nielsen. A critical assessment of visual identification of marine microplastic using Raman spectroscopy for analysis improvement. *Marine Pollution Bulletin*, 100(1):82–91, nov 2015. ISSN 0025-326X. doi: 10.1016/J.MARPOLBUL.2015.09.026. URL https://www.sciencedirect.com/science/article/pii/S0025326X15300424.

J. Lever, M. Krzywinski, and N. Altman. Points of Significance: Principal component analysis. *Nature Methods*, 14(7):641–642, 2017. ISSN 15487105. doi: 10.1038/nmeth.4346. URL http://www.nature.com/doifinder/10.1038/nmeth.4346.

J. Linder and J.-P. Hansen. Foton. *Store Norske Leksikon*, Jan 2019. URL https://snl.no/foton.

Y. Mato, T. Isobe, H. Takada, H. Kanehiro, C. Ohtake, and T. Kaminuma. Plastic resin pellets as a transport medium for toxic chemicals in the marine environment. *Environmental Science & Technology*, 35(2):318–324, 2001. doi: 10.1021/es0010498. URL https://doi.org/10.1021/es0010498.

M. Mehrubeoglu, M. Y. Teng, and P. V. Zimba. Resolving mixed algal species in hyperspectral images. *Sensors (Switzerland)*, 2013. ISSN 14248220. doi: 10.3390/s140100001.

I. Nilssen, Øyvind Ødegård, A. J. Sørensen, G. Johnsen, M. A. Moline, and J. Berge. Integrated environmental mapping and monitoring, a methodological approach to optimise knowledge gathering and sampling strategy. *Marine Pollution Bulletin*, 96(1):374 – 383, 2015. ISSN 0025-326X. doi: https://doi.org/10.1016/j.marpolbul.2015.04.045. URL http://www.sciencedirect.com/science/article/pii/S0025326X15002477.

Norsk Elektro Optikk AS, Skedsmokorset, Norway. Hyperspectral imaging, 2019. URL https://www.hyspex.no/products/disc/swir-320m-e.php.

Ø. Ødegård, A. A. Mogstad, G. Johnsen, A. J. Sørensen, and M. Ludvigsen. Underwater hyperspectral imaging: a new tool for marine archaeology. *Appl. Opt.*, 57(12):3214–3223, Apr 2018. doi: 10.1364/AO.57.003214. URL http://ao.osa.org/abstract.cfm?URI=ao-57-12-3214.

Ødegård, G. Johnsen, and A. J. Sørensen. Use of Underwater Hyperspectral Imager (UHI) in Marine Archaeology. Technical report.

O. Oluniyi Solomon and T. Palanisami. Microplastics in the Marine Environment: Current Status, Assessment Methodologies, Impacts and Solutions. *Journal of Pollution Effects & Control*, 04 (02), 2016. ISSN 23754397. doi: 10.4172/2375-4397.1000161.

L. Parker. In a first, microplastics found in human poop, 2018. URL https://www.nationalgeographic.com/environment/2018/10/news-plastics-microplastics-human-feces/.

W. W. Peatross, Justin. *Physics of Light and Optics*. available at optics.byu.edu, 2015 edition, 2015.

R. Pettersen, G. Johnsen, P. Bruheim, and T. Andreassen. Development of hyperspectral imaging as a bio-optical taxonomic tool for pigmented marine organisms. *Organisms Diversity Evolution*, 14(2):237–246, Nov 2013. doi: 10.1007/s13127-013-0163-1. URL https://link.springer.com/article/10.1007/s13127-013-0163-1.

R. Pettersen, G. Johnsen, P. Bruheim, and T. Andreassen. Development of hyperspectral imaging as a bio-optical taxonomic tool for pigmented marine organisms. *Organisms Diversity and Evolution*, 2014. ISSN 16181077. doi: 10.1007/s13127-013-0163-1.

REV Ocean. Rev ocean. 2018. URL https://revocean.org/about/testimonials/.

C. D. Rummel, A. Jahnke, E. Gorokhova, D. Kühnel, and M. Schmitt-Jansen. Impacts of biofilm

formation on the fate and potential effects of microplastic in the aquatic environment. *Environmental Science & Technology Letters*, 4(7):258–267, 2017. doi: 10.1021/acs.estlett.7b00164. URL https://doi.org/10.1021/acs.estlett.7b00164.

A. Savitzky and M. J. E. Golay. Smoothing and differentiation of data by simplified least squares procedures. *Analytical Chemistry*, 36(8):1627–1639, 1964. doi: 10.1021/ac60214a047. URL https://doi.org/10.1021/ac60214a047.

J. Shlens. A Tutorial on Principal Component Analysis. Technical report, University of California, San Diego, San Diego, 2005. URL https://datajobs.com/data-science-repo/PCA-Tutorial-[Shlens].pdf.

F. Signernes. Lecture notes ttk20: Basic hyper spectral imaging, NTNU, fall 2018, 2018. Accessed: 2018-09-23.

R. C. Smith and K. S. Baker. Optical properties of the clearest natural waters (200–800 nm). *Applied Optics*, 20(2):177–184, 1981. ISSN 0003-6935. doi: 10.1364/AO.20.000177. URL https://www.osapublishing.org/abstract.cfm?URI=ao-20-2-177.

G. Socrates. *Introduction*, chapter 1, pages 1–48. John Wiley Sons, Ltd, 2002. ISBN 978-0-470-09307-8. doi: 10.1021/0153520. URL https://doi.org/10.1021/0153520.

V. L. St. Louis, A. E. Derocher, I. Stirling, J. A. Graydon, C. Lee, E. Jocksch, E. Richardson, S. Ghorpade, A. K. Kwan, J. L. Kirk, I. Lehnherr, and H. K. Swanson. Differences in Mercury Bioaccumulation between Polar Bears (Ursus maritimus) from the Canadian high- and sub-Arctic. *Environmental Science & Technology*, 45(14):5922–5928, 7 2011. ISSN 0013-936X. doi: 10.1021/es2000672. URL https://doi.org/10.1021/es2000672.

Stein M. Nornes. Lecture notes, tmr4240: Unmanned underwater vehicles, NTNU, fall 2017, 2017. Accessed: 2018-11-15.

A. Ø. R. Stien and E. M. H. Dahl. Identification of plastics using hyperspectral imaging. *Identification of plastics using Hyperspectral Imaging*, Dec 2018.

A. J. Sørensen. Lecture notes, tmr4240: Control lecture navigation and payload sensors, NTNU, fall 2018, 2018. Accessed: 2018-11-03.

The Ocean Cleanup. The ocean cleanup. *The Ocean Cleanup*, 2018. URL https://www.theoceancleanup.com/about/.

The Unscrambler User Manual. The Unscrambler User Manual Camo Software AS The Unscrambler Methods By CAMO Software AS. Technical report, 1996. URL www.camo.com.

TOMRA. Tomra. *TOMRA*, 2018. URL https://www.tomra.com/en/about-us.

E. van Sebille, C. Wilcox, L. Lebreton, N. Maximenko, B. D. Hardesty, J. A. van Franeker, M. Eriksen, D. Siegel, F. Galgani, and K. L. Law. A global inventory of small floating plastic debris. *Environmental Research Letters*, 10(12):124006, Dec 2015. doi: 10.1088/1748-9326/10/12/124006. URL https://doi.org/10.1088/2F1748-9326/2F10/2F12/2F124006.

Z. Volent. Improved monitoring of phytoplankton bloom dynamics in a Norwegian fjord by integrating satellite data, pigment analysis, and Ferrybox data with a coastal observation network. *Journal of Applied Remote Sensing*, 2011. ISSN 1931-3195. doi: 10.1117/1.3658032.

A. J. R. Watts, C. Lewis, R. M. Goodhead, S. J. Beckett, J. Moger, C. R. Tyler, and T. S. Galloway. Uptake and Retention of Microplastics by the Shore Crab Carcinus maenas. *Environmental Science & Technology*, 48(15):8823–8830, 8 2014. ISSN 0013-936X. doi: 10.1021/es501090e. URL https://doi.org/10.1021/es501090e.

J. Williams. Optical properties of the ocean. *Reports on Progress in Physics*, 36(12):1567–1608, Dec 1973. doi: 10.1088/0034-4885/36/12/002. URL https://doi.org/10.1088/0034-4885/36/12/002.

WITec GmbH. Alpha00 R - Confocal Raman Imaging, 2019. URL https://www.witec.de/assets/Literature/Files/WITec-alpha300-Brochure.pdf.

H. Xiong, L. Shi, L. Wei, Y. Shen, R. Long, Z. Zhao, and W. Min. Stimulated raman excited fluorescence spectroscopy and imaging. *Nature Photonics*, 13:1, Apr 2019. ISSN 1749-4893. doi: 10.1038/s41566-019-0396-4.

A. Yamashita, M. Fujii, and T. Kaneko. Color registration of underwater images for underwater sensing with consideration of light attenuation. *Proceedings - IEEE International Conference on Robotics and Automation*, (Apr):4570–4575, 2007. ISSN 10504729. doi: 10.1109/ROBOT.2007.364183.

L. Zada, H. A. Leslie, A. D. Vethaak, G. H. Tinnevelt, J. J. Jansen, J. F. de Boer, and F. Ariese. Fast microplastics identification with stimulated Raman scattering microscopy. *Journal of Raman Spectroscopy*, 49(7):1136–1144, jul 2018. ISSN 03770486. doi: 10.1002/jrs.5367. URL http://doi.wiley.com/10.1002/jrs.5367.

L. M. Ziccardi, A. Edgington, K. Hentz, K. J. Kulacki, and S. Kane Driscoll. Microplastics as vectors for bioaccumulation of hydrophobic organic chemicals in the marine environment: A state-of-the-science review. *Environmental Toxicology and Chemistry*, 35(7):1667–1676, 2016. doi: 10.1002/etc.3461. URL https://setac.onlinelibrary.wiley.com/doi/abs/10.1002/etc.3461.

Appendix A

The Set-Up

A.1 Collecting and Pulverizing Plastics

Figure A.1.1: Filtering sea-mass aboard the boat

Figure A.1.2: Poring liquid nitrogen

Figure A.1.3: Pulverizing plastic in the tissuelyser

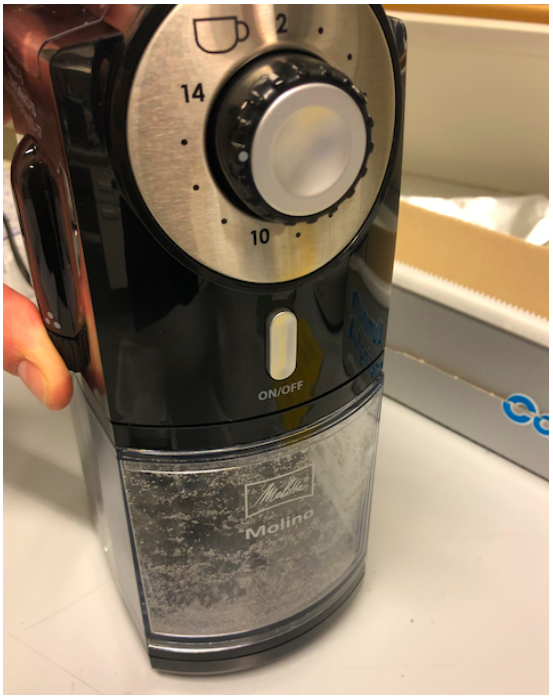

Figure A.1.4: Grinding plastic in the coffee grinder

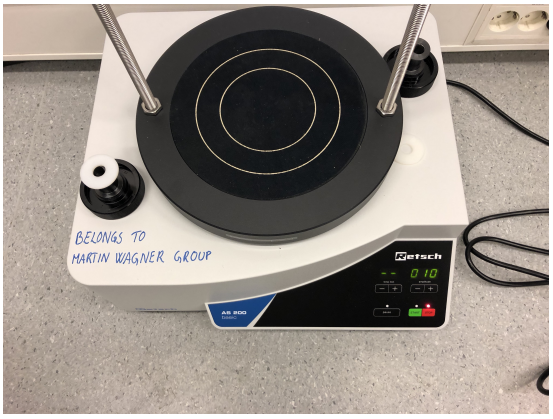

Figure A.1.5: The particles were sifted to retrieve different sizes

Figure A.1.6: Trying to count the plastic particles with the Beckman Coulter

A.2 SilCam Laboratory

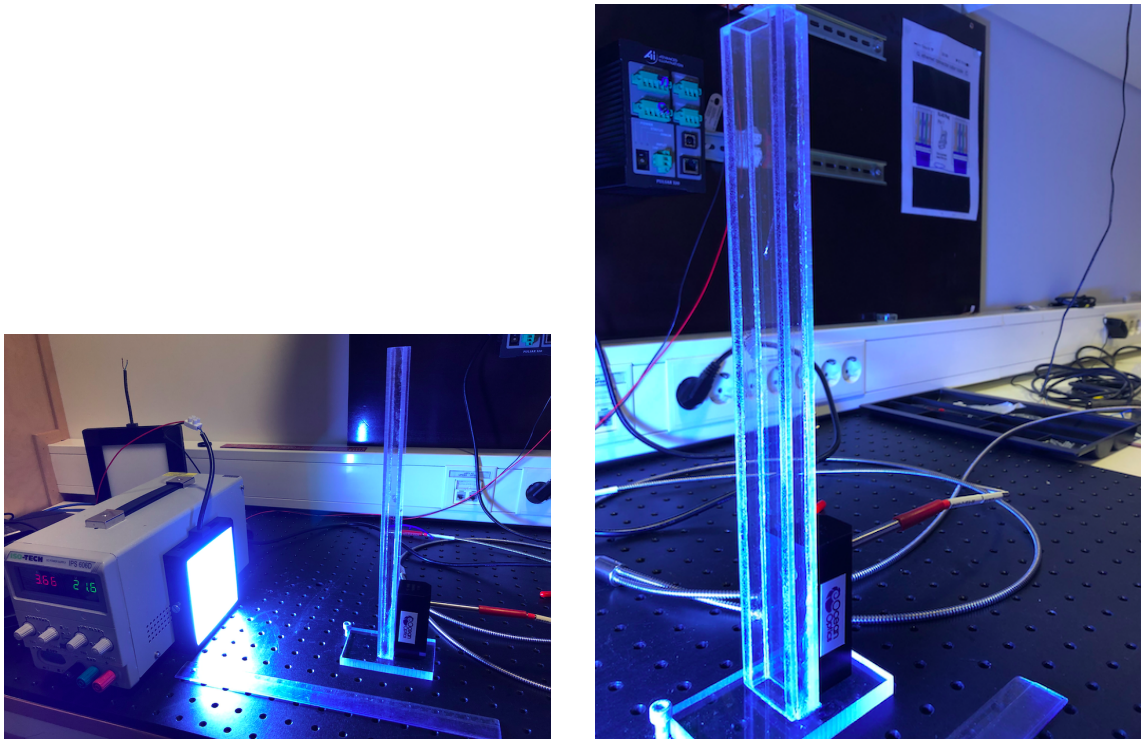

Figure A.2.1: SilCam laboratory set-up

A.3 NIR HI Laboratory

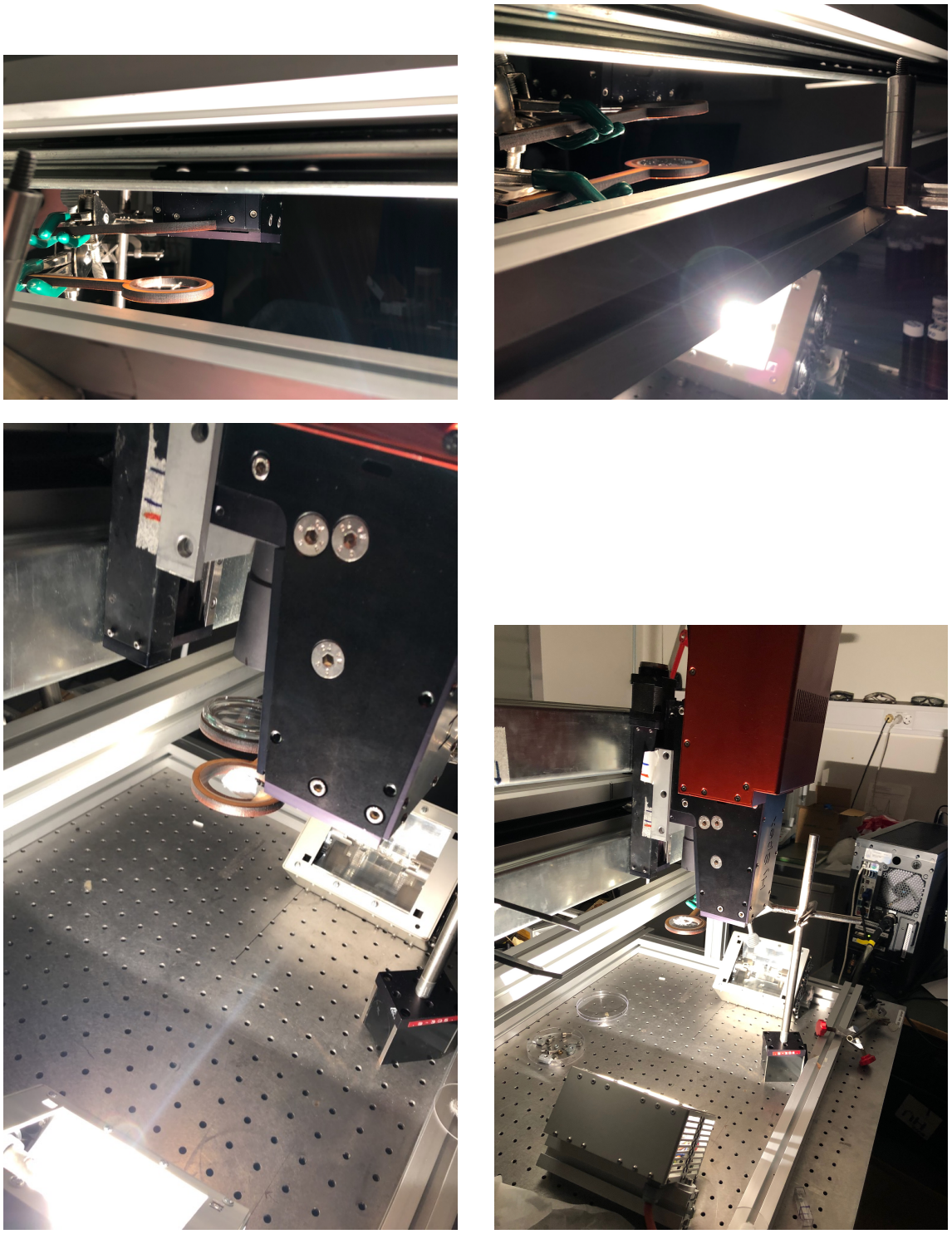

Figure A.3.1: Hyperspectral imaging laboratory set-up

A.4 Raman Laboratory

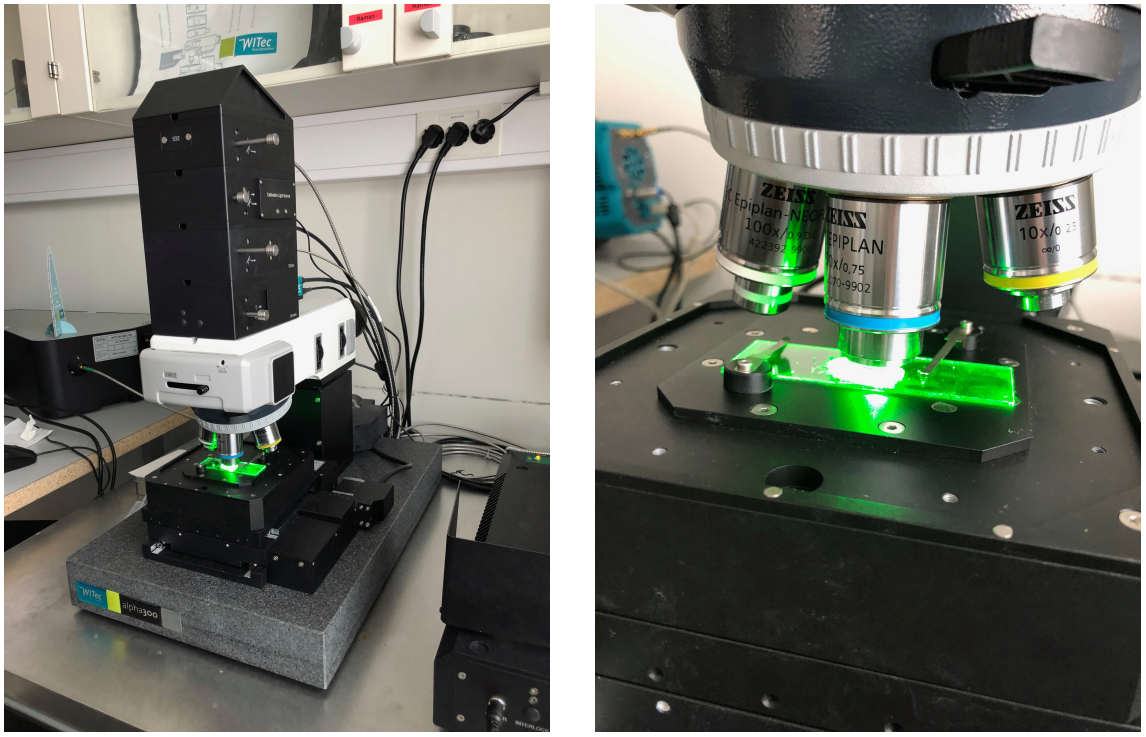

Figure A.4.1: Raman set-up with the microscope and laser

Appendix B

NIR HI - Results

B.1 NIR HI - Signatures

B.1.1 HDPE

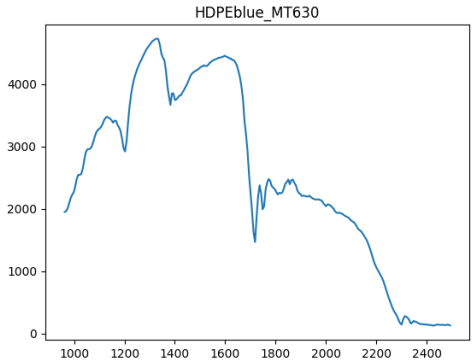

(a) HDPE Blue, Larger than 630 microns

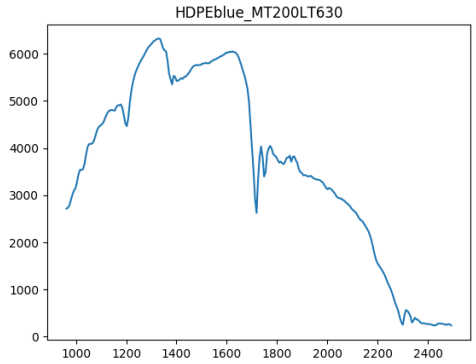

(b) HDPE Blue, Smaller than 630, but larger than 200 microns

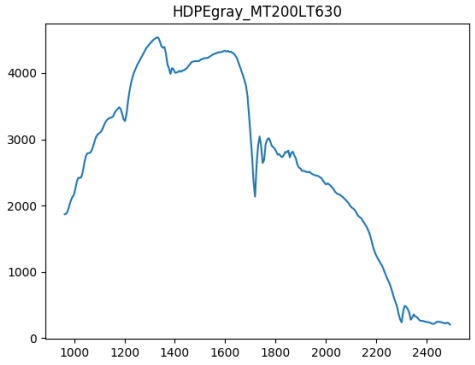

(c) HDPE Gray, Smaller than 630, but larger than 200 microns

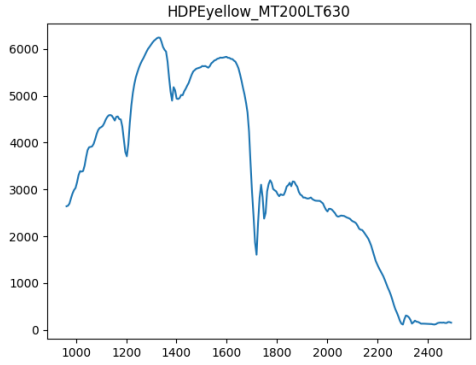

(d) HDPE Yellow, Smaller than 630, but larger than 200 microns

Figure B.1.1: NIR HI signatures of HDPE

In Water

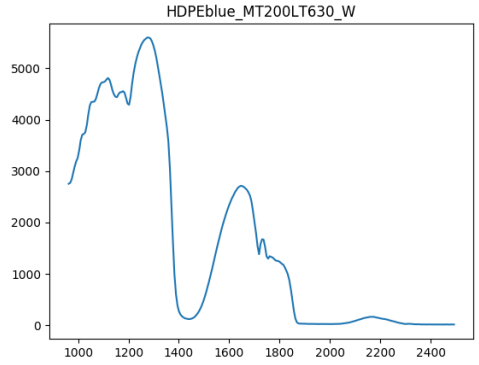

(a) HDPE Blue in Water, Smaller than 630, but larger than 200 microns

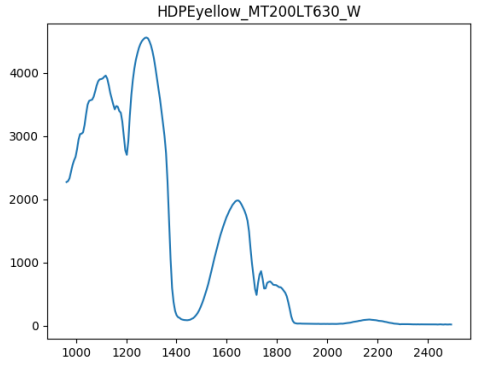

(b) HDPE Yellow in Water, Smaller than 630, but larger than 200 microns

Figure B.1.2: NIR HI signatures of HDPE in Water

B.1.2 LDPE

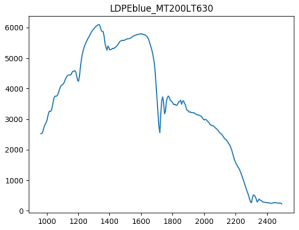

(a) LDPE Blue, Smaller than 630, but larger than 200 microns

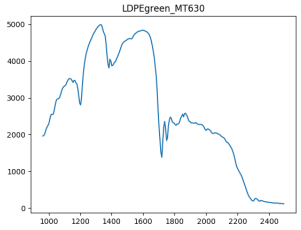

(b) LDPE Green, Larger than 630 microns

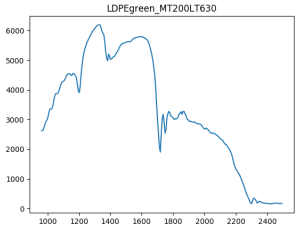

(c) [LDPE Green, Smaller than 630, but larger than 200 microns

Figure B.1.3: NIR HI signatures of LDPE

In Water

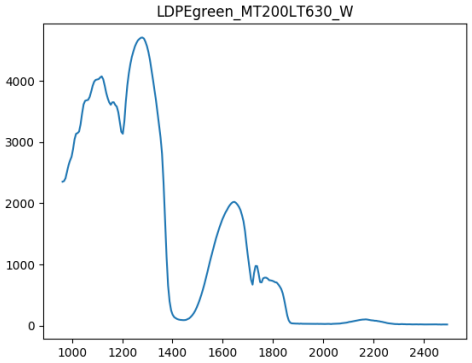

(a) LDPE Green in Water, Smaller than 630, but larger than 200 microns

Figure B.1.4: NIR HI signatures of LDPE in Water

B.1.3 PET

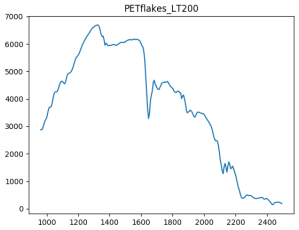

(a) PET Flakes, Smaller than 200 microns

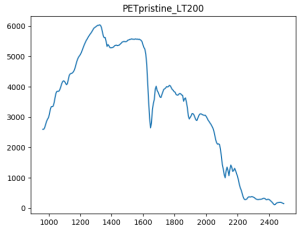

(b) PET Pristine, Smaller than 200 microns

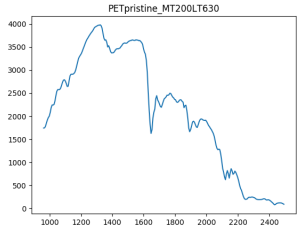

(c) PET Pristine, Smaller than 630, but larger than 200 microns

Figure B.1.5: NIR HI signatures of PET

In Water

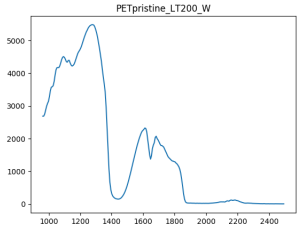

(a) PET Prstine in Water, Smaller than 200 microns

Figure B.1.6: NIR HI signatures of PET in Water

B.1.4 PP

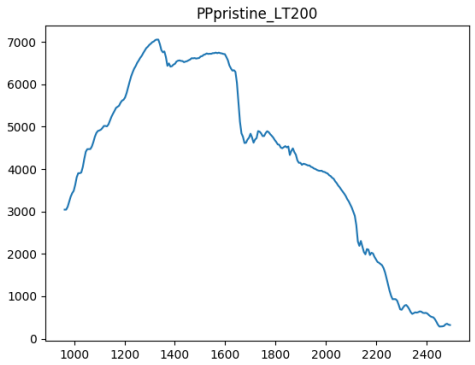

(a) PP Pristine, Smaller than 200 microns

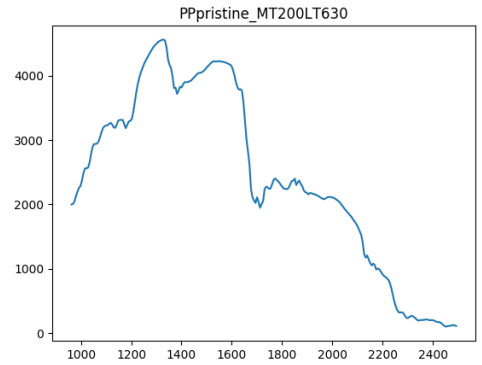

(b) PP Pristine, Smaller than 630, but larger than 200 microns

(c) PP Recycled, Smaller than 200 microns

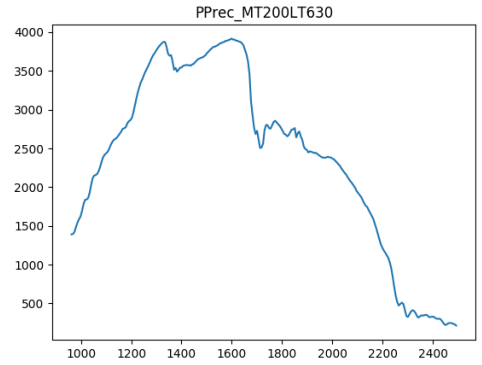

(d) PP Recycled, Smaller than 630, but larger than 200 microns

Figure B.1.7: NIR HI signatures of PP

In Water

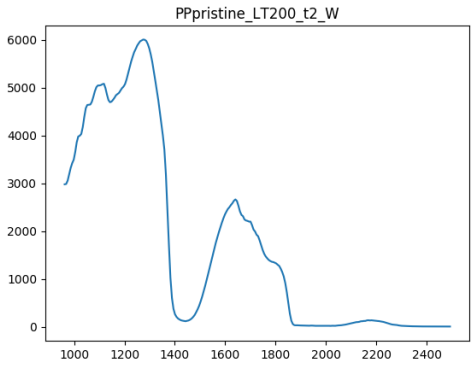

(a) PP Pristine in Water, Smaller than 200 microns

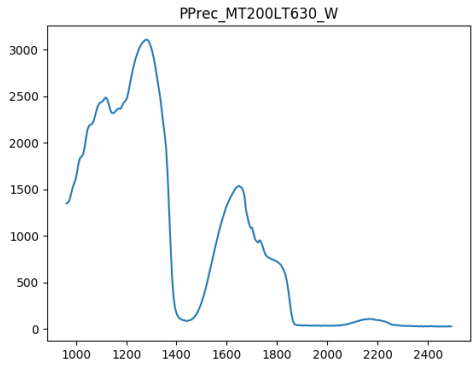

(b) PP Recycled in Water, Smaller than 630, but larger than 200 microns

Figure B.1.8: NIR HI signatures of PP in Water

B.1.5 PS

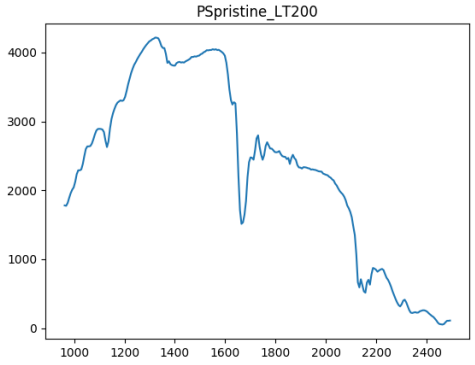

(a) PS Pristine, Smaller than 200 microns

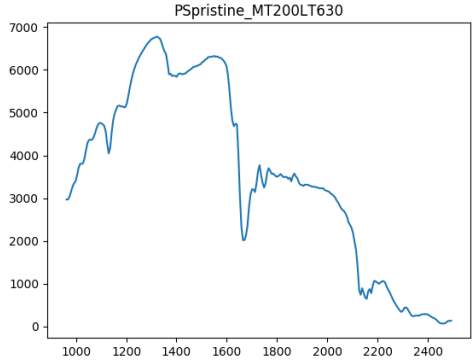

(b) PS Pristine, Smaller than 630, but larger than 200 microns

Figure B.1.9: NIR HI signatures of PS

In Water

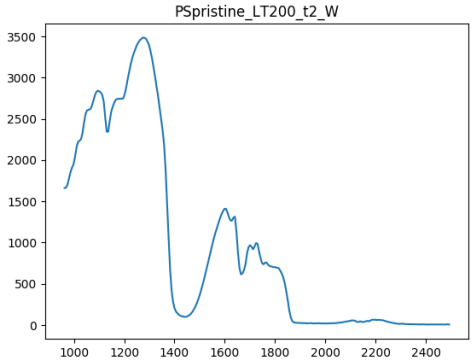

(a) PS Prstine in Water, Smaller than 200 microns

Figure B.1.10: NIR HI signatures of PS in Water

B.1.6 PVC

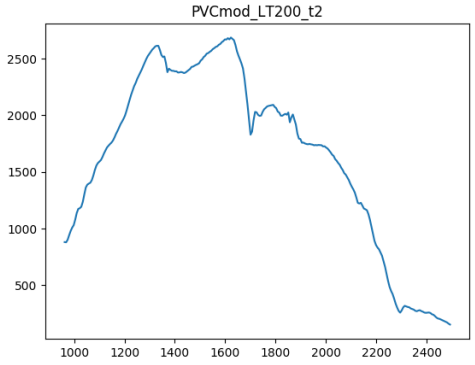

(a) PVC Modified, Smaller than 200 microns

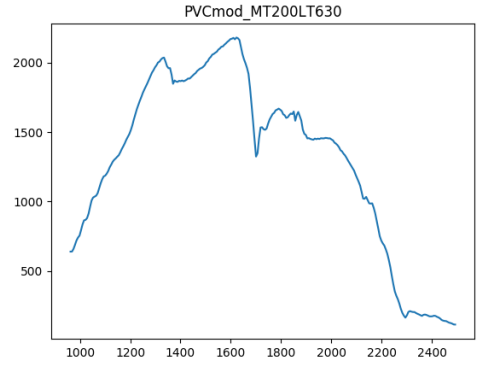

(b) PVC Modified, Smaller than 630, but larger than 200 microns

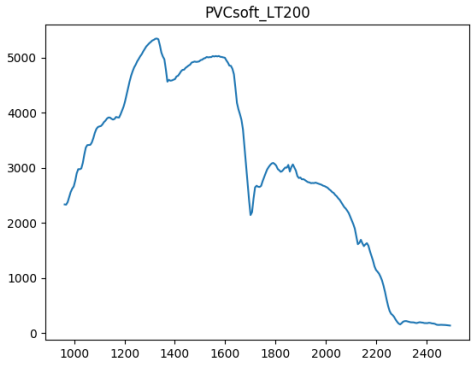

(c) PVC Soft, Smaller than 200 microns

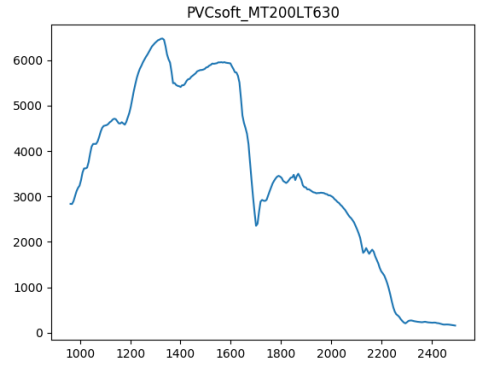

(d) PVC Soft, Smaller than 630, but larger than 200 microns

Figure B.1.11: NIR HI signatures of PVC

In Water

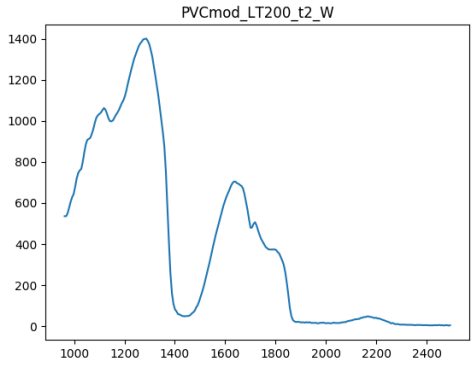

(a) PVC Modified in Water, Smaller than 200 microns

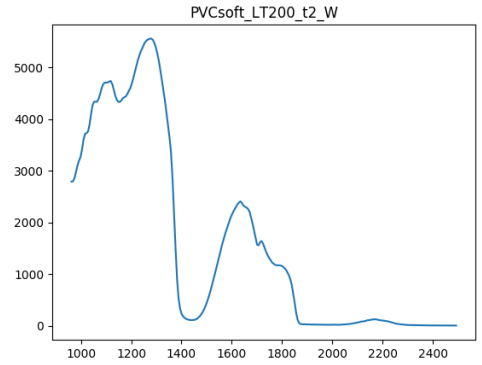

(b) PVC Soft in Water, Smaller than 200 microns

Figure B.1.12: NIR HI signatures of PVC in water

B.1.7 Reference and Organic

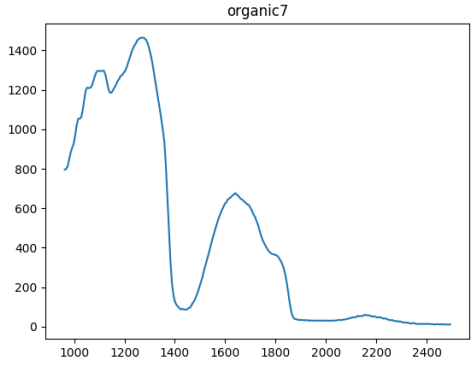

(a) Organic material from Sample 7

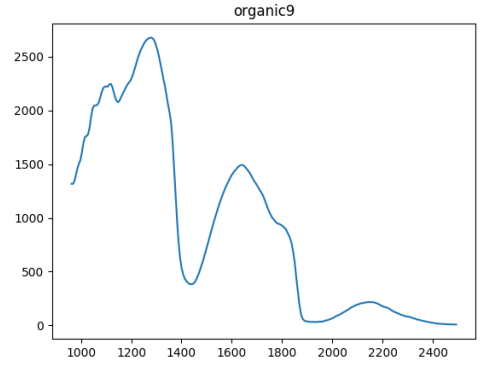

(b) Organic material from Sample 9

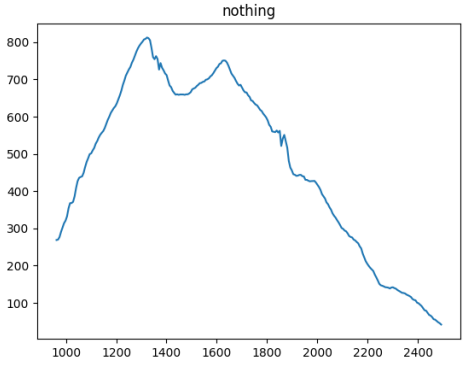

(c) Reference

Figure B.1.13: NIR HI signatures of organic matter and reference

B.2 NIR HI - Evince Plots

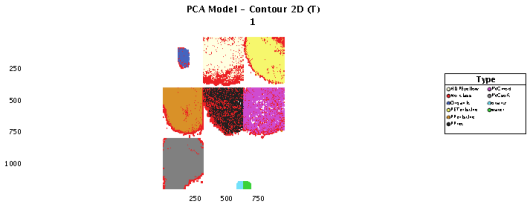

(a) Classified contour plots from Evince

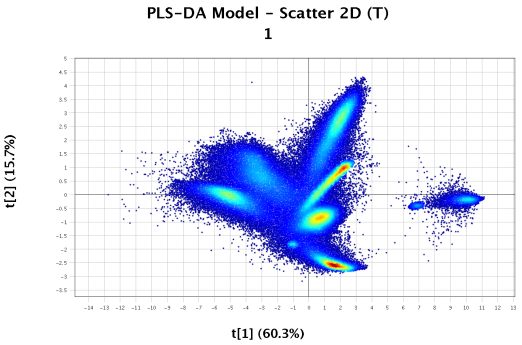

(b) PLS-DA Scatter plot

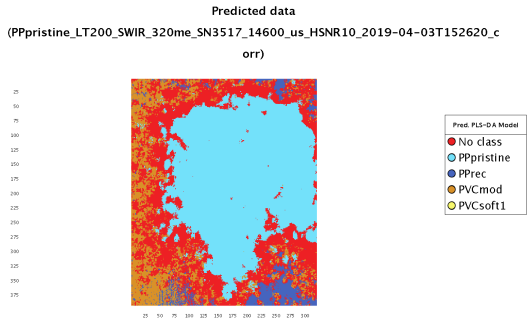

(c) Prediciton on dry PP

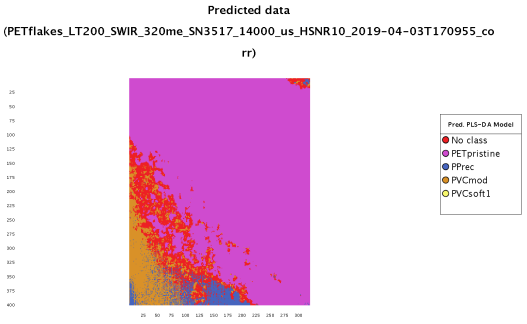

(d) Prediciton on dry PET flakes

Figure B.2.1: Representative selection of plots from Evince

Appendix C

Raman Spectroscopy - Signatures

C.1 Dry Microplastic

C.1.1 HDPE

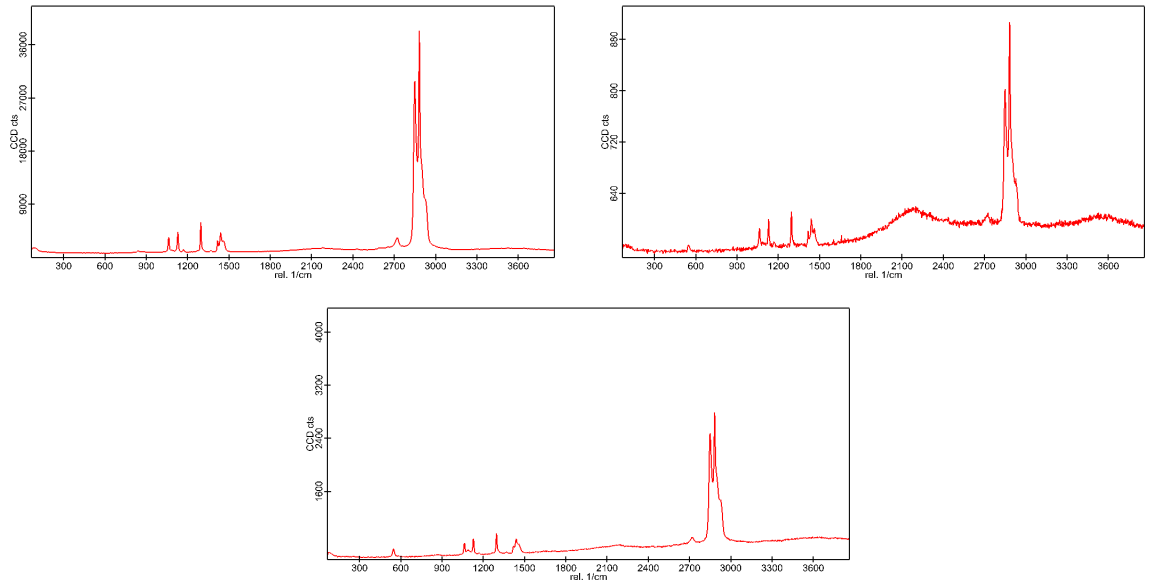

Figure C.1.1: HDPE blue

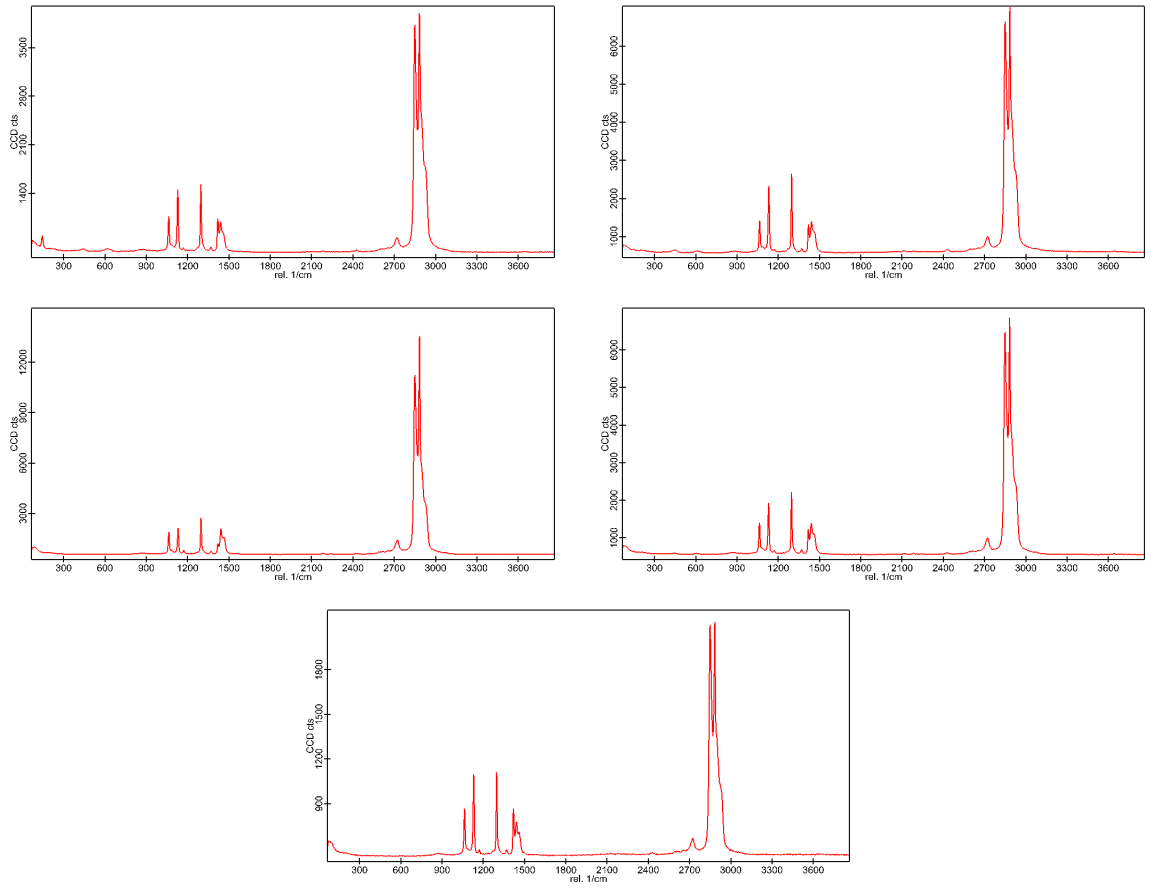

Figure C.1.2: HDPE gray

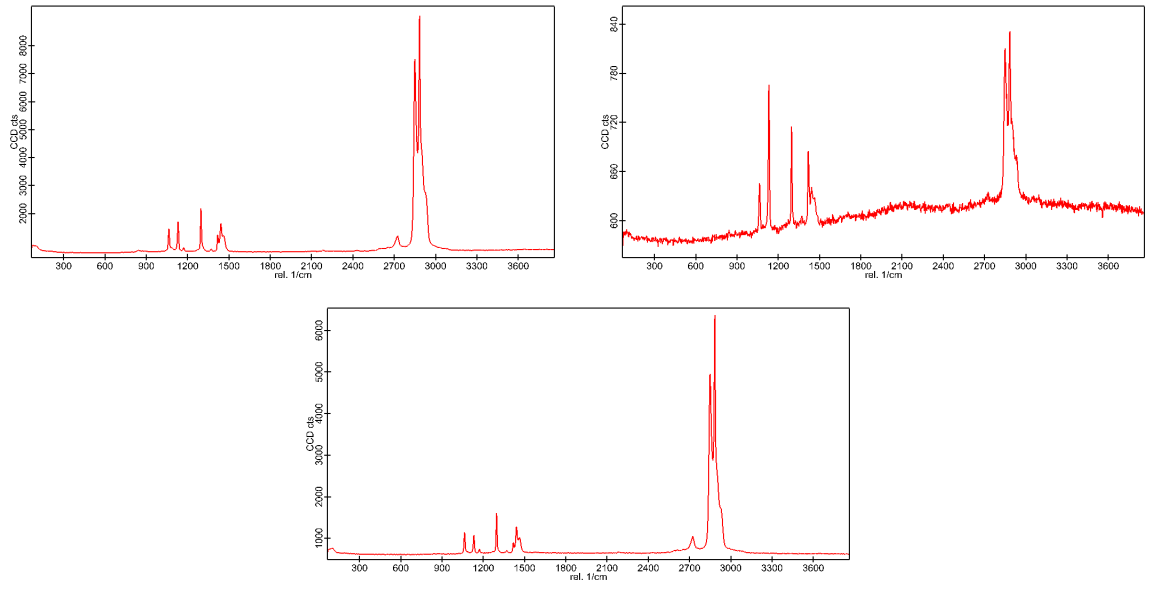

Figure C.1.3: HDPE yellow

C.1.2 LDPE

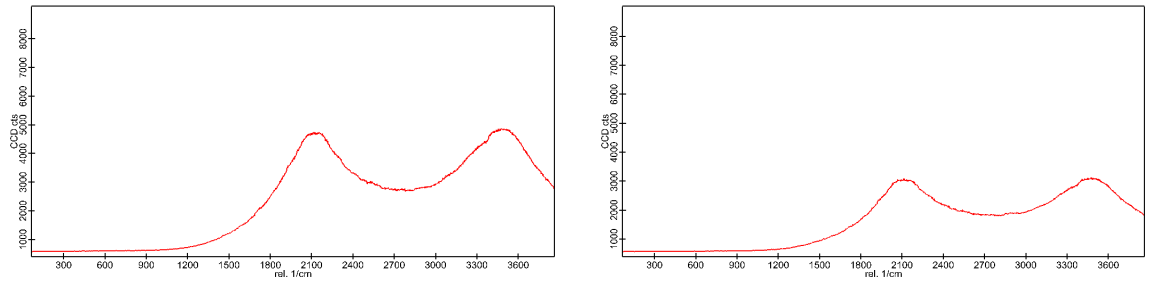

Figure C.1.4: LDPE blue

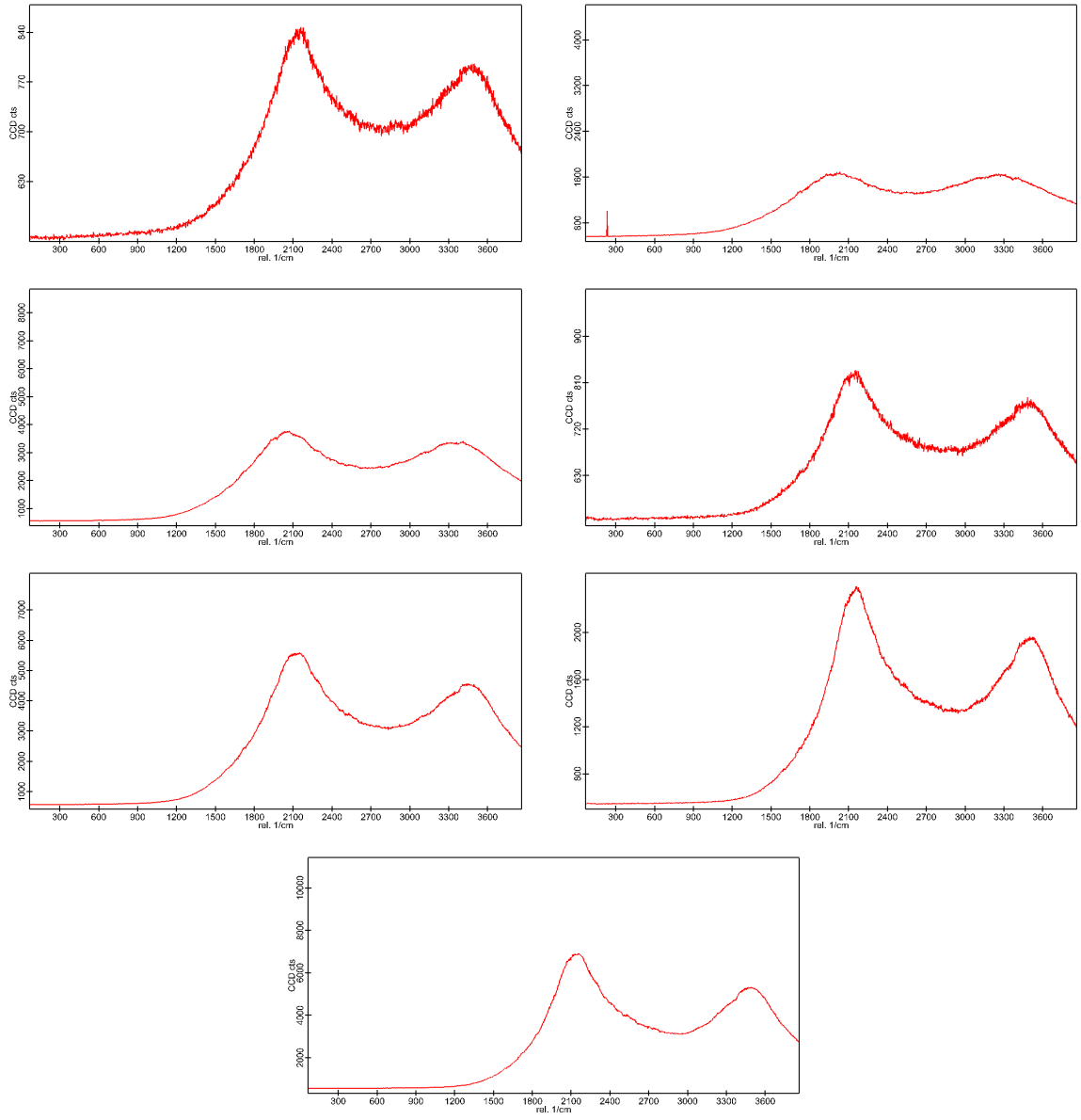

Figure C.1.5: LDPE gray

C.1.3 PET Flakes

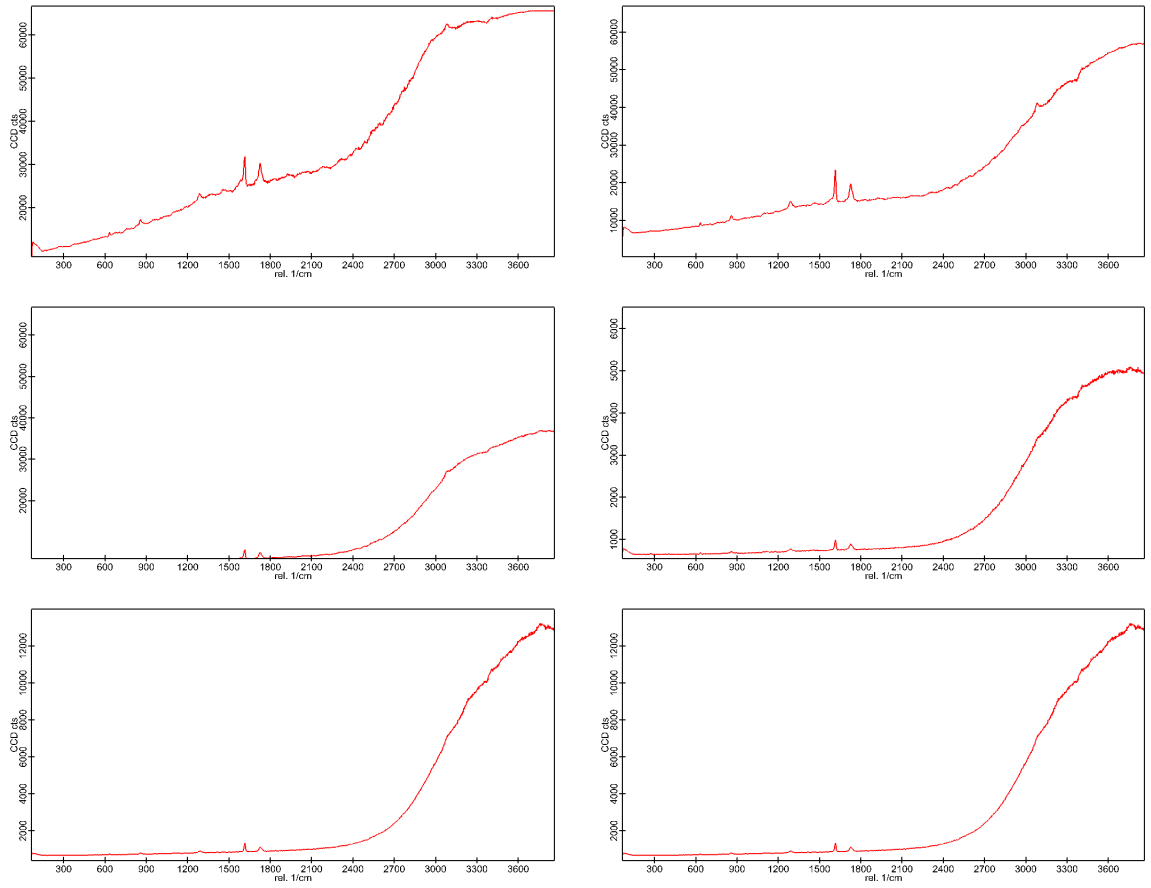

Figure C.1.6: PET flakes

C.1.4 PET Pristine

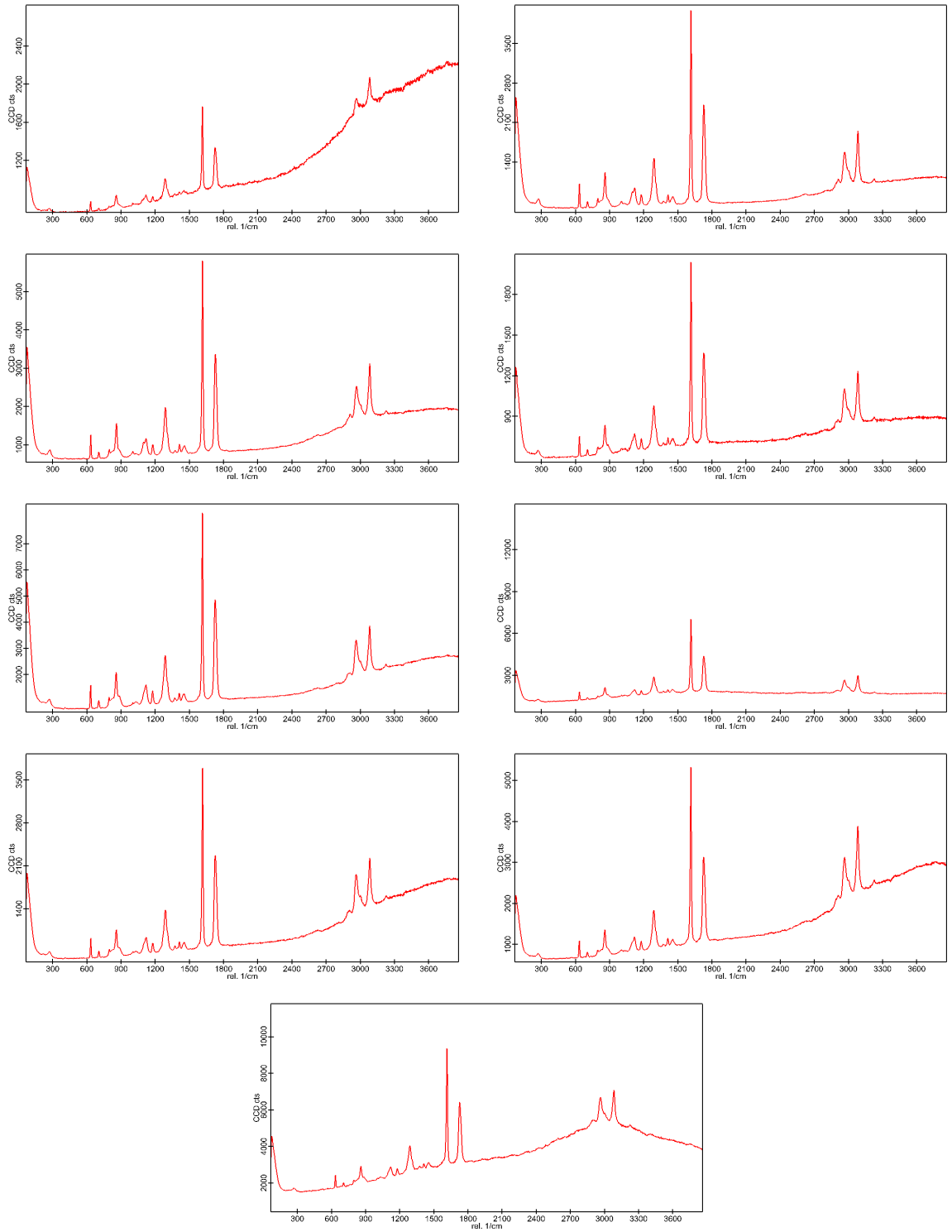

Figure C.1.7: PET pristine

C.1.5 PP Pristine

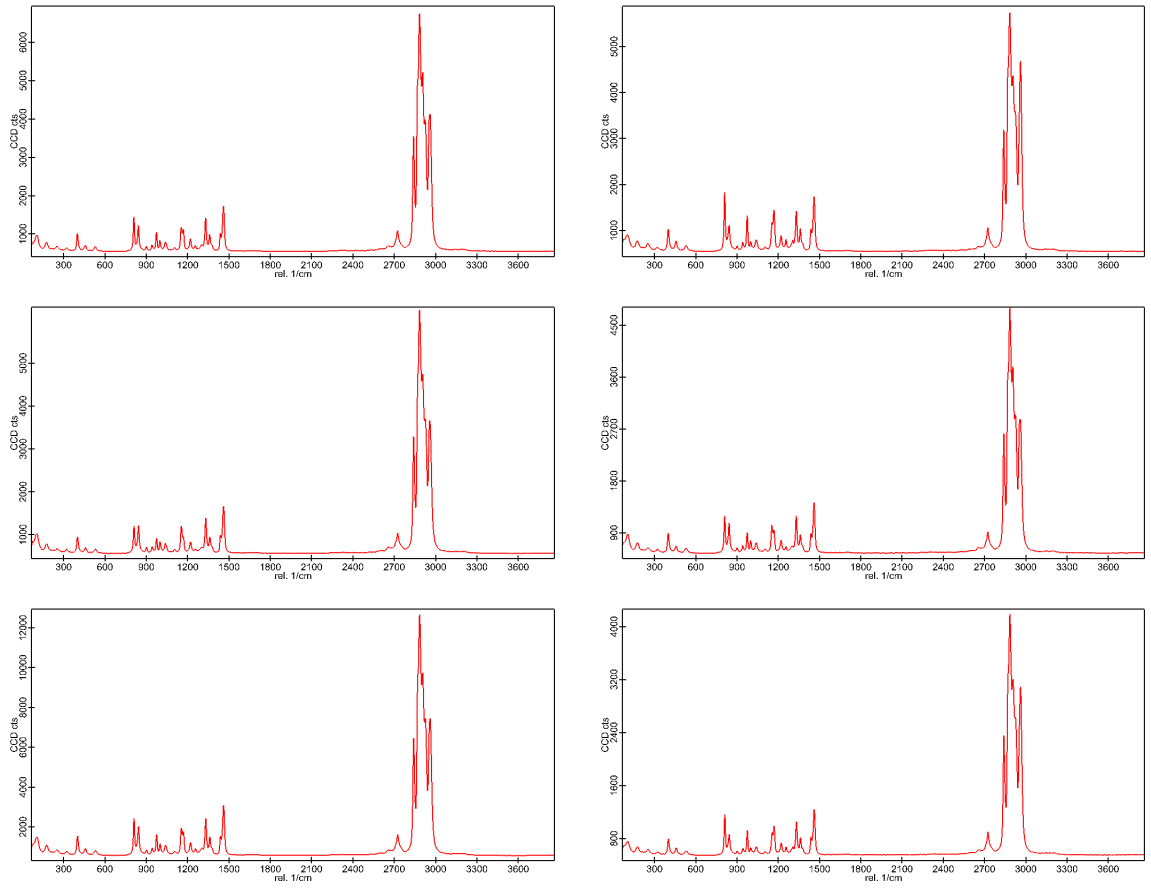

Figure C.1.8: PP pristine

C.1.6 PP Recycled

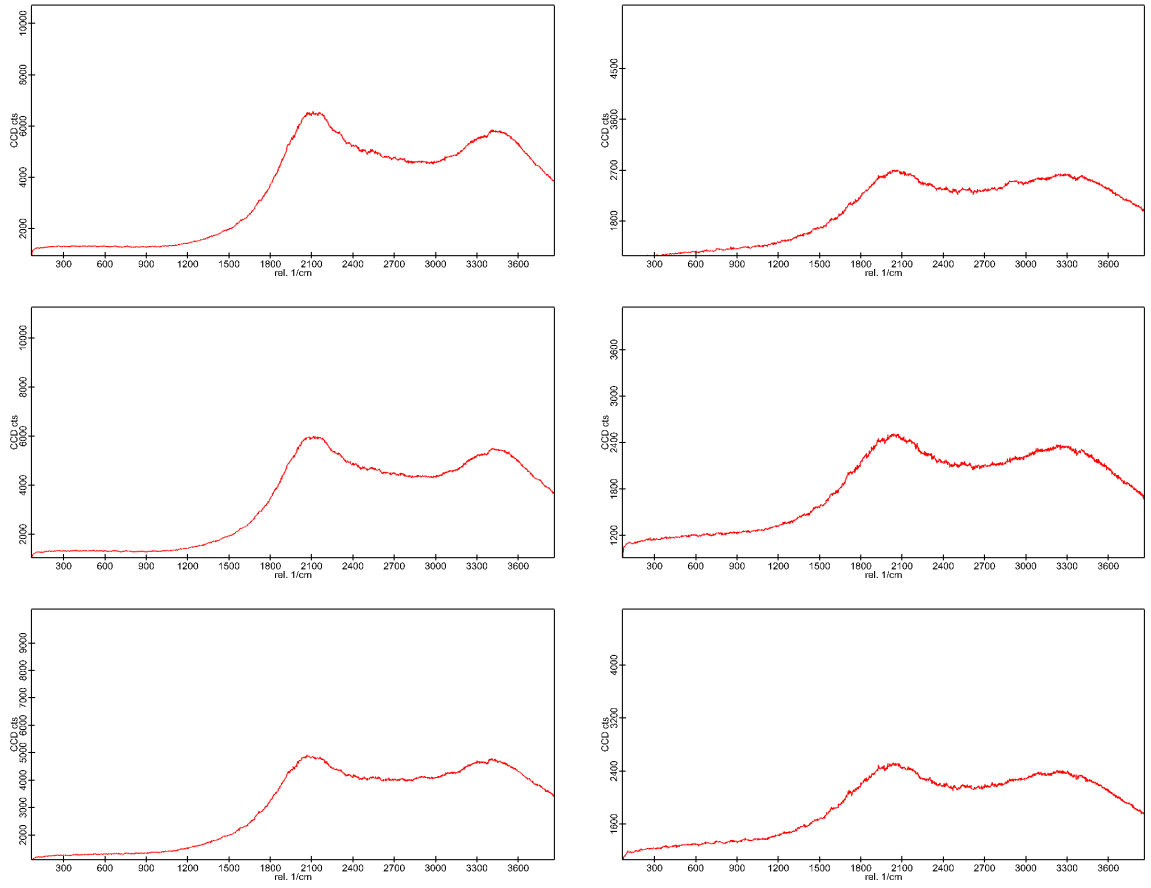

Figure C.1.9: PP recycled

C.1.7 PS Pristine

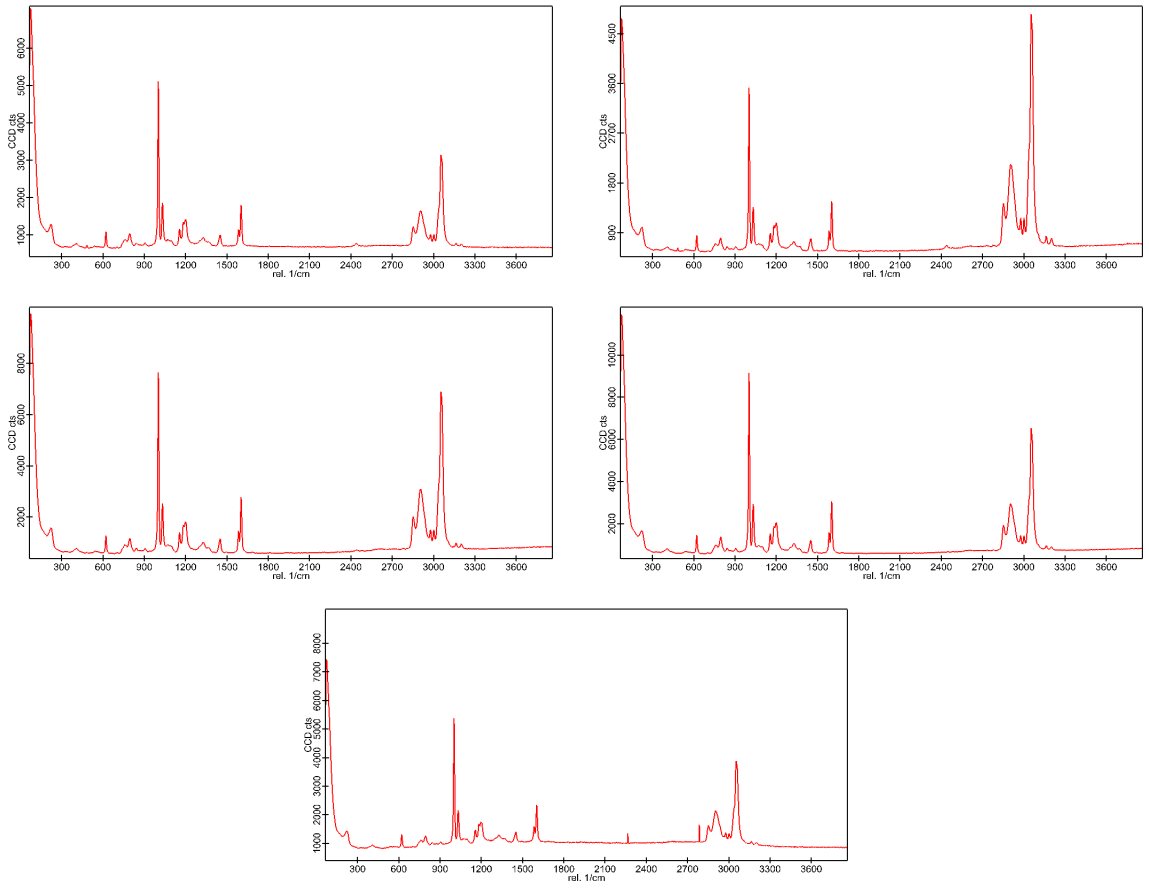

Figure C.1.10: PS pristine

C.1.8 PVC Modified

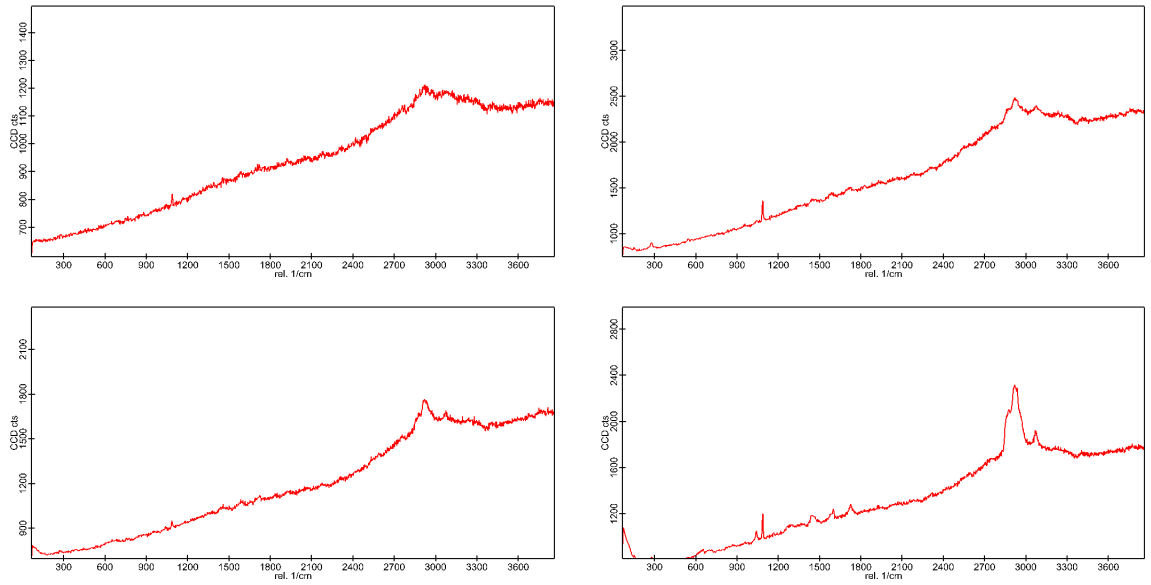

Figure C.1.11: PVC modified

C.1.9 PVC Soft

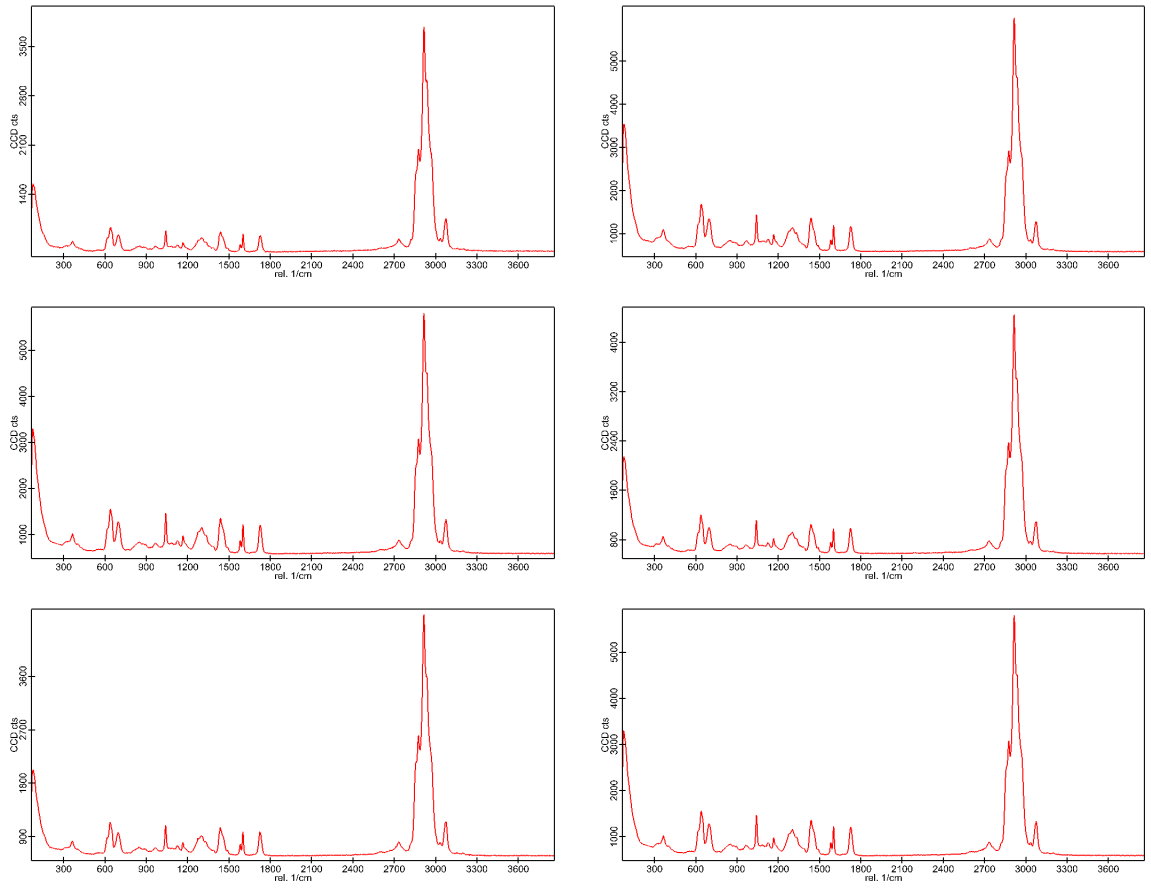

Figure C.1.12: PVC soft

C.2 Microplastic in Water

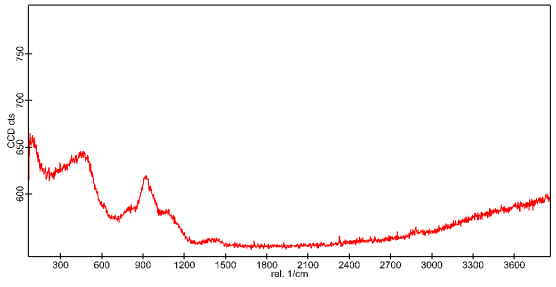

Figure C.2.1: Water signature

C.2.1 HDPE

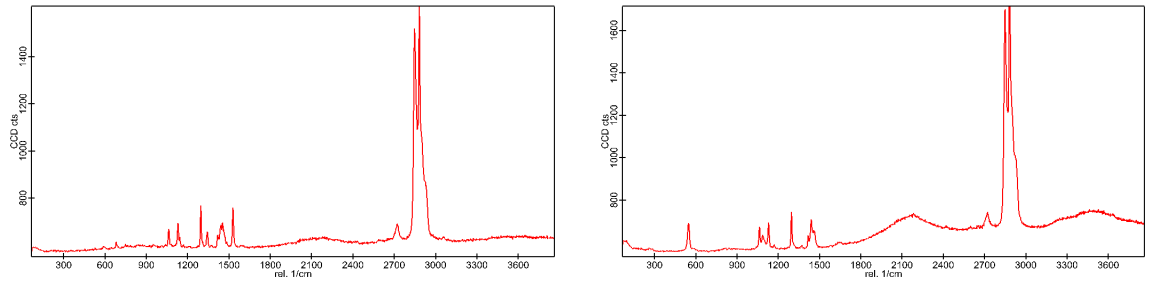

Figure C.2.2: HDPE blue

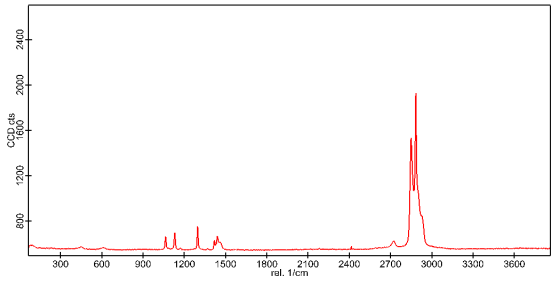

Figure C.2.3: HDPE gray in water

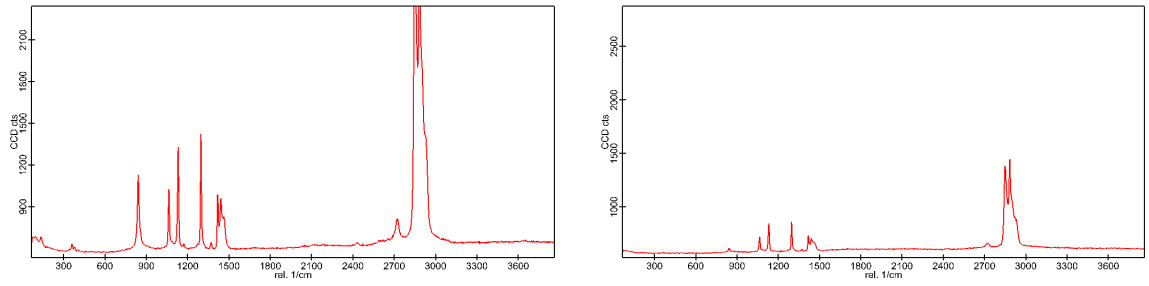

Figure C.2.4: HDPE yellow in water

C.2.2 LDPE

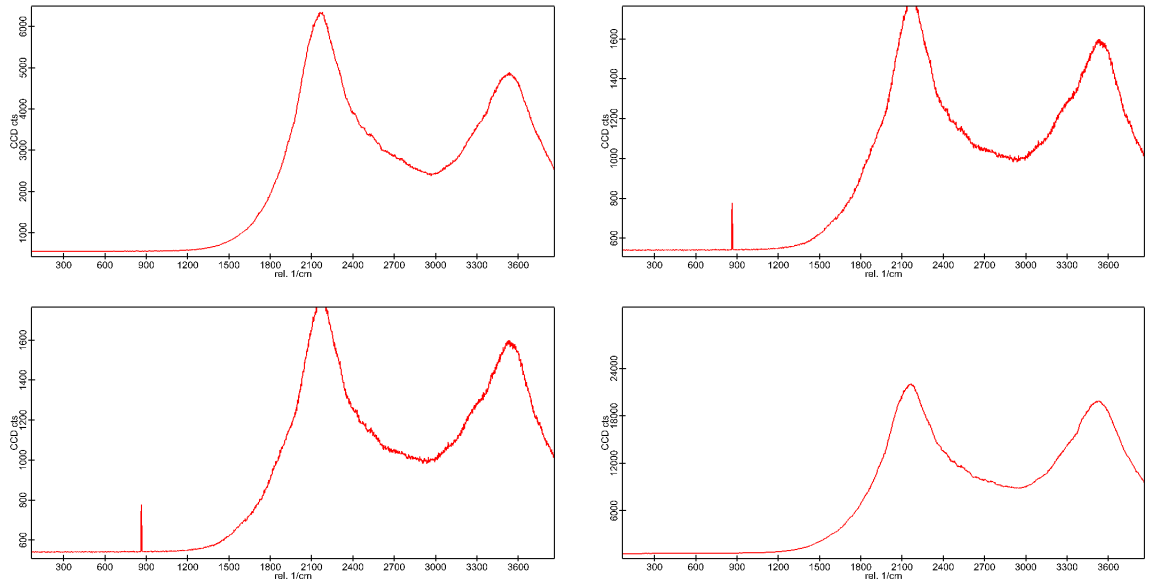

Figure C.2.5: LDPE blue in water

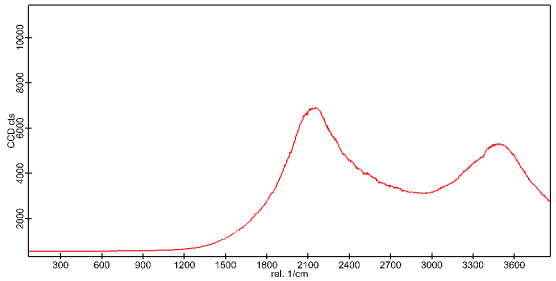

Figure C.2.6: LDPE gray in water

C.2.3 PET Flakes

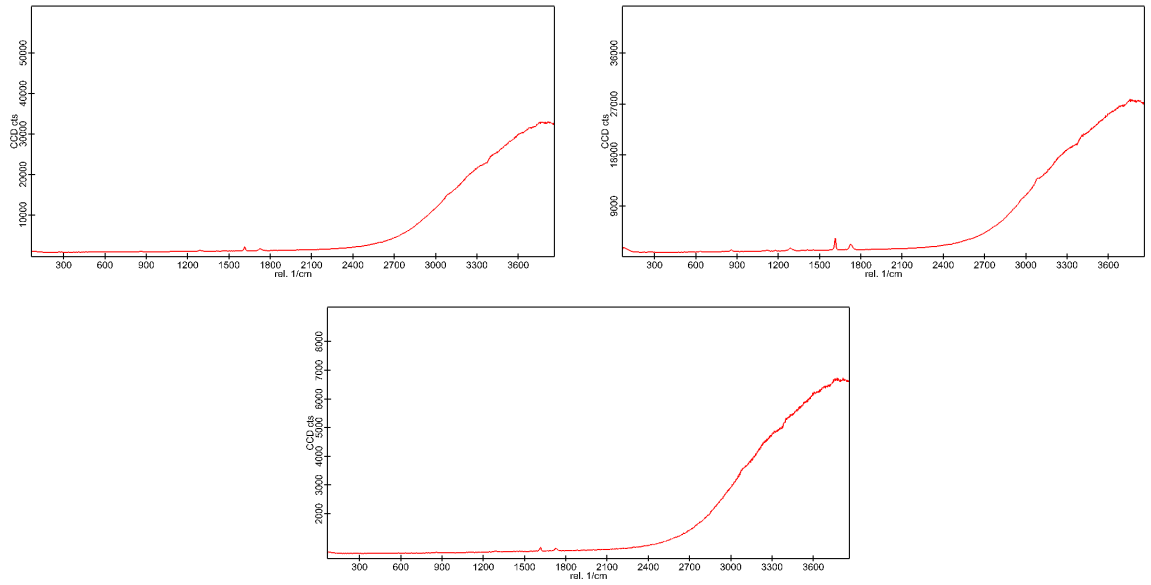

Figure C.2.7: PET flakes in water

C.2.4 PET Pristine

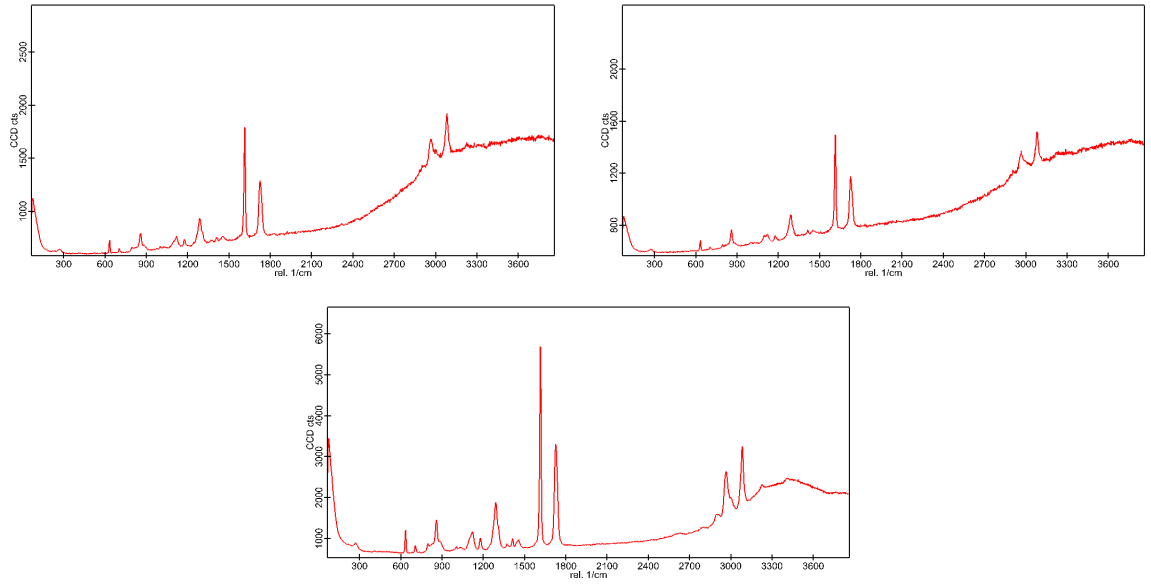

Figure C.2.8: PET pristine in water

C.2.5 PP Pristine

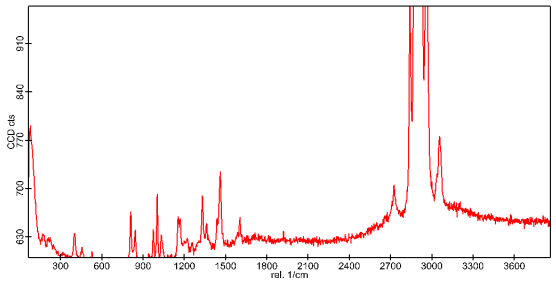

Figure C.2.9: PP pristine in water

C.2.6 PP Recycled

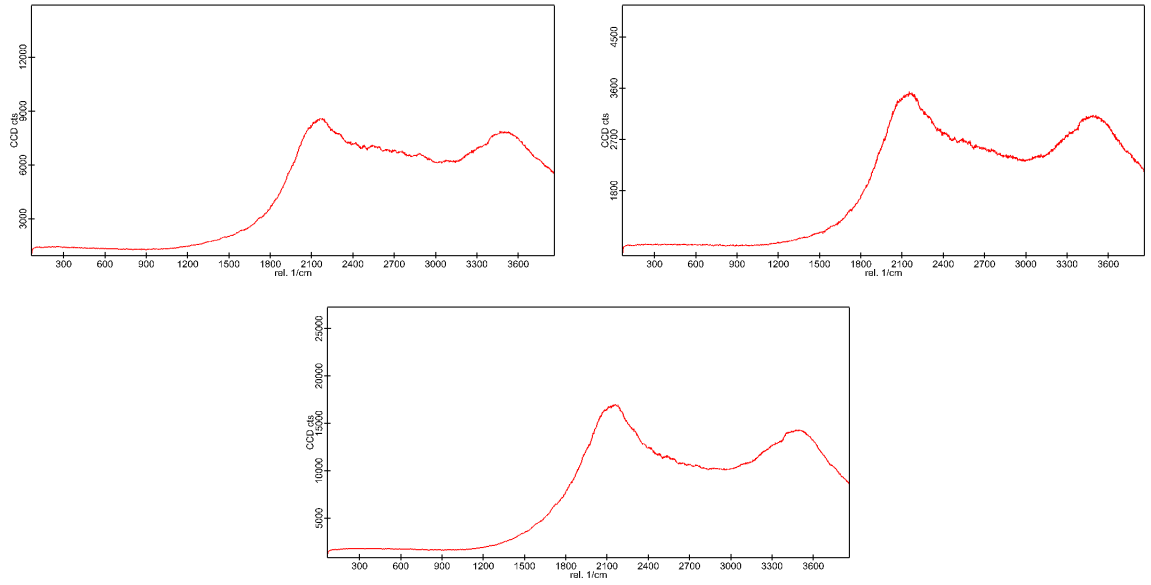

Figure C.2.10: PP recycled in water

C.2.7 PS Pristine

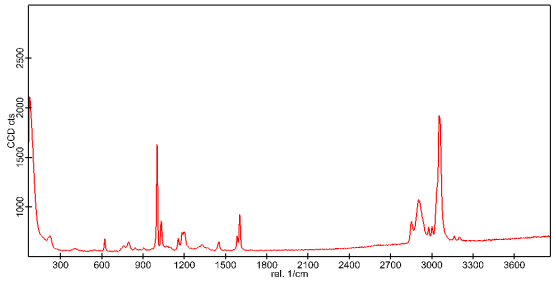

Figure C.2.11: PS pristine in water

C.2.8 PVC Modified

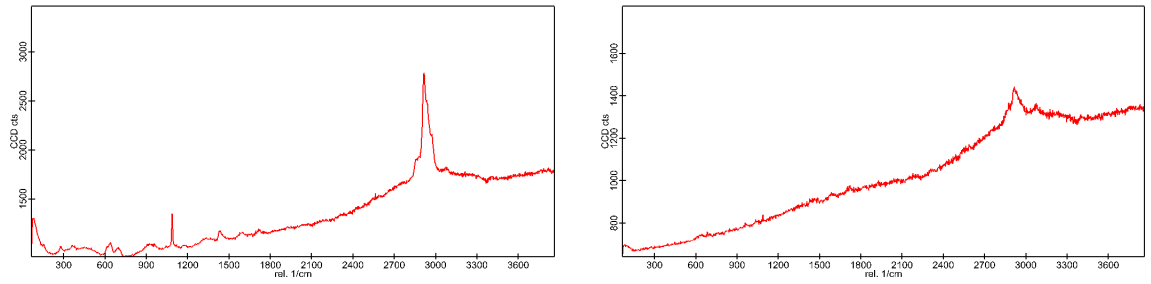

Figure C.2.12: PVC modified in water

C.2.9 PVC Soft

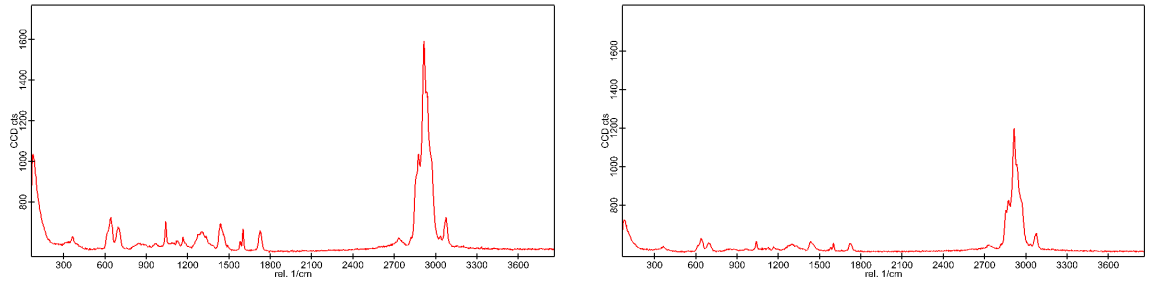

Figure C.2.13: PVC soft in water

C.3 Micro Particles from Lofoten

C.3.1 I

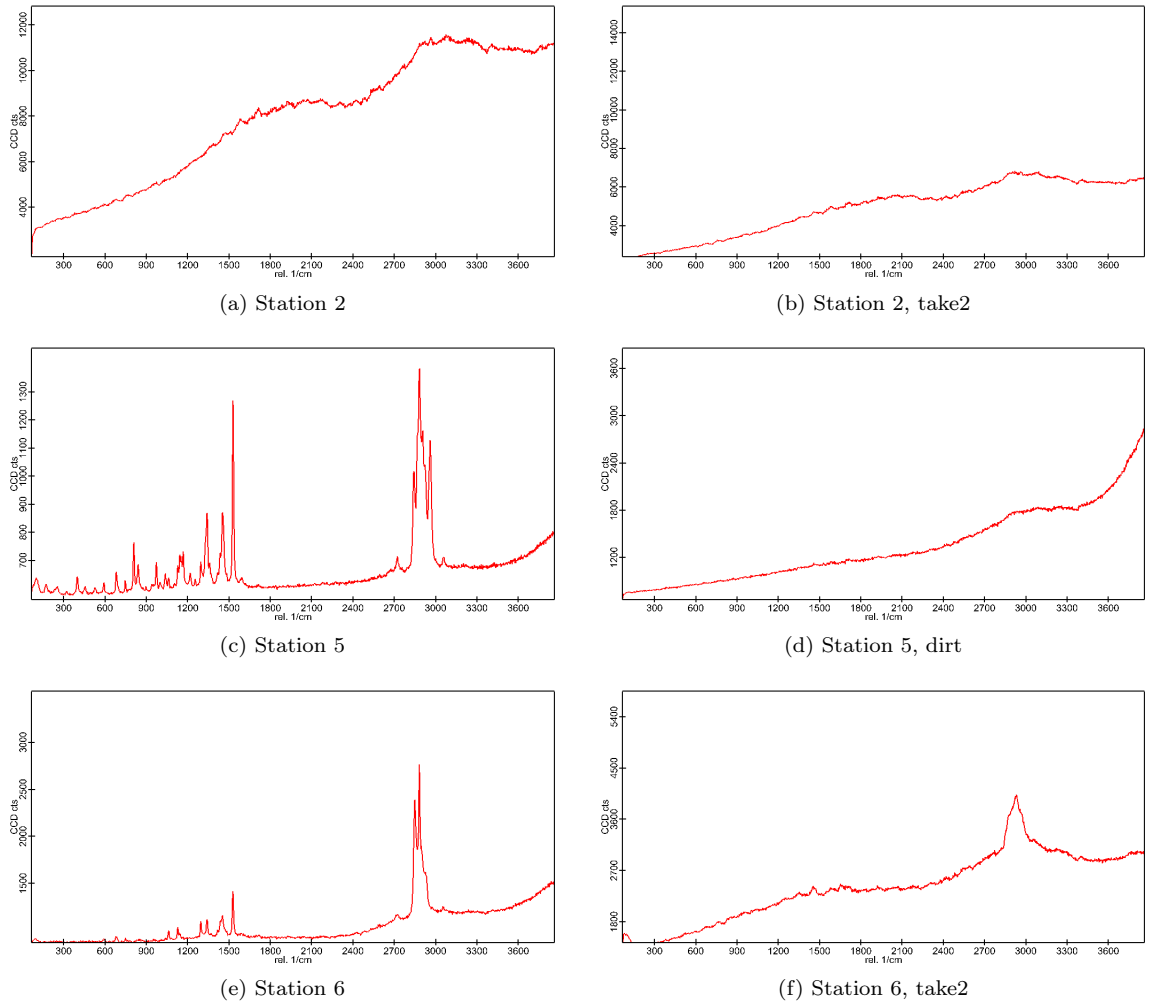

(a) Station 2

(b) Station 2, take2

(c) Station 5

(d) Station 5, dirt

(e) Station 6

(f) Station 6, take2

Figure C.3.1: Lofoten particles day 1

C.3.2 II

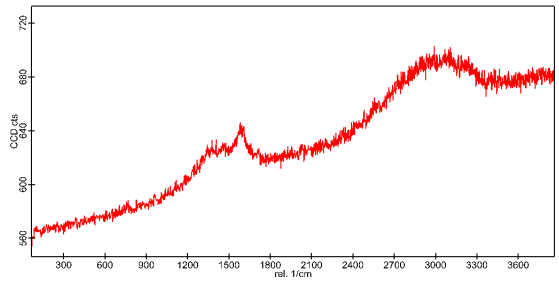

(a) Station 6, new particle

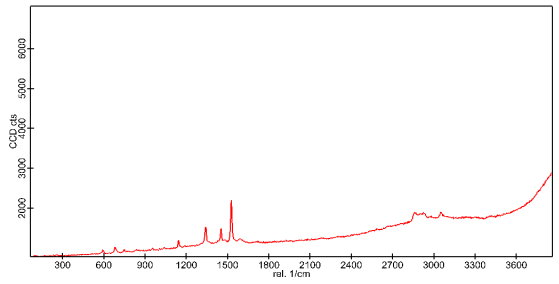

(b) Station 7

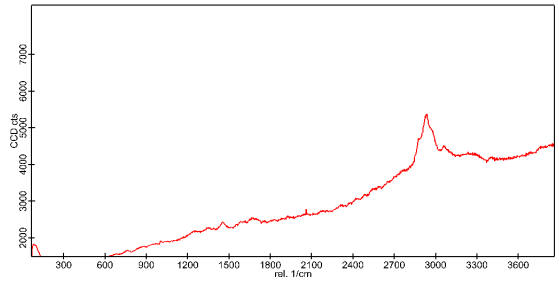

(c) Station 8

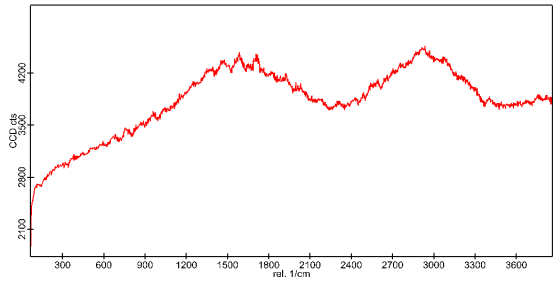

(d) Station 8, new particle

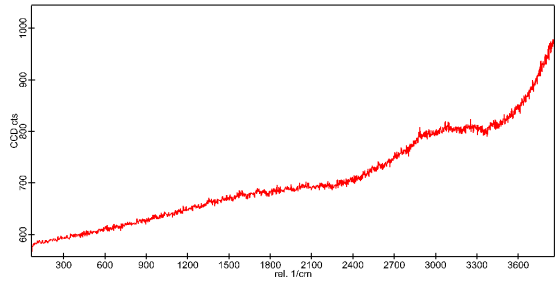

(e) Station 8, new particle II

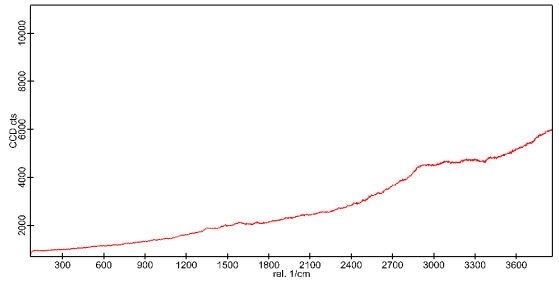

(f) Station 8, new particle III

Figure C.3.2: Lofoten particles day 1

C.3.3 III

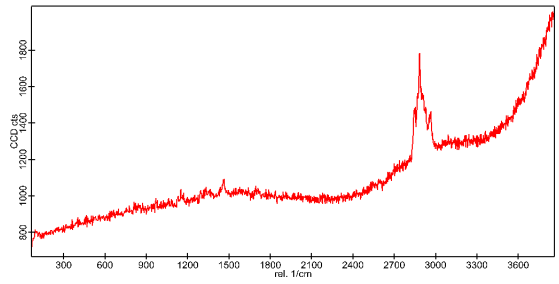

(a) Station 8, new particle IV

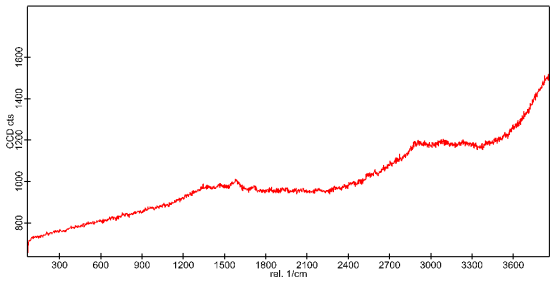

(b) Station 8, new particle V

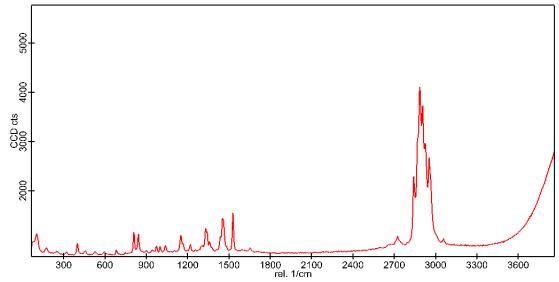

(c) Station 10

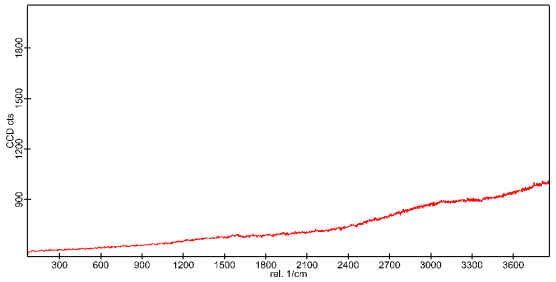

(d) Station 11

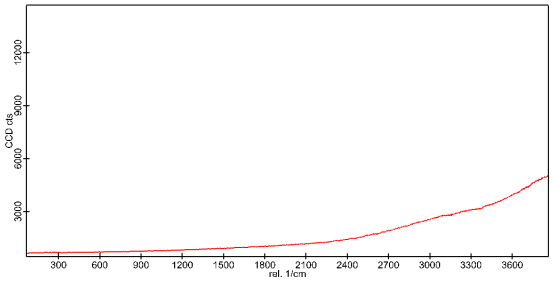

(e) Station 11, new particle

Figure C.3.3: Lofoten particles day 1 and 2

C.3.4 IV

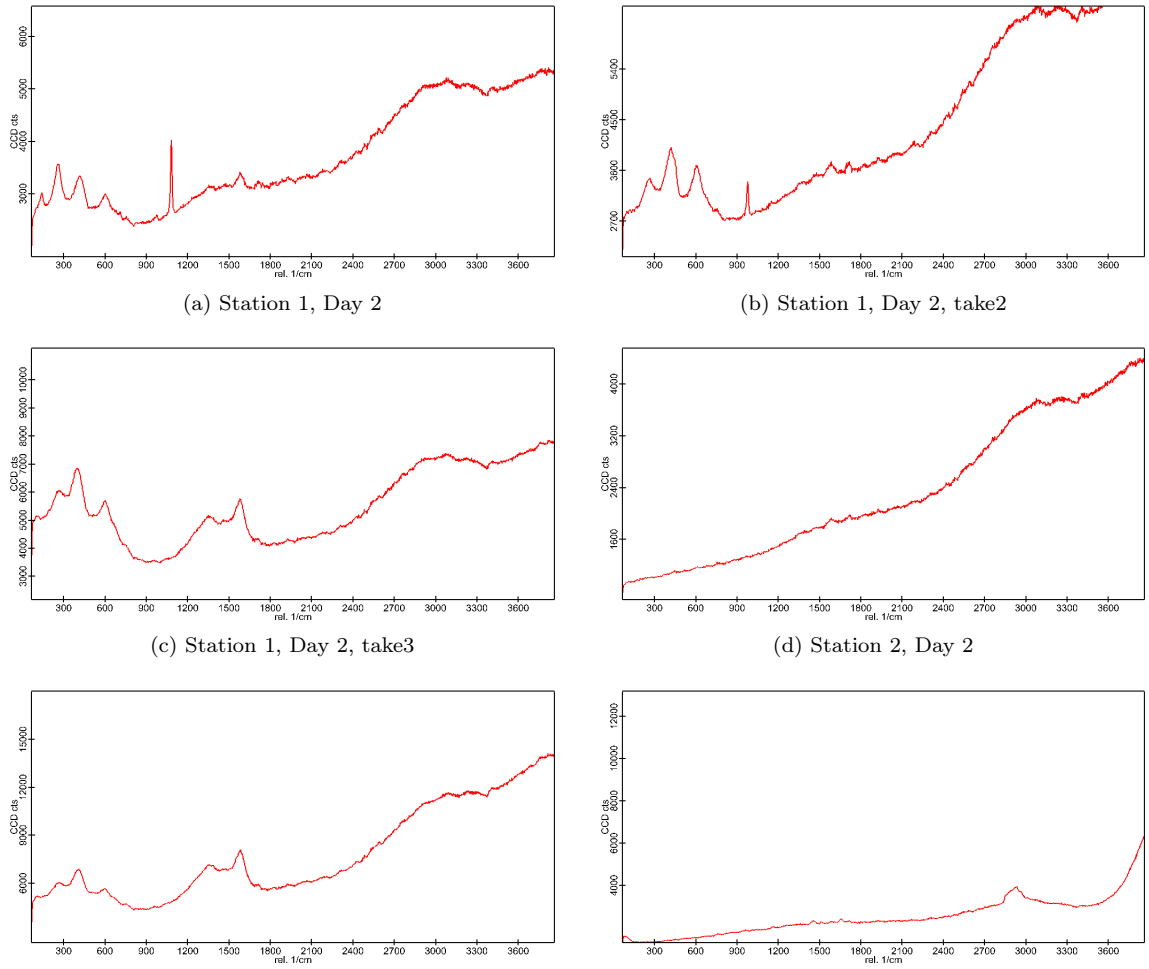

(a) Station 1, Day 2

(b) Station 1, Day 2, take2

(c) Station 1, Day 2, take3

(d) Station 2, Day 2

(e) Station 1, Day 2, organic particle

(f) Station 6, Day 2

Figure C.3.4: Lofoten particles day 1 and 2

Appendix D

Photos of the Samples

D.1 HDPE

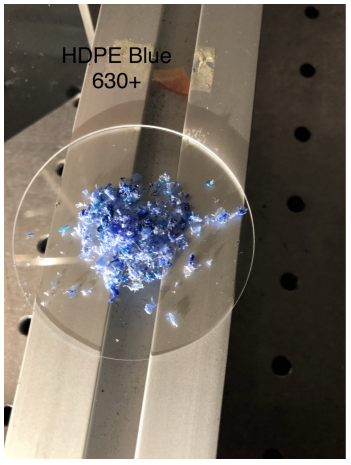

(a) HDPE Blue, larger than 630 microns

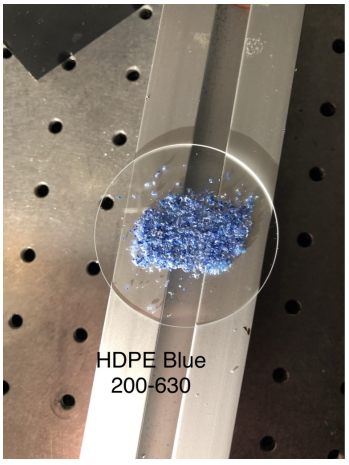

(b) HDPE Blue, smaller than 630, but larger than 200 micron

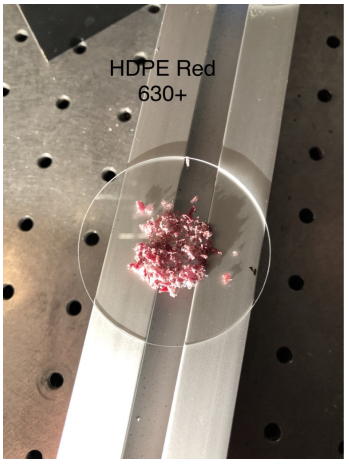

(c) HDPE Red, larger than 630 micron

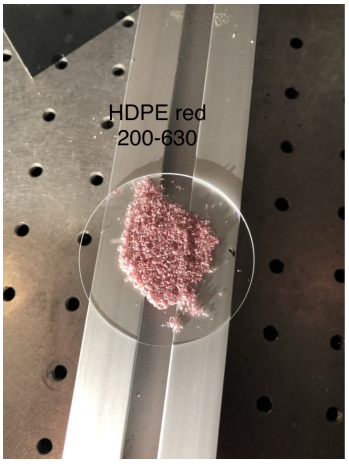

(d) HDPE Red, smaller than 630, but larger than 200 micron

Figure D.1.1: Pictures of HDPE samples

D.2 LDPE

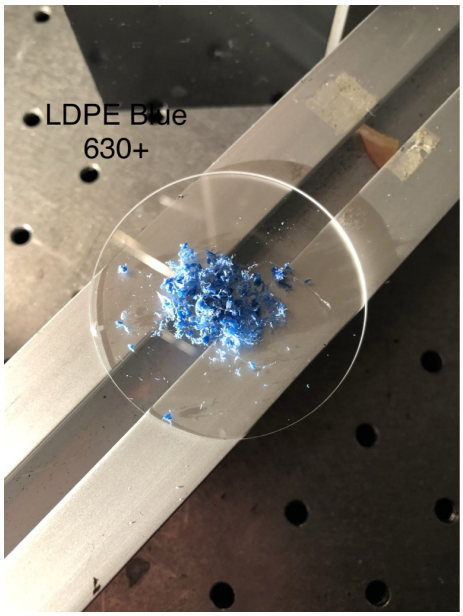

(a) LDPE Blue, larger than 630 micron

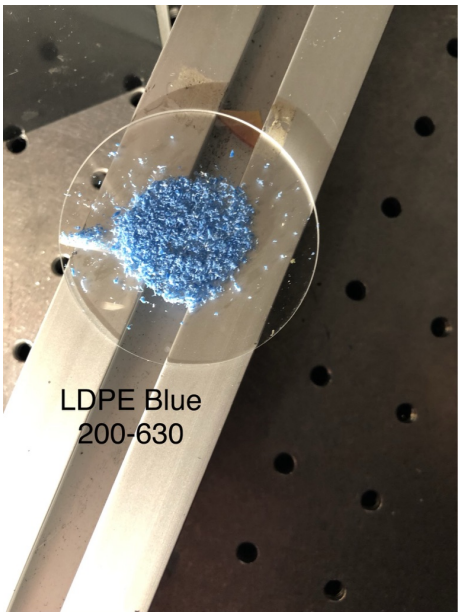

(b) LDPE Blue, smaller than 630, but larger than 200 micron

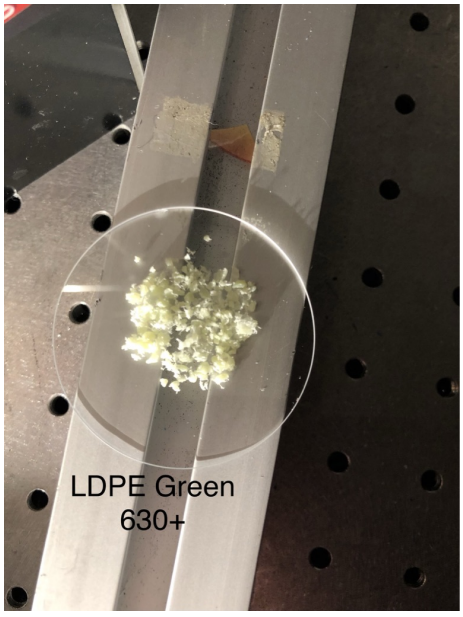

(c) LDPE Green, larger than 630 micron

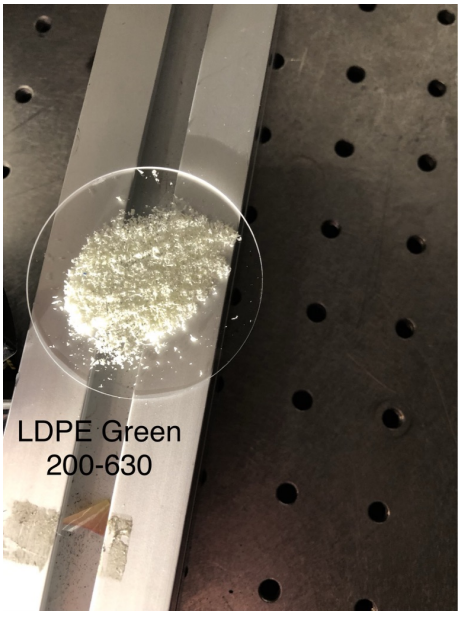

(d) LDPE Green, smaller than 630, but larger than 200 micron

Figure D.2.1: Pictures of LDPE samples

D.3 PET

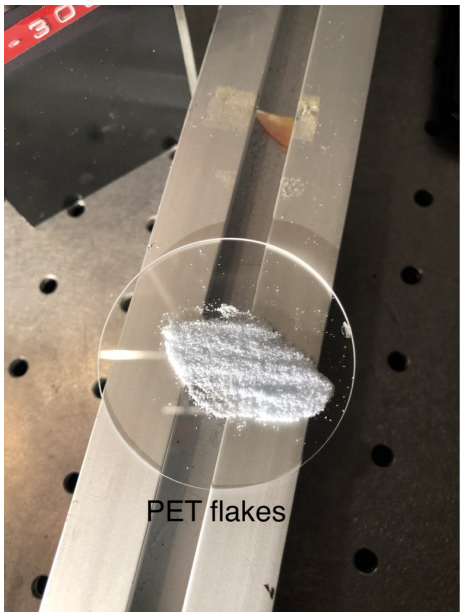

(a) PET Flakes, smaller than 200 micron

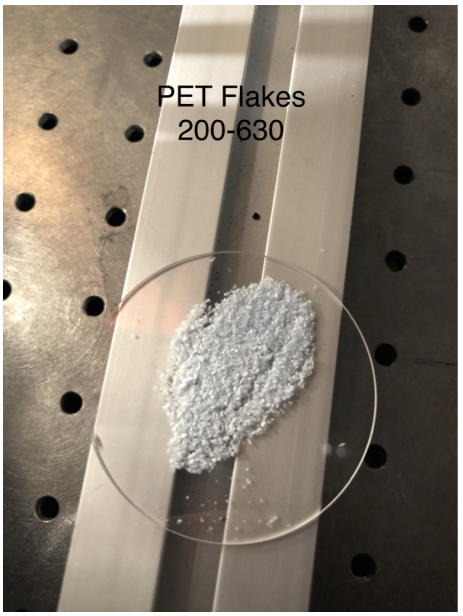

(b) PET Flakes, smaller than 630, but larger than 200 micron

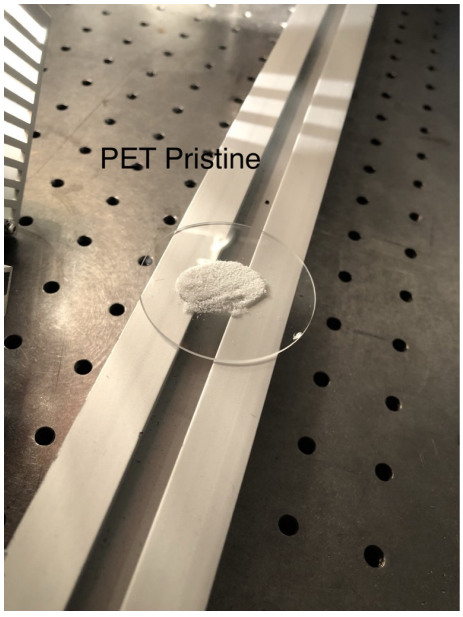

(c) PET Pristine, smaller than 200 micron

(d) PET Pristine, smaller than 630, but larger than 200 micron

Figure D.3.1: Pictures of PET samples

D.4 PP

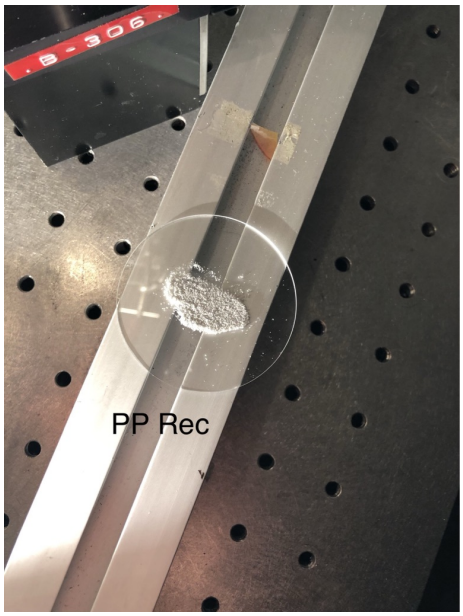

(a) PP Recycled, smaller than 200 micron

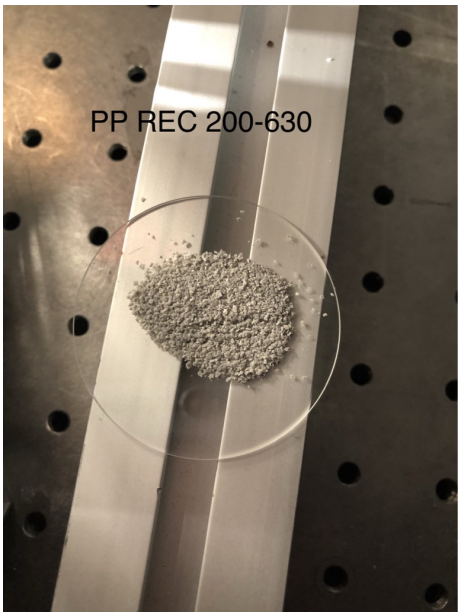

(b) PP Recycled, smaller than 630, but larger than 200 micron

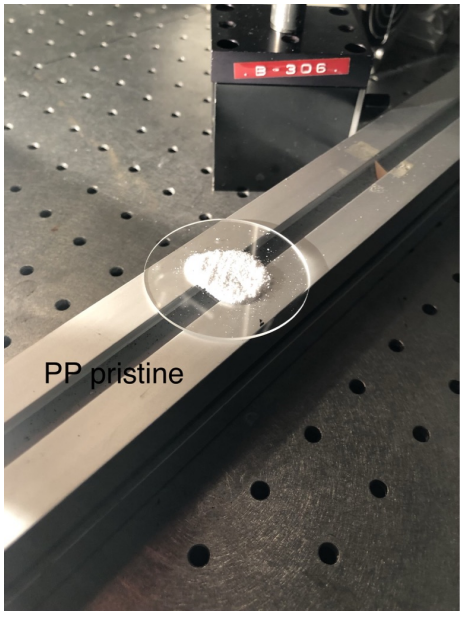

(c) PP Pristine, smaller than 200 micron

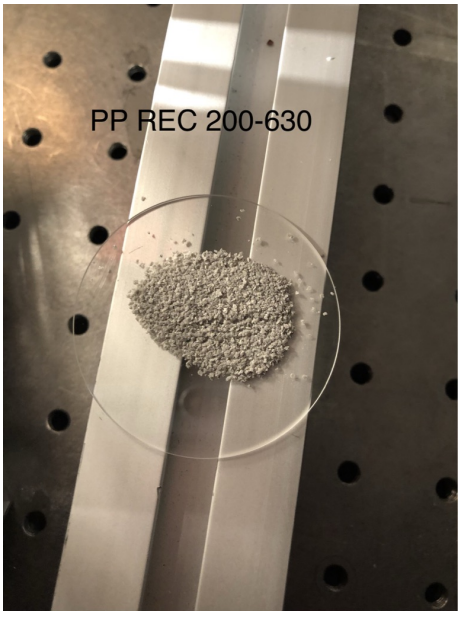

(d) PP Pristine, smaller than 630, but larger than 200 micron

Figure D.4.1: Pictures of PP samples

D.5 PS

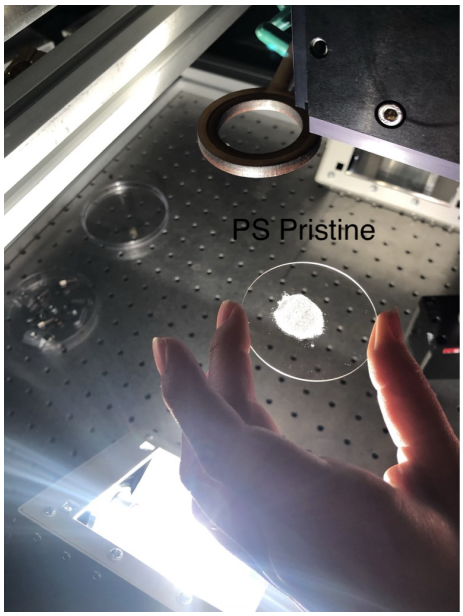

(a) PS Pristine, smaller than 200 micron

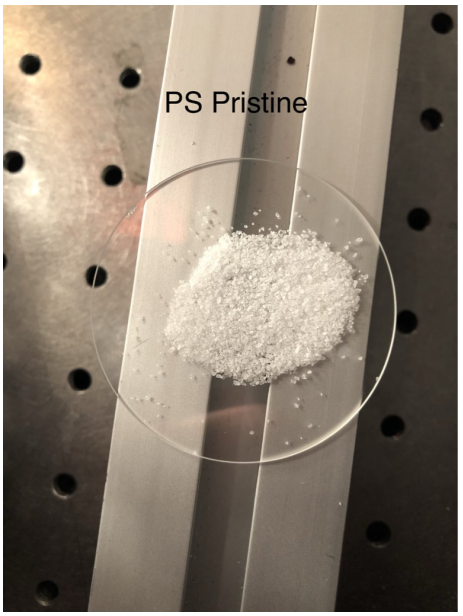

(b) PS Pristine, smaller than 630, but larger than 200 micron

Figure D.5.1: Pictures of PS samples

D.6 PVC

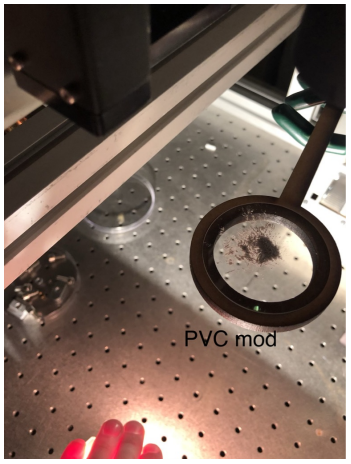

(a) PVC Modified, smaller than 200 micron

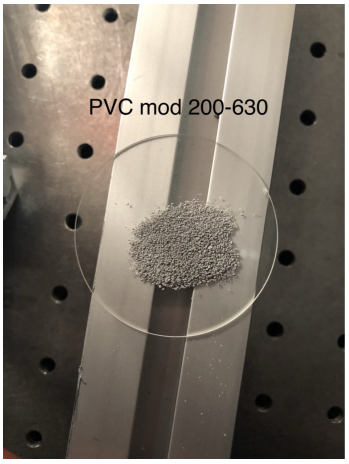

(b) PVC Modified, smaller than 630, but larger than 200 micron

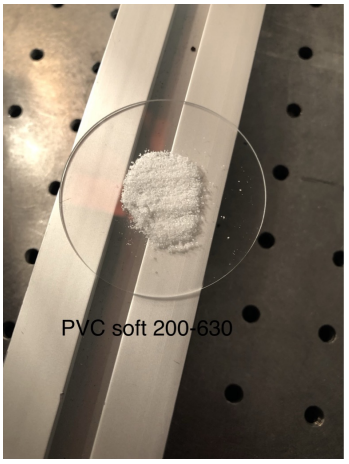

(c) PVC Soft, smaller than 630, but larger than 200 micron

Figure D.6.1: Pictures of PVC samples

D.7 Through Microscope

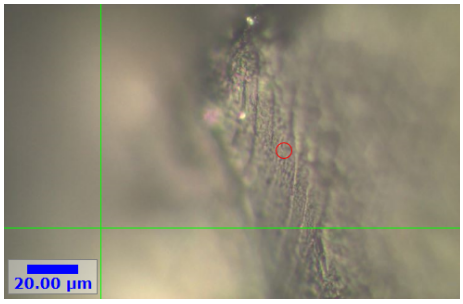

(a) PSpristine, smaller than 630, but larger than 200 micron, take 1

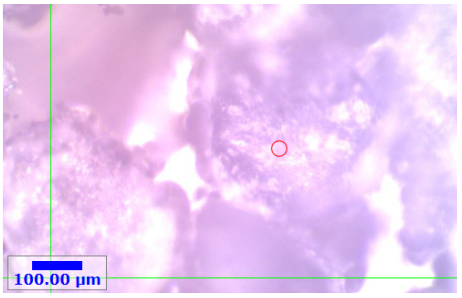

(b) PSpristine, smaller than 630, but larger than 200 micron, take 1 with water

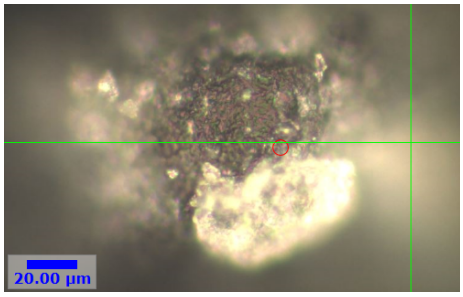

(c) PSpristine, smaller than 630, but larger than 200 micron, take 2

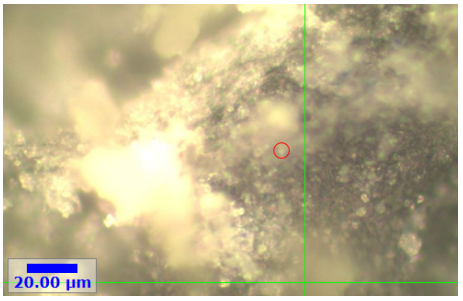

(d) PVCmodified, smaller than 630, but larger than 200 micron, take 1

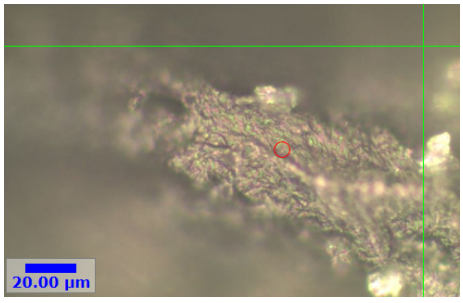

(e) PVCsoft, smaller than 630, but larger than 200 micron, take 2

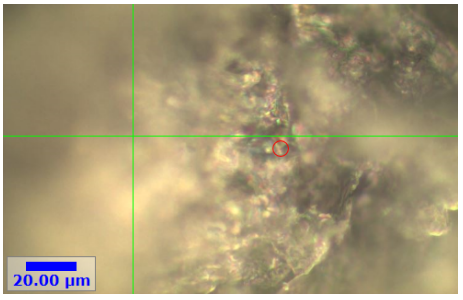

(f) PPpristine, smaller than 630, but larger than 200 micron, take 2

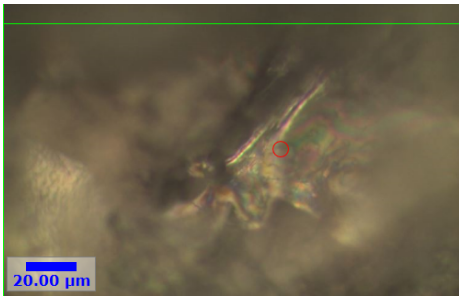

(g) PETflakes, smaller than 630, but larger than 200 micron, take 2

Figure D.7.1: Plastic samples through the microscope

Appendix E

Photos from Field trip to Lofoten

Figure E.0.1: Photos from field trip to Lofoten

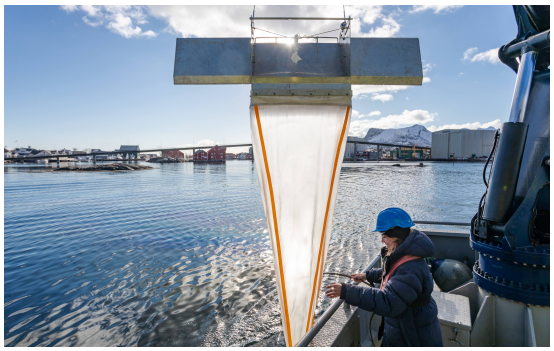

Figure E.0.2: Photos from field trip to Lofoten II

Emilie M. Hyrum Dahl & Andreas Ø.R. Stien

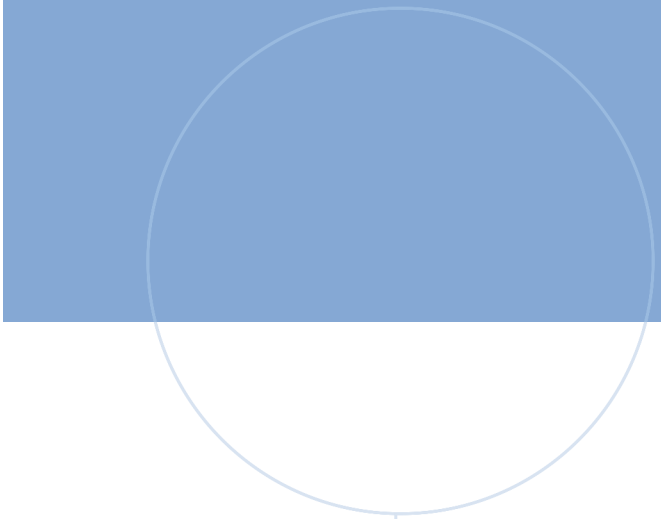

NTNU
Kunnskap for en bedre verden